



THÈSE

# Thermal-hydraulic numerical simulation of fuel sub-assembly for Sodium-cooled Fast Reactor

*(Simulation numérique de la thermohydraulique de l'assemblage  
combustible du Réacteur à Neutrons Rapides refroidi au sodium)*

présentée devant  
L'UNIVERSITÉ D'AIX-MARSEILLE

pour obtenir le grade de

**DOCTEUR**

ÉCOLE DOCTORALE (ED 353)  
"Sciences pour l'Ingénieur : Mécanique, Physique, Micro et Nanoélectronique"

DISCIPLINE : Mécanique et physique des fluides

présentée par :

**Aakanksha SAXENA**

soutenue le 2/10/2014

a été évaluée par un jury composé des personnes suivantes :

Jean-Luc HARION	Professeur, Ecole des Mines de Douai	Rapporteur
Camille SOLLIEC	Chargé de recherche, Ecole des Mines de Nantes	Rapporteur
Marc MEDALE	Professeur, Ecole Polytechnique de Marseille	Examineur
Pablo RUBIOLO	Professeur, INP Grenoble	Examineur
Manuel SAEZ	Chef de Laboratoire, CEA Cadarache	Examineur
Thierry CADIOU	Ingénieur, CEA Cadarache	Invité
Stéphane VIAZZO	Maître de conférences, Université Aix-Marseille	Directeur de thèse

---

\*Thèse préparée au Laboratoire d'Etudes et de Simulation des Systèmes de Commissariat à l'Energie Atomique et aux Energies Alternatives, Cadarache (13115 Saint Paul lez Durance)



*“In a day, when you don't come  
across any problems - you can be  
sure that you are travelling in a  
wrong path”*

*— Swami Vivekananda*





*Dedicated to my dear grandfather*  
*Late Shri. L.N. Saxena*



# ABSTRACT

---

The thesis focuses on the numerical simulation of sodium flow in wire wrapped sub-assembly of Sodium-cooled Fast Reactor (SFR).

First calculations were carried out by a time averaging approach called RANS (Reynolds-Averaged Navier-Stokes equations) using industrial code STAR-CCM+. This study gives a clear understanding of heat transfer between the fuel pin and sodium. The main variables of the macroscopic flow are in agreement with correlations used hitherto. However, to obtain a detailed description of temperature fluctuations around the spacer wire, more accurate approaches like LES (Large Eddy Simulation) and DNS (Direct Numerical Simulation) are clearly needed. For LES approach, the code TRIO\_U was used and for the DNS approach, a research code was used. These approaches require a considerable long calculation time which leads to the need of representative but simplified geometry.

The DNS approach enables us to study the thermal hydraulics of sodium that has very low Prandtl number inducing a very different behavior of thermal field in comparison to the hydraulic field. The LES approach is used to study the local region of sub-assembly. This study shows that spacer wire generates the local hot spots ( $\sim 20^{\circ}\text{C}$ ) on the wake side of spacer wire with respect to the sodium flow at the region of contact with the fuel pin. Temperature fluctuations around the spacer wire are low ( $\sim 1^{\circ}\text{C}$ - $2^{\circ}\text{C}$ ). Under nominal operation, the spectral analysis shows the absence of any dominant peak for temperature oscillations at low frequency (2-10 Hz). The obtained spectra of temperature oscillations can be used as an input for further mechanical studies to determine its impact on the solid structures.

**Key words** : Turbulent heat transfer, Low Prandtl number, Sodium cooled Fast Reactor (SFR), Sub-assembly with spacer wire, Thermal-hydraulic, ASTRID, Direct Numerical Simulation (DNS), Large Eddy Simulation (LES)

# RÉSUMÉ

---

La thèse porte sur la simulation numérique de l'écoulement du sodium pour les assemblages de réacteurs à neutrons rapides à caloporteur sodium de type aiguille à fil espaceur.

Des premiers calculs réalisés par une approche moyennée de type RANS (Reynolds-Averaged Navier-Stokes) à l'aide du code industriel STAR-CCM+. De cette modélisation, il ressort une meilleure compréhension des transferts de chaleur opérés entre les aiguilles et le sodium. Les principales grandeurs macroscopiques de l'écoulement sont en accord avec les corrélations. Cependant, afin d'obtenir une description détaillée des fluctuations de température au niveau des fils espaceur, une approche plus détaillée de type LES (Large Eddy Simulation) et DNS (Direct Numerical Simulation) est apparue indispensable. Pour la partie LES, le code TRIO\_U a été utilisé. Concernant la partie DNS, un code de recherche a été utilisé. Ces approches requièrent des temps de calculs considérables qui ont nécessité des géométries représentatives mais simplifiées.

L'approche DNS permet d'étudier l'écoulement à bas nombre de Prandtl, qui induit un comportement très différent du champ thermique relativement au champ hydraulique. Le calcul LES de l'assemblage montre que la présence du fil espaceur génère l'apparition de points chauds locaux ( $\sim 20^\circ\text{C}$ ) en aval de celui-ci par rapport à l'écoulement sodium, au niveau de son contact avec l'aiguille. Les fluctuations de température au niveau des fils espaceur sont faibles ( $\sim 1^\circ\text{C}$ - $2^\circ\text{C}$ ). En régime nominal, l'analyse spectrale montre l'absence de grande amplitude d'oscillations de température à basse fréquence (2-10 Hz); les conséquences sur la tenue mécanique des structures devront être analysées.

**Mots clés :** Transfert de chaleur, Bas nombre de Prandtl, Réacteurs à Neutrons Rapides, Assemblage avec fil espaceur, Ecoulement turbulent de Sodium, Thermohydraulique, ASTRID, Large Eddy Simulation (LES), Direct Numerical Simulation (DNS)

# ACKNOWLEDGEMENTS

---

A large number of people have contributed during the three years of my work to obtain the important results that have enabled me to defend my Ph.D. thesis.

I would first like to thank **Stéphane Viazzo** for accepting the proposition of being the director of my thesis project and his full support during these three years. Subsequently, I would like to thank my supervisor **Thierry Cadiou** and the head of my lab **Manuel Saez** for their unremitting advice and guidance throughout my thesis. Their efforts to help me control and improve this manuscript are very much appreciated. I would also like to thank my jury for taking time to read and judge this work along with their valuable remarks to perfect this manuscript.

My thanks also go to **David Plancq** for accepting me as a Ph.D. candidate in the lab and providing his support during and after his tenure as the head of my lab. I want to thank him for the “entretien annule 2012” that was very motivating and confidence boosting.

I would also take this opportunity to thank **Ulrich Bieder** for his indispensable help in facilitating my understanding of the subject and code Trio\_U. His expertise and guidance helped me to successfully complete my simulations. Thanks to him for all the video conference sessions, coming to Cadarache for meetings, hosting me in CEA Grenoble and giving me an opportunity to present my work in front of thermal-hydraulic experts.

I am also grateful to **Alain Conti** to give acces to his powerful computer in order to perform my long simulations, **Michel Pelletier** for the valuable discussion on mechanics of fuel pin, **Bernard Valentin** for presenting me the sub-channel approach and **Guillaume Brillant** for sharing his experience with LES approach.

Again much thanks to my director **Stéphane Viazzo** who welcomed me a number of times in his lab for learning the university in-house code developed by him and helping me with the difficulties encountered during my DNS simulations. The time and help provided by him for the development of his code in context to the subject of my thesis is also highly appreciated.

My thanks also go to **Frederic Ducros** for valuable discussions on my subject and proposition of various possible directions in order to solve the challenges. Thanks to **J-M. Seiler** who made me realize the challenges faced by experimentalist for accurate measurements at the scale of spacer wire. Thanks to him for sharing his valuable knowledge about GR19 experiment performed in CEA Grenoble and providing me information about other experiments performed with sodium in CEA.

I would also like to thank the **Pierre Leduc** from TRIO\_U support team and **Oliver Bachman** from STAR\_CCM+ support team, Paris for being readily available throughout the course of my thesis.

Much thanks goes again to **Thierry Cadiou** who not only guided me for my thesis project but also made my stay and journey from India to south of France much easier. Not to forget all the initial help to deal with the French administration. He also helped me with the translation of French conversations and documents during the initial phase that lasted for at least a year until I improved my French skills.

Thanks to **SESI service** for financing my French lessons in CEA which helped me to learn French and enabled me to have access to the French only speaking community of France in order to learn more about France and French culture. The real thanks would have been by writing my acknowledgements in French but in that case I would have been short of words to express my sincere gratitude to all of you. Also even if I have improved my French still it is limited to only speaking skills. Writing in French is a completely different and still the most difficult task.

I want to thank my lab mates for their kind hospitality. Thanks to their efforts and patience to understand my slow French as well as fast English. The different social, scientific and personal discussions helped me in various ways. Thank to you all - **Nicolas Alpy** for discussions on sodium; **David Haubensack** for helping me in STARCCM+; **Yves Lejeail** for discussions on mechanics; **Nicolas Shmidt and Annick Tosello** for sharing information on various social activities and CEA médiathèque; **Romain Dos Santos, Alex and Lucile** for the lunch time conversations in French; **Jorge Perez Manes and Hong-Son Pham** for sharing with me the experience of being a foreigner in France; **Gilles Avakian** for giving me encouragement to keep on improving my French so that I can participate with him in his

laugh on the funny jokes; **Thierry Jeanne** for the continuous motivation; **Pierre Allegre, Pierre Lamagnere, David Gentet, Helene Lelaidier, Joseline Ayme** for morning coffee room conversations. Thanks to **Olivier Fabbri** who has been a good “colleague de bureau” and a good friend without whom the time I passed in my lab would not have been as enjoyable as it was.

Thanks to **Raboin Serge** for morning Indian salutation ‘Namaste’ and the inspiration I have after seeing your interest in Yoga and Sanskrit. **Pierre Richard** who has probably seen much more parts of India than I and gives me the motivation to do a “Tour d’Inde” when I go back.

I want to thank my **fellow Ph.D.** colleagues and **ASTHEC association**. They made my stay comfortable and made these three years an enriching experience. I not only enhanced my knowledge scientifically but also culturally. Thanks to all my friends in France and India along with special thanks to **high score group**. You all made a home away from home and helped me to deal with the cultural differences between India and France. The travel we had together and the cooking sessions helped to explore many new things. Thanks to **Claudia Norscini** for being a great friend and my stress reliever who made me realize Indians and Italians share a great bonding.

Much thanks to my former professors and teachers. Without their continuing efforts, I would never have gotten this far and as such I’m greatly indebted to them. Special thanks to **Prof. Raghuvir Singh** who’s counselling during my masters and also during my thesis helped me at the phase when I was confronted with difficult phase at work.

I will like to thank my **grandfather** to whom I dedicate my thesis, **Late Shri. L. N. Saxena**. His support and his confidence in me gave me the motivation and conviction to my parents to let me come all the way from India to France to pursue this thesis project. I am sure that if he was amongst us then he would have been the happiest and the proudest person to see me finishing up my work. I want to thank my parents **Ajai Saxena and Anju Saxena** who have been really supportive throughout my life. Thanks to my sister **Arunima Saxena** who has been my best friend and my teacher throughout my studies. Special thanks to my brother in law **Nikhil Bhardwaj** for his support and care towards me and my family. At the end, I don’t know whether I should thank my husband **Ronak Patel** or I should thank my thesis project because of which I met him in France. Nonetheless, without his support, the last and the most

difficult phase of my thesis project would not have been as soothing as it was. Last but not the least I want to thank my new family my in-laws in Gujarat – my dad **Vrajesh Patel**, my mom **Seema Patel** and my sister **Neha Patel** for their love and wishes.

Thanks to everyone for your wishes and support in one way or another. My sincere apologies to the people not explicitly mentioned here but my thanks go to you as well.



Aakanksha Saxena

18/09/2014

CEA Cadarache



# TABLE OF CONTENTS

---

<b>ABSTRACT .....</b>	<b>vii</b>
<b>RESUME.....</b>	<b>viii</b>
<b>ACKNOWLEDGEMENTS .....</b>	<b>ix</b>
<b>TABLE OF CONTENTS.....</b>	<b>xiii</b>
<b>NOMENCLATURE.....</b>	<b>xvii</b>
<b>INTRODUCTION .....</b>	<b>1</b>
<b>CHAPTER 1-STATUS OF ART .....</b>	<b>10</b>
1.1 Generalities.....	11
1.1.1 Instantaneous equations of fluid flow and heat transfer .....	11
1.1.2 Turbulence .....	12
1.1.3 CFD methods.....	16
1.2 Heat transfer in liquid sodium .....	21
1.2.1 Introduction .....	21
1.2.2 Prandtl number .....	21
1.2.3 Energy Spectrum .....	23
1.2.4 Wall bounded flows.....	26
1.2.5 Reynolds analogy limitation.....	31
1.2.6 Turbulent Prandtl number.....	32
1.3 Thermal hydraulic study of sub-assembly .....	38
1.3.1 Introduction .....	38
1.3.2 Experiments.....	38
1.3.3 RANS studies .....	41
1.3.4 LES studies .....	45
1.3.5 DNS studies .....	46
1.3.6 Hot spot studies .....	48
1.4 Summary .....	49
<b>CHAPTER 2-NUMERICAL METHODS AND TOOLS.....</b>	<b>51</b>
2.1 Equations for incompressible flow.....	52
2.2 CFD –Introduction and Methods.....	54
2.3 Reynolds Averaged Navier-Stokes method (RANS) .....	56

2.3.1 Principle.....	56
2.3.2 RANS equation.....	57
2.3.3 Closure Problem .....	58
2.3.4 RANS turbulence models .....	61
2.3.5 STAR-CCM+ code.....	65
2.4 Large Eddy Simulation (LES).....	66
2.4.1 Principle.....	66
2.4.2 LES equations.....	69
2.4.3 Closure problem .....	69
2.4.4 LES turbulence model .....	72
2.4.5 TRIO_U code .....	74
2.5 Direct Numerical Simulation (DNS).....	76
2.5.1 Principle.....	76
2.5.2 DNS equations.....	77
2.5.3 DNS code.....	78
2.5.4 Modified DNS code.....	85
2.6 Boundary conditions .....	87
2.7 Wall treatment .....	90
2.8 Summary .....	93
<b>CHAPTER 3-NUMERICAL STUDY OF TURBULENT HEAT TRANSFER IN LIQUID SODIUM .....</b>	<b>94</b>
3.1 Introduction .....	95
3.2 Data set.....	97
3.3 Numerical method .....	101
3.4 Meshing.....	101
3.5 Boundary and initial conditions .....	104
3.5.1 Source term for periodic flow in axial direction .....	105
3.5.2 Initial condition .....	106
3.5.3 Auto-correlation in periodic directions .....	106
3.6 Validation with DNS of air (Pr-0.7).....	111
3.6.1 Mean velocity .....	112
3.6.2 Root-mean-square velocity fluctuations and Reynolds shear stresses .....	114
3.6.3 Mean temperature .....	117
3.6.4 Root-mean-square temperature fluctuations and turbulent heat flux .....	118

3.7 Results for DNS of sodium ( $Pr=0.004$ ) .....	120
3.7.1 Instantaneous flow and temperature fields .....	122
3.7.2 Mean Temperature profile .....	125
3.7.3 Root-mean-square of temperature fluctuations .....	127
3.7.4 Turbulent heat flux .....	128
3.7.5 Energy and temperature spectra .....	130
3.8 Asymptotic behavior .....	131
3.9 LES study for sodium.....	138
3.9.1 Numerical method .....	139
3.9.2 Meshing .....	140
3.9.3 Boundary condition .....	142
3.9.4 Initial conditions .....	143
3.9.5 Post processing tool for time averaged results .....	145
3.9.6 Mean velocity and turbulent statistics .....	146
3.9.7 Mean temperature and thermal statistics .....	148
3.10 Summary .....	151
<b>CHAPTER 4-THERMAL-HYDRAULIC STUDIES OF SUB-ASSEMBLY BY CFD</b>	<b>152</b>
4.1 RANS .....	153.
4.1.1 Computational domain.....	153
4.1.2 Numerical tool .....	156
4.1.3 Meshing .....	156
4.1.4 Boundary and initial conditions.....	159
4.1.5 Pressure drop .....	162
4.1.6 Velocity.....	163
4.1.7 Temperature.....	165
4.1.8 Nusselt number .....	167
4.1.9 Summary.....	168
4.2 LES.....	169
4.2.1 Numerical tool .....	169
4.2.2 Computational domain.....	170
4.2.3 Meshing .....	172
4.2.4 Boundaryconditions.....	173
4.2.5 Initial conditions .....	175
4.2.6 Flow visualization.....	177

4.2.7 Time averaged results – Comparison with RANS study .....	179
4.2.8 Time averaged results – Axial distribution .....	182
4.2.9 Statistics of order 1: Root mean square values.....	184
4.2.10 Power spectral density .....	187
4.2.11 Summary.....	190
<b>CONCLUSIONS. ....</b>	<b>191</b>
<b>FUTURE PERSPECTIVES .....</b>	<b>195</b>
<b>BIBLIOGRAPHY .....</b>	<b>197</b>
<b>APPENDIX .....</b>	<b>212</b>
A Meshing tool .....	212
B Pressure drop correlations.....	215
C Version abrégée en Français .....	217
<b>TABLE OF FIGURES .....</b>	<b>241</b>
<b>LIST OF TABLES .....</b>	<b>245</b>

# NOMENCLATURE

Symbol	Unit	Description	Formula
<b>Latin</b> (capital letters)			
$A_f$	$m^2$	Flow area	
$C_p$	J/kg-K	Specific heat capacity	
$D_h$	m	Hydraulic diameter	$D_h = 4A_f/P_w$
$D_p$	m	Diameter of fuel pin in SFR sub-assembly	
$D_w$	m	Diameter of spacer wire in SFR sub-assembly	
$E_T$	W/Hz	Spectral energy density for temperature fluctuations	
$E$	W/Hz	Spectral energy density for velocity fluctuations	
$E_f$	$W/m^2/K/s^{0.5}$	Thermal Effusivity	$\sqrt{\lambda\rho C_p}$
$H$	m	Helical pitch of the spacer wire	
$K$	$m^{-1}$	Wave number	$K = \frac{2\pi}{l}$
$L_z$	m	Axial (streamwise direction) length of the computational domain	
$L$	m	Side of hexagonal wall	
$N_{pins}$	-	Number of fuel pins in the sub-assembly	
$N_{rings}$	-	Number of rings of fuel pins in sub-assembly	
$Nu$	-	Nusselt number	
$P$	m	Pitch of the fuel pin	
$Pr$	-	Prandtl number	$Pr = \nu/\alpha$
$P_w$	m	Wetted perimeter for the sub-assembly	
$P_{w-pins}$	m	Wetted perimeter for the fuel pins	
$Pr_t$	-	Turbulent Prandtl number	
$R_j$	m	Radius of surface j	
$R^*$	-	Radius ratio	$\frac{R_{int}}{R_{ext}}$
$Re_{Dh}$	-	Reynolds number	$\frac{u_b D_h}{\nu}$
$Re_\tau$	-	Friction Reynolds number	$\frac{u_\tau D_h}{\nu}$
$Re_c$	-	Critical Reynolds number	

$Re$	-	Reynolds number	$\frac{u^* l^*}{\nu}$
$S_{ij}$	Hz	Rate of deformation	$\frac{1}{2} \left( \frac{\partial u_i}{\partial x_j} + \frac{\partial u_j}{\partial x_i} \right)$
$\bar{S}_{ij}$	Hz	Mean rate of deformation	$\frac{1}{2} \left( \frac{\partial \bar{u}_i}{\partial x_j} + \frac{\partial \bar{u}_j}{\partial x_i} \right)$
$\langle S_{ij} \rangle$	Hz	Filtered rate of deformation	$\frac{1}{2} \left( \frac{\partial \langle u_i \rangle}{\partial x_j} + \frac{\partial \langle u_j \rangle}{\partial x_i} \right)$
$s_T$	K/s	Body force term for transport equation of temperature	
$f$	m <sup>2</sup> /s	Momentum source term	
$T$	K	Temperature	
$T_b$	K	Bulk temperature	
$T^+$	-	Dimensionless temperature	$\frac{T - T_b}{T_\tau}$
$T_\tau$	K	Friction temperature	$\frac{q_w}{\rho C_p u_\tau}$
$T_w$	K	Wall temperature	
<b>Latin</b> (small letters)			
$e$	m	Flat plate-to-plate distance	
$f_{ext}$	m/s <sup>2</sup>	External momentum source	
$l^*$	m	Characteristic length scale	
$g$	m	Gap between the hexagonal can and fuel pin	
$k$	m <sup>2</sup> /s <sup>2</sup>	Turbulent kinetic energy	$k = \frac{1}{2} (\overline{u_1'^2} + \overline{u_2'^2} + \overline{u_3'^2})$
$l^*$	m	Characteristic length scale	
$l_t$	m	Inertial length scale	
$m$	kg	Mass	
$\dot{m}$	kg/s	Mass flow rate	
$p$	Pa	Pressure	
$q_l$	W/m <sup>2</sup>	Heat flux of surface $l$	
$q^*$	-	Heat flux ratio	$q^* = q_{int}/q_{ext}$
$q_w$	W/m <sup>2</sup>	Wall heat flux	
$r$	-	Coordinate in radial direction	
$t_{transit}$	s	Time taken for one transit in axial direction	

$t$	s	Time	
$u_b$	m/s	Bulk velocity	
$u_l$	m/s	Kolmogorov velocity scale	
$u^*$	m/s	Characteristic velocity scale	
$u_\tau$	m/s	Friction velocity	
$\vec{u}$	m/s	Velocity vector	$(u_1, u_2, u_3)$ or $(u, v, w)$
$w$	m/s	Axial velocity (streamwise velocity)	
$y^+$	-	Wall normal dimensionless distance	
$z$	-	Coordinate in axial direction	
<b>Greek (capital letters)</b>			
$\theta_i^{RANS}$	mK/s	Turbulent heat flux	$-(\overline{u_j T} - \bar{u}_j \bar{T}) = -\overline{u'_j T'}$
$\theta_j^{sgs}$	mK/s	Sub-grid heat flux	$-(\langle u_j T \rangle - \langle u_j \rangle \langle T \rangle)$
$\Delta$	m	Mesh size	
$\bar{\Delta}$	m	LES filter size	
<b>Greek (small letters)</b>			
$\alpha$	m <sup>2</sup> /s	Thermal diffusivity	$\frac{\lambda}{\rho C_p}$
$\alpha_K$	-	Constant of proportionality	
$\alpha'$	-	Coefficient in Ef_stab scheme	
$\delta$	m	Half gap width	$\frac{(R_{ext} - R_{int})}{2}$
$\delta_v$	m	Thickness of hydraulic boundary layer	
$\delta_t$	m	Thickness of thermal boundary layer	
$\varepsilon$	m <sup>2</sup> /s <sup>3</sup>	Energy dissipation rate	
$\varepsilon_T$	m <sup>2</sup> /s <sup>3</sup>	Energy dissipation rate for thermal eddies	
$\eta$	m	Kolmogorov length scale for velocity	
$\eta_T$	m	Kolmogorov length scale for temperature	
$\rho$	kg/m <sup>3</sup>	Fluid density	
$\mu$	kg/m-s	Dynamic viscosity	
$\nu$	m <sup>2</sup> /s	Kinematic viscosity	
$\nu_t$	m <sup>2</sup> /s	Eddy viscosity	
$\nu_t^{sgs}$	m <sup>2</sup> /s	Sub-grid viscosity	
$\theta$	-	Coordinate in circumferential direction	

$\lambda$	W/m-K	Thermal conductivity	
$\tau_{ij}$	Pa	Viscous stress	
$\tau_{ij}^{sgs}$	Pa	Sub-grid stress	$-(\langle u_i u_j \rangle - \langle u_i \rangle \langle u_j \rangle)$
$\tau_{ij}^{RANS}$	Pa	Reynolds stress	$-(\overline{u_i u_j} - \overline{u_i} \overline{u_j}) = -\overline{u_i' u_j'}$
$\tau_w$	Pa	Wall shear stress	
$\tau_\eta$	s	Kolmogorov time scale	
$\phi$	-	Flow variable (Pressure, Velocity or Temperature)	
<b>Subscripts</b>			
$int$	Inner wall		
$ext$	Outer wall		
$l$	Surface of the wall, $l=int$ or $ext$		
$b$	Bulk value		
$rms$	Root mean square		
$i,j,k$	Tensor indices		
<b>Superscripts</b>			
$+$	Normalized by $u_\tau, \nu$ and $T_\tau$		
$'$	Fluctuations in time		
$-$	Variable for RANS modelling (statistically averaged in time)		
$\langle \rangle$	Variable in LES modelling (filtered quantity)		
$''$	Sub-grid quantities		



---

**Abbreviations**

---

CEA	Alternative Energies and Atomic Energy Commission (Commissariat à l’Energie Atomique et aux Energies Alternatives in French)
SFR	Sodium-cooled Fast Reactor
CFD	Computational Fluid Dynamics
RANS	Reynolds Averaged Navier-Stokes
LES	Large Eddy Simulation
DNS	Direct Numerical Simulation
PWR	Pressurized Water Reactors
IHX	Intermediate Heat eXchanger
ASTRID	Advanced Sodium Technological Reactor for Industrial Demonstration
CFV	French acronym for Low sodium void effect core
SGS	Sub-Grid Scale
SST	Shear Stress Transport
ORNL	Oak-Ridge National Laboratory
ANL	Argonne National Laboratory
WALE	Wall Adapting Local Eddy
CFL	Courant Friedrichs Lewy
MILES	Monotone Integrated Large Eddy Simulation
1-D	1 Dimensional
2-D	2-Dimensional
3-D	3-Dimensional
RSM	Reynolds Stress Model
EVM	Eddy Viscosity Model
AMG	Algebraic Multi Grid
PSD	Power Spectra Density

---

# INTRODUCTION

---

## 1. Context

Contrary to a large majority of Nuclear Reactors in the world cooled by water, the Sodium Fast Reactor (SFR) is a concept cooled by sodium which may play an important role in the future of nuclear energy production because of the excellent potential for natural resource utilization and ability to reduce the volume and lifetime of nuclear waste.

The ASTRID project: Advanced Sodium Technological Reactor for Industrial Demonstration (Gauché, 2011) originated the law of 28 June 2006, which calls for the service of a fourth-generation reactor 2020. After 3 years of study and R & D to explore innovative solutions, the ASTRID project was launched in late 2009; the choice was made for a fast neutron generator power plant cooled by sodium. As a prototype of the SFR technology, ASTRID has the main objective of demonstrating on an industrial scale the advances particularly in terms of safety and operability. ASTRID will be a 1500 MWth reactor, i.e. generating about 600 MWe, which is required to guarantee the representativeness of the reactor core and main components. ASTRID must also integrate feedback from past reactors, especially PHENIX and SUPERPHENIX, with improved safety features to meet the specifications of Generation IV forum. The ASTRID design work is in progress in “Commissariat à l’Energie Atomique et aux Energies Alternatives” (CEA), France.

ASTRID will be a pool type SFR (see Figure 1). In pool type primary system, all the primary sodium is contained inside the main vessel where primary pumps and intermediate heat exchangers (IHX) are plunged through the cover slab of the vessel. The core contains the fissile fuel that undergoes nuclear chain reaction. The energy produced by fission is deposited in fuel in the form of heat and transported to the coolant i.e. liquid sodium that flows from bottom to the top of the core. The hot sodium then circulates through the intermediate heat exchanger where it transfers the energy to the secondary loop and gets cooled down. The cold sodium is then pumped again to the core by pump and the cycle continues. The secondary loop routes the secondary sodium from the IHX to steam generators producing steam that rotates the turbine.

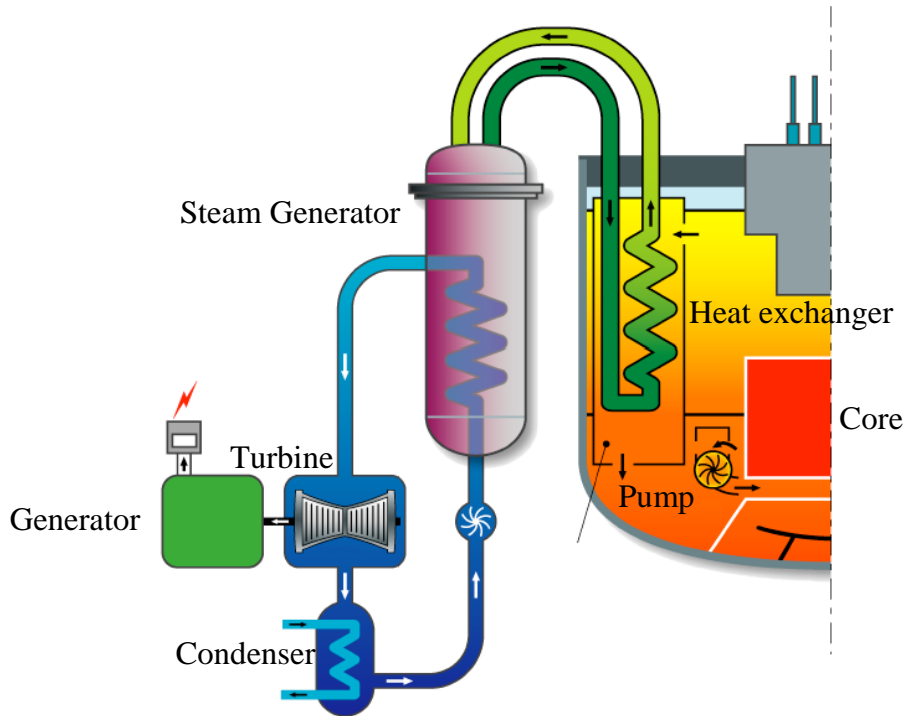


**Figure 1- Schema diagram of SFR pool type reactor**

The heart of the nuclear reactor is the core where energy production takes place. Since 2010, the reference concept for ASTRID core is the CFV (French acronym for low sodium void effect core). Some design optimizations of the core are still going to enhance its performances. The CFV concept is based on negative sodium void effect on the reactivity which implies that the reactivity of the core should decrease in the case of loss of coolant. It is necessary requirement to ensure safety of the reactor and prevent the threat of core melt down. The increase in the reactivity due to sodium void effect is reduced by increasing the neutron leakages. It is characterized by radial and axial heterogeneous geometry design. The radial heterogeneity can be seen in Figure 2. The asymmetrical, crucible-shaped core is composed of inner / outer core fuel assemblies that contains the fissile fuel and undergoes fission reaction producing heat energy. Apart from fuel sub-assemblies there are reflectors sub-assemblies, shielding sub-assemblies and a number of control / shutdown rods. The energy production takes place inside the fuel sub-assembly and so in this thesis we have focused on the fuel sub-assembly. As the core sub-assembly geometry differs from that designed in past, new studies will be required to specify the sodium flow and heat transfer characteristics in the pin bundle.

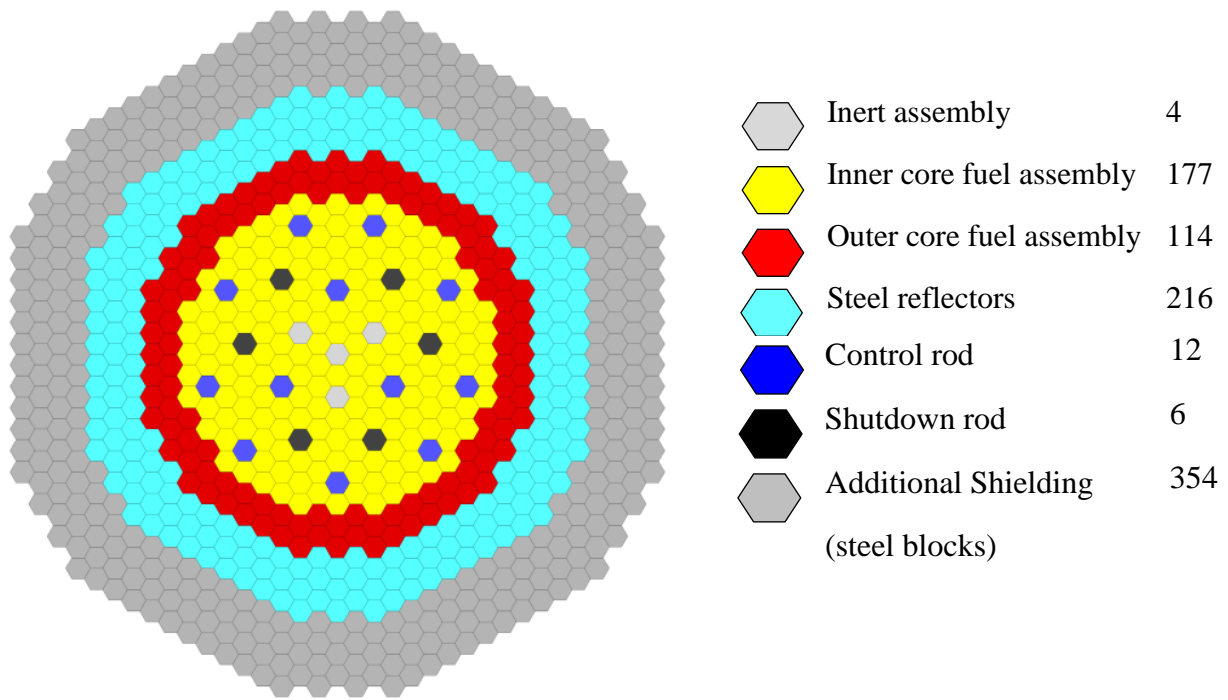


**Figure 2-Representation of the CFV core of ASTRID showing radial heterogeneity**

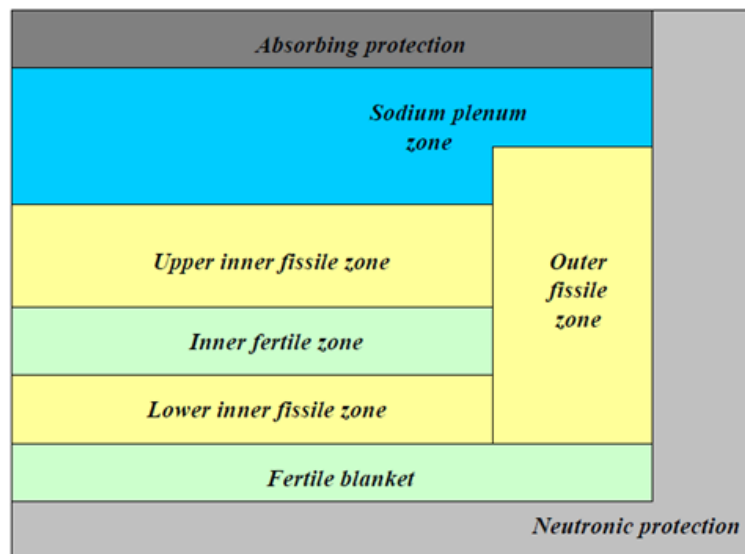


**Figure 3- Representation of the CFV core of ASTRID showing axial heterogeneity**

The CFV inner core has heterogeneous axial fuel column with fertile zone sandwiched between the two fissile zones (see Figure 3). The fissile zone in the inner part of the core is made of  $\text{UPuO}_2$  pellets that undergo nuclear chain reaction producing energy. The thick fertile zone contains fertile material that becomes fissile with neutron bombardment. The liquid sodium is pumped from the side at the bottom of the sub-assembly, extracts the heat generated

in the wire wrapped fuel pins and the heated sodium exits the sub-assembly and goes to the heat exchangers to cool down. The fuel pins contain the fissile material that produces heat energy and fertile material that gets converted in to fissile material (by absorbing neutrons) during the life time of the reactor.

Indeed, the fuel sub-assembly consists of a hexagonal duct wall with 217 fuel pins. The cylindrical fuel pins of diameter  $D_p$  are arranged in a triangular lattice with pitch  $P$  that represents the minimum distance between the two adjacent fuel pins measured from the center of the pin. The fuel pins are separated from each other by a helical wire wrap called as spacer wire. The helical pitch of the spacer wire is represented as  $H$ . The main functions of the spacer wire are:

- To avoid pin-to-pin contact.
- To guard the pin bundle against the flow induced vibrations.
- To avoid the trapping of the coolant.

The helical wire also acts as a mixing device that enhances the heat and mass transfer and also increases the pressure loss.

The top view of the section of sub-assembly for ASTRID with 217 fuel pins and a wire wrapped fuel pin is represented in figure 4.

The two parameters characterizing the sub-assembly geometry are pitch to diameter ratio ( $P/D_p$ ) and helical pitch to diameter ratio ( $H/D_p$ ). The CFV-v2 core (version 2) has  $P/D_p=1.11$  and  $H/D_p=21$ . There are three kinds of sub-channels present in the sub-assembly represented with black dotted lines in Figure 4.

- i. Interior sub-channel which are triangular in shape and present in the center of the sub-assembly.
- ii. Edge sub-channel present along the hexagonal duct wall.
- iii. Corner sub-channel present in the corners of the hexagon.

Due to different shape of the sub-channels, the thermal hydraulic characteristics of the sodium flowing through the sub-assembly are also different which needs a through and deep understanding.

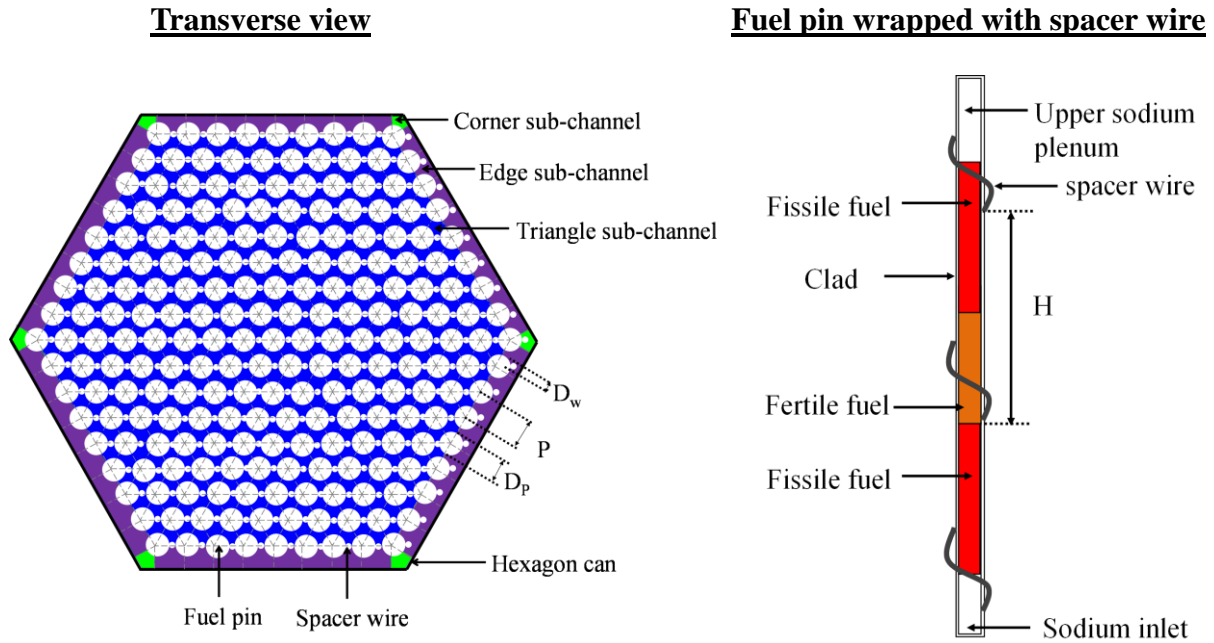


**Figure 4-Representation of different parts of 217 fuel pins sub-assembly on the left (view from above) and fuel pin with helical wrapped spacer wire on the right**

## 2. Thesis objectives

Thermal-hydraulics is recognized as a key scientific subject in the development of SFR (Tenchini, 2010). A thorough understanding of the thermal-hydraulic behavior of core is essential. The goal of the thesis is to understand the thermal-hydraulics at the level of sub-assembly especially near the spacer wire.

The main parameters to be evaluated in the thermal-hydraulic studies are the pressure, temperature and velocity distributions in the sub-assembly that helps to determine the following quantities:

- The total sub-assembly pressure drop including the lower and upper regions of the sub-assembly.
- The clad temperature and especially the clad maximum temperature.
- The hexagonal can temperature for thermo-mechanical analysis.
- The temperature gradients and the maximum temperature of the coolant liquid sodium also referred as hot-spot.

These previous parameters are required for steady-state conditions and for transient situations (reactor shutdown for instance). The maximum clad temperature requires an accurate knowledge of the global and local thermal-hydraulics in the pin bundle. The characteristic feature of sodium flow is the transversal flow and the mixing induced by the spacer wire that

imposes local thermal-hydraulic coupling between the sub-channels. Thus, it is necessary to take into account three kinds of sub-channels shown in Figure 4.

The other parameters which influence the clad temperature are the axial and radial power distribution in the pin bundle. The average heat flux on SFR fuel pin is very large ( $10^6 \text{ W/m}^2$ ) and there are significant variations in the heat generation rates of fuel pins, in both axial and radial directions, due to variation in the neutron flux.

Furthermore, the mass flow rates of sodium coolant are not uniform in the flow sub-channels surrounding the fuel pins. As a consequence, there are strong temperature variations around the fuel pins that give rise to local hot spots at locations of deficient coolant supply, such as wake of the spacer wire. The axial velocity distribution in a triangular sub-channel is non-uniform and is strongly influenced by the wire. The location of maximum axial velocity (19% to 21% of the total velocity) is near the gap that is opposite to the gap containing the wire wrap and minimum axial velocity (0-10% of the total velocity) is in the wake of wire (Figure 5).

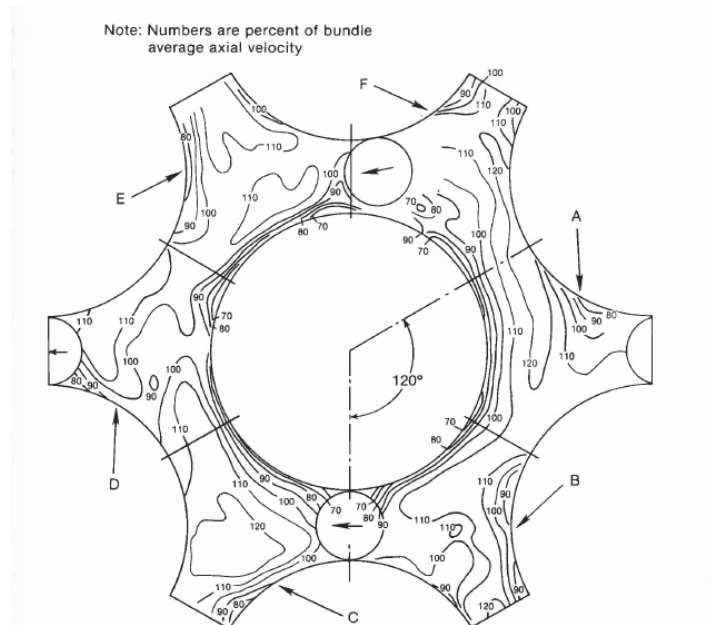


**Figure 5-Velocity distribution in the interior sub-channel (Bishop, 1980)**

The reduction of velocity in the wake of wire can result in insufficient cooling locally and thus producing local hot spots. These hot spots can modify the flow regime and affect the strength of the clad. As the clad is the first layer of defense, such temperature non-uniformities could influence the life of the fuel pin and also have direct bearing on the reactor safety. Hence a detailed study at the level of sub-assembly is necessary to study the hot spots.

### 3. Thesis approach

The different ways to perform the thermal-hydraulic studies are experiment, the correlation approaches and the Computational Fluid Dynamics (CFD) software.

Experimental study gives the most reliable information about a physical process by actual measurement but a full-scale experiment set up in most cases is prohibitively expensive and often impossible. The use of liquid sodium and complex geometry of heat generating fuel pin bundles makes the thermal-hydraulic study by experiment more challenging. Major challenges are summarized below (Schulenberg, 2010):

- Sub-channel dimensions are very small (about 3mm hydraulic diameter).
- Measuring instruments are required to function at elevated temperature (200-600°C).
- Flow visualization is hampered by the opaque nature of sodium.
- Water flow cannot correctly simulate sodium heat transfer.
- Safety measurements needed to avoid sodium-water and sodium-air reaction.

Second approach is use of numerical sub-channel codes like CADET (Valentin, 2000) SABRE-4 (Macdougall, 1984), COBRA-IV-I (Wheeler, 1976) and MATRA-LMR (Kim, 2002) which gives the sub-channel averaged values for pressure, velocity and temperature using experimental and analytical correlations. The spacer wire is modelled with some assumptions. Evaluations of the behavior of the total core are traditionally performed using sub-channel codes. However, uncertainties rise when three-dimensional effects start playing a role which cannot be captured in such codes.

The third one is CFD which is a numerical tool that is able to capture all the flow and heat transport details with effect of helical wires and is best suited for our study. CFD solves the conservation equations of physics that describes the flow and heat transport using numerical method. These equations are Navier-Stokes equations (conservation of momentum), continuity equation (conservation of mass) and conservation of energy. Thus, a system of five equations consisting of five variables (three velocity components, pressure and temperature) is established. However, the Navier-Stokes equations are non-linear and time-dependent partial differential equations, therefore no analytical solution exists except for some very simple flow cases. Thus, one has to calculate the solutions of the Navier-Stokes equations numerically with the aid of supercomputers.

Three different levels of approach are present in CFD to solve the equations depending on the computational time and the extent of modelling used. They are Reynolds-Averaged Navier-Stokes method (RANS), Large Eddy Simulation (LES) and Direct Numerical Simulation



(DNS). RANS is a time averaging method with least computational time but more modelling. DNS is an exact method with complete resolution of flow features without any modelling but costly in terms of computational power. LES is a space filtering method where large scales of motions are exactly solved and small scales of motions are modelled. Figure 6 represents a summary of differences between the three approaches.

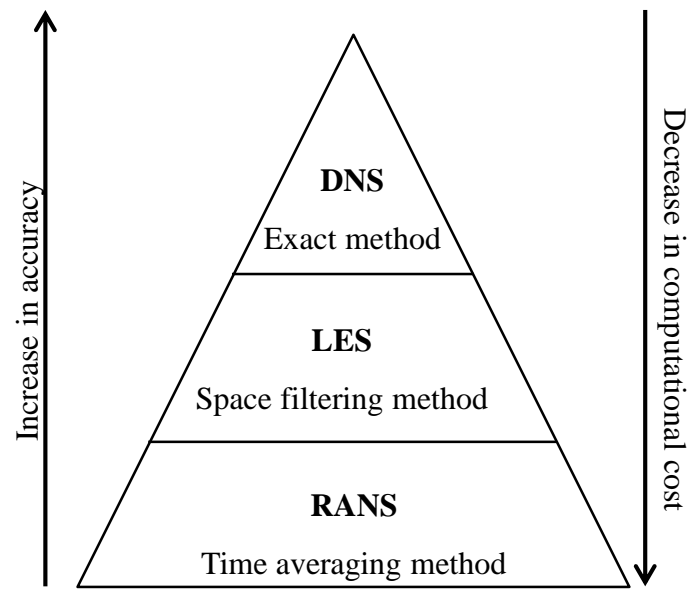


**Figure 6-Schematic representation of the CFD methods – DNS, LES and RANS**

With the increase of the computational power in the last decades the use of much accurate CFD methods to understand the fluid dynamics in complex geometries has increased. Hence, CFD methods are used in this thesis to perform the thermal-hydraulic study of the SFR sub-assembly.

## 4. Thesis structure

The thesis report is presented in four chapters.

- **Chapter 1** presents the status of art for the thermal-hydraulic studies of sub-assembly. It is divided into three parts presenting the current knowledge of heat transfer in sodium, then the experiments performed in the past on the sub-assembly with different number of pins and the numerical studies realized in the past using the three levels of approach -RANS, LES and DNS.
- **Chapter 2** presents the basic laws of physics governing the fluid flow and heat transfer along with the numerical methods and the turbulence methods –RANS, LES and DNS that forms the basis of the numerical simulations. It will also contain the detailed description of the different CFD software used to perform the studies in the next two chapters.
- **Chapter 3** is devoted to the study of heat transfer between heated wall and sodium coolant using the most accurate CFD method that is direct numerical simulation (DNS). This demands huge computational resources and with the current computer power the study has been done on a simple geometry – flow inside concentric annular cylinder. This geometry is a simple representation of flow inside reactor fuel sub-assembly and is also encountered in the study of control rods and heat exchangers. DNS permits to validate the LES approaches to do the thermal hydraulic studies in sodium.
- **Chapter 4** presents the use of validated LES and RANS approaches to study the thermal hydraulics of the sodium flow in sub-assembly. The RANS is performed on complete sub-assembly containing 217 fuel pins with 5 axial pitch of the spacer wire. This study gives the boundary conditions for the LES study that is performed on the central local region of the sub-assembly with only one helical pitch. The LES calculation gives detailed information about the hot spots.

# CHAPTER 1

---

## *Status of art*

*This chapter introduces the equations of physics describing fluid flow and heat transfer and presents the concept of the turbulence and CFD. The specific features of heat transfer phenomena in liquid sodium coolant used in SFR are presented in comparison to conventional fluids like air and water along with the limitations of commonly used concept for heat transfer modelling. A status-quo of the different thermal-hydraulic studies of SFR sub-assembly using experiments and CFD that are available in open literature have been studied.*

# 1.1 Generalities

This section will present the important concepts of fluid dynamics – the basic equations of physics, concept of turbulence and the CFD methods used to solve these equations. It forms a basis for the concepts introduced in next section. The concepts introduced here are recalled again in Chapter 2 Numerical tools and methods where a detail mathematical description is provided for better understanding of these concepts.

## 1.1.1 Instantaneous equations of fluid flow and heat transfer

The basic equations of physics that governs the instantaneous motion of an incompressible fluid in single phase flow with constant thermal-hydraulic properties are written below:

- i. **Continuity equation (conservation of mass):**

$$\nabla \cdot \vec{u} = 0 \quad (1.1)$$

- ii. **Navier-Stokes equation (conservation of momentum):**

$$\frac{\partial \vec{u}}{\partial t} + (\vec{u} \cdot \vec{\nabla}) \vec{u} = -\frac{\vec{\nabla} p}{\rho} + \nu \nabla^2 \vec{u} + f_{ext} \quad (1.2)$$

- iii. **Transport equation of temperature (conservation of energy):**

$$\frac{\partial T}{\partial t} + \vec{u} \cdot \vec{\nabla} T = \alpha \nabla^2 T + s_{ext} \quad (1.3)$$

Where  $p$  is the pressure,  $\vec{u}$  is the velocity vector,  $f_{ext}$  is the external momentum source,  $s_{ext}$  is the external energy source and  $T$  is the temperature.  $\rho$ ,  $\alpha$  and  $\nu$ , represents the density, thermal diffusivity and dynamic viscosity of the fluid respectively.

Although these set of equations form a closed system to have a unique solution but the Navier-Stokes equation is non-linear. Therefore, no analytical solution exists except for some very simple flow cases. Thus, to solve the practical complex engineering problems it is necessary to calculate the solutions of the Navier-Stokes equations numerically with the aid of super computers. This is a branch of science called as Computational Fluid Dynamics (CFD). Before presenting the different CFD approaches, it is important to introduce the omnipresent phenomena in fluid motion i.e. the concept of turbulence.

## 1.1.2 Turbulence

Turbulence is not a fluid property but property of flow itself. Turbulent flow can be simply defined as a flow that is disordered in time and space. But precisely turbulent flows may possess fairly different dynamics, may be three dimensional or sometimes quasi two-dimensional, and may exhibit well-organized rotational structures called as eddies. The most useful property of turbulent flows is that they are able to mix transported quantities much more rapidly than if only molecular diffusion processes were involved. This could be a desired property because it enhances the mixing of physical and chemical properties within a flow.

Turbulence is an omnipresent phenomena found in nature and industrial. Figure 1.1 gives visualization of turbulent flows applied to aircraft industry (Figure 1.1a.) and second to environment (Figure 1.1b). From an industrial point of view, its applications are varied: flow around aircraft, vehicles from submarines, turbulent flow generated by combustion, flow in a nuclear reactor.

Thus, turbulence denotes a state of fluid in which all properties (velocity, pressure, density, etc.) fluctuate continuously in an irregular, chaotic, non-repeating and unpredictable manner (Hinze, 1975).

(a)



(b)

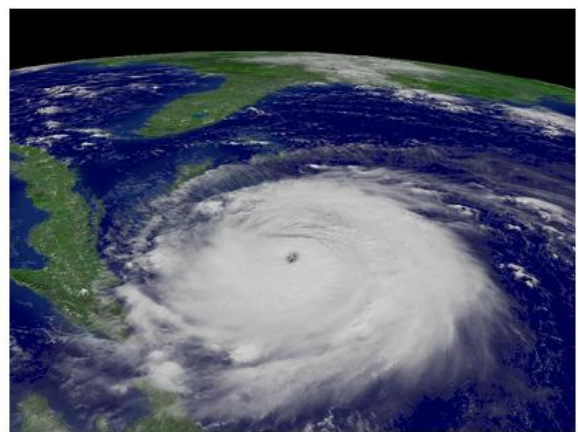


**Figure 1.1-Examples of turbulence in nature (a) Visualization of wake vortices consecutive passage of a light aircraft through a plume of smoke (Source NASA Langley Research Center - EL 1996 00130) (b) Radiograph of Hurricane Frances approaching the coasts of Florida and taken by the satellite GOES-12.**

Reynolds (Reynolds, 1895) was the first to propose a criterion for differentiation between laminar and turbulent flows in his classic dye visualization. He observed that a dimensionless parameter called as Reynolds number,  $Re$  regulates the onset of turbulence. This dimensionless parameter is defined as ratio of inertial to viscous force and mathematically given as follows:

$$Re = \frac{u^* l^*}{\nu} \quad (1.4)$$

Where  $u^*$  is the velocity scale,  $l^*$  is the characteristic length of the flow domain and  $\nu$  is the kinematic viscosity of fluid. Reynolds showed that above a critical value of Reynolds number ( $Re_c=2100$  for fluid flow in pipe) the topology and dynamics of the flow changes considerably and the flow becomes turbulent.

Turbulence can be decomposed into rotational structures called eddies that are characterized by very different scales of length, time and speed. Many turbulent structures of very different sizes coexist in a same flow and possess a specific dynamics of space-time scales that characterize them. The largest structures have the characteristic length of the domain  $L$  and contain most of the energy. Large eddies extract energy from the mean motion, become unstable and breakup, transferring their energy to smaller size eddies. The small eddies undergo a similar break-up process, and transfer their energy to smaller and smaller eddies until this energy is dissipated by viscosity. This is called energy cascade (Richardson, 1992).

Kolmogorov describes the complexity of the structure of turbulent flow. The theory advanced by Kolmogorov is stated in the form of three hypotheses (Kolmogorov, 1941):

**i. Kolmogorov's hypothesis of local isotropy**

*It states that at sufficiently high Reynolds number, the small scale turbulent motions are statistically isotropic.* The anisotropy of the large scale turbulent motions is lost in the chaotic scale-reduction process of energy cascade so that the small-scale motions are statistically isotropic. He also argued that not only does the directional information get lost as the energy passes down the cascade, but that all information about eddies geometry gets also lost. As a result, the statistics of the small-scale motions are universal: they are similar at every high Reynolds number turbulent flow, independent of the mean flow field and the boundary conditions.

## ii. Kolmogorov's first similarity hypothesis

It states that *in every turbulent flow at sufficiently high Reynolds number, the statistics of the small scale motions ( $\eta \ll L$ ) have a universal form that is uniquely determined by the rate at which the small scales receive energy from the large scales i.e.  $\varepsilon$ , and the kinematic viscosity,  $\nu$* . These two parameters determine the unique length ( $\eta$ ), velocity ( $u_\eta$ ) and time scales ( $\tau_\eta$ ) called as Kolmogorov scales:

$$\eta = \left( \frac{\nu^3}{\varepsilon} \right)^{\frac{1}{4}} \quad (1.5)$$

$$u_\eta = (\varepsilon \nu)^{\frac{1}{4}} \quad (1.6)$$

$$\tau_\eta = \left( \frac{\nu}{\varepsilon} \right)^{\frac{1}{2}} \quad (1.7)$$

Reynolds number based on Kolmogorov scales  $Re_\eta = \frac{u_\eta \eta}{\nu}$  is equal to 1 (using (1.5) and (1.6)). This is consistent with the notion that the energy cascade proceeds to smaller and smaller scales until the Reynolds number is small enough for dissipation to be effective.

## iii. Kolmogorov's second similarity hypothesis

It is also called as Kolmogorov's which states that *in every turbulent flow at sufficiently high Reynolds number, the statistics of motions of scale,  $l_t$  in the range  $L \gg l_t \gg \eta$  has a universal form that is uniquely determined by turbulent dissipation,  $\varepsilon$  and is independent of kinematic viscosity,  $\nu$* . The characteristic velocity ( $u_l$ ) and time scales ( $\tau_l$ ) are determined from  $\varepsilon$  and  $l_t$  and are given as

$$u_l = (\varepsilon l_t)^{\frac{1}{3}} \quad (1.8)$$

$$\tau_l = \left( \frac{l_t^2}{\varepsilon} \right)^{\frac{1}{3}} \quad (1.9)$$

The Kolmogorov's hypothesis and Richardson's energy cascade phenomena identifies there dominant processes (Figure 1.2):

- i. **Energy production** ( $l > L$ ) - In this region the large eddies are produced by extracting energy from the mean motion. These eddies contain the bulk of the energy.
- ii. **Energy transfer** ( $L > l_t > \eta$ ) - It is the inertial region where the transfer of energy takes place to successively smaller scales. According to second similarity hypothesis the motion in inertial zone are determined by only inertial effects-viscous effects being negligible. Thus, turbulence is in equilibrium between production and dissipation in this region.

- iii. **Energy dissipation** ( $\eta < l$ ) - In this range viscous effects are dominant. The very small eddies undergoes viscous dissipation and all turbulent kinetic energy gets converted in to thermal energy through molecular dissipation.

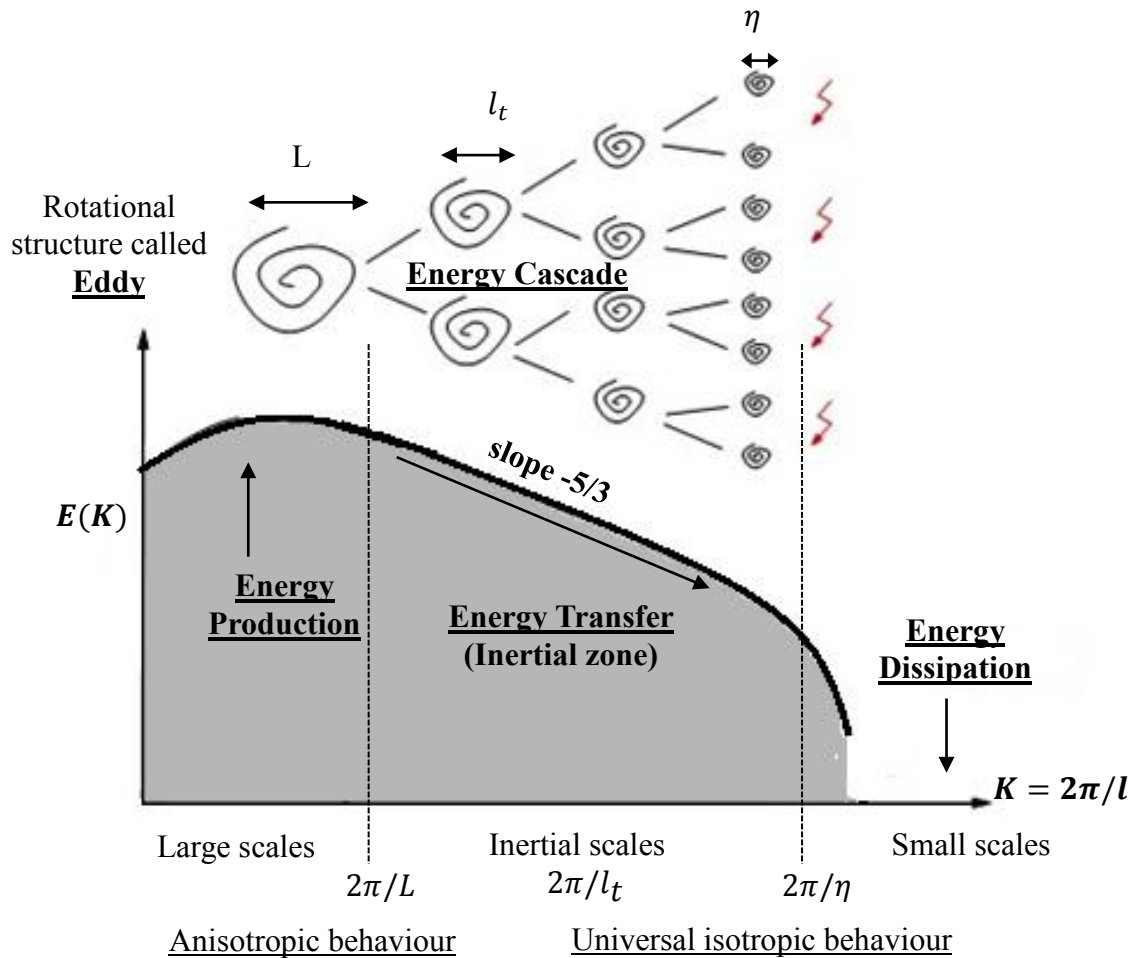


**Figure 1.2-Energy cascade and spectral energy density of a turbulent flow traced in logarithmic scales**

Based on these the hypothesis, Kolmogorov gave mathematical description of energy contained in the eddy as a function of its size represented by wave number (inverse of length). This is called energy spectrum  $E(K)$  and Figure 1.1 shows energy spectrum with wave number. The slope of the energy spectrum in the inertial range is  $-5/3$ . This is Kolmogorov -  $5/3$  law.

$$E(K) = C_K \varepsilon^{2/3} K^{-5/3} \quad (1.10)$$



Apart from transfer of energy from inertial zone to dissipation zone there also exists some energy transfer from dissipation zone to inertial zone due to presence of wall this is called energy back scatter.

There are different CFD methods to solve the equations of fluid flow and heat transfer (section 1.1.1) based on the resolved scales of turbulence. These methods are presented in the next section.

### 1.1.3 CFD methods

Computational Fluid Dynamics involves prediction of fluid flow, heat transfer and related phenomena by solving the mathematical equations that govern these processes using a numerical method. The main steps involved in a CFD study are as follows:

- i. Creation of mesh to represent the desired geometry.
- ii. Provide appropriate boundary and initial conditions for the problem.
- iii. Selection of appropriate turbulence models depending on the desired level of accuracy.
- iv. Solving the equations of mass, momentum and energy throughout the domain of interest.

Since the development of computers, numerical simulation has an important place in research and in industry. It predicts many results, both qualitative and quantitative without setting up experiments that can be costly.

If we look at a turbulent fluid flow from a statistical point of view, a mean field appears on which fluctuations of different scales are superimposed. The problem of numerical simulation of turbulent flows is to assess with more or less accuracy the average and fluctuations of these fields for a wide range of scales present in the flow.

The numerical simulations can be divided in to three major families depending on the level of accuracy and extent of modelling used. They are Direct Numerical Simulation (DNS), Large Eddy Simulation (LES) and Reynolds averaged Navier-Stokes simulation (RANS).

These three simulation techniques are used differently depending on the needs and available computational resources. A schematic representation of the main difference is given in Figure 1.3 that shows the spectrum of turbulent kinetic energy,  $E(K)$  for different wave numbers,  $K$  defined as inverse of the length scale.

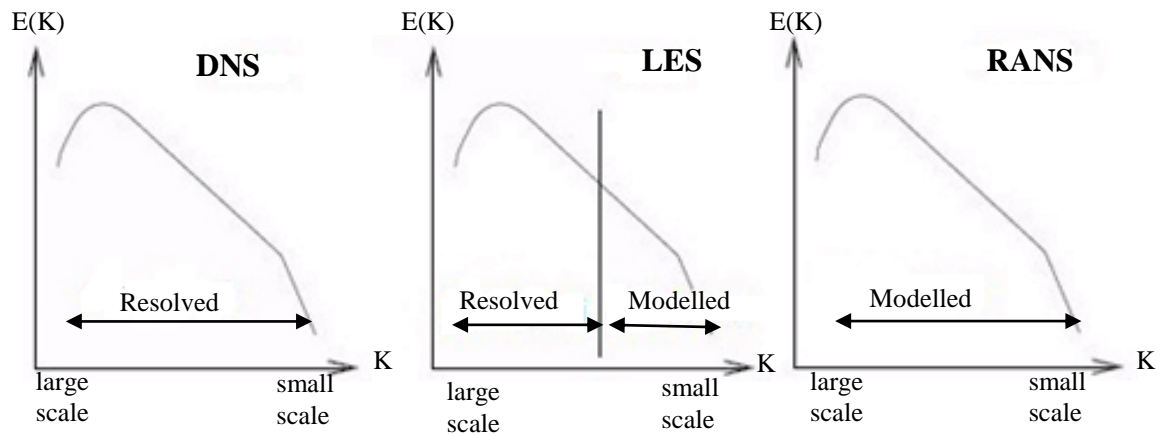


**Figure 1.3-Difference between RANS, LES and DNS method on wave number (K)-energy spectrum ( $E(K)$ )**

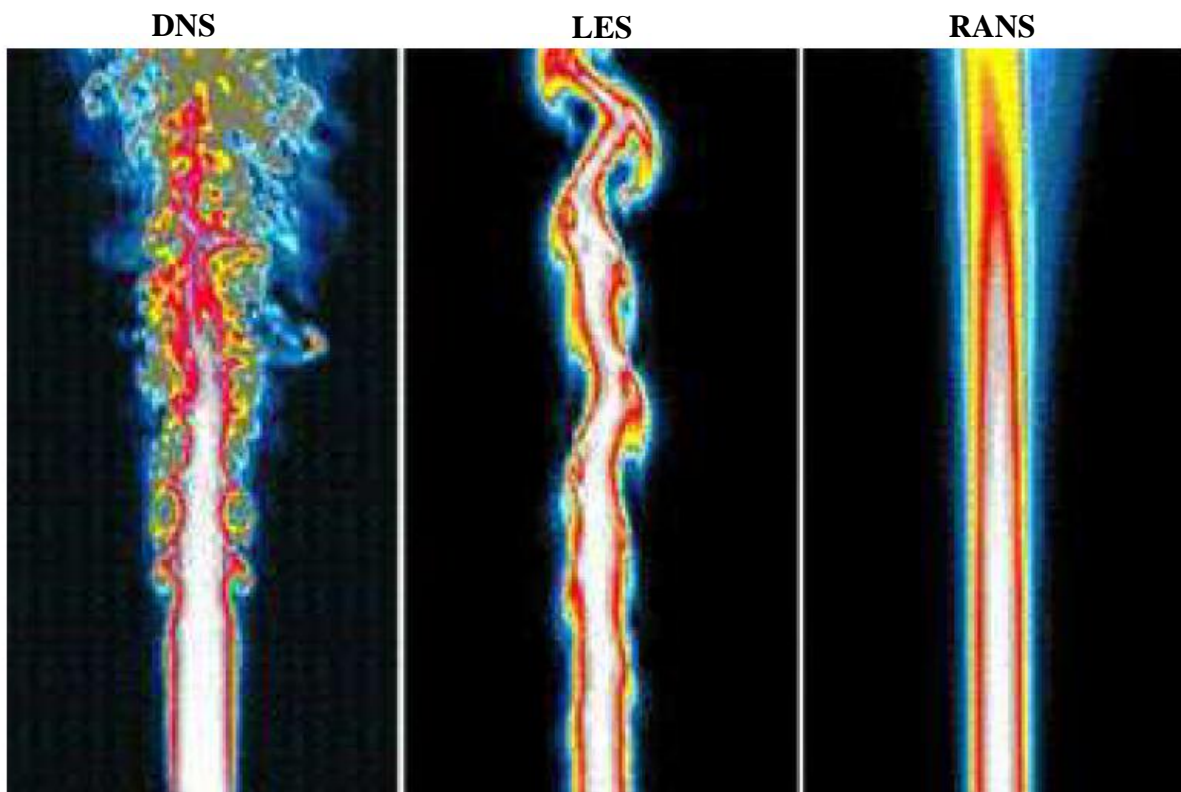


**Figure 1.4-Flame simulated by DNS, LES and RANS (Poitou, 2009)**

The energy spectrum permits to distinguish schematically the scales resolved and modelled by the different numerical methods. The full spectrum of the turbulent kinetic energy is completely resolved in DNS method without any modelling. In LES approach, the large-scale structures with low wave number are resolved and the small-scale structures having isotropic characters are modelled. In RANS method, a single point in the wave number-energy spectrum is computed and all the rest is modelled.

Figure 1.4 shows turbulent flame simulated by these three methods. The flame simulated by DNS method shows very small structures because in this method all the scales of motion are resolved. In the flame simulated by LES method these small structures disappears and only the large scales of motion are visible. RANS method does not distinguish the different scales of motion and models the whole spectrum with one length and time scales giving a steady state field.

### 1.1.3.a Direct Numerical Simulation (DNS)

It provides maximum precision as it solves the set of equations for fluid flow and heat transfer accurately with numerical methods without any modelling. In DNS, all space-time phenomena are resolved. However, the computational resources required are enormous and vary with Reynolds number ( $Re^{9/4}$ ). The Reynolds number for the flow in sub-assembly is around 50000-70000. The current computational power is still not enough to perform a DNS at this high Reynolds number on a complex geometry. DNS is therefore limited to simple geometries with low Reynolds number that can be reasonably dealt with the current computational power. The complete resolution of the space and time scales of the turbulent flow in DNS helps to study accurately the physical phenomena of fluid flow and heat transfer in detail and provides data for validation of the turbulence model used in RANS and LES methods.

### 1.1.3.b RANS (Reynolds Average Navier-Stokes)

It is the most common method where the flow variables (velocity, pressure and temperature) say  $\varphi(x, y, z, t)$  undergoes Reynolds decomposition i.e. separating in to a time averaged part,  $\bar{\varphi}(x, y, z)$  and a fluctuating part,  $\varphi'(x, y, z, t)$ .

$$\varphi(x, y, z, t) = \bar{\varphi}(x, y, z) + \varphi'(x, y, z, t) \quad (1.11)$$

This results in time averaged continuity equations, Navier-Stokes and the transport equation for temperature. The Reynolds averaging leads to appearance of new unknown terms:

- In Navier-Stokes equations, the new terms “ $-(\overline{u_i u_j} - \overline{u_i} \overline{u_j})$ ” are called Reynolds stresses or turbulent stresses represented by  $\tau_{ij}^{RANS}$ .
- In energy equation, the new terms “ $-(\overline{u_j T} - \overline{u_j} \overline{T})$ ” are the thermal analogs of the Reynolds-stress and are called as turbulent heat flux represented by  $\Theta_j^{RANS}$ .

As a consequence of Reynolds decomposition and the presence of these two extra terms, the Reynolds equations do not form a closed set of equation; so a turbulence model that uses empirical knowledge is required. These models are presented in chapter 2. The main advantage of RANS method over others is its low computational cost and its ability to study the flow in complex geometries.

### 1.1.3.c Large Eddy Simulation (LES)

It is a filtered approach in which large-scale turbulent structures larger than a threshold size are completely resolved while the turbulent structures smaller than this size have more isotropic or universal nature so they are modelled. This threshold size is called as cut-off filter size. The flow variable  $\varphi(x, y, z, t)$  is decomposed into a filtered field represented by  $\langle \varphi(x, y, z, t) \rangle$  and a sub-grid term represented by  $\varphi''(x, y, z, t)$ :

$$\varphi(x, y, z, t) = \langle \varphi(x, y, z, t) \rangle + \varphi''(x, y, z, t) \quad (1.12)$$

Filtering method also leads to appearance of the new unknown terms like in RANS method and these terms are modelled using sub-grid scale (SGS) models so that the set of equations can form a closed system.

- In Navier-Stokes equations, the new term “ $-(\langle u_i u_j \rangle - \langle u_i \rangle \langle u_j \rangle)$ ” is called sub-grid scale (SGS) stresses represented by  $\tau_{ij}^{sgs}$ .
- In energy equation, the new term “ $-(\langle u_j T \rangle - \langle u_j \rangle \langle T \rangle)$ ” is called as sub-grid scale (SGS) heat flux represented by  $\Theta_j^{sgs}$ .

The turbulent stress and turbulent heat flux in RANS approach, and SGS stress and SGS heat flux in LES approach has almost similar representation, but their physical interpretation is completely different. In RANS approach, they represent the effect of all the length and time scales of motion whereas in LES approach these terms represent only the effect of small-scale motions that are not completely resolved by the mesh.

The difference between time averaging and filtering method is shown in Figure 1.5 where time variation of a flow variable,  $\varphi$  is plotted with time. The time averaging in RANS method

discards the information about the fluctuations around the mean value and solves only the time-averaged quantities. Unlike in RANS method, the resolved flow field in LES method is time dependent but represents the time scale associated with only the large-scale structures and modelling the small scales. The advantage of LES method over DNS is that it can deal with much higher Reynolds numbers.

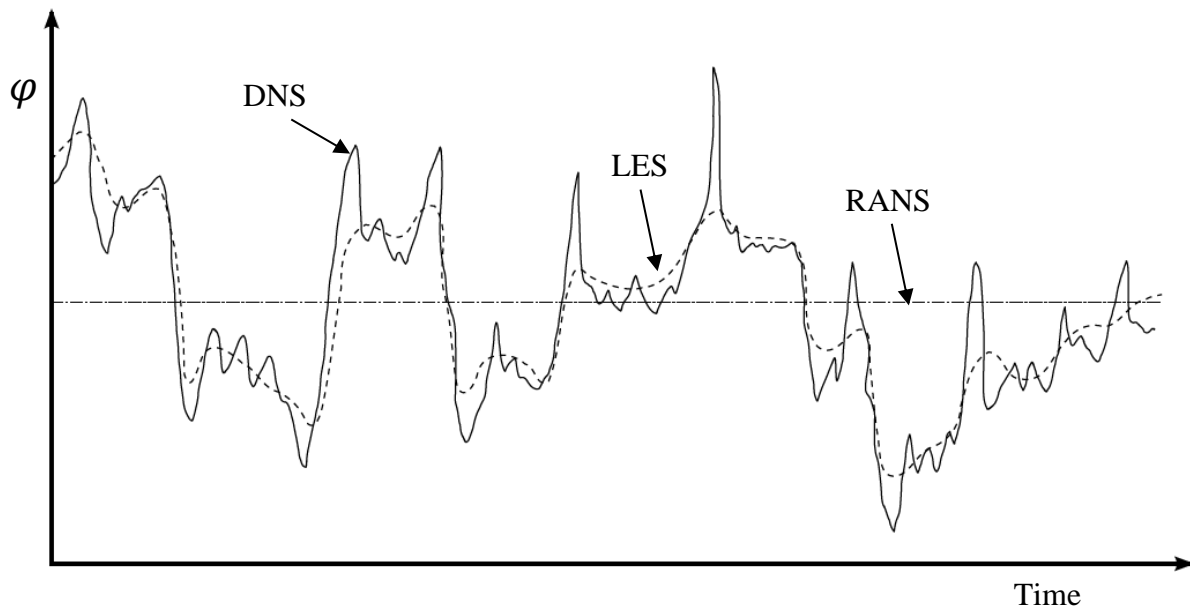


**Figure 1.5-Time evolution of a flow variable  $\varphi$  obtained by approach DNS, LES and RANS (Dorey, 2012)**

## 1.2 Heat transfer in liquid sodium

### 1.2.1 Introduction

Liquid sodium is preferred coolant in liquid metal cooled fast spectrum reactors. Sodium has high boiling point and remains in liquid state up to temperature of 900°C at atmospheric pressure. This permits to have high operating temperature for reactor without any need for pressurization of the system. It has excellent heat transfer properties as compared to water that is the preferable coolant for Pressurized water reactors (PWR). The properties of water and sodium at temperature of 300°C and 470°C (corresponding to mean of inlet and outlet coolant temperature in PWR and SFR) are compared in Table 1.1. The kinematic viscosity of sodium and water are of same order of magnitude but their thermal properties are very different. The thermal conductivity of sodium is about 130 times of water and thermal diffusivity is about 480 times of water. As a consequence, the Prandtl number, which is an important non-dimensional parameter for heat transfer, is about 1000 times smaller for sodium than that for water. In the following sections we present that how the difference of about 3 orders of magnitude in Prandtl number affects the heat transfer mechanism in sodium.

Properties		units	Sodium (470°C)	Water (300°C)
Kinematic viscosity	$\nu$	m <sup>2</sup> /s	$2.98 \cdot 10^{-7}$	$1.35 \cdot 10^{-7}$
Specific heat	$C_p$	J/kg/K	1268.4	5.728
Thermal conductivity	$\lambda$	W/m/K	68.18	0.54
Thermal diffusivity	$\alpha$	m <sup>2</sup> /s	$6.41 \cdot 10^{-5}$	$1.32 \cdot 10^{-7}$
Prandtl number	$Pr$	-	0.004	1.019

Table 1.1-Physical properties of sodium and water (Cebeci, 1984)

### 1.2.2 Prandtl number

The Prandtl number,  $Pr$  is defined as the ratio of kinematic viscosity,  $\nu$ , to thermal diffusivity,  $\alpha$  i.e.

$$Pr = \frac{\nu}{\alpha} \quad (1.13)$$

Prandtl number provides a measure of the relative effectiveness of momentum transport by diffusion with respect to energy transport by thermal diffusion. The conventional fluids like

air and water have Prandtl number near unity so the energy and momentum transfer by diffusion is comparable. But the liquid sodium has very high thermal diffusivity so the Prandtl number is much lower than 1 ( $Pr \sim 10^{-3}$ ). Hence, the energy diffusion greatly exceeds the momentum diffusion in case of liquid sodium flow. Therefore, the Prandtl number strongly influences the relative growth of the velocity and thermal boundary layers. Equation 1.14 (Tennekes, 1972) gives a quantitative estimation of the effect of Prandtl number on the relative growth of boundary layers:.

$$\frac{\delta_v}{\delta_{th}} \sim Pr^n \quad (1.14)$$

Where  $\delta_{th}$  is the thermal boundary layer thickness,  $\delta_v$  is the velocity or momentum boundary layer and  $n$  is a positive exponent whose value depends on Prandtl number:

$$n = \begin{cases} 0.5 & \text{for } Pr \ll 1 \\ 0.33 & \text{for } Pr \gg 1 \end{cases} \quad (1.15)$$

Hence, the thermal boundary layer,  $\delta_{th}$  for liquid metals extend to a much larger distance than velocity boundary layer for  $Pr \ll 1$ . This difference in the thickness of the thermal and velocity boundary layer is clearly shown in the Figure 1.3. The thickness of thermal and velocity boundary layer is similar only if the Prandtl number is of the order of 1.

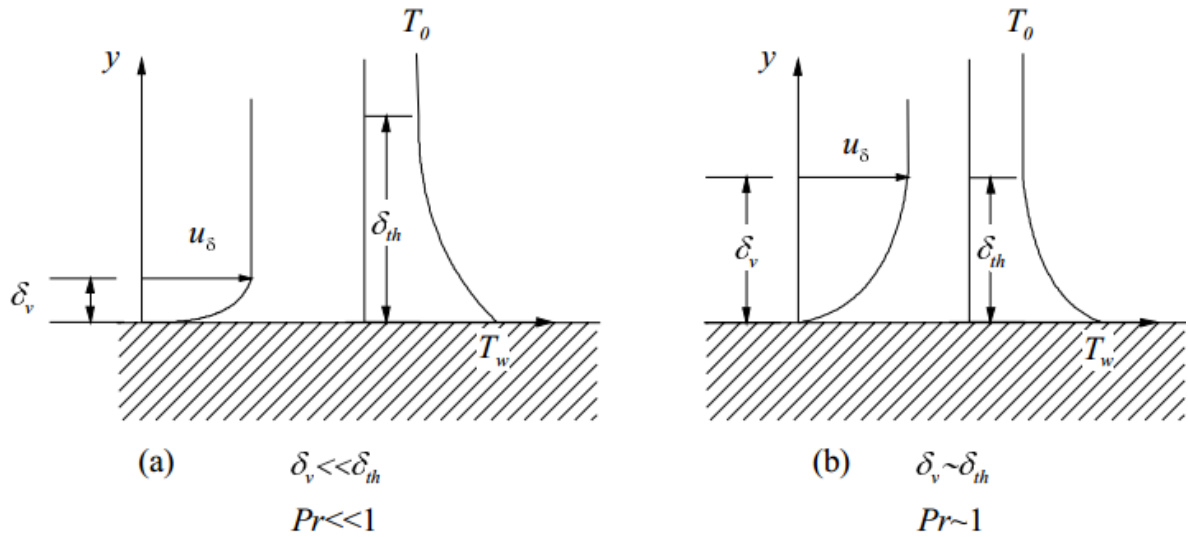


**Figure 1.6-Scale difference and similarity of the thermal and momentum field in fluids with different molecular Prandtl numbers,  $Pr$  (LBE Handbook, 2007)**

## 1.2.3 Energy Spectrum

The energy spectrum determines how the energy contained in the turbulent structures of flow is distributed among the eddies of different sizes.

### 1.2.3.a Spectral energy density for velocity fluctuations

The energy contained in turbulent eddies is called turbulent kinetic energy. The decomposition of this turbulent kinetic energy as a function of the size of eddies is called as energy spectrum. The energy spectrum has been already described in section 1.1.2. In this section the mathematical formulation is given to be used

If  $u'_1, u'_2$  and  $u'_3$  represents the velocity fluctuations for the three velocity components then the turbulent kinetic energy,  $k$  is defined as:

$$k = \frac{1}{2} (\overline{u_1'^2} + \overline{u_2'^2} + \overline{u_3'^2}) \quad (1.16)$$

The turbulent kinetic energy can be decomposed in space to know the distribution of energy among different sized eddy. The decomposition of  $k$  can be written as:

$$k = \int_0^\infty E(K) dK \quad (1.17)$$

Where  $E(K)$  represents the energy spectra of turbulent kinetic energy and  $K$  represents the wave number ( $K = \frac{2\pi}{l}$ ) of the eddy of size  $l$ .

The dimensional analysis of the spectral energy density  $E(K)$  corresponding to the wave number  $K$  indicates that:

$$E(K) = C_K \varepsilon^{2/3} K^{-5/3} f(K.\eta) \quad (1.18)$$

Where  $C_K$  is a constant,  $\varepsilon$  is the energy dissipation rate and  $f(K.\eta)$  is a function of Kolmogorov scale,  $\eta$  and wave number,  $K$ .

In the inertial range with length scales between  $L$  and  $\eta$  and corresponding wave number in the range ( $\frac{2\pi}{L} \ll K \ll \frac{2\pi}{\eta}$ ) the viscosity effects are negligible so  $f(K.\eta)$  can be neglected and we get the equation (1.10) that is called as Kolmogorov -5/3 law:

$$E(K) = C_K \varepsilon^{2/3} K^{-5/3} \quad (1.10)$$

Thus, the energy spectra of velocity has -5/3 slope in the inertial region. The energy spectrum is shown in Figure 1.2.



### 1.2.3.b Spectral energy density for temperature fluctuations

A similar analysis can be done to identify the length scales of different structures in the temperature fluctuations. If  $E_T$  is the spectral density then  $E_T(K)dK$  represents the variance of temperature fluctuations for the turbulent eddies between lengths scale  $2\pi/K$  and  $2\pi/(K+dK)$ :

$$\overline{T'^2} = \int_0^\infty E_T(K) dK \quad (1.19)$$

Let  $l = \frac{2\pi}{K}$  represents the length of the thermal eddy structure and  $\eta_T = \frac{\alpha^{3/4}}{\varepsilon^{1/4}}$  represents the length scale for which the temperature fluctuations start to dissipate by thermal conduction (Grötzbach, 2011). Using dimensional analysis, the ratio of dissipation of thermal energy by thermal conduction ( $\alpha \nabla^2 T'$ ) to the transport of thermal energy by turbulence ( $u' \cdot \nabla T'$ ), is written as follows:

$$\frac{\alpha \nabla^2 T'}{u' \cdot \nabla T'} = \left( \frac{\eta_T}{l} \right)^{4/3} \quad (1.20)$$

The spectral density  $E_T$  for the turbulent structures of size much less than the large turbulent eddies should depend on (Chabard, 2000):

- $\varepsilon_T$  that represents the power transmitted to the small structures of size  $\eta_T$  to be dissipated.
- Spectral energy density for velocity,  $E(K)$ , at the considered length scale i.e.  $\varepsilon$ ,  $K$  and  $\nu$ . This is applicable only if the length scale of eddies are very small ( $\sim \eta$ ) for which the viscosity is not negligible.
- Thermal diffusivity  $\alpha$  if the scales are very small of the order of  $\eta_T$  for which the thermal conduction is not negligible.

The dimensional analysis indicates that:

$$E_T(K) = C_T \varepsilon_T \varepsilon^{-1/3} K^{-5/3} f_1(\text{Pr}) f_2(K \cdot \eta_T) \quad (1.21)$$

In the convective inertial range where the length scales are larger than  $\eta_T$  and also  $\eta$  i.e. ( $L \gg l \gg \eta_T \gg \eta$ ) the influence of viscosity and thermo conduction are negligible. This implies that for wave number  $K$  in the range  $\frac{2\pi}{L} \ll K \ll \frac{2\pi}{\eta_T} \ll \frac{2\pi}{\eta}$  the thermal energy spectra can be written as:

$$E_T(K) = C_T \varepsilon_T \varepsilon^{-1/3} K^{-5/3} \quad (1.22)$$

Equation (1.22) shows that the spectral energy density for temperature also follows the **Kolmogorov 5/3 law** in the convective inertial region.

Figure 1.7 shows the distribution of energy spectra of two fluctuating fields - velocity and temperature at two different Prandtl numbers ( $Pr=1$  and  $Pr \ll 1$ ). This allows us to understand the effect of Prandtl number on their spatial scales. The main differences shown in the figure are summarized below.

- i. The velocity fluctuation spectra  $E(K)$  distribute over a wide range of wave numbers  $K$ . Most energy is found at large scales and at smallest scales the energy is dissipated.
- ii. With the increase in Reynolds number, the velocity spectral energy  $E(K)$  distributes to even higher wave numbers.
- iii. At  $Pr=1$ , the temperature spectrum  $E_T(K)$  has the same distribution as of  $E(K)$  and same dependence on Reynolds number. The inertial convective region for temperature coincides with the inertial range for velocity i.e.  $\eta_T = \eta$ .
- iv. Another notable feature for temperature spectra of fluids with  $Pr \ll 1$  is that there is sharp decrease in the  $E_T(K)$  in the range  $l > \eta_T$  as compared to the decrease in  $E_T(K)$  in the convective inertial range. This is also attributed to dominant thermal conduction in range  $l > \eta_T$ .
- v. At  $Pr \ll 1$ , the temperature spectra extend to somewhat larger scales ( $\eta_T > \eta$ ) i.e. lower wavenumber  $\left(\frac{2\pi}{\eta_T} < \frac{2\pi}{\eta}\right)$  (Grötzbach, 2011). This signifies that the smallest length scale of eddies that undergo conductive dissipation are much larger than the length of the eddies that undergo viscous dissipation. This can also be the consequence of the thicker thermal boundary layer as compared to the velocity boundary layer for fluids with  $Pr \ll 1$ .

As a result, the size of thermal structures is expected to be much larger than the turbulent eddies for velocity in case of sodium. This gives a possibility to completely resolve the thermal scales while filtering the smallest velocity scales in LES.

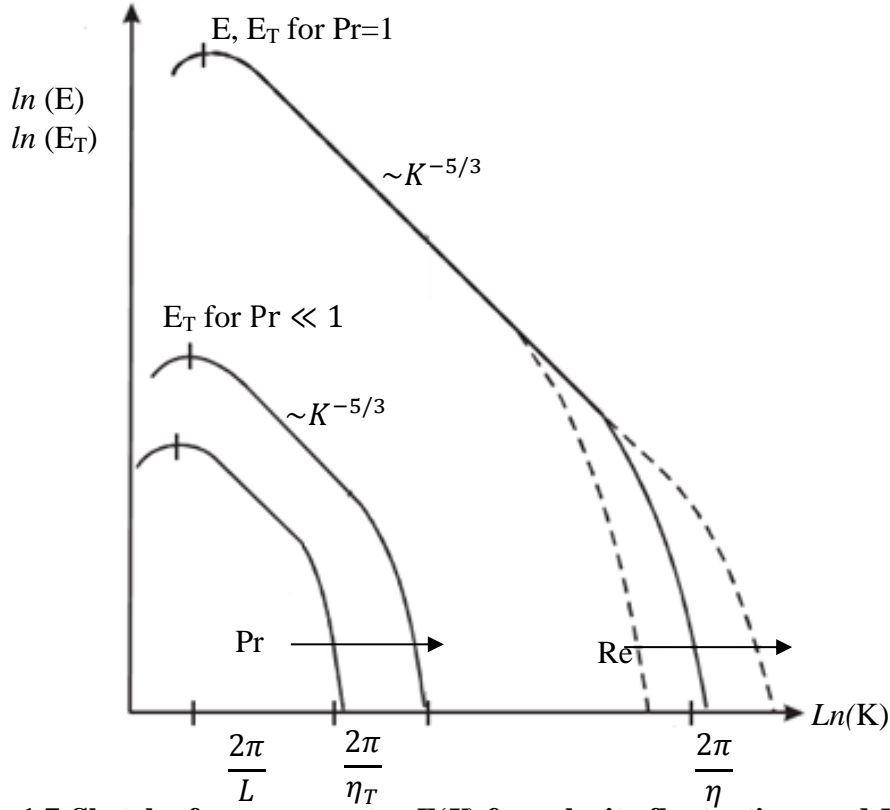


**Figure 1.7-Sketch of energy spectra  $E(K)$  for velocity fluctuations and  $E_T(K)$  for temperature fluctuations in forced channel flows at  $Pr=1$  and  $Pr<<1$  (Grötzbach, 2013; Lesieur, 1997)**

## 1.2.4 Wall bounded flows

The knowledge of the variation of temperature, pressure and velocity field (flow variables in general) in wall-bounded flow is important. The dominating molecular dissipative forces near the wall lead to steep gradient in the flow variables. It is important to capture correctly these wall gradients in order to have successful and correct results using numerical simulations. There are two possible ways to capture the flow near the wall. First method is to use a very refined mesh near the wall leading to large number of mesh cells and huge memory requirements. Second method is to define some wall functions that are empirical correlations validated against the DNS results and experiments. Wall functions remove the stringent requirement of refined mesh and allow the use of CFD for flows at higher Reynolds number with larger mesh size and less computational resources.

The simplest wall bounded turbulent flow that has been widely studied in the literature by DNS is the plane channel flow. In the following section, the profile near the wall for velocity

and temperature as studied by the DNS calculation on channel flow is presented. The wall functions used in CFD are presented in chapter 3.

### 1.2.4.a Velocity field

In the fully developed turbulent flows confined by wall, the turbulence is directly influenced by the presence of solid wall that acts on the fluid by the intermediate viscous stress. In the region near the wall, we define the first zone, the sub-viscous layer where the effect of viscosity is dominating. To analyze the turbulence near wall, it is necessary to define the appropriate scales. In the hypothesis of incompressibility, the scales of velocity (friction velocity) and the length are respectively defined by:

$$u_\tau = \sqrt{\nu \left. \frac{\partial u_y}{\partial y} \right|_{y=0}} \quad (1.23)$$

$$l_\tau = \frac{\nu}{u_\tau} \quad (1.24)$$

The distance from the wall measured starting from the scale  $l_\tau$  is then expressed in units of wall:

$$y^+ = \frac{y}{l_\tau} = \frac{u_\tau y}{\nu} \quad (1.25)$$

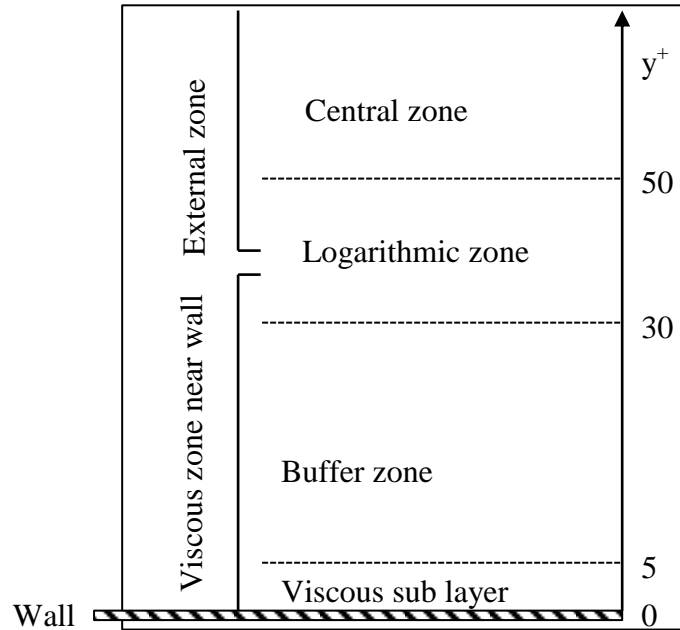


**Figure 1.8-The different zones of turbulence near wall: hydraulic boundary layer**

Figure 1.8 shows the different layers of the flow starting from the wall until the center of the flow.

1. **Sub viscous layer:** It extends until the distance  $y^+ \sim 5$ . In this zone, the dissipative viscous effects are dominant and the convective effects are negligible. The shear stress is almost only due the normal gradient of the longitudinal velocity so that we have:

$$u^+ = \frac{u}{u_\tau} = y^+ \text{ for } y^+ < 5 \quad (\text{Pope 2000}) \quad (1.26)$$

2. **Buffer zone:** It extends between  $y^+ = 5$  and  $y^+ = 30$ : It is in this zone where we have maximum production of the turbulent kinetic energy.
3. **Logarithmic zone:** At  $y^+ > 30$  there is a logarithmic zone where the profile of longitudinal velocity follows a law of the form:

$$u^+ = \frac{1}{\kappa} \ln(y^+) + B \quad (1.27)$$

Where  $\kappa = 0.41$  (Spalart, 1988) is the Karman constant and  $B = 5.5$

4. **External zone:** Beyond  $y^+ = 50$  we pass to external zone in which the effects of wall become negligible: the turbulence is then homogeneous.

The velocity profile as a function of wall normal distance is shown in Figure 1.8 representing the three zones viscous sub layer with linear law of velocity, logarithmic region and the transition or buffer region in between the two.

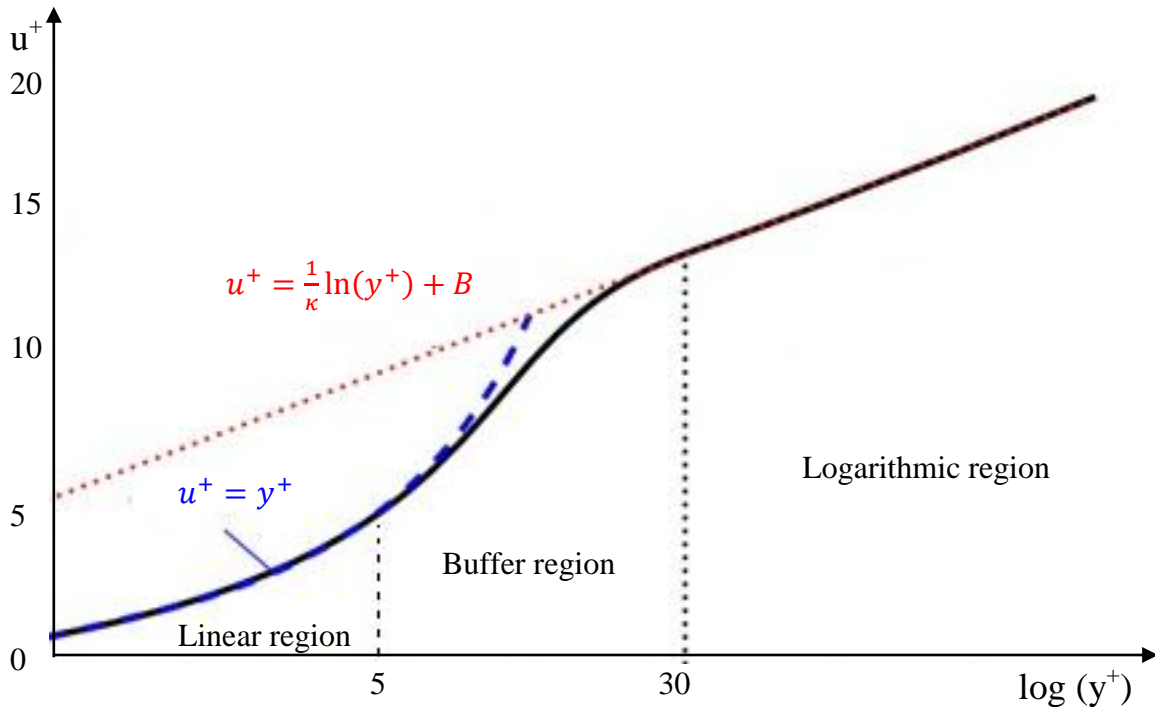


Figure 1.9-Non-dimensional velocity profile

### 1.2.4.b Temperature field

The average profile of thermal field presents the same topology like that of hydraulic boundary layer. The different layers described earlier are still present; the only difference is that the thickness of each zone depends on the value of Prandtl number (Waltar, 1981).

The friction temperature  $T_\tau$  is defined by:

$$T_\tau = \frac{q_w}{\rho C_p u_\tau} \quad (1.28)$$

Where  $\rho$  is the density of the fluid,  $C_p$  is the heat capacity of the fluid,  $u_\tau$  is the friction velocity and  $q_w$  is the rate of the heat transfer from the wall to the flow which is defined by:

$$q_w = -\lambda \left. \frac{\partial T}{\partial y} \right|_{y=0} \quad (1.29)$$

Where  $\lambda$  is the thermal conductivity and this equation is referred to as the heat conduction law or Fourier's law.

Thus, friction temperature  $T_\tau$  can also be written as follows:

$$T_\tau = \frac{\alpha}{u_\tau} \left( \frac{\partial T}{\partial y} \right)_{y=0} \quad (1.30)$$

Where  $\alpha$  is the thermal diffusivity. The friction temperature allows us to define non-dimensional temperature as shown below:

$$T^+ = \frac{T_w - T}{T_\tau} \quad (1.31)$$

Where  $T_w$  is temperature at the wall.

Similar to velocity field, the temperature field also presents the three characteristic zones near the wall- conductive sub-layer, buffer layer and logarithmic layer (Figure 1.10). But, the thickness of these layers is determined by the molecular Prandtl number.

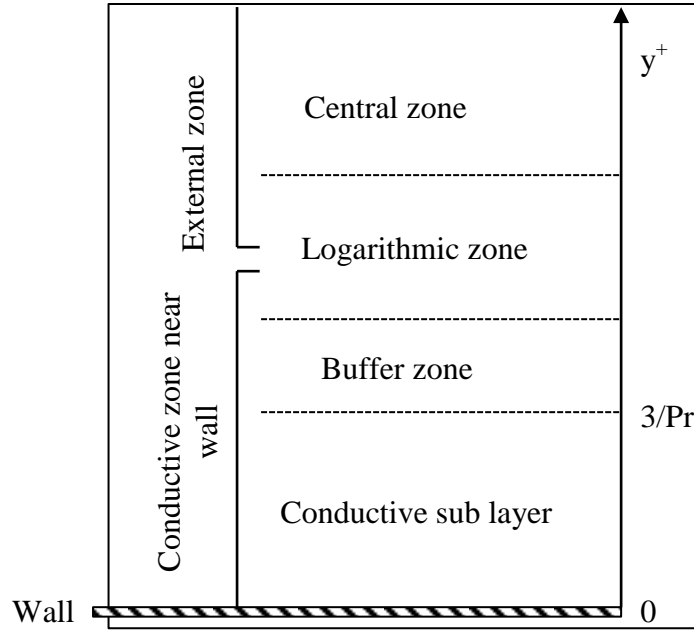


**Figure 1.10-The different zones of turbulence near wall: thermal boundary layer**

1. **Conductive sub-layer:** Analogously, very close to the wall, a conductive sub-layer exists for temperature as a viscous sub-layer for the velocity field. In this region, the effects of molecular conduction are dominating as compared to convection. From the heat conduction law, we can derive the equation for the conductive sub-layer:

$$T^+ = \text{Pr } y^+ \quad (1.32)$$

This zone extends until a distance of  $\text{Pr } y^+ < 3$  (Cebeci, 1984)

2. **Buffer layer:** It marks the transition between linear and logarithmic layer.
3. **Logarithmic layer** where the temperature follows the following law

$$T^+ = \frac{1}{\kappa_T} \ln(\text{Pr } y^+) + B_T \quad (1.33)$$

Where  $\kappa_T$  Karman constant for scalar field = 0.33 (Wikstrom, 1998),  $B_T$  is a function of Pr.

The effect of Prandtl number on the extent of linear and logarithmic region can be seen in Figure 1.11. The temperature profile for the Prandtl number 0.7 reveals that the thermal resistance is mainly concentrated in the conductive sub layer which is immersed in the viscous sub layer. Beyond the conductive sub layer, there is a rapid transport of heat in the pipe. When the Prandtl number decreases to 0.025, the conductive sub layer spreads from the wall to the core region indicating that the molecular heat transfer is dominant. It should be noted that the logarithmic region can be better distinguished from the buffer region when the

Prandtl number is around 1. For small Prandtl numbers, the logarithmic part of the temperature profile appears only at high Reynolds numbers ( $Re > 10^5$ ) (Kawamura, 1999).

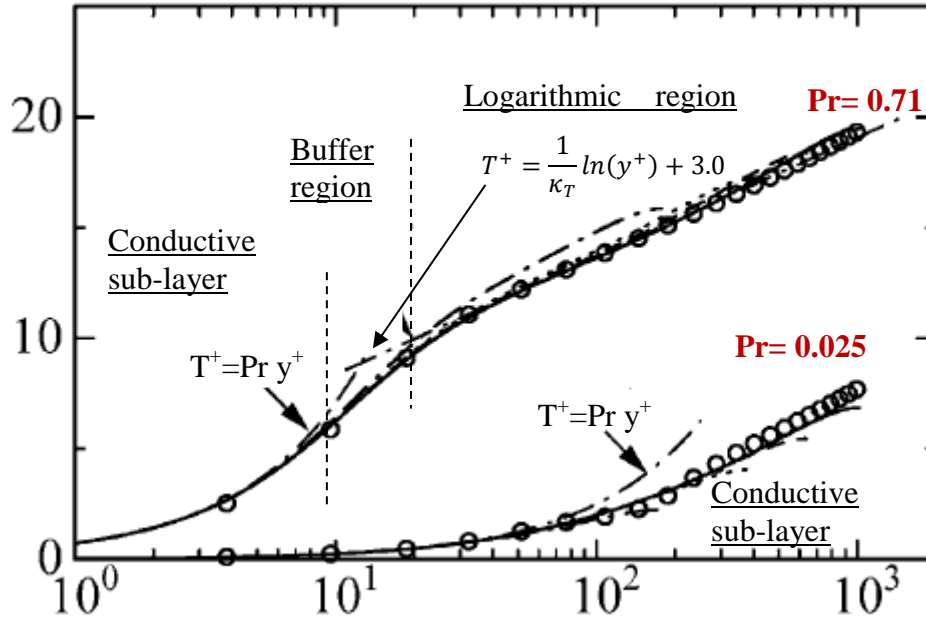


**Figure 1.11-Effect of molecular Prandtl number on the non-dimensional temperature profile at  $Re_\tau=1020$  (Abe, 2004). Symbol “O” represents the result of Kader (1981)**

## 1.2.5 Reynolds analogy limitation

The time-averaging of the flow variables in RANS method and space filtering of the flow variables in the LES method leads to appearance of new convective terms which needs some modelling to solve the set of fluid dynamic equations. These terms are Reynolds stresses,  $\tau_{ij}^{RANS}$  and turbulent heat flux,  $\theta_j^{RANS}$  in RANS method and SGS stress,  $\tau_{ij}^{LES}$  and SGS heat flux,  $\theta_j^{LES}$  in LES method. The method used to determine the turbulent heat flux and SGS heat flux is based on Reynolds-analogy hypothesis. In order to present this hypothesis firstly the turbulent viscosity is introduced.

The Reynolds stresses are modelled in a similar way as shear stress i.e. gradient of velocity and the constant of proportionality is turbulent viscosity also called as eddy viscosity,  $\nu_t^{ij}$ .

$$\tau_{ij} = \nu_t^{ij} \frac{\partial u_i}{\partial x_j} \quad (1.34)$$

The modelling of eddy viscosity for first order and second order closure models is discussed in chapter 2. The objective of this section is to present the modelling techniques of turbulent heat flux which is modelled in a similar way as Reynolds stress. The turbulent heat flux is



assumed to be proportional to gradient of temperature with  $\alpha_t$  as constant of proportionality that is called as turbulent diffusivity for heat or eddy conductivity:

$$u_i' T' = -\alpha_t^{il} \frac{\partial T}{\partial x_l} \quad (1.35)$$

Ideally, eddy conductivity should be a tensor quantity but in most of the models the anisotropic eddy conductivity tensor is replaced by isotropic scalar. Each heat flux component is governed by the same and still unknown eddy conductivity:

$$u_i' T' = -\alpha_t^{il} \frac{\partial T}{\partial x_l} = \alpha_t \frac{\partial T}{\partial x} = \frac{\nu_t}{Pr_t} \frac{\partial T}{\partial x} \quad (1.36)$$

The experimental determination of eddy conductivity is difficult and most of the commercial codes do not have a well-validated model for  $\alpha_t$  rather they are based on Reynolds analogy. Reynolds analogy assumes that there is similarity in the turbulent transport features of momentum and heat, and that the eddy conductivity is proportional to the eddy viscosity (Equation 1.41). The proportionality factor is the turbulent Prandtl number that is discussed in detail in next section. This means, we have highly sophisticated turbulent momentum transfer models in our commercial codes (explained in chapter 2), up to second order, solving a large number of additional transport equations, but the turbulent transfer of the scalars is calculated by using one factor, which is mostly assumed to be constant in space. Reynolds analogy is applicable for conventional fluids like air and water with Prandtl number around 1 where the boundary layer thickness and energy spectra for momentum and energy are similar but not for fluids like sodium with  $Pr \ll 1$  where the momentum and energy fields show no similar behavior (section 2.1, 2.2).

## 1.2.6 Turbulent Prandtl number

In the last section the limitation of Reynolds analogy was discussed for fluids with  $Pr \ll 1$ . The turbulent Prandtl number can be expressed as follows:

$$Pr_t = \frac{\nu_t}{\alpha_t} = \frac{u_i' u_j' \frac{\partial T}{\partial x}}{\frac{\partial u}{\partial x_j} u_i' T'} \quad (1.37)$$

In most non-adiabatic CFD computations, two equation RANS models are used in combination with the turbulent Prandtl number concept, in which the turbulent thermal diffusivity is linked to the turbulent eddy diffusivity by a simple ratio, the turbulent Prandtl number (Grötzbach, 2011). In most of the CFD codes the value of  $Pr_t$  is taken as 0.9 by default. This implies that the importance of turbulence diffusivity is same as turbulent

viscosity. According to Schlichting et al. (2000), the concept was developed for close to unity Prandtl number fluids, which possess similar scales for the thermal and momentum field. This is however not true in the case of fluids with  $Pr \ll 1$  where molecular conduction plays an important role in heat transfer. In case of sodium, the turbulent thermal diffusivity  $\alpha_t$  is smaller than the molecular thermal diffusivity,  $\alpha$ . The turbulent thermal diffusivity gains importance only when Reynolds number based on bulk velocity and hydraulic diameter is more than 214000 for sodium with  $Pr=0.004$  (Grötzbach, 2013). In SFR, the Reynolds number is about 50000 to 60000 so it is in conduction-dominated range. Figure 1.12 shows the curve for ratio of turbulent to molecular thermal diffusivity with Peclet number for three simple geometries- plane channel flow, pipe flow and flow in concentric annulus. At very low Prandtl number ( $\sim 10^{-3}$ ) and low Peclet number,  $Pe$  where  $Pe=RePr$ , the thermal conduction gets more and more dominant over the turbulent or convective heat flux. Indeed, the experimental data by Fuchs (Fuchs, 1973) and the combined LES/DNS data by Grötzbach (Grötzbach, 1981) show for the Prandtl number of sodium,  $Pr=0.007$ , that the ratio of  $\alpha_t/\alpha$  is for a fixed position in the channel at  $Re$  of about  $10^5$  is around 1 and decreases far below 1 for smaller  $Re$ . This means, the turbulent eddy conductivity is small compared to the molecular thermal diffusivity  $\alpha$ , and thus turbulence gives only a small contribution to heat conduction. From this dependence, one can understand that there are really parameter ranges in which calculations perform better by neglecting the turbulent heat flux model, or by setting  $Pr_t$  to infinity.

For the Prandtl number of mercury or lead bismuth,  $Pr=0.0214$ ,  $\alpha_t/\alpha$  takes values between 1 and 10 for  $Re$  around 25000. Thus, the turbulent heat flux model gets important and an adequate local  $Pr_t$  formula is required. And for the Prandtl number of air,  $Pr=0.7$ ,  $\alpha_t/\alpha$  takes values of 30 and larger, which means, the turbulent heat flux model is transporting nearly the complete heat and the contribution by conduction is of minor importance. Therefore, when the conductive wall layers are resolved, the quality of the results is almost entirely determined by the adequacy of the local  $Pr_t$  formula.

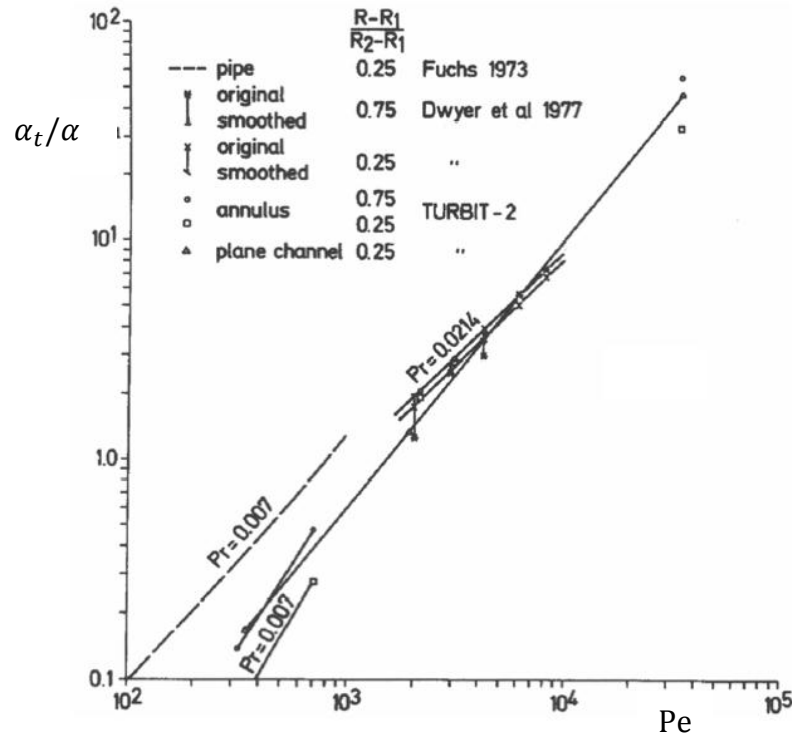


**Figure 1.12-Influence of Peclet number on the turbulent thermal diffusivity normalized by molecular thermal diffusivity (Grötzbach, 1981)**

This assessment means, at very low molecular Prandtl number, like for sodium, and at low Reynolds numbers a qualitatively accurate, but not a quantitatively accurate  $Pr_t$  formula may be sufficient, but with increasing Reynolds number and with slightly increasing Prandtl number, e.g. at that one for heavy liquid metals, we are in a transition range where the value of  $Pr_t$  becomes more and more important, and at Prandtl number around one the  $Pr_t$  formula governs in all low Reynolds number formulations completely the numerical temperature results. Therefore, in most applications an accurate formulation for the spatial distribution of  $Pr_t$  is essential, especially in the near wall area. And in applications using high Peclet number, formulations at Prandtl number from 0.02 to about 1, the formula has in addition to be consistent with the applied wall functions to avoid unphysical dependence on the numerical grid.

Grötzbach (Grötzbach, 2007) has summarized the typical problems with the turbulent Prandtl number concept and some important points are presented below:

- The similarity in the transport features implies also similarity in the statistical features of the velocity and temperature fields. This assumption is often violated, e.g. in

channels with one adiabatic wall where neither the first statistical moments of  $u$  and  $T$  are similar, nor their second moments

- The spatial dependence of both velocity and thermal eddy diffusivities may be different for fluids with molecular Prandtl number differing from 1 because of the difference in the boundary layer thickness (section 1.2.1)
- Smaller modelling deficiencies may become irrelevant with increasing Reynolds number so the dependence of  $Pr_t$  on the Reynolds number should be known

There are many correlations for turbulent Prandtl number as a function of  $Re$  and  $Pr$  in the literature for channel flows. Table 1.2 presents some of these correlations for  $Pr_t$  available in the literature. These correlations have been developed for fluids with Prandtl number equal to 0.02.

Azer, 1960	$Pr_t = \frac{1 + 380 \frac{e^{-(y^+)^{1/4}}}{Pe^{0.58}}}{1 + 135 \left( \frac{e^{-(y^+)^{1/4}}}{Re^{0.45}} \right)}$	(1.38)
Kays, 1980	$\frac{1}{Pr_t} = 0.5 Pr_{t\infty} + 0.3 Pe_t \sqrt{\frac{1}{2Pr_{t\infty}}} - (0.3Pe_t)^2 \left[ 1 - e^{-\left(\frac{1}{Pe_t}\right)} \right]$	(1.39)
Aloki, 1963	$\frac{1}{0.014 Re^{0.45} Pr^{0.2} \left[ 1 - e^{-\left(\frac{1}{0.014 Re^{0.45} Pr^{0.2}}\right)} \right]}$	(1.40)
Reynolds, 1975	$(1 + 100Pe^{-0.5}) \left( \frac{1}{1 + 120Re^{-0.5}} - 0.15 \right)$	(1.41)
Jischa, 1979	$0.9 + \frac{182.4}{Pr Re^{0.888}}$	(1.42)
Weigand, 1997	$Pr_{t\infty} = 0.85 + \frac{100}{Pr Re^{0.888}}$	(1.43)
Cheng, 2006	$Pr_t = \begin{cases} \frac{0.01Pe}{0.018 Pe^{0.8} - (7 - A)^{1.25}} & \text{for } 1000 < Pe \leq 6000 \\ 4.2 & \text{for } Pe < 1000 \end{cases}$ where $A = 5.4 - 9 \times 10^{-4} Pe$	(1.44)

**Table 1.2-List of correlations for turbulent Prandtl number**

The correlation (1.38) by Azer and Chao, 1960 was given for pipe flow and they analyzed the variation of turbulent Prandtl number as a function of wall normal distance in wall units. Kays and Crawford, 1980 suggested the correlation (1.39) based on theoretical analysis with correction from Weigand, 1997 given by (1.43) so that it can be used for fluids with low Prandtl number. Alok, 1963 and Reynolds, 1975 are empirical models. Reynolds, 1975 reviewed and assessed the available studies on turbulent Prandtl number in open literature and give the correlation (1.41). These two correlations (1.40) and (1.41) are recommended for  $Re \leq 170,000$ . Cheng and Tak, 2006 studied flow in Lead bismuth Eutectic flows in tube with constant heat flux and their correlation (1.44) is based on experimental data and CFD simulations. The validity of these correlations for other flow conditions is questionable (Cheng, 2006). However we evaluate these correlations for sodium flow at Prandtl number 0.004 and Reynolds number 50000 corresponding to flow in sub-assembly.

These correlations have been plotted in Figure 1.13a as a function of only Prandtl number by keeping Reynolds number constant and equal to 50000. These correlations give the value of turbulent Prandtl number more than 1 for lower Prandtl numbers. The value of turbulent Prandtl for sodium with  $Pr=0.004$  varies from 1.5 to 4.2. However, the variation of  $Pr_t$  at Reynolds number lower than 50000 is even higher. This is visible from Figure 1.13b where the same correlations are traced for fixed Prandtl number (equal to 0.004 for liquid sodium) and varying only Reynolds number. At  $Re=20000$  we get turbulent Prandtl number varying from 2.5 to 8 and this variation increases at  $Re<20000$ . The overall behavior of  $Pr_t$  seen from Figure 1.13 is that the turbulent Prandtl number decreases with increase in Prandtl number or Reynolds number. Therefore the usage of the turbulent Prandtl number concept at low Reynolds number and low Prandtl number needs to be applied with care.

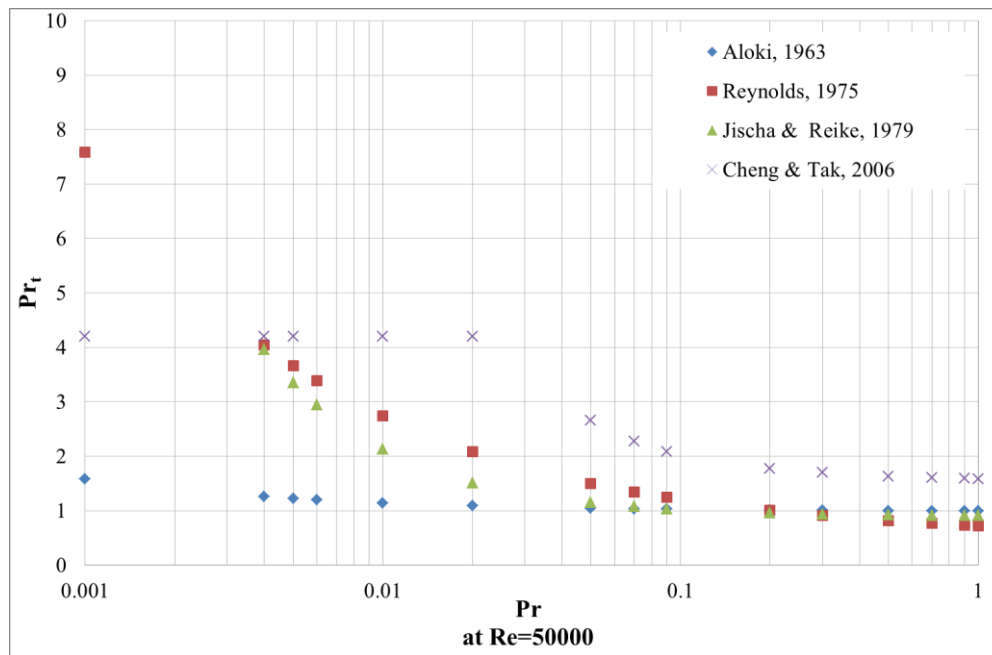


**Figure 1.13a- Turbulent Prandtl number from various correlations as a function of Prandtl number by keeping Reynolds number constant**

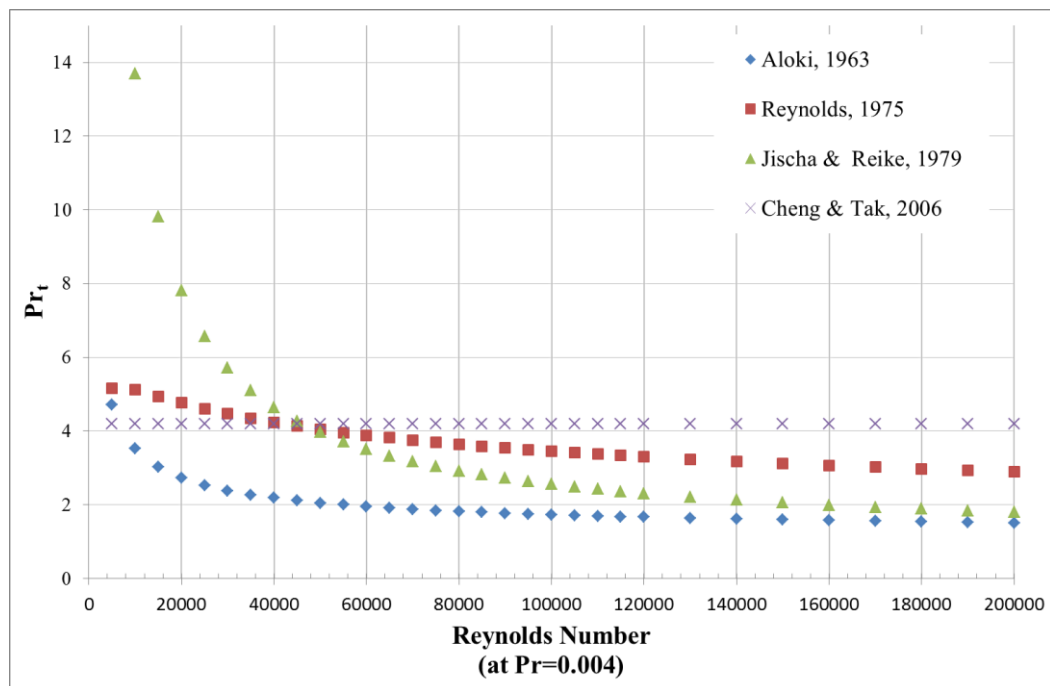


**Figure 1.13b- Turbulent Prandtl number from various correlations as a function of Reynolds number by keeping Prandtl number constant**

# 1.3 Thermal hydraulic study of sub-assembly

## 1.3.1 Introduction

Sub assembly thermal-hydraulics is a key scientific subject in the development of SFR reactors. This section presents the current knowledge of the experiments performed in the past on the sub-assembly and the numerical studies realized in the past using the three levels of CFD approach: RANS, LES and DNS.

## 1.3.2 Experiments

Experiments play a vital role in understanding of the physical phenomena and validation of the results from numerical simulations as the mesh size remains limited and the turbulence models are based on some assumptions. However, there are only limited experimental data sets available. There are few experiments with wire-wrapped pin bundles and even fewer experiments with sodium as the coolant in forced convection regime. Some of these experiments are the:

- Oak-Ridge National Laboratory (ORNL) 19-pin bundle (M. Fontana, R. E. MacPherson, et al. 1973) where they measured the temperature distribution on the duct wall and at the exit of a 19-pin spacer wire fuel sub-assembly.
- 19-pin bundle GR19-I (Berger, 1975) and GR19-BP (Piettre, 1985) for sodium boiling experiments.
- ECONA 37-pin bundle (Piettre, 1987), the Toshiba 37-pin bundle (Namekawa, 1984).
- FETUNA 91 pin (Rameau, 1982).

There are also hydraulic experiments on wire-wrapped sub-assembly using air and water as the coolant have been performed with various number of fuel pins

- 19 pin bundle (Lafay, 1975; Tong, 1968; Chun, 2001; Vijayan, 1999).
- 37 pin bundle (Marten, 1982).
- 61 pin bundle (Arwika, 1979; Chiu, 1979; Rehme, 1973).
- 271 pin bundle experiment (Collingham, 1971).
- Roidt et al. (Roidt, 1980) investigated the hydraulic field inside a 217-pin wire-spacer assembly.

- Chun et al. (Chun, 2001) performed an experimental evaluation of existing correlations for the pressure drop in a 19-pin wire-wrapped fuel assembly.
- Choi et al. (Choi, 2003) carried out experimental work to measure the pressure drop in a 271-pin fuel assembly and compared the available data with existing correlations for friction factor.
- Fernandez et al. (Fernandez, 2000) performed an experimental investigation to obtain static pressure.
- The ESTAIR experiment with 19 pin bundle cooled by air (Berthouex, 2008).

The main characteristics of the flow field learned from the above experiments can be summarized below (Figure 1.14):

- i. There is significant circular flow and wake downstream of the spacer wire;
- ii. The flow has two distinct region – the central flow and the peripheral flow;
- iii. The peripheral flow around the hexagonal can is characterized by higher axial velocity as compared to the flow in central region;
- iv. The axial sub-channel flow velocity and cross flow velocity are cyclic with a spatial parody corresponding to the helical pitch of the spacer wire.

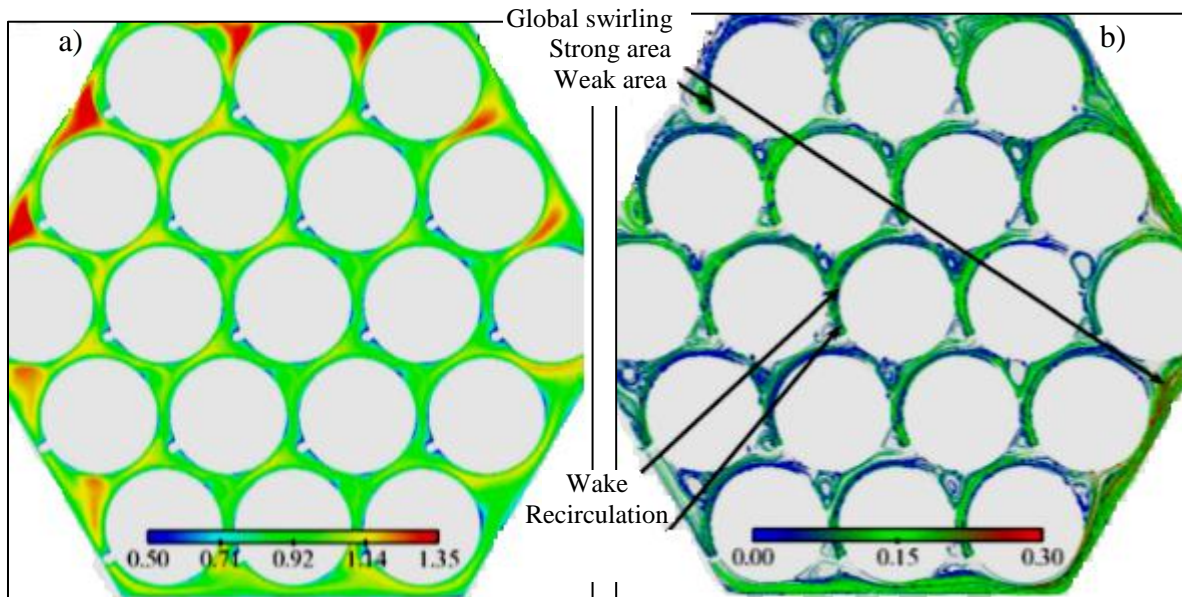


**Figure 1.14-The velocity distribution for 19 pin sub-assembly showing (a) dimensionless streamwise velocity and (b) transverse velocity (Rolfo, 2012)**



These experiments are useful for the validation of friction factor, the pressure drop calculations and to understand the effects of wire wrap spacer system on the flow in rod bundles.

The recent work of Bubelis et al. (Bubelis, 2008) presents a complete evaluation of several pressure drop correlations, taking into account arrangements with different numbers of pins and different types of coolant. In case of liquid sodium, authors validate the correlations against CFD data from Gajapathy et al. (Gajapathy, 2007). On the other hand, Gajapathy et al. use Rehme's correlation to validate the numerical results.

An even more difficult task is to find precise and accurate experimental data for heat transfer. Several studies were conducted during the sixties and analytical correlations were derived for the Nusselt number (Kirillov, 1963). In recent years those data were revisited in the context of international collaborations for advanced nuclear reactor core configurations in the literature by Pfrang et al. (Pfrang, 2007) and Mikityuk et al. (Mikityuk, 2009). Both reviews present several correlations for the Nusselt number as function of the Peclet number  $Pe = Re Pr$  and the Pitch to Diameter ratio for both triangular and square arrays. The major problem is that the pins are considered without the wire wrapping typical of more recent and future designs.

The experiments with air and water cannot be used for the validation of heat transfer and the hot spot studies in SFR. The experiments available with sodium are very old experiments performed in 1970's and 1980's. The age of the experiments has two important implications, first, as noted above, the tests were not designed to address CFD validation and therefore do not contain all the necessary information and uncertainty. The uncertainty in the experimental measurements is too important for CFD validation. The CFD study performed by Frianco et al. (Frianco, 2014) who studied the ORNL 19 pin experiment highlights the limitation of current experiments for heat transfer validation. Therefore, with the lack of experimental data to validate the sodium heat transfer it is necessary to be as accurate as possible while performing the numerical simulations.

Another important phenomenon seen from the experiments is the existence of hot spot in the wake of spacer wire. Figure 1.15 shows the photograph of the 19 fuel pin sub-assembly of GR19BP experiment that was performed with sodium loop in 1980's at CEA Grenoble. In this photograph the clad melt down at the wake of wire is clearly visible. There can be many reasons for this melt down because what we are looking at is after the series of many boiling experiments but one of the plausible reasons can also be the local dry out on a small cladding area due to hot spot boiling. Due to decrease in the coolant velocity at the wake of spacer wire the rod surface might locally heat up above the saturation temperature of the coolant. This

might lead to evaporation of the coolant and create vapor bubbles which on their part can influence the neutron fluxes. This phenomenon is called the hot spot boiling which is a form of sub-cooled boiling present due to a local stagnant zone of sodium between wire spacer and the fuel pin. This vapor bubble can only grow until it encounters the sub-cooled core of the sub-channel flow. In the sub-assembly, the wire spacer geometry creates the conditions that can lead to a relatively steep temperature profile and the associated sub-cooling. The Ph.D. thesis on the sodium boiling studies on heated sub-assembly by Menant (Menant, 1976) highlights the phenomena of hot spot boiling. This is later supported by Vanderhaegen (Vanderhaegen, 2014) in his review of sodium boiling phenomena in reactor systems.



**Figure 1.15-Photograph of GR19 sub-assembly used for boiling experiments showing the clad melt down locally at the wake of wire**

It is thus of main interest to understand both, the global temperature distribution in the assembly and the possible occurrence of hot spots in the wake of the spacer wire locally. Numerical simulations give the access to perform detailed study of a local region of the sub-assembly and to understand this phenomenon of hot-spots in detail.

### **1.3.3 RANS studies**

Numerous numerical results are available on the flow behavior in wire spacer rod bundles. Hereby, the analyzed domain range from basic 7 pin bundles to realistic 61 or even 217 pin bundles and from simplified one wire pitch with axial periodic conditions to full-scale assemblies with varying axial power in the fuel pin. Study of 7 and 19 pins configurations (Gajapathy, 2007) (Natesan, 2010) (Peniguel, 2010) (Kim, 2005), (Ahmad, 2006) analyzed

precisely the three-dimensional turbulent flow and heat transfer in a 7-pin wire-wrapped assembly based on Reynolds-averaged Navier–Stokes (RANS) calculations. Raza et al. (Raza 2008) performed the numerical optimization of 7-pin wire-wrapped assembly based on three-dimensional RANS analysis.

These results are encouraging and it appears that RANS computations can provide detailed flow analysis that will be required for improved modelling insight. The linear  $k$ – $\varepsilon$  models of RANS model still remain most widely adopted for the analysis of practical problems. It is currently the most popular model and applicable to a large variety of flow cases with reasonable prediction accuracy.

RANS modelling approaches for tight lattice sub-assembly (Pitch to diameter ratio,  $P/D < 1$ ) without spacer wires were assessed by Chang et al. (Chang, 2007 and Chang, 2008), Baglietto et al. (Baglietto, 2007), Cheng et al. (Cheng 2006), Baglietto et al. (Baglietto, 2003). Anisotropic effects are important so that they cannot be accounted for in RANS. The usual formulations of the model assume isotropic eddy diffusivity in modelling the Reynolds stress tensor, which prevents them from accounting for the inequality of the normal stresses. In simple terms, since the viscosity is a scalar, each component of the stress affects its strain to the same extent. For this reason, for flows where turbulent intensity gradients are important, cannot be accurately predicted. The anisotropic turbulence models are required to capture the secondary flows which influence the heat transport.

Another alternative RANS model is the  $k$ – $\omega$  model (Wilcox, 1988) and the Shear Stress Transport (SST) model (Menter, 1994), which in place of the dissipation rate,  $\varepsilon$ , adopts an equation for the turbulent frequency,  $\omega$ , of the large scales. These models have gained recent popularity, claiming accurate predictions of the turbulent length scale which should improve the wall shear stress and heat transfer predictions, and due to the very simple low-Reynolds formulation, which does not require additional non-linear wall damping terms. But these models also have eddy viscosity approximation and thus unable to account properly for anisotropy of turbulence.

Thus, eddy viscosity models are not adapted to model correctly the anisotropy of turbulence. Still they have been used widely to study the wire-wrapped bundles. We notice that existing studies lack sufficiently detailed comparisons to local measurements, which are necessary to ensure that the CFD model is correctly predicting the experimental behavior.

Recent publications more often focus on comparing the effects of various parameters like

- Turbulence model (Smith, 2008, 2009).
- Bundle size (Gajapathy, 2009).

- Cell aspect ratio (Smith, 2009 Pointer, 2009), and wire wrap contact representation (Pointer, 2009, Merzari, 2012 and Hamman, 2010).
- Multi-scale approach and to benchmark models of different scales against each other, i.e. LES to RANS or Sub-Channel methods (Fanning, 2009).

The second order closure models like Reynolds Stress Models (RSM) are often used instead, because they offer a greater potential for predicting the anisotropic phenomena (Cheng, 2006; Baglietto, 2005). Anyhow, the higher order correlations need to be modelled with some drastic assumptions of unknown validity, where even the principles and basic techniques for their modelling have not been established yet, at least in the near wall region.

Pointer et al. (Pointer, 2008) focused on the benchmarking of flow field predictions on in 7-pin by comparing the LES and RANS calculations. The 19-pin, and 37-pin fuel assemblies and flow field was benchmarked against LES results for 7 pins as shown in the Figure 1.16 and Figure 1.17. A good comparison between LES and RANS results is clearly seen. Pointer et al. (Pointer, 2009) extended these studies to 217-pin assemblies in support of initial efforts to benchmark heat transfer predictions using the RANS models against conventional sub-channel models.

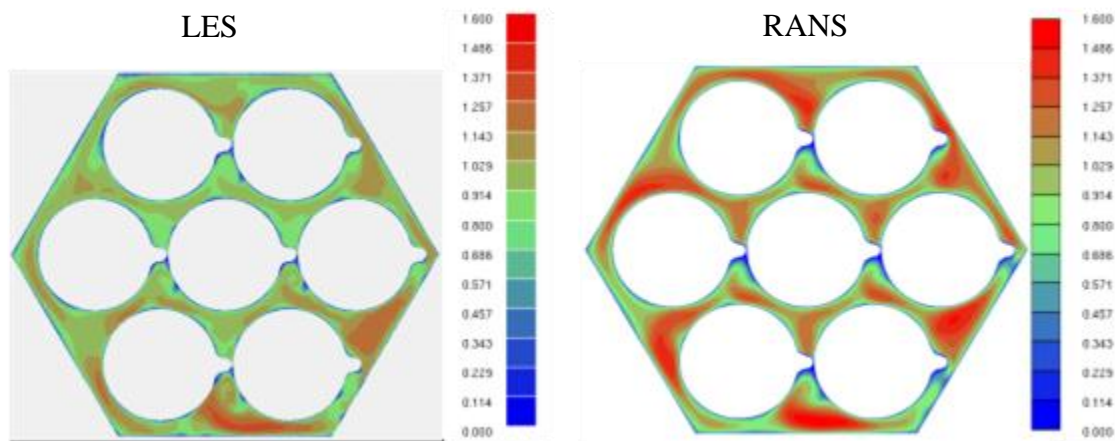


**Figure 1.16-Time averaged velocity field predicted by LES simulation using Nek5000 on the left and steady state velocity field predicted by RANS simulations using Star-CD (Pointer, 2009)**

Rolfo et al. (Rolfo, 2012) follows the same methodology as of Natesan et al. (Natesan, 2010). The range of Reynolds number considered is  $5000 \leq Re \leq 50000$ , which is just below the nominal Reynolds number of the real assembly ( $Re \sim 70000$ ), but with respect to previous

studies this work increases the number of pins up to 271 of the real geometry. Indeed, the present investigation tries to establish the influence on the results of some other important parameters, such as, geometry, meshing, representation of the pin/wire contact and also takes into account some “preliminary” tests on heat transfer. The heat transfer analysis employs simplified boundary conditions for the temperature (i.e. A Dirichlet constant wall temperature and a Neumann constant wall heat flux), whereas the real situation at the fluid/solid interface is far more complicated: the fuel is only located inside the pin and there is no energy deposit inside the wire. The wall modelling used by them takes in to account the linear thermal region that extends up to  $y^+ = 450$ .

They also examined the effect of turbulent Prandtl number. Since the low value of the Peclet number, higher turbulent Prandtl number  $Pr_t = 3$ , as suggested in Cheng et al. (Cheng, 2006), has also been tested in some configuration (7 and 19 pins geometries at  $Re = 25,000$ ), but without noticing a large variation of results (the percentage variation of the Nusselt number for the Dirichlet BC is below 1% and below 3% in the case of a Neumann BC).

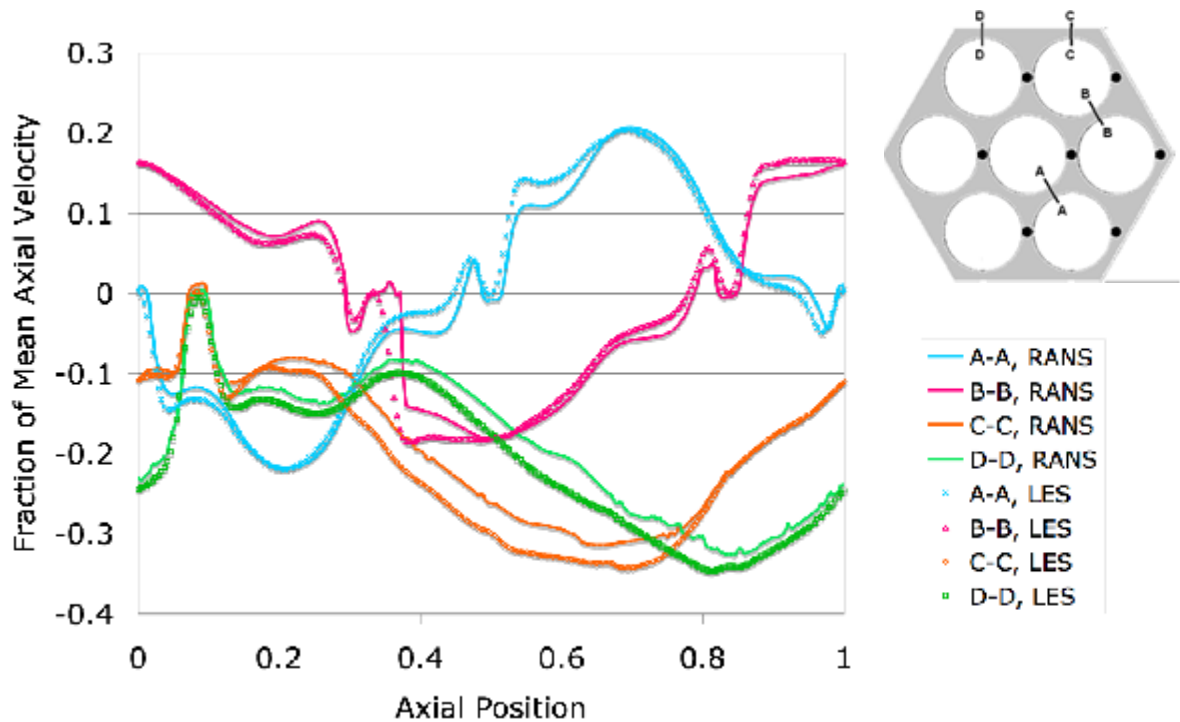


**Figure 1.17-Comparison of LES and RANS simulation predictions of axial distribution of cross-channel flow velocities for four channels (Pointer, 2009)**

The widely used RANS method has been used for parametric and sensitivity studies. Most of the studies involve comparison with the reference calculation and correlations. This no doubt gives additional information about the thermal hydraulic studies for sub-assembly and effect

of these parameters on the flow variables but a more accurate method like LES and DNS are envisaged for more confidence in the results and to have more information about the flow features.

### 1.3.4 LES studies

In the last years a lot of progress has been made in large eddy simulations due to improved numerical models and increased computational power. This technique, previously restricted to very simple test cases, can now be applied to some industrial cases. The main applications presented here are related to thermal fluctuations. However, the applications are still restricted to rather limited domains, since they require a fine grid modelling, especially for identifying the unsteady heat transfer at the walls (Simoneau, 2010).

LES modelling approaches have been recently assessed for bare rod bundles by, e.g. Merzari et al. (Merzari, 2008), Popov et al. (Popov, 2008), Ikeno et al. (Ikeno, 2007) and Merzari et al. (Merzari, 2007). These simulations allow capturing both the temperature and the momentum fluctuations and are considered more accurate than RANS simulations. They are able to capture the anisotropic flow due to tight lattice of the fuel bundles.

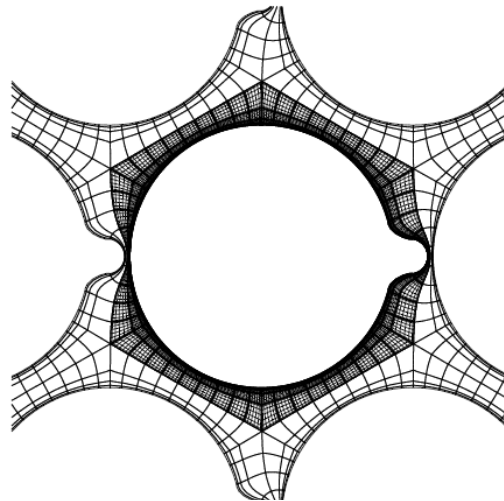


**Figure 1.18-Computational domain used by fisher (Fischer, 2007) for hydraulic LES study**

Application of LES to the geometry of sub-assembly with spacer-wire has been limited. Fischer (Fischer, 2007) studied the hydrodynamic field in the wire-wrapped sub-assembly using nek5000 code (Patera, 1984; Fischer, 2002; Deville, 2002). The domain studied by him

is shown in Figure 1.18 that has a central pin with a part of neighboring pins and axial periodicity is imposed in radial direction. Whether this periodicity well represents the effect of the neighboring pins on the physics of the coolant flow is examined in this paper. The flow in bare rod bundles for different local geometries with radial periodicity is studied by LES model and the results are compared qualitatively and quantitatively to the theoretical and experimental knowledge of physics of the flow in bare rod bundles (Ninokata, 2009). The domain is well represented for the velocity field in the complete sub assembly. LES studies of heat transfer in sub-assemblies with spacer wire were not found in the open literature but they have been performed recently on a simple representative geometry. This study is discussed in section 1.3.6.

However, an important limitation of both RANS and LES method is the use of Reynolds analogy to model the turbulent and SGS heat flux for fluids with  $Pr \ll 1$ . The value of turbulent Prandtl number has to be optimized in order to consider a distinct scale separation between heat and momentum transfer (see section 1.2.5 and 1.2.6). A more sophisticated modelling like DNS is envisaged.

### 1.3.5 DNS studies

DNS calculation of a simple channel flow with a wire embedded in one of the walls is performed by Ranjan et al. (Ranjan, 2010, Ranjan, 2011) (Figure 1.19).

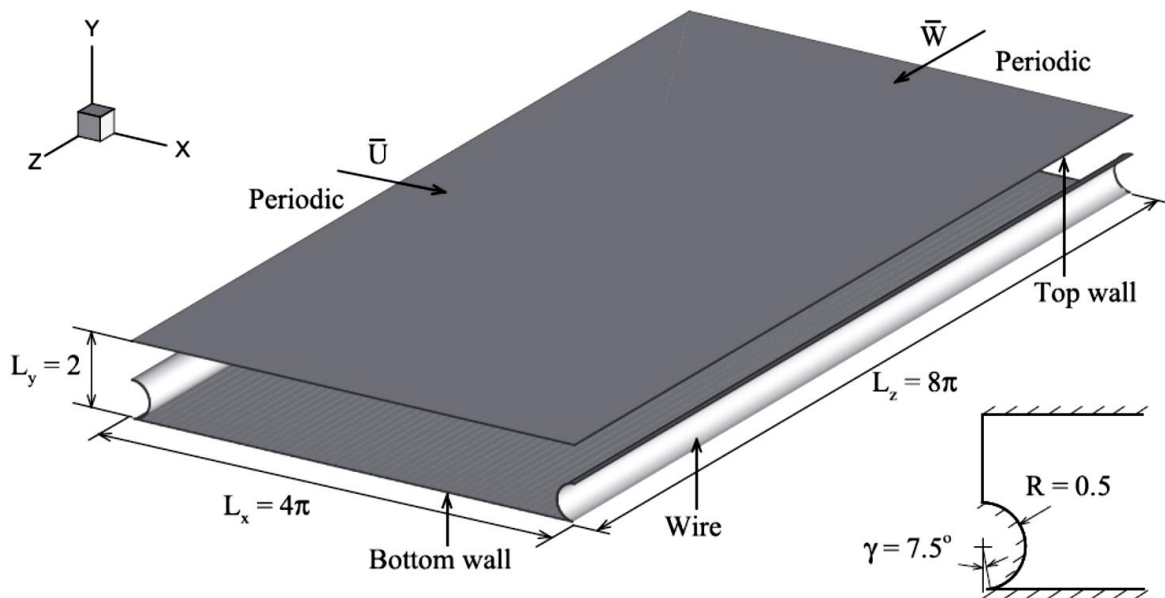
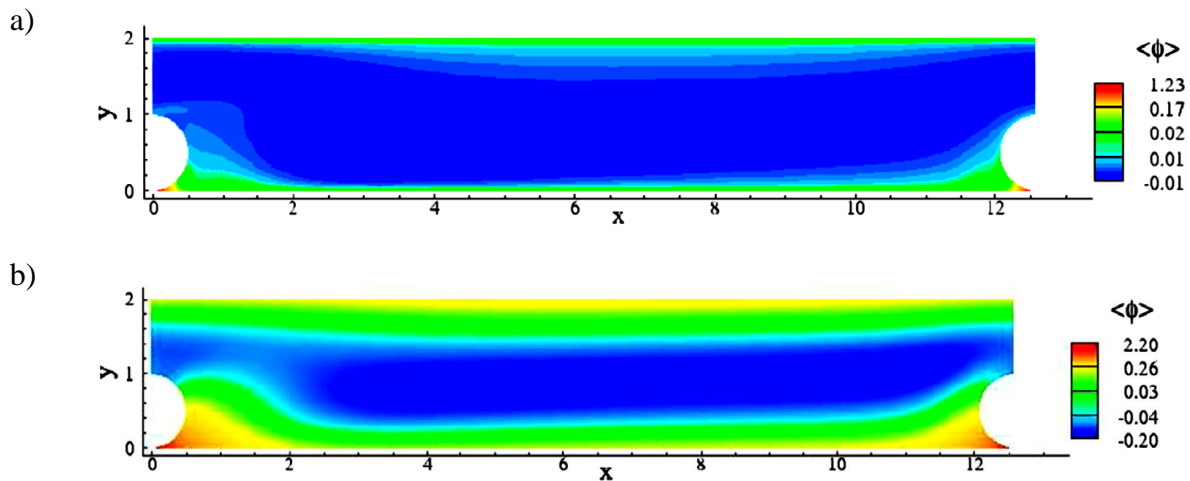


Figure 1.19-Schematic geometry studied by Ranjan et al. (Ranjan, 2010)

They investigated heat transfer characteristics of a turbulent swept flow in a channel with a wire placed over one of its walls using direct numerical simulation. The swirling or the cross flow created by helical turn of the spacer wire in sub-assembly is generated in this simple representation by imposing a flow in the transverse direction  $x$ . A key aspect of this flow is the presence of a high temperature region at the contact line between the wire and the channel wall, due to thermal confinement (stagnation). The temperature field is simulated at three different Prandtl numbers:  $10^{-2}$ ,  $10^{-1}$  and 1. Figure 1.18 shows the temperature field at two Prandtl number equal to 1 and  $10^{-2}$ . The temperature field at  $Pr = 10^{-2}$  (Figure 1.20b) is much smoother than that at  $Pr = 1$  (Figure 1.20a) and also the non-dimensional temperature at hot spot is almost double than that  $Pr = 1$ . The peak Nusselt number occurs close to the reattachment location, on the lee side of the wire, and is about 50–60% higher compared to the case without cross flow. The high temperature region follows the growth of the recirculation bubble which increases by about 65% from the lowest to highest amount of cross flow. Although it gives detailed distribution for velocity, temperature fields and turbulent statistics but the phenomena like local rotational velocity and mixing coolant velocity due to the helical turn of wire cannot be studied in this geometry. Also, in reality the spacer wire is present on a circular fuel pin whereas in the work by Ranjan et al. the wall is flat so the effect of curvature on the temperature results is still unknown.



**Figure 1.20-Iso-contours of non-dimensional temperature at (a)  $Pr=1$  and (b)  $Pr=10^{-2}$  (Ranjan, 2011)**



### **1.3.6 Hot spot studies**

The hot spots can modify the flow regime and affect the strength of the clad. As the clad is the first layer of defense, such temperature non-uniformities could influence the life of the fuel pin and also have direct bearing on the reactor safety. Hence a detailed study at the level of sub-assembly is necessary to study the hot spots.

Merzari et al. (Merzari, 2012) investigated the effect of pin-wire contact modelling on the prediction of the hot spot. They performed conjugate heat-transfer calculations by solving the conduction equation in the solid part using LES. Like Ranjan et al. (Ranjan, 2010), this study was done on a channel flow with a wire embedded in one of the walls. To study the effect of pin-wire contact modelling two different cases were studied:

- 1) Wire and wall are considered in contact and merged with an angle of  $7.5^\circ$  as studied by Ranjan et al 2010 (Figure 1.21a).
- 2) Wire and wall are separated by a nominal gap of height,  $g$ , equal to 0.05 times the channel height,  $h$  (Figure 1.21b).

The results presented by them suggest that it is necessary to have contact between wire and the modelling of the contact between wire and wall as the flow field and the temperature field are significantly affected (Figure 1.21). In case of contact between the wire and wall the temperature at the hot spot is higher than in the case with nominal gap. Therefore in the case of hot spot studies the uncertainty due to the contact modelling is more significant than the uncertainty due to the turbulence modelling. Additional conclusion drawn from their work is that RANS-based techniques are sufficient to reach accurate results for the prediction of the hot spot and peak fluid temperature due to the conduction-dominated nature of heat transfer for low-Prandtl fluid conjugate heat transfer cases. However, this result is limited to the present geometry of channel flow with straight wire at  $Re$  of 6000 and 1000 in streamwise and transverse direction respectively and  $Pr = 10^{-2}$ . These results cannot be extrapolated to sodium flow in sub-assembly at  $Re \sim 50000$  and  $Pr \sim 10^{-3}$ .

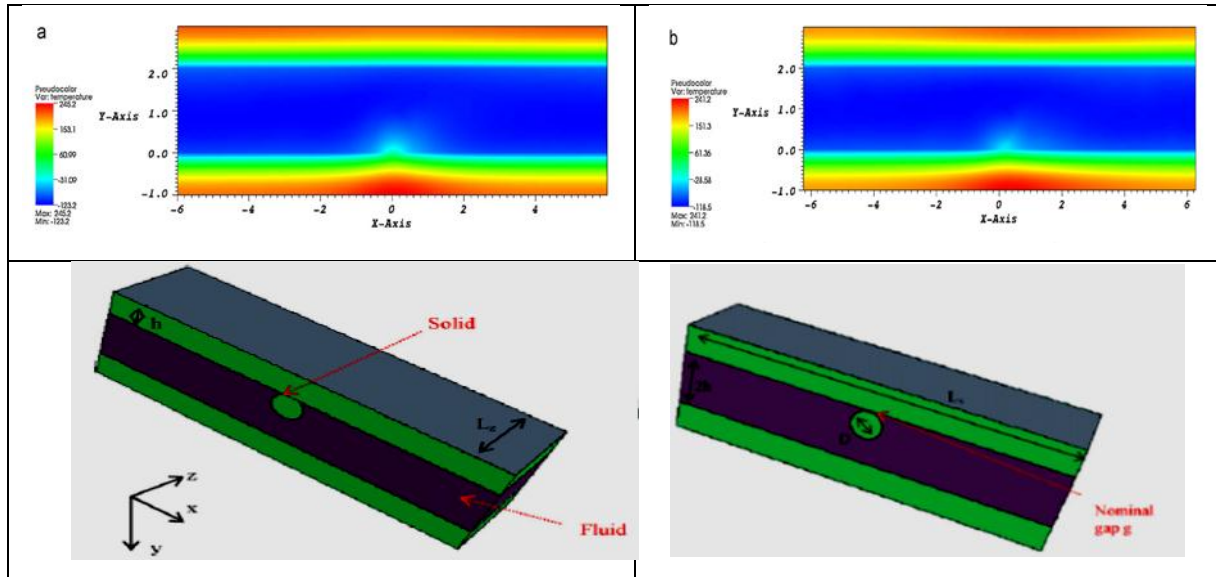


**Figure 1.21-Average temperature distribution at a horizontal cut plane (top) and the three dimensional geometry for the two cases a) with contact b) with no contact between the wire and wall studied by Merzari (Merzari, 2012)**

## 1.4 Summary

The thermal-hydraulic studies of the hexagonal sub-assembly of SFR by experiment and numerical simulations shows that in the contact region between rod and spacer wire, the flow velocity is significantly reduced, in particular in the wake of the wire. At this location, the rod surface might locally heat up above the saturation temperature of the coolant. In transient condition this might lead to evaporation of the coolant and create vapor bubbles which on their part can influence the neutron fluxes.

The thesis objective is to study the hot spot at the wake of spacer wire in the sub-assembly at the nominal operating conditions of SFR and bring out thermal characteristics of this region by using computational fluid dynamics.

Liquid sodium is characterized by very low Prandtl number ( $Pr = 0.004$  at  $450^\circ\text{C}$ ) as compared to water ( $Pr \sim 1$ ) which makes the temperature field much smoother than the velocity field, and for moderate Reynolds number (around 50000 to 70000) the heat transfer at the wall could be governed by conduction while the flow is fully turbulent. The classical Reynolds analogy used in RANS and LES methods assumes the turbulent Prandtl concept and the wall function approach, fails to correctly predict the local heat transfer in this case. Also, the experimental data available published to date is limited and high precision results are needed for validation.

DNS can serve as numerical reference data due to its high precision and accuracy. It has been used to study the effect of Prandtl number on the heat transfer characteristics in simple geometries like channel flow (Kawamura, 1998b; Kawamura, 1999), pipe flow (Redjem-Saad, 2007) and annular flow (Ould-Rouiss, 2010), and. However these studies have been limited to  $Pr$  as low as  $10^{-2}$  only and only one LES-DNS is available at  $Pr = 0.007$  (Grötzbach, 1981).

The thermal-hydraulic study of the complete sub-assembly containing 217 fuel pins using RANS methods have been performed in the past (Pontier, 2009) but are few as compared to studies with 7, 19, 37 and 61 fuel pins due to reasonable mesh size and computational time. Using RANS method sensitivity studies has been done for the turbulence model, geometric parameters, and boundary conditions. However, the validation of thermal field with experimental data is limited and we need more accurate CFD methods like LES and DNS to study the thermal field of sodium in sub-assembly. The LES calculation of the sub-assembly with 217 fuel pins is costly in terms of computational requirements so a smaller region representative of the flow has to be decided. Fischer (Fischer, 2007) performed hydraulic calculation using LES method on central local region of fuel pin. This domain is sufficient for the representation of hydraulic flow and will be used in this thesis for thermal hydraulic studies. The thermal-hydraulic LES study of sub-assembly with spacer wire available in open literature is less and limited to simple geometry. The LES study of Merzari et al. (Merzari, 2012) gives detail information about hot spot in spacer wire as it also considers conduction in the solid part of fuel pin. Their work follows the DNS work of Ranjan et al. (Ranjan, 2011) who performed DNS to study heat transfer in channel flow with spacer wire. The two studies have substantial contribution to the knowledge of heat transfer in liquid metals but have following limitations:

- 1) The simplified geometry does not take in to account the curvature effect of fuel pin.
- 2) The effect of helical turn of spacer wire is modelled artificially by cross flow.
- 3) The Prandtl number is  $10^{-2}$ .

# CHAPTER 2

---

## *Numerical methods and tools*

*This chapter describes the numerical methods for modelling the single-phase incompressible fluid flow. Firstly, the conservation equations of physics that governs the fluid flows and heat transfer are presented. Then, the procedure of numerical methods (CFD) to solve these equations is described. In the third section, the different approaches available in CFD-RANS, LES and DNS having different resolutions of flow structures are presented in detail with the basic principle, equations and the method used to model the unresolved terms corresponding to turbulence effects. The choice of the turbulence model and the tool used to perform the numerical simulation are presented thereafter along with the wall treatment and source terms to treat periodic boundary condition.*



## 2.1 Equations for incompressible flow

The governing equations of fluid flow represent the mathematical statements of the following conservation law of physics:

- i. **Conservation of mass**-The mass of fluid is conserved.
- ii. **Conservation of momentum**-The rate of change of momentum is equal to the sum of forces on a fluid particle (Newton's second law).
- iii. **Conservation of energy**-The rate of change of energy is equal to the sum of rate of heat addition and the rate of work done on fluid particles (first law of thermodynamics)

**Hypothesis:** The mathematical statement of the three conservation laws mentioned above takes into account the following hypothesis for the fluid and fluid flow:

- Fluid is regarded as continuum and obeys the Newtonian law i.e. viscous stresses,  $\tau_{ij}$  are proportional to rate of deformation,  $S_{ij}$  with dynamic viscosity  $\mu$  as constant of proportionality.

$$\tau_{ij} = 2\mu S_{ij} - p\delta_{ij} \quad (2.1)$$

Where  $S_{ij}$  is defined as follows,

$$S_{ij} = \frac{1}{2} \left( \frac{\partial u_i}{\partial x_j} + \frac{\partial u_j}{\partial x_i} \right) \quad (2.2)$$

- The fluid flow is incompressible which implies that the density of the fluid,  $\rho$ , as it moves along, is assumed constant. Mathematically it is written as follows:

$$\frac{D\rho}{Dt} = \frac{\partial \rho}{\partial t} + u \cdot \nabla \rho = 0 \quad (2.3)$$

- The incompressibility assumption includes implicitly that the pressure,  $p$  is not a thermodynamic property and plays a purely mechanical role. The thermodynamic properties of fluid (density  $\rho$ , thermal diffusivity  $\alpha$ , dynamic viscosity  $\mu$ , heat capacity  $C_p$ ) are independent of local pressure but can be function of local fluid temperature.

$$\rho = \rho(T) \text{ but } \rho \neq \rho(p) \quad (2.4)$$

- Flows considered do not take into account the gravitational force. The buoyancy effects are neglected.
- Energy conservation equation is reduced to transport equation of a passive scalar, temperature. A passive scalar implies that it has no influence on the fluid motion but

transported by diffusion. Thus, the momentum and energy equations are completely decoupled.

If  $\vec{u}$  represents the flow velocity vector with components  $(u_1, u_2, u_3)$ ,  $p$  represents pressure,  $T$  represents temperature then using Einstein notation on repeated indices  $i, j$  the above three equations are written as follows:

**Continuity equation (conservation of mass):**

$$\frac{\partial u_i}{\partial x_i} = 0 \quad (2.5)$$

**Navier-Stokes Equation (conservation of momentum):**

$$\frac{\partial u_i}{\partial t} + u_j \frac{\partial u_i}{\partial x_j} = -\frac{1}{\rho} \frac{\partial p}{\partial x_i} + \nu \frac{\partial^2 u_i}{\partial x_j \partial x_j} + f_i \quad (2.6)$$

Where  $f_i$  represents external body force and energy source term and  $\nu = \mu/\rho$  is kinematic viscosity. The terms in equation (2.6) from left to right are transient term, non-linear convective term, pressure term, diffusive term and source term.

**Transport equation of temperature (conservation of energy):**

$$\frac{\partial T}{\partial t} + u_i \frac{\partial T}{\partial x_i} = \alpha \frac{\partial^2 T}{\partial x_i \partial x_i} + s_T \quad (2.7)$$

Where  $s_T$  represents the external energy source term and  $\alpha = \frac{\lambda}{\rho C_p} = \frac{\nu}{Pr}$  is the thermal diffusivity of the fluid with  $Pr$  as the Prandtl number of the fluid.

These set of equations form a closed system with five equations consisting of five variables (three velocity components, pressure and scalar concentration). In principle, the Navier-Stokes equations are capable of describing all kind of flows- from steady (non-time-dependent) laminar solutions to very complicated turbulent flows. However, the Navier-Stokes equations are non-linear partial differential equations so no analytical solution exists for these complex turbulent flows. Thus, for the practical problems, one has to calculate the solutions of the Navier-Stokes equation numerically with the aid of supercomputers.

## 2.2 CFD –Introduction and Methods

Computational Fluid Dynamics (CFD) is the analysis of systems involving fluid flow and heat transfer by means of computer based simulation. Since the development of computers, CFD has an important place in research and in industry. It predicts many results, both qualitative and quantitative without setting up experiments that can be expensive.

The numerical tool or the CFD code used to solve the conservation equations of fluid mechanics and heat transfer using the numerical methods are structured around the numerical algorithms that can tackle the fluid flow problems. In order to provide easy access to their solving power all commercial CFD packages include sophisticated user interfaces to input the problem parameters and to examine the results. Hence, all codes contain three main elements:

### **1. Pre-processor:**

It consists of defining the problem to a CFD program in a form suitable for use by the solver. It includes:

- Definition of the geometry of the region of interest: the computational domain
- Grid generation – the sub-division of the domain into a number of smaller, non-overlapping sub-domains
- Selection of the physical phenomena to be studied
- Definition of fluid properties
- Specification of appropriate boundary conditions at cells which coincide with or touch the domain boundary

### **2. Solver:**

There are four distinct streams of numerical solution techniques: finite difference, finite volume, finite element and spectral elements. The three basic steps performed by solver are:

- Approximation of the unknown flow variables by means of simple functions
- Discretization by substitution of the approximations into the governing flow equations and subsequent mathematical manipulations
- Solution of algebraic equations

### **3. Post-processor**

It includes the data visualization tool to see the solution of the flow fields. These include

- Domain geometry and grid display
- Vector plots
- 2D and 3D surface plots
- Particle tracking, etc.

One of the main concepts of fluid mechanics is the concept of turbulence. If we look at a turbulent fluid flow from a statistical point of view, a mean field appears on which fluctuations of different scales are superimposed. The problem of numerical simulation of turbulent flows is to assess with more or less accuracy the average and fluctuations of these fields for a wide range of scales present in the flow.

For the simulation of turbulent fluid flows, there are three major families of CFD: Direct Numerical Simulation (DNS), Large Eddy Simulation (LES) and Reynolds Averaged Navier-Stokes Simulation (RANS).



## 2.3 Reynolds Averaged Navier-Stokes method (RANS)

### 2.3.1 Principle

It is the most common method where the flow variables undergo Reynolds decomposition i.e. separating the variables into a time averaged part and a fluctuating part. Only the equations for time averaged variables are simulated while the fluctuations are modelled. The main advantage of this method is its low computational cost and time taken to have average steady state results.

#### Reynolds decomposition

When we study the momentum or thermal field of a turbulent fluid flow then at each point of this flow, each variable say  $\phi(x_i, t)$  is depending on time and space. For a statistically stationary flow the variables could be decomposed into time averaged,  $\Phi(x_i)$  and turbulent fluctuation terms,  $\phi'(x_i, t)$ .

$$\phi(x_i, t) = \overline{\phi(x_i, t)} + \phi'(x_i, t) = \Phi(x_i) + \phi'(x_i, t) \quad (2.8)$$

Where the time averaging operator,  $\bar{\cdot}$  is defined as follows:

$$\overline{\phi(x_i, t)} = \Phi(x_i) = \lim_{T \rightarrow \infty} \frac{1}{T} \int_0^T \phi(x_i, t) dt \quad (2.9)$$

And the fluctuating quantity  $\phi'(x_i, t)$  is like a new variable whose time-averaged value is zero.

$$\overline{\phi'(x_i, t)} = 0 \quad (2.10)$$

If the flow is statistically stationary and the observation time,  $T$  is sufficiently long such that the flow variable satisfies the following condition:

$$\lim_{T \rightarrow \infty} \frac{1}{T} \int_0^T \phi(x_i, t) \phi(x_i, t + \tau) d\tau = 0 \quad (2.11)$$

Then the turbulent process is said to be ergodic. The principle of ergodicity states that an infinite number of different realizations (called as ensemble averaging) are equivalent to the same realization repeated for an infinite time.

$$\overline{\phi(x_i, t)}_{ensemble} = \lim_{N \rightarrow \infty} \frac{1}{N} \sum_{n=1}^N \phi(x_i, t_n) \Leftrightarrow \overline{\phi(x_i, t)} = \lim_{T \rightarrow \infty} \frac{1}{T} \int_0^T \phi(x_i, t) dt \quad (2.12)$$

### 2.3.2 RANS equation

For a flow of incompressible fluid, all the flow variables are decomposed in to one averaged value and one turbulent fluctuation.

Let  $u = (u_1, u_2, u_3)$  be the components of velocity field,  $p$  be the pressure and  $T$  be the temperature variables which undergo Reynolds decomposition as shown below:

$$u_i = \bar{u}_i + u_i' \quad (2.13)$$

$$p = \bar{p} + p' \quad (2.14)$$

$$T = \bar{T} + T' \quad (2.15)$$

Put the variables  $u_i$ ,  $p$  and  $T$  in equations (2.5), (2.6) and (2.7) do Reynolds averaging of the equation using the property of the fluctuating quantities mentioned in (2.10) to get the Reynolds averaged equations:

**Reynolds Averaged Continuity equation:**

$$\frac{\partial \bar{u}_i}{\partial x_i} = 0 \quad (2.16)$$

**Reynolds Averaged Navier-Stokes equation:**

$$\frac{\partial \bar{u}_i}{\partial t} + \bar{u}_j \frac{\partial \bar{u}_i}{\partial x_j} = -\frac{1}{\rho} \frac{\partial \bar{p}}{\partial x_i} + \nu \frac{\partial^2 \bar{u}_i}{\partial x_j \partial x_j} + \frac{\partial (-\overline{u_i' u_j'})}{\partial x_j} + \bar{f}_i \quad (2.17)$$

**Reynolds Averaged scalar transport equation:**

$$\frac{\partial \bar{T}}{\partial t} + \bar{u}_j \frac{\partial \bar{T}}{\partial x_j} = \alpha \frac{\partial^2 \bar{T}}{\partial x_j \partial x_j} + \frac{\partial (-\overline{u_j' T'})}{\partial x_j} + \bar{s}_T \quad (2.18)$$

The Reynolds decomposition of variables into time averaged and fluctuating quantities leads to additional term in the NSE equations – product of fluctuating velocities called as turbulent or Reynolds stresses,  $\tau_{ij}^{RANS}$ . They constitute additional momentum transfer due to fluctuating velocity field and are also referred as turbulent flux of momentum. The Reynolds stress in Einstein and Tensor form is given below.

$$\tau_{ij}^{RANS} = -\overline{u_i' u_j'} = -(\overline{u_i u_j} - \bar{u}_i \bar{u}_j) \quad \text{Einstein notation} \quad (2.19)$$

$$\tau^{RANS} = \begin{pmatrix} \overline{u_1' u_1'} & \overline{u_1' u_2'} & \overline{u_1' u_3'} \\ \overline{u_2' u_1'} & \overline{u_2' u_2'} & \overline{u_2' u_3'} \\ \overline{u_3' u_1'} & \overline{u_3' u_2'} & \overline{u_3' u_3'} \end{pmatrix} \quad \text{Tensor form}$$

The second additional term is turbulent heat flux,  $\Theta_j^{RANS}$  in transport equation which is given as follows:

$$\Theta_j^{RANS} = -\overline{u_j' T'} = -(\overline{u_j T} - \bar{u}_j \bar{T}) \quad (2.20)$$

$$\Theta^{RANS} = \begin{pmatrix} \overline{u_1' T'} \\ \overline{u_2' T'} \\ \overline{u_3' T'} \end{pmatrix} \quad \text{Tensor form}$$

The turbulent heat flux gives both the direction and the magnitude of the turbulent transport of the temperature.

### 2.3.3 Closure Problem

There are five independent equations governing the mean velocity field with three components (2.17) together with the mean continuity equation (2.16) and transport equation for temperature (2.18). Reynolds decomposition leads to new unknowns like Reynolds stresses ( $\tau_{ij}^{RANS}$ ) which is a second order symmetric tensor (6 components) and scalar flux ( $\Theta_i^{RANS}$ ) which is a vector quantity (3 components). Thus, the system of five equations contains more than five unknowns and hence, the Reynolds equations do not form a closed set of equations. The Reynolds equations cannot be solved unless the Reynolds stresses and turbulent heat flux are somehow determined. The determination of Reynolds stresses and turbulent heat flux is based on the following hypothesis:

#### Boussinesq hypothesis

It is also called as eddy viscosity hypothesis introduced by Boussinesq in 1877. According to this hypothesis, the anisotropic part of the Reynold stress tensor can be expressed in terms of the mean rate of strain in the same way as viscous stress for Newtonian isotropic fluid (2.1), except that the coefficient of the molecular viscosity is replaced by eddy viscosity, also called as eddy viscosity. The Reynolds stress tensor can be divided in to isotropic part represented by  $\tau_{kk}^{RANS}$  and the anisotropic part represented by  $(\tau_{ij}^{RANS} - \frac{1}{3}\tau_{kk}^{RANS}\delta_{ij})$ . Thus, according to Boussinesq hypothesis, the anisotropic part of the Reynolds stress is proportional to mean rate of strain,  $\bar{S}_{ij}$  with eddy viscosity,  $\nu_t$  as the constant of proportionality

$$\tau_{ij}^{RANS} - \frac{1}{3}\tau_{kk}^{RANS}\delta_{ij} = 2\nu_t\bar{S}_{ij} \quad (2.21)$$

Where  $\delta_{ij}$  is Kronecker delta and  $\bar{S}_{ij}$  is the mean rate of strain given as

$$\bar{S}_{ij} = \frac{1}{2} \left( \frac{\partial \bar{u}_i}{\partial x_j} + \frac{\partial \bar{u}_j}{\partial x_i} \right) \quad (2.22)$$

Recalling the definition of turbulent kinetic energy,  $k$  from chapter 1:

$$k = \frac{1}{2} \left( \overline{u_1'^2} + \overline{u_2'^2} + \overline{u_3'^2} \right) \quad (1.16)$$

In Einstein notation and using the definition of Reynolds stress turbulent kinetic energy can be written as

$$k = \frac{1}{2} \overline{u_i' u_i'} = -\frac{1}{2} \tau_{kk}^{RANS} \delta_{ij} \quad (2.23)$$

From (2.23) and (2.21) we have:

$$\tau_{ij}^{RANS} + \frac{2k}{3} = 2\nu_t \bar{S}_{ij} \quad (2.24)$$

The mean momentum equation incorporating the eddy viscosity hypothesis i.e. using (2.19), (2.24) in (2.17) is:

$$\frac{\partial \bar{u}_i}{\partial t} + \bar{u}_j \frac{\partial \bar{u}_i}{\partial x_j} = -\frac{1}{\rho} \frac{\partial}{\partial x_i} \left( \bar{p} + \frac{2}{3} \rho k \right) + (\nu + \nu_t) \frac{\partial}{\partial x_j} \left( \frac{\partial \bar{u}_i}{\partial x_j} + \frac{\partial \bar{u}_j}{\partial x_i} \right) + \bar{f} \quad (2.25)$$

Where  $\bar{p} + \frac{2}{3} \rho k$  is the modified pressure that includes the isotropic part of the Reynolds stress. Therefore only the anisotropic part of Reynolds stress is modelled by eddy viscosity concept. Thus, knowing the eddy viscosity the Navier-Stokes equation and continuity equation form a closed set of system.

### **Gradient-diffusion hypothesis**

The gradient-diffusion hypothesis implies that the turbulent heat flux vector is aligned with the mean temperature gradient vector. Thus, turbulent heat flux  $\Theta_j^{RANS}$  is taken to be proportional to gradient of mean temperature with turbulent thermal diffusivity,  $\alpha_t$  as constant of proportionality.

$$\Theta_j^{RANS} = -\overline{u_j' T'} = \alpha_t \frac{\partial \bar{T}}{\partial x_j} \quad (2.26)$$

Mathematically the gradient-diffusion hypothesis is analogous to Fourier's law of heat conduction. The mean temperature equation incorporating the gradient-diffusion hypothesis i.e. using (2.26) in (2.18) is given as:

$$\frac{\partial \bar{T}}{\partial t} + u_j \frac{\partial \bar{T}}{\partial x_j} = (\alpha + \alpha_t) \frac{\partial^2 \bar{T}}{\partial x_j \partial x_j} + \bar{s}_T \quad (2.27)$$

The mean temperature equation can be solved if the unknown turbulent diffusivity is determined.

### **Reynolds Analogy hypothesis**

The turbulent diffusivity is determined from eddy viscosity using Reynolds analogy hypothesis which assumes that there is similarity in the turbulent transport features of momentum and heat. The two quantities are linked together by a dimensionless number called as turbulent Prandtl number,  $Pr_t$  which is given as

$$Pr_t = \frac{\nu_t}{\alpha_t} = \frac{\Theta_j^{RANS} \frac{\partial \bar{u}}{\partial x_i}}{\tau_{ij}^{RANS} \frac{\partial \bar{T}}{\partial x_j}} \quad (2.28)$$

Using equation (2.28) in the mean equation for temperature (equation (2.27)) we have

$$\frac{\partial \bar{T}}{\partial t} + u_j \frac{\partial \bar{T}}{\partial x_j} = \left( \frac{\nu}{Pr} + \frac{\nu_t}{Pr_t} \right) \frac{\partial^2 \bar{T}}{\partial x_j \partial x_j} + \bar{s}_T \quad (2.29)$$

The value of turbulent Prandtl number is fixed to 0.9 in most of the CFD codes. This value is correct for fluids with Prandtl number around 1 but not for sodium. For fluids with Prandtl number smaller than one the turbulent Prandtl number is greater than 1.

Therefore, to solve the closure problem all that remains is to determine an appropriate specification of the eddy viscosity,  $\nu_t$ . This can be written as product of a characteristic velocity scale,  $u^*$  and length scale,  $l^*$ :

$$\nu_t = u^* l^* \quad (2.30)$$

The task of specifying  $\nu_t$  is now reduced to determine  $u^*$  and  $l^*$  for which many turbulence model are present in literature. In algebraic models- the mixing length model for example –  $l^*$  is specified on the basis of the geometry of the flow. In two-equation models- for example k- $\epsilon$  model -  $u^*$  and  $l^*$  are related to turbulent kinetic energy, k and turbulent diffusion rate,  $\epsilon$ , for which modelled transport equations are solved.

### 2.3.4 RANS turbulence models

There are two major categories of RANS turbulence model – Eddy Viscosity Model (EVM) and Reynolds Stress Models (RSM). The EVM is a first order turbulence model that uses the Boussinesq hypothesis. The RSM is the second order turbulence model that solves a separate differential transport equations for each component of Reynolds stress.

The eddy viscosity concept is based on Boussinesq hypothesis as introduced in last equation. EVMs are sub-divided dependent on the way the eddy viscosity is modelled. It consists of many models: zero equation model like mixing length model, one equation model based on equation for turbulent kinetic energy  $k$ , two equations model like  $k$ - $\epsilon$  model,  $k$ - $\omega$  model (Wilcox, 1988), Shear Stress Transport (SST) model (Menter, 1994).

The  $k$ - $\epsilon$  model has many variant – standard  $k$ - $\epsilon$ , Realizable  $k$ - $\epsilon$  and RNG  $k$ - $\epsilon$  model. The major differences in these models are as follows:

- The method of calculating eddy viscosity
- The turbulent Prandtl number governing the turbulent diffusion of  $k$  and  $\epsilon$ .
- The generation and destruction terms in  $\epsilon$  equation

We will present the standard  $k$ - $\epsilon$  model and the realizable  $k$ - $\epsilon$  model that have been used in the study. The details of other turbulence models can be found in the references.

#### **Standard $k$ - $\epsilon$ model**

This model is based on model transport equations for the turbulence kinetic energy,  $k$  and its dissipation  $\epsilon$ . The transport equation for  $k$  is derived from the exact equation for the total energy whereas the transport equation for  $\epsilon$  is empirical based on physical reasoning. In derivation of the equations for  $k$ - $\epsilon$  model the assumption is that the flow is fully turbulent and the effects of molecular viscosity are negligible. Thus, this model is valid only for fully turbulent flows. This model has been extended to low Reynolds number.

In  $k$ - $\epsilon$  model, the eddy viscosity is given as follows:

$$\nu_t = \frac{C_\nu k^2}{\epsilon} \quad (2.31)$$

Where  $C_\nu$  is a model constant.

**Model equation for k:**

$$\frac{\partial(\rho k)}{\partial t} + \frac{\partial(\rho k u_i)}{\partial x_i} = \frac{\partial}{\partial x_j} \left[ \left( \mu + \frac{\mu_t}{\sigma_k} \right) \frac{\partial k}{\partial x_j} \right] + G_k + G_b - \rho \varepsilon - Y_M + S_k \quad (2.32)$$

**Model equation for  $\varepsilon$ :**

$$\frac{\partial \rho \varepsilon}{\partial t} + \frac{\partial(\rho \varepsilon u_i)}{\partial x_i} = \frac{\partial}{\partial x_j} \left[ \left( \mu + \frac{\mu_t}{\sigma_\varepsilon} \right) \frac{\partial \varepsilon}{\partial x_j} \right] + C_{1\varepsilon} \frac{\varepsilon}{k} (G_k + C_{3\varepsilon} G_b) - \rho C_{2\varepsilon} \frac{\varepsilon^2}{k} + S_\varepsilon \quad (2.33)$$

Where  $\sigma_k, \sigma_\varepsilon, C_{1\varepsilon}, C_{2\varepsilon}$  are model constants,  $G_k$  represents the generation of turbulence of kinetic energy due to the mean velocity gradients,  $G_b$  is the generation of turbulence kinetic energy due to buoyancy and  $Y_M$  represents the contribution of the fluctuating dilation in compressible turbulence to the overall dissipation rate (Table 2.1).  $S_k$  and  $S_\varepsilon$  are the user defined source terms.

Model constants: The default values of the model constants are given below:

$$\sigma_k = 1.0, C_v = 0.09, \sigma_\varepsilon = 1.3, C_{1\varepsilon} = 1.44, C_{2\varepsilon} = 1.92$$

The value of model constants have been determined from experiment for fundamental turbulent flows including frequently encountered shear flows like boundary layers, mixing layers and jets as well as for decaying isotropic grid turbulence. They have been found to work fairly well for a wide range of wall-bounded and free shear flows.

### **Realizable k- $\varepsilon$ model**

The Realizable k- $\varepsilon$  model (Shih, 1995) differs from standard k- $\varepsilon$  model in two ways:

- It contains alternative formulation for eddy viscosity
- The transport equation for the dissipation rate,  $\varepsilon$  has, has been derived from an exact equation for the transport of the mean-square vorticity fluctuation.

**Model equation for k:**

$$\frac{\partial \rho k}{\partial t} + \frac{\partial(\rho k u_j)}{\partial x_j} = \frac{\partial}{\partial x_j} \left[ \left( \mu + \frac{\mu_t}{\sigma_k} \right) \frac{\partial k}{\partial x_j} \right] + G_k + G_b - \rho \varepsilon - Y_M + S_k \quad (2.34)$$

Where  $\sigma_k$  is the model constant.

**Model equation for  $\varepsilon$ :**

$$\frac{\partial \rho \varepsilon}{\partial t} + \frac{\partial(\rho \varepsilon u_j)}{\partial x_j} = \frac{\partial}{\partial x_j} \left[ \left( \mu + \frac{\mu_t}{\sigma_\varepsilon} \right) \frac{\partial \varepsilon}{\partial x_j} \right] + \rho C_1 S_\varepsilon - \rho C_2 \frac{\varepsilon^2}{k + \sqrt{\nu \varepsilon}} + C_{1\varepsilon} \frac{\varepsilon}{k} C_{2\varepsilon} G_b + S_\varepsilon \quad (2.35)$$

Where  $C_1 = \max \left[ 0.43, \frac{\eta}{\eta+5} \right]$ ,  $\eta = S \frac{k}{\varepsilon}$ , and  $S = \sqrt{2 S_{ij} S_{ij}}$

In these equations  $G_k$  represents the generation of turbulence of kinetic energy due to the mean velocity gradients,  $G_b$  is the generation of turbulence kinetic energy due to buoyancy and  $Y_M$  represents the contribution of the fluctuating dilation in compressible turbulence to the overall dissipation rate.  $S_k$  and  $S_\varepsilon$  are the user defined source terms.

The transport equation for  $k$  is same as in standard  $k$ - $\varepsilon$  model except that the model constants have different values. The default values of the model constants are given below:

$$\sigma_k = 1.0, \sigma_\varepsilon = 1.2, C_{1\varepsilon} = 1.44, C_{2\varepsilon} = 1.9$$

The form of  $\varepsilon$  equation (2.35) is different from standard  $k$ - $\varepsilon$  model (2.33). The production term in  $\varepsilon$  equation does not involve the production of  $k$  i.e. it does not contain the same  $G_k$  term. It is believed that the present form better represents the spectral energy transfer. Another feature is that the destruction term does not have singularity i.e. the denominator term does not vanish even if the  $k$  vanishes in contrast with the standard model where singularity exists due to  $k$  in denominator.

In realizable  $k$ - $\varepsilon$  model, the eddy viscosity has similar relation as in standard  $k$ - $\varepsilon$  model (2.31) except that  $C_v$  is no more a constant. It is a function of mean strain ( $S_{ij}$ ) and rotation rates ( $\Omega_{ij}$ ), the angular velocity of the system rotation ( $\omega_k$ ), the turbulence fields ( $k, \varepsilon$ )

$$C_v = \frac{1}{A_0 + A_s \frac{kU^*}{\varepsilon}} \quad (2.36)$$

Where,

$$U^* = \sqrt{S_{ij}S_{ij} + \tilde{\Omega}_{ij}\tilde{\Omega}_{ij}} \quad (2.37)$$

With  $\tilde{\Omega}_{ij} = \Omega_{ij} - 2\varepsilon_{ijk}\omega_k$ ,  $\Omega_{ij} = \overline{\Omega_{ij}} - \varepsilon_{ijk}\omega_k$

And the value of model constants  $A_0$  and  $A_s$  are given as

$A_0=4.04$  and  $A_s=\sqrt{6} \cos \phi$  with

$$\phi = \frac{1}{3} \cos^{-1}(\sqrt{6} W), W = \frac{\overline{S_{ij}} \overline{S_{jk}} \overline{S_{ki}}}{\overline{S}^3}, \tilde{S} = \sqrt{\overline{S_{ij}} \overline{S_{ij}}}$$



Term	Description	Representation
$G_k$	Generation of k due to velocity gradients	$-\rho\mu_t S^2$
$G_b$	Generation of k due to buoyancy	$-g_i \frac{\mu_t}{\rho Pr_t} \frac{\partial \rho}{\partial x_i}$
$Y_M$	Compressibility effects	$2\rho\epsilon M_t^2$
$M_t$	Turbulent Mach number with a representing velocity of sound in the medium	$\sqrt{\frac{k}{a^2}}$

**Table 2.1-Coefficients and terms for the standard k-ε model and Realizable k-ε model**

This model has been extensively validated for a wide range of flows (Kim, 1997; Shih, 1995) including rotating homogeneous shear flows, free flows, channel and boundary layer flows and separated flows. For all these cases, the performance of the model has been found to be substantially better than that of the standard k-ε model. This turbulence model will be used in the thesis to perform RANS study.

In many cases, models based on the Boussinesq hypothesis perform very well, and the additional computational expense of the Reynolds stress model (RSM) (Launder, 1975) is not justified. However, the RSM is clearly superior in situations where the anisotropy of turbulence has a dominant effect on the mean flow. Such cases include highly swirling flows and stress-driven secondary flows.

The RANS study has been performed using the industrial code STAR-CCM+ which is presented in section 2.6.3.

### **2.3.5 STAR-CCM+ code**

This part describes the different numerical schemes and numerical method used to perform RANS simulation described in chapter 4. These methods are present in the CFD tool called STAR-CCM+ which is an industrial code developed by CD-Adapco. It is based on object oriented programming technology. It is designed to handle large models quickly and efficiently using a unique client-server architecture that allows meshing, solving and post processing. These numerical aspects are presented concisely because they do not fit into the framework of this thesis study. Nevertheless, the reader may refer to the user guide (STAR-CCM+) for more details.

STAR-CCM+ is based on finite volume method, the solution domain is subdivided into a finite number of control volumes, corresponding to the cells of a computational grid. The discrete versions of the integral form of the continuum transport equations are applied to each control volume. The objective is to obtain a set of linear algebraic equations where total number of unknowns in each equation system corresponding to the number of cells in the grid. The discretization of the equations in space is done using second order upwind scheme. The time discretization uses first order implicit scheme where the system is solved implicitly in an iterative manner. The basis of the iterative methods is that given an approximate solution, a better solution is sought and then the process is repeated. The iterative methods available in STAR-CCM+ are Jacobi and Gauss-Seidel iteration. This provides second order of accuracy in space and first order accuracy in time.

The gradients are calculated using Hybrid Gauss least square method and weighted least squares method. It uses a blending factor to determine how the two gradient method options are used in calculating the gradient. The discretized linear system is solved iteratively by Algebraic Multi Grid (AMG) methods. The pressure solver uses preconditioned conjugate-Gradient method. It uses the AMG solver as pre-conditioner and uses conjugate-gradient method to accelerate the convergence of iterative solution of linear system in the Pressure solver. This method can provide robust convergence for those cases where numerical instability results from a lack of incomplete convergence of the linear system of the pressure solver.

## 2.4 Large Eddy Simulation (LES)

### 2.4.1 Principle

In this method only the large scales of motions which are carriers of energy are simulated, and the smaller scales of motion which undergo energy dissipation are modelled using sub-grid model. This principle is illustrated in Figure 2.1. Formally, this scale separation results in the application of a high-pass wavelength filter (or low-pass frequency). In practice, it is done by the choice of the mesh size used to discretize the computational domain. Similar to the DNS, LES also provides a three dimensional, time dependent solution to the filtered governing equations. However, in LES, turbulent fields are resolved at and above a characteristic cut-off filter size, which is typically much larger than the Kolmogorov scales required in a DNS approach. In view of this, given the same computational resources, LES can deal with much higher Reynolds numbers and much more complex geometries than DNS. Thus, it offers an excellent compromise between the quality of results and the computation time.

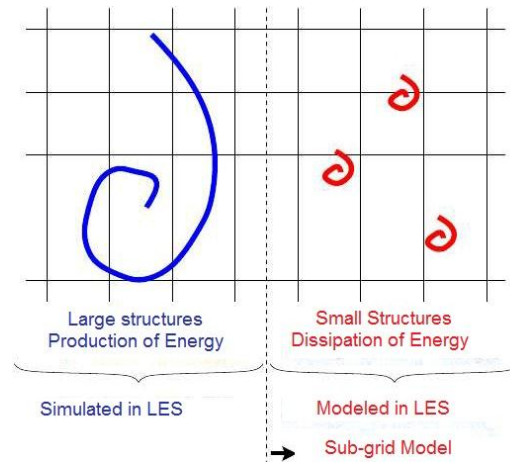


**Figure 2.1- Schematic representation of separation of scales in LES on a calculation grid (Husson, 2007)**

The Reynolds averaged Navier-Stokes (RANS) equations were derived assuming that all of the unsteadiness due to the turbulent nature of the flow could be modelled with empirically derived correlations. This reduces the time and length scales that must be simulated, but also limits the applicability of the simulation for unsteady flows. Large eddy simulations (LES) were developed to extend the simulation of unsteady flows beyond DNS. The desired result of

an LES computation is to obtain a DNS equivalent solution for the large-scale turbulence on a much coarser grid than is required for DNS.

### **Filtering operation**

The filtering operation is critical to LES as it filters out the turbulent scales that are completely resolved and that are modelled. Consider a filtering operation with a uniform characteristic filter width  $\bar{\Delta}$  (which implies isotropic grid elements). Leonard (Leonard, 1974) defined the following filter in physical space

$$\langle \varphi(x, t) \rangle = \int_{-\infty}^{+\infty} G(x - \xi) \varphi(\xi) d\xi \quad (2.38)$$

Note that angular bracket represents a filtered quantity. The filtering operation is a spatial operation as opposed to the Reynolds averaging operation that is a temporal operation. In LES the filtered value is still function of time unlike in RANS.

The original function  $\varphi(x, y, z, t)$  is then decomposed into a filtered field (or grid resolved) representing the large length scales (represented by angular brackets-  $\langle . \rangle$ ) and the sub-grid value for the small isotropic scales (represented by inverted commas-  $''$ ) as shown below:

$$\varphi(x, t) = \langle \varphi(x, t) \rangle + \varphi''(x, t) \quad (2.39)$$

The function  $G$  is defined in (2.38) is the filter function. The filter function may be any function defined on an infinite domain that satisfies the following requirements:

- i.  $G(-\xi) = G(\xi)$
- ii.  $\int_{-\infty}^{\infty} G(\xi) d\xi = 1$
- iii.  $G(\xi) \rightarrow 0$  as  $|\xi| \rightarrow \infty$  such that all moments  $\int_{-\infty}^{\infty} G(\xi) \xi^n d\xi$  ( $n \geq 0$ ) exist
- iv.  $G(\xi)$  is small outside  $\left(-\frac{\bar{\Delta}}{2}, \frac{\bar{\Delta}}{2}\right)$

One important and useful feature of this choice of filter is commutation with space derivative.

$$\left\langle \frac{\partial \varphi}{\partial x} \right\rangle = \frac{\partial \langle \varphi \rangle}{\partial x} \quad (2.40)$$

Unlike the Reynolds decomposition operator, the filtering operator has following properties:

$$\langle \langle \varphi \rangle \rangle \neq \langle \varphi \rangle \text{ and } \langle \varphi'' \rangle \neq 0 \quad (2.41)$$

In practice, for the industrial flow configurations the filter length is determined by the size of the mesh of the discretized problem. Thus the filter is implicit. The formulation for homogeneous structured mesh is given as

$$\bar{\Delta} = (\Delta x \Delta y \Delta z)^{1/3} \quad (2.42)$$

Where  $\Delta x$ ,  $\Delta y$  and  $\Delta z$  are the mesh size in the different directions of the mesh.

In case of tetrahedral mesh as used in this thesis the filter size is defined as follows:

$$\bar{\Delta} = (\text{volume of tetrahedrals})^{1/3} \quad (2.43)$$

A two-step smoothing operation is applied to the filter length in order to avoid strong variations of filter length from one tetrahedral to next in heterogeneous meshing:

Firstly, each vertex of the tetrahedral cell is associated with a maximum filter length of all the tetrahedrons connected to that vertex.

$$\bar{\Delta}_{vertex} = \max(\bar{\Delta}_i), \text{ for } i=1, \text{ elements} \quad (2.44)$$

Where element refers to all the tetrahedrons connected to the vertex

Secondly, each tetrahedron of the mesh is re-associated to the maximum filter length of all connected vertices

$$\bar{\Delta} = \max(\bar{\Delta}_j), \text{ for } j=1, \text{ vertex} \quad (2.45)$$

Where vertex refers to the four corners of the tetrahedral for which the filter length is calculated

Despite this formulation gives the cut-off length of the filter, the filtering operation in LES also depends on various other parameters given below (Ghoshal, 1996):

- The space-time discretization
- The order of numerical scheme (Convection scheme, diffusion scheme and time scheme)
- The errors introduced due to sub grid scale modelling

## 2.4.2 LES equations

Using filter operator the physical quantities velocity, pressure and temperature can be filtered in to resolved quantities and the sub-grid value as shown below:

$$u_i = \langle u \rangle + u'' \quad (2.46)$$

$$p = \langle p \rangle + p'' \quad (2.47)$$

$$T = \langle T \rangle + T'' \quad (2.48)$$

Put the variables  $u_i$ ,  $P$  and  $T$  in (2.5), (2.6) and (2.7) to get the LES space filtered equations.

**Filtered Continuity Equation:**

$$\frac{\partial \langle u_i \rangle}{\partial x_i} = 0 \quad (2.49)$$

**Filtered Navier Stokes Equation:**

$$\frac{\partial \langle u_i \rangle}{\partial t} + \langle u_j \rangle \frac{\partial \langle u_i \rangle}{\partial x_j} = -\frac{1}{\rho} \frac{\partial \langle p \rangle}{\partial x_i} + \nu \frac{\partial^2 \langle u_i \rangle}{\partial x_j \partial x_j} + \frac{\partial}{\partial x_j} (\langle u_i \rangle \langle u_j \rangle - \langle u_i u_j \rangle) + \langle f_i \rangle \quad (2.50)$$

**Filtered Transport equation for passive scalar:**

$$\frac{\partial \langle T \rangle}{\partial t} + \langle u_j \rangle \frac{\partial \langle T \rangle}{\partial x_j} = \alpha \frac{\partial^2 \langle T \rangle}{\partial x_j \partial x_j} - \frac{\partial}{\partial x_j} (\langle u_j \rangle \langle T \rangle - \langle u_j T \rangle) + \langle s_T \rangle \quad (2.51)$$

As with Reynolds averaging, the filtering operation produces terms that must be modelled in order to have a closed set of filtered equations. The new terms are sub-grid-scale stress tensor,  $\tau_{ij}^{sgs}$  and sub-grid heat flux,  $\theta_i^{sgs}$  which represents the transfer of momentum and heat, respectively due to sub-grid viscous forces.

$$\tau_{ij}^{sgs} = -(\langle u_i u_j \rangle - \langle u_i \rangle \langle u_j \rangle) \quad (2.52)$$

$$\theta_j^{sgs} = -(\langle u_j T \rangle - \langle u_j \rangle \langle T \rangle) \quad (2.53)$$

## 2.4.3 Closure problem

The sub-grid scale stress represents the effect of small scales of velocity on the large scales. The method that we use suppose that the direct transfer towards the sub-grid scales (energy transferred from large scale to small scale) can be represented by a diffusion term i.e. sub-grid viscosity based on Boussinesq hypothesis. The sub-grid eddy viscosity accounts for the turbulence that cannot be resolved on the computational grid. The inverse energy transfer

from small scale towards the large scale is supposed negligible. Therefore only the anisotropic part of Reynolds stress is modelled by eddy viscosity concept.

The sub-grid-scale turbulence models employ the Boussinesq hypothesis (Hinze, 1975) as in the RANS models, computing sub-grid-scale turbulent stresses from filtered rate of strain as shown below:

$$\tau_{ij}^{sgs} - \frac{1}{3} \tau_{kk}^{sgs} \delta_{ij} = 2 \nu_t^{sgs} \langle S_{ij} \rangle \quad (2.54)$$

Where,  $\nu_t^{sgs}$  is the sub-grid viscosity,  $\langle S_{ij} \rangle$  is the filtered rate of deformation representing for the resolved scale of motions defined by

$$\langle S_{ij} \rangle = \frac{1}{2} \left( \frac{\partial \langle u_i \rangle}{\partial x_j} + \frac{\partial \langle u_j \rangle}{\partial x_i} \right) \quad (2.55)$$

The sub-grid kinetic energy,  $k^{sgs}$  is defined as

$$k^{sgs} = \frac{1}{2} (\langle u_i u_i \rangle - \langle u_i \rangle \langle u_i \rangle) \quad (2.56)$$

In Einstein notation and using the definition of sub grid stress, the turbulent kinetic energy can be written as

$$k^{sgs} = -\frac{1}{2} \tau_{kk}^{sgs} \delta_{ij} \quad (2.57)$$

The filtered Navier-Stokes equation using the Boussinesq hypothesis (2.54) is written as follows:

**Filtered Navier-Stokes Equation:**

$$\begin{aligned} \frac{\partial \langle u_i \rangle}{\partial t} + \langle u_j \rangle \frac{\partial \langle u_i \rangle}{\partial x_j} \\ = -\frac{1}{\rho} \frac{\partial}{\partial x_i} (\langle p \rangle + \frac{2}{3} \rho k^{sgs}) + (\nu + \nu_t^{sgs}) \frac{\partial}{\partial x_j} \left( \frac{\partial \langle u_i \rangle}{\partial x_j} + \frac{\partial \langle u_j \rangle}{\partial x_i} \right) + \langle S \rangle \end{aligned} \quad (2.58)$$

Where  $\langle p \rangle + \frac{2}{3} \rho k^{sgs}$  is the modified filtered pressure that includes the isotropic part of the sub-grid stress. Thus, knowing the sub-grid-scale viscosity the Navier-Stokes equation and continuity equation form a closed set of system.

The sub-grid viscosity is determined in a similar way as in RANS using the gradient-diffusion hypothesis and Reynolds analogy.

### **Gradient-diffusion hypothesis**

The gradient-diffusion hypothesis implies that the turbulent heat flux vector is aligned with the mean temperature gradient vector. Thus, turbulent heat flux  $\Theta_j^{sgs}$  is taken to be proportional to gradient of mean temperature with sub-grid thermal diffusivity,  $\alpha_t^{sgs}$  as constant of proportionality.

$$\Theta_j^{sgs} = -\overline{u_j T'} = \alpha_t^{sgs} \frac{\partial \bar{T}}{\partial x_j} \quad (2.59)$$

The mean temperature equation can be solved if the unknown turbulent diffusivity is determined.

$$\frac{\partial \langle T \rangle}{\partial t} + \langle u_j \rangle \frac{\partial \langle T \rangle}{\partial x_j} = \left( \frac{\nu}{Pr} + \frac{\nu_t^{sgs}}{Pr_t^{sgs}} \right) \frac{\partial^2 \langle T \rangle}{\partial x_j \partial x_j} + \langle S_T \rangle \quad (2.60)$$

$$\Theta_j^{sgs} = \frac{\nu_t^{sgs}}{Pr_t^{sgs}} \frac{\partial \langle T \rangle}{\partial x_j} \quad (2.61)$$

Where  $Pr_t^{sgs}$  is the sub-grid Prandtl number. The simplest model assumes that the turbulent Prandtl number is constant.  $Pr_t^{sgs}$  is equal to 0.9 (Husson, 2007). This considers that the sub-grid thermal phenomena are determined by the evolution of sub-grid flow dynamics and not by resolved temperature. This hypothesis is wrong for sodium flow where the thermal boundary layer is much larger than hydraulic boundary layer. Second disadvantage is that it cannot take in to account the anisotropy effect. Brilliant (Brilliant, 2004) showed that it does not allow the sub grid thermal diffusivity to have correct asymptotic behavior near the wall (See Chapter 1-section 1.2.6 for more discussion).

The Filtered Transport equation for passive scalar using Reynolds analogy (2.61) can be written as

$$\frac{\partial \langle T \rangle}{\partial t} + \langle u_j \rangle \frac{\partial \langle T \rangle}{\partial x_j} = \left( \frac{\nu}{Pr} + \frac{\nu_t^{sgs}}{Pr_t^{sgs}} \right) \frac{\partial^2 \langle T \rangle}{\partial x_j \partial x_j} + \langle S_T \rangle \quad (2.62)$$

In order to close the LES equations, we have to model sub-grid eddy viscosity,  $\nu_t^{sgs}$ . This is done by using a sub-grid model. The sub-grid model represents the interactions between the large scales (production zone of turbulence) and the small scales (near the dissipation zone of turbulence). The sub-grid models are based on a local equilibrium hypothesis between the production of turbulence and the dissipation. Thus, all the models should have cut-off frequency in the inertial zone of the spectra where this hypothesis is valid.



There two main models Smagorinsky-Lilly model, the dynamic Smagorinsky-Lilly model and the WALE model.

## 2.4.4 LES turbulence model

There are many turbulence models that propose an expression of sub grid eddy viscosity,  $\nu_t^{sgs}$ . The most commonly known model is Smagorinsky model (Smagorinsky, 1963) based on the hypothesis in which we consider that the sub-grid viscosity is proportional to one length scale,  $l^{sgs*}$  associated to filtering of equations that is characteristic of the size of the mesh ( $\bar{\Delta}$ ) and one velocity scale  $u^{sgs*}$  determined by the product of mesh size and filtered rate of deformation  $\bar{\Delta} \|\langle S_{ij} \rangle\|$

$$\nu_t^{sgs} = u^{sgs*} l^{sgs*} \propto (\bar{\Delta}) (\bar{\Delta} \|\langle S_{ij} \rangle\|) \quad (2.63)$$

### Smagorinsky model

This simple model was first proposed by Smagorinsky. In the Smagorinsky-Lilly model, the eddy-viscosity is modelled by

$$\nu_t^{sgs} = L_s^2 \|\langle S_{ij} \rangle\| \quad (2.64)$$

Where  $\|\langle S_{ij} \rangle\|$  represents norm of the filtered rate of strain.

$$\|\langle S_{ij} \rangle\| = \sqrt{2 \langle S_{ij} \rangle \langle S_{ij} \rangle} \quad (2.65)$$

$L_s$  is the mixing length for sub-grid scales

$$L_s = \min(\kappa d, C_s \bar{\Delta}) \quad (2.66)$$

Where,  $\kappa$  is Karman constant,  $d$  is the distance to the closet wall,  $C_s$  is the Smagorinsky constant and  $\bar{\Delta}$  is the filter length.

The determination of the constant  $C_s$  is based on the hypothesis of local equilibrium between production and the dissipation of the turbulent kinetic energy. Lilly et al (Lilly, 1996) derived a value of 0.23 for  $C_s$  for homogeneous isotropic turbulence in the inertial sub range. However, this value was found to cause excessive damping of large-scale fluctuations in the presence of mean shear and in transitional flows as near solid boundary, and has to be reduced in such regions. In short,  $C_s$  is not a universal constant, which is the most serious shortcoming of this simple model. Nonetheless, a  $C_s$  value of around 0.1 has been found to yield the best results for wall bounded flows (Deardoff, 1973).

The three main defects of this model are (Métais, 2002-03).

- i. Constant  $C_s$  is not constant it must be adapted from case to case
- ii. It is very diffusive and so it inhibits the transition laminar/turbulent in a boundary layer flow.
- iii. The behavior of sub-grid viscosity in the zone near to wall is incorrect. The ratio  $\frac{\nu_t^{sgs}}{\nu}$  must be proportional to  $(y^+)^3$  whereas it varies according to  $(y^+)^2$ . This is usually corrected by introduction of a damping function.
- iv. It does not take in to account the back-scatter of energy that is a possible transmission of energy of small scales to large scales.
- v. Sub-grid viscosity does not vanish at wall.

### **Wall-Adapting Local Eddy-viscosity (WALE) model**

WALE model (Nicoud & Ducros, 1999) combines the symmetric and non-symmetric part of the velocity gradient. It takes in to account at the same time the filtered rate of deformation and filtered rate of rotation to improve the performance. The advantage of taking in to account the rotation tensor is to make the model invariant by translation or rotation of coordinates and to be able to be used for complex geometries. The sub-grid viscosity in this model has the following form:

$$\nu_t^{sgs} = (C_w \bar{\Delta})^2 \frac{(S_{ij}^d S_{ij}^d)^{3/2}}{(\langle S_{ij} \rangle \langle S_{ij} \rangle)^{5/2} + (S_{ij}^d S_{ij}^d)^{5/4} + e} \quad (2.67)$$

Where,

$$S_{ij}^d = \frac{1}{2} (\langle g_{ij}^2 \rangle + \langle g_{ji}^2 \rangle) - \frac{1}{3} \delta_{ij} \langle g_{kk}^2 \rangle \quad (2.68)$$

$$\langle g_{ij}^2 \rangle = \frac{\partial \langle u_i \rangle}{\partial x_j} \quad (2.69)$$

And  $e$  is a constant with value equal to  $10^{-6}$  (Chatelain, 2004).

The default value of the WALE constant,  $C_w$ , is 0.5 and has been found to yield satisfactory results for a wide range of flow with homogeneous isotropic turbulence. The rest of the notation is the same as for the Smagorinsky-Lilly model.

This WALE model has the following advantages:

- i. Sub-grid viscosity shows correct asymptotic ( $y^{+3}$ ) behaviour for wall-bounded flows.
- ii. Unlike in Smagorinsky model the sub-grid eddy viscosity is naturally vanished at the wall so no need of extra damping functions.
- iii. This model is capable of reproducing the laminar/turbulent transition

The WALE model is therefore preferable compared to the Smagorinsky-Lilly model.

This section has described the numerical method of LES method. The numerical tool used to perform the LES study in this thesis is Trio\_U code that is presented in section 2.4.5.

## **2.4.5 TRIO\_U code**

The code TRIO\_U is a multi-physics calculation code developed by CEA Grenoble designed for incompressible, turbulent flows in complex geometries (Calvin, 2002; Bieder, 2003). The code is especially designed for industrial large eddy simulations (LES) on structured and non-structured grids of several tens of millions of nodes (Bieder, 2005). The platform independent code is based on an object oriented, intrinsically parallel approach and is coded in C++.

For unstructured grids, TRIO\_U uses a hybrid Finite Volume based Finite Element method (Bieder, 2000). This method determines a discrete solution in space for the finite element by maintaining the equilibrium between flux entering and leaving the finite volumes.

The space discretization is performed with triangles in the 2D case and with tetrahedral cells in the 3D case. In TRIO\_U, the main unknowns (velocity, temperature and concentration) are located in the center of the faces of an element (triangle or tetrahedron) whereas the pressure is discretized in the center and in the vertices of the element. This staggered mesh arrangement can be characterized as P1 nonconforming for the velocities and scalars and P0-P1 for the pressure (Heib, 2003).

The implemented solution method is a matrix projection scheme (Ferziger, 2001) derived from the SOLA method (solution algorithm for transient fluid flow) originally developed by Hirt (Hirt, 1975).

In this method, the pressure is taken implicitly in the momentum equations and the velocities are taken implicitly in the continuity equation. All other terms are taken explicitly. A

conjugated gradient method is used to calculate this pressure field for each new time step (Ferziger, 2001).

The problem of solving a large non-linear system is thus converted into a linear problem of minimizing residuals, where a more accurate solution is obtained after any iteration. The SSOR (symmetric successive over relaxation) preconditioning technique is applied to improve convergence (incomplete preconditioning for parallel calculations). The user has to verify that the mass conservation is satisfied.

Since the application is intrinsically parallel, only one problem is treated which is solved in parallel by several processors. Therefore, the calculation domain is distributed in a load-balanced way among the available processors where the distribution is achieved using the partitioning tool METIS (Karypis 1999). Frontier values of the sub-domains are exchanged only when needed to optimize the communication between processors. The parallel efficiency is in the order of 80%, checked on various clusters with a weak scaling method on up to 256 processors.

## 2.5 Direct Numerical Simulation (DNS)

### 2.5.1 Principle

DNS can be regarded as a numerical experiment as it provides maximum precision. It solves the conservation equations of physics – continuity equation, Navier-Stokes equation and energy equation without any further approximations other than the numerical discretization. Thus, all space-time phenomena i.e. until the Kolmogorov scales are completely resolved. The computation domain for a DNS approach should be at least as large as the largest eddy in the system (integral scale) and the meshing must be as fine as the dimension of the dissipating eddies (Kolmogorov scale).

Therefore, the mesh size ( $\Delta$ ) should be smaller than Kolmogorov scale,  $\eta$  in order to capture the smallest swirl and in general it should follow the following relation (Ninokata, 2009):

$$\frac{\pi\eta}{\Delta} > 1.5 \quad (2.70)$$

The increase in Reynolds number leads to excitation of smaller and larger length scales. The ratio of largest to smallest length scales ( $L/\eta$ ) in one direction varies with the Reynolds as  $Re^{-3/4}$  and ratio of biggest to smallest time scales ( $T/\tau_\eta$ ) varies as  $Re^{-1/2}$ . Thus, a DNS calculation resolving all the length scales in three dimensions should have the number of points of the order of  $Re^{9/4}$ . Then, to simulate all the time scales the total number of time steps should be at least around  $Re^{1/2}$  that gives a total number of required operations as at least  $Re^{11/4}$ .

Thus, despite the current trend of increase in computing power; DNS remains limited to flows with low to moderate Reynolds number. Some of the attractive features of DNS (Kasagi, 1995)

- i. Unlike experimental measurement, DNS approach gives access to all the instantaneous flow variables at all the positions in space. Hence, turbulent structures and transport mechanisms can be analyzed in details through various theoretical and visualization techniques (Robinson, 1991; Kasagi, 1995)
- ii. Even experimental measurement techniques can be validated in simulated turbulent flow and thermal fields (Moin, 1989; Suzuki, 1992)

- iii. DNS approach provides precise turbulence statistics including pressure and any spatial derivatives which are extremely difficult to measure. They are undoubtedly helpful for evaluating and developing turbulence models.
- iv. The effects of various influential parameters like Reynolds number, Prandtl number and many others can be studied systematically by DNS (Kasagi, 1999).

The numerical tool to perform a DNS calculation is presented in section 2.6.3.

## 2.5.2 DNS equations

As already mentioned above the DNS method solves exactly the instantaneous conservation equations of mass (2.5), momentum (2.6) and energy (2.7) without any time averaging or space filtering resolving all the scales of motion in space and time. In cylindrical coordinate system, where

- $r, \theta, z$  represents radial, azimuthal and axial directions respectively and
- velocity  $\vec{u}(r, \theta, z, t)$  is represented by  $(u_r, u_\theta, u_z)(t)$

Then equation (2.5), (2.6) and (2.7) can be written as

**Continuity equation:**

$$\frac{1}{r} \frac{\partial(r u_r)}{\partial r} + \frac{1}{r} \frac{\partial u_\theta}{\partial \theta} + \frac{\partial u_z}{\partial z} = 0 \quad (2.71)$$

**Navier-Stokes equation:**

r component

$$\begin{aligned} \frac{\partial u_r}{\partial t} + u_r \frac{\partial u_r}{\partial r} + u_\theta \frac{\partial u_r}{r \partial \theta} + u_z \frac{\partial u_r}{\partial z} - \frac{u_\theta^2}{r} \\ = -\frac{1}{\rho} \frac{\partial p}{\partial r} + \nu \left[ \Delta u_r - \frac{u_r}{r^2} - \frac{2}{r^2} \frac{\partial u_\theta}{\partial \theta} \right] + f_r \end{aligned} \quad (2.72)$$

$\theta$  component:

$$\begin{aligned} \frac{\partial u_\theta}{\partial t} + u_r \frac{\partial u_\theta}{\partial r} + u_\theta \frac{\partial u_\theta}{r \partial \theta} + u_z \frac{\partial u_\theta}{\partial z} + \frac{u_r u_\theta}{r} \\ = -\frac{1}{\rho r} \frac{\partial p}{\partial \theta} + \nu \left[ \Delta u_\theta - \frac{u_\theta}{r^2} + \frac{2}{r^2} \frac{\partial u_r}{\partial \theta} \right] + f_\theta \end{aligned} \quad (2.73)$$

z component:

$$\frac{\partial u_z}{\partial t} + u_r \frac{\partial u_z}{\partial r} + u_\theta \frac{\partial u_z}{r \partial \theta} + u_z \frac{\partial u_z}{\partial z} = -\frac{1}{\rho} \frac{\partial p}{\partial z} + \nu \Delta u_z + f_z \quad (2.74)$$

Where  $\Delta$  represents the Laplacian operator which in cylindrical coordinates is written as

$$\Delta = \frac{\partial^2}{\partial r^2} + \frac{1}{r} \frac{\partial}{\partial r} + \frac{1}{r^2} \frac{\partial^2}{\partial \theta^2} + \frac{\partial^2}{\partial z^2} \quad (2.75)$$

And the three components of external force are written as  $\vec{F} = (f_r, f_\theta, f_z)$ .

### 2.5.3 DNS code

The set of equations mentioned above are solved with pseudo-spectral scheme using Fourier series in  $\theta$  direction and fourth-order compact schemes in  $r$  and  $z$  directions. Space discretization makes use of a fully staggered mesh. The time integration is based on a second-order accurate semi-implicit time scheme. The convective terms are advanced in time using explicit Adams-Bashforth scheme whereas diffusive terms are advanced in time with the implicit backward Euler scheme. The discretized equations are solved using projection method where pressure is decoupled from velocity. This results in Helmholtz and Poisson-Neumann problem for each variable resolved by using a diagonalization method (Abide, 2005). This technique makes it a powerful tool in terms of CPU cost because it is not an iterative method but it is a direct solver.

#### 2.5.3.a Space discretization

Space discretization makes use of a staggered mesh. If number of discretization points are, respectively  $N_r$ ,  $N_\theta$  and  $N_z$  in the  $r$ ,  $\theta$  and  $z$  directions and  $\Delta R$ ,  $\Delta\theta$  and  $\Delta Z$  represents the corresponding grid spacing then velocity  $u$ ,  $v$ ,  $w$  are, respectively, located at nodes  $((i + \frac{1}{2})\Delta R, j\Delta\theta, k\Delta Z)$ ,  $(i\Delta R, (j + \frac{1}{2})\Delta\theta, k\Delta Z)$  and  $(i\Delta R, j\Delta\theta, (k + \frac{1}{2})\Delta Z)$  while the pressure nodes are located at  $(i\Delta R, j\Delta\theta, k\Delta Z)$  as shown in Figure 2.2.

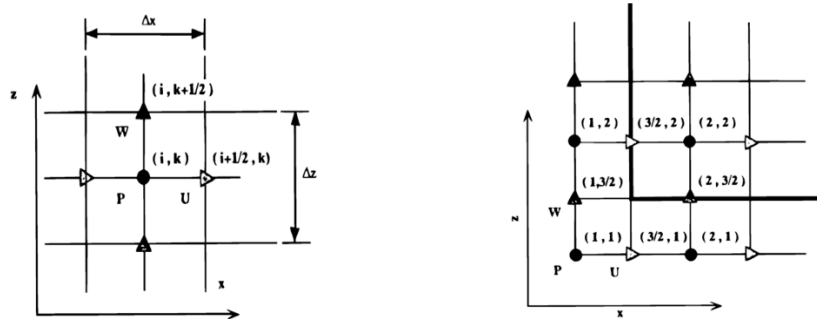


Figure 2.2-Staggered arrangement for interior grid points (left) and at the boundaries of the mesh in  $r$ - $z$  plane

The first and second order derivatives in the two non-homogeneous directions ( $r$  and  $z$ ) are given by Hermitian relations which have accuracy of order 4.

### 1) **Discretization formula in non-homogeneous directions**

#### **First order Hermitian derivatives**

The derivatives with respect to  $\xi$  (which denotes R or Z) of a function  $f$  defined at nodes  $j-1$ ,  $j$ ,  $j+1$  are given on non-staggered grids by the following implicit relations:

At interior grid points

$$\Delta\xi \left( \left( \frac{\partial f}{\partial \xi} \right)_{j-1} + 4 \left( \frac{\partial f}{\partial \xi} \right)_j + \left( \frac{\partial f}{\partial \xi} \right)_{j+1} \right) = 3(f_{j+1} - f_{j-1}) \quad (2.76)$$

At the boundaries

$$2\Delta\xi \left( 2 \left( \frac{\partial f}{\partial \xi} \right)_2 + \left( \frac{\partial f}{\partial \xi} \right)_1 \right) = f_3 + 4f_2 - 5f_1 \quad (2.77)$$

Since the variables are located at different nodes we need first-order derivatives at staggered grid nodes as well as interpolation operators. These derivatives are provided by the implicit fourth-order accurate relations deduced from Taylor expansions:

At interior grid points

$$\Delta\xi \left( \left( \frac{\partial f}{\partial \xi} \right)_{j-1} + 22 \left( \frac{\partial f}{\partial \xi} \right)_j + \left( \frac{\partial f}{\partial \xi} \right)_{j+1} \right) = 24(f_{j+1/2} - f_{j-1/2}) \quad (2.78)$$

At the boundaries

$$\Delta\xi \left( 23 \left( \frac{\partial f}{\partial \xi} \right)_2 + \left( \frac{\partial f}{\partial \xi} \right)_1 \right) = -f_{7/2} + 26f_{5/2} - 25f_{3/2} \quad (2.79)$$

#### **Second order Hermitian derivatives**

They are evaluated on non-staggered grid nodes with the following formulation:

At interior grid points

$$11 \left( \frac{\partial^2 f}{\partial \xi^2} \right)_{j-1} + \left( \frac{\partial^2 f}{\partial \xi^2} \right)_j + 11 \left( \frac{\partial^2 f}{\partial \xi^2} \right)_{j+1} = 13 \frac{(f_{j+1} - 2f_j + f_{j-1}))}{\Delta\xi^2} \quad (2.80)$$

At the boundaries

$$\left( \frac{\partial^2 f}{\partial \xi^2} \right)_1 + 11 \left( \frac{\partial^2 f}{\partial \xi^2} \right)_2 = \frac{13f_1 - 27f_2 + 15f_3 - f_4}{\Delta\xi^2} \quad (2.81)$$



### Discretization of convective terms

Convective terms like  $u\partial u/\partial r$  in the  $u$  momentum equation are computed by an interpolation on non-staggered nodes  $(i, j, k)$  followed by a derivative on staggered nodes  $(i+1/2, j, k)$

$$\left(u \frac{\partial u}{\partial r}\right)_{i+\frac{1}{2},j,k} = u_{i+\frac{1}{2},j,k} \left(\frac{\partial u_{i,j,k}}{\partial r}\right)_{i+\frac{1}{2},j,k} \quad (2.82)$$

### 2) Discretization in homogeneous direction

In the homogeneous or azimuthal direction ( $\theta$ ), interpolations, first- and second-order derivatives are based on Fourier polynomial expansions. The method is developed in the physical space using pseudo spectral formalism. The mesh still remains staggered where normal nodes are for pressure and shifted grids for velocity:

$$\theta_j = j\Delta\theta = jL_\theta/N_\theta \quad (2.83)$$

$$\theta_{j+1/2} = (j + 1/2)\Delta\theta = (j + 1/2) L_\theta/N_\theta \quad (2.84)$$

The wave numbers are defined by

$$k_\theta = 2\pi j/L_\theta \quad (2.85)$$

The couple of direct and inverse discrete Fourier transform are chosen in the following form:

$$\hat{f}(k_p) = \frac{1}{N_\theta} \sum_{j=0}^{N_\theta-1} f(x_j) e^{-ik_p x_j} \quad (2.86)$$

$$f(x_j) = \sum_{p=-N_\theta/2}^{(N_\theta/2)-1} \hat{f}(k_p) e^{-ik_p x_j} \quad (2.87)$$

Where  $\hat{f}(k_p)$  represents the Fourier transform of  $f$  with the wave number  $k_p$ . Where  $p$  varies from  $(\frac{-N_\theta}{2})$  to  $(\frac{N_\theta}{2} - 1)$ .

Thus, derivatives on normal and shifted nodes are given below and similar relations are also used for second-order derivatives and for interpolations.

$$\frac{\partial f}{\partial \theta}(\theta_j) = \sum_{p=-N_\theta/2}^{(N_\theta/2)-1} ik_p \hat{f}(k_p) e^{-ik_p \theta_j} \quad (2.88)$$

And

$$\frac{\partial f}{\partial \theta}\left(\theta_j + \frac{\Delta\theta}{2}\right) = \sum_{p=-N_\theta/2}^{(N_\theta/2)-1} ik_p \hat{f}(k_p) e^{-ik_p \left(\theta_j + \frac{\Delta\theta}{2}\right)} \quad (2.89)$$

### 2.5.3.b Time discretization

The time integration is based on a second-order accurate semi implicit fractional time scheme. The convective terms represented by  $H$  are solved with explicit Adams-Bashforth scheme and the diffusive terms are solved with implicit backward Euler scheme. Among diffusive terms  $\frac{2}{r^2} \frac{\partial u_\theta}{\partial \theta}$  and  $\frac{2}{r^2} \frac{\partial u_r}{\partial \theta}$  that are treated explicitly and rest are treated implicitly.

Let  $H$  represents the terms treated by Adams-Bash forth scheme. It includes the convective terms.

$$H = \frac{1}{2} U \cdot \nabla U + \frac{1}{2} \nabla(U \cdot U) \quad (2.90)$$

Thus, the time and space discretized equations can be written as

$$\frac{1}{2\Delta t} (3U^{n+1} - 4U^n + U^{n-1}) = 2H^n - H^{n-1} - \nabla p^{n+1} + \frac{1}{Re} \nabla^2(U^{n+1}) \quad (2.91)$$

$$\nabla \cdot U^{n+1} = 0 \quad (2.92)$$

Where,

$\nabla(\cdot)$ =approximation of gradient operator

$\nabla \cdot (\cdot)$ =approximation of divergence operator (Hermitian approximation in  $r, z$  and Fourier approximation in  $\theta$  direction)

$\nabla^2(\cdot)$ =discrete second order Laplacian in the  $(r,z)$  plane

The superscript  $n, n+1$  refers to values at times  $n\Delta t$  and  $(n+1)\Delta t$ .

The time interval  $\Delta t$  of the calculation has to be sufficiently small in order to capture all the time scales of turbulent motion. The time step should meet the following two requirements in order to have numerical stability:

- 1) The Courant-Friedrichs-Lewy condition,

$$C.F.L = \frac{u\Delta t}{\Delta r} < 0.3 \quad (2.93)$$

- 2) Viscous constraint for the viscous time interval  $\Delta t_v$

$$\Delta t_v \propto \frac{\Delta r^2}{\nu} \quad (2.94)$$

The semi-discrete form (equation 2.90) ensures a second-order time accuracy. This equation is solved using Project decomposition method that is presented in the next section.

### 2.5.3.c Project decomposition method

The method of solving the set of equation 2.91 and 2.92 is based on projection method. It is based on decoupling pressure from velocity by solving firstly a provisional velocity and then an elliptic step to enforce the free divergence constraint. This method is a 2-step technique presented below:

- a) A provisional velocity,  $U^*$  with components  $(u^*, v^*, w^*)$  is computed first by ignoring the pressure term to obtain a velocity that is not divergence free.

$$U^* - \frac{2\Delta t}{3Re} \nabla^2 U^* = \frac{4}{3} U^n - \frac{1}{3} U^{n-1} + \frac{2\Delta t}{3} (2H^n - H^{n-1}) \quad (2.95)$$

- b) Projection stage is performed to ensure the incompressibility condition i.e. to get a corrected value of velocity  $U$  that is divergence free. This is done by an additive gradient term  $\nabla p$ .

$$\begin{aligned} U^{n+1} &= U^* - \Delta t \nabla p^{n+1} \\ \nabla \cdot U^{n+1} &= 0 \end{aligned} \quad (2.96)$$

Where  $p^{n+1}$  is pressure that is given as solution of Poisson-Neumann system.

$$\nabla \cdot \nabla p^{n+1} = \nabla^2 p^{n+1} = \frac{1}{\Delta t} \nabla \cdot U^* \quad (2.97)$$

The project decomposition method ensures second order accuracy in time for velocity and first order for pressure.

Equation (2.95) is finally solved using a direct method. The benefits of direct methods are that firstly the memory requirements are very limited, due to the fact that the technique only involves two-dimensional arrays. Also, the operators can be calculated in the preamble stage of the computer code, out of the main loops, saving a lot of time.

Rewriting the equation (2.95) and (2.97) we obtain

$$\begin{aligned} \nabla^2 U^* - \frac{3Re}{2\Delta t} U^* &= -\frac{3Re}{2\Delta t} \left( \frac{4}{3} U^n - \frac{1}{3} U^{n-1} + \frac{2\Delta t}{3} (2H^n - H^{n-1}) \right) \\ \nabla^2 p^{n+1} &= \frac{1}{\Delta t} \nabla \cdot U^* \end{aligned}$$

This equation can be written in the general form

$$\nabla^2 \Phi - \kappa \Phi = S \quad (2.98)$$

Where  $\Phi$  represents provisional velocity  $U^*$  or pressure  $p$ ,  $S$  is the source term and  $\kappa$  is a constant. The value of  $S$  and  $\kappa$  depends on  $\Phi$  and are given below:

$$\kappa = \begin{cases} \frac{3Re}{2\Delta t} & \text{for } \Phi = U^* \\ 0 & \text{for } \Phi = p \end{cases} \quad (2.99)$$

And,

$$S = \begin{cases} -\frac{3Re}{2\Delta t} \left( \frac{4}{3} U^n - \frac{1}{3} U^{n-1} + \frac{2\Delta t}{3} (2H^n - H^{n-1}) \right) & \text{for } \Phi = U^* \\ \frac{1}{\Delta t} \nabla \cdot U^* & \text{for } \Phi = p \end{cases} \quad (2.100)$$

Taking Fourier transform (FT) of equation (2.98) in azimuthal direction  $\theta$  we get the following set of Helmholtz equations:

$$(\delta_{rr}^2(k_\theta) + \delta_{zz}^2) \hat{\Phi} - \kappa \hat{\Phi} = \hat{S} \quad \text{for } k_\theta = \frac{N_\theta}{2}, \frac{N_\theta}{2} - 1 \quad (2.101)$$

Where  $\delta_{rr}^2(k_\theta)$  and  $\delta_{zz}^2$  represents the radial and axial terms, respectively, in Fourier transform the Laplacian operator. These terms are given in following equation:

$$\delta_{rr}^2(k_\theta) = \begin{cases} \frac{\partial^2}{\partial r^2} + \frac{1}{r} \frac{\partial}{\partial r} + \frac{(-k_\theta^2 - 1)}{r^2} & \text{For u and v components} \\ \frac{\partial^2}{\partial r^2} + \frac{1}{r} \frac{\partial}{\partial r} + \frac{(-k_\theta^2)}{r^2} & \text{For w components} \end{cases} \quad (2.102)$$

$$\delta_{zz}^2 = \frac{\partial^2}{\partial z^2}$$

The term  $\delta_{rr}^2(k_\theta)$  is a function of the wave number in azimuthal direction,  $k_\theta$ . For each wave number  $k$ , the set of 3-D equations can be reduced to a 2-D problem. This 2-D problem is solved by diagonalization method.

### 2.5.3.d Diagonalization method

We can write the above equation in following matrix form:

$$D_{rr}^2 \Phi + \Phi D_{zz}^{2T} - k_\theta^2 \Phi = S \quad (2.103)$$

Where,

$\Phi = (N_r - 2) \times (N_z - 2)$  matrix of unknowns  $\Phi_{i,k} (i = 2, N_r - 1, k = 2, N_z - 1)$ ;

$D_{rr}^2$  and  $D_{zz}^2$  are tri-diagonal matrices corresponding to  $\delta_{rr}(k)$  and  $\delta_{zz}$  with dimensions  $(N_r - 2) \times (N_r - 2)$  and  $(N_z - 2) \times (N_z - 2)$  respectively.

This equation is solved using a diagonalization technique which expresses  $D_{rr}^2$  and  $D_{zz}^2$  in terms of products:

$$D_{rr}^2 = P_r \Lambda_r P_r^{-1} \quad (2.104)$$

And,

$$D_{zz}^2 = P_z \Lambda_z P_z^{-1} \quad (2.105)$$

Where  $\Lambda_r$  and  $\Lambda_z$  are diagonal matrices composed of the eigenvalues of  $D_{rr}^2$  and  $D_{zz}^2$ . The matrices  $P_r$  and  $P_z$  are built on their corresponding eigenvectors. Both matrices  $D_{rr}^2$  and  $D_{zz}^2$  are diagonalizable i.e. they can be written as the products of a diagonal and a tri-diagonal symmetric matrix.

If,

$$\tilde{\Phi} = P_r^{-1} \Phi \text{ and } \tilde{S} = P_r^{-1} S$$

Then, equation (2.103) gives:

$$\Lambda_r \tilde{\Phi} + \tilde{\Phi} D_{zz}^{2T} - k_\theta^2 \tilde{\Phi} = \tilde{S} \quad (2.106)$$

Again setting,

$$\begin{aligned} \check{\Phi} &= \tilde{\Phi} P_z^{-1T} \\ \check{S} &= \tilde{S} P_z^{-1T} \end{aligned} \quad (2.107)$$

We get,

$$\Lambda_r \check{\Phi} + \check{\Phi} \Lambda_z - k_\theta^2 \check{\Phi} = \check{S} \quad (2.108)$$

Thus, the solution is given as :

$$\check{\Phi}_{i,k} = \frac{\check{S}_{i,k}}{\lambda_{r_i} + \lambda_{z_k} - k_\theta^2} \quad (2.109)$$

Where  $2 < i < n_{\theta-1}$  and  $2 < j < n_{\theta-1}$

The values of  $\Phi$  are finally deduced from the following relation,

$$\Phi = P_\theta \check{\Phi} = P_\theta \check{\Phi} P_z^T \quad (2.110)$$

Since  $D_{rr}^2$  and  $D_{zz}^2$  are only space dependent, the calculation of their eigenvalues and eigenvectors is needed once for all, before starting the whole iteration process. This saves a lot of computational time as the matrix operators are calculated only once.

The extension of the above method to multi domain approach can be found in Abide and Viazzo (Abide, 2005).

## 2.5.4 Modified DNS code

In order to solve the geometries having non-homogeneous azimuthal direction for example an obstacle in the cylinder the numerical scheme of DNS code has been modified. The modified version of the DNS code is referred as Version 2 (V2). The overall procedure of solving the set of equations is similar. We will not repeat the same procedure and present only the difference existing in the new and old versions of the code. This version uses the same space discretization and time discretization method as presented in the previous section. However, the new version uses Fourier discretization in the axial direction ( $z$ ) and finite difference discretization in radial ( $r$ ) and azimuthal direction ( $\theta$ ) unlike the last version that uses Fourier discretization in azimuthal direction  $\theta$  and finite difference discretization in axial and radial direction. With the use of finite difference discretization in azimuthal direction the azimuthal direction need not be homogenous and it now permits to have a straight obstacle parallel to the axial direction in azimuthal direction.

### 2.5.4.a Space discretization

The space discretization still uses a staggered mesh with velocity at half integral positions and pressure at integral positions as shown in Figure 2.2.

The first and second order derivatives in the two non-homogeneous directions ( $r$  and  $\theta$ ) are given by Hermitian relations which have accuracy of order 4 presented in equations (2.76) to (2.82) but in these equations  $\xi$  represents (which denotes  $R$  or  $\theta$ ).

Fourier polynomial expansions are used in the homogeneous direction ( $\theta$ ), interpolations, first- and second-order derivatives are based on. The method is developed in the physical space using pseudo spectral formalism.

$$z_j = j\Delta z = jL_z/N_z \quad (2.111)$$

$$z_{j+1/2} = (z + 1/2)\Delta\theta = (z + 1/2) L_z/N_z \quad (2.112)$$

The wave numbers in axial direction represented by  $k_z$  are defined by

$$k_z = 2\pi j/L_z \quad (2.113)$$

The couple of direct and inverse discrete Fourier transform are chosen in the following form:

$$\hat{f}(k_p) = \frac{1}{N_z} \sum_{j=0}^{N_z-1} f(x_j) e^{-ik_p x_j} \quad (2.114)$$

$$f(x_j) = \sum_{p=-N_z/2}^{(N_z/2)-1} \hat{f}(k_p) e^{-ik_p x_j} \quad (2.115)$$

Where  $\hat{f}(k_p)$  represents the Fourier transform of  $f$  with the wave number  $k_p$ . Where  $p$  varies from  $\left(\frac{-N_z}{2}\right)$  to  $\left(\frac{N_z}{2} - 1\right)$ .

Thus, derivatives on normal and shifted nodes are given below and similar relations are also used for second-order derivatives and for interpolations.

$$\frac{\partial f}{\partial z}(z_j) = \sum_{p=-N_z/2}^{(N_z/2)-1} ik_p \hat{f}(k_p) e^{-ik_p z_j} \quad (2.116)$$

And,

$$\frac{\partial f}{\partial z}\left(z_j + \frac{\Delta z}{2}\right) = \sum_{p=-N_z/2}^{(N_z/2)-1} ik_p \hat{f}(k_p) e^{-ik_p\left(z_j + \frac{\Delta z}{2}\right)} \quad (2.117)$$

### 2.5.4.b Time discretization

The time discretization is the same as previous version and based on semi-implicit method of Adams-Bashforth and backward Euler scheme. The semi-discrete form (equation 2.91) ensures a second-order time accuracy. This equation is solved using Project decomposition method.

### 2.5.4.c Project decomposition method

The method of solving the set of equation 2.95 and 2.97 is based on projection method presented in section 2.5.3.c. Recalling the general form of the equation to be solved by

$$\nabla^2 \Phi - \kappa \Phi = S \quad (2.118)$$

Where  $\Phi$  represents provisional velocity  $U^*$  or modified pressure  $\varphi$ ,  $S$  is the source term and  $\kappa$  is a constant with values defined in equation (2.99) and (2.100).

In this case the radial and azimuthal derivative terms in Laplacian cannot be separated because the two are related in cylindrical coordinates as  $\frac{1}{r^2} \frac{\partial^2 \theta}{\partial r^2}$ . In order to solve this problem the whole equation is multiplied by  $r^2$ .

Therefore the general equation is modified as

$$r^2 \nabla^2 \Phi - r^2 \kappa \Phi = r^2 S \quad (2.119)$$

Now to solve this equation we take Fourier transform (FT) of equation 2.119 in axial direction and not in azimuthal direction  $z$ .

$$(\delta_{rr}^2(k_z) + \delta_{zz}^2)\hat{\Phi} - r^2\kappa\hat{\Phi} = r^2\hat{S} \quad \text{for } k_z = \frac{N_z}{2}, \frac{N_z}{2} - 1 \quad (2.120)$$

Where  $\delta_{rr}^2(k_z)$  and  $\delta_{zz}^2$  represents the radial and axial terms, respectively, in Fourier transform the Laplacian operator. These terms are given in following equation:

$$\delta_{rr}^2 = \begin{cases} r^2 \left( \frac{\partial^2}{\partial r^2} + \frac{1}{r} \frac{\partial}{\partial r} \right) + r^2(-k_j^2 - 1) & \text{For u and v components} \\ \frac{\partial^2}{\partial r^2} + \frac{1}{r} \frac{\partial}{\partial r} + \frac{(-k_j^2)}{r^2} & \text{For w component} \end{cases} \quad (2.121)$$

$$\delta_{\theta\theta}^2 = \frac{\partial^2}{\partial \theta^2} \quad (2.122)$$

The term  $\delta_{rr}^2(k_z)$  is a function of the wave number in axial direction,  $k_z$ . For each wave number  $k$ , the set of 3-D equations can be reduced to a 2-D problem. This 2-D problem is solved by Diagonalization method that remains unchanged in the two versions of the code. It is presented in section 2.5.3.d.

## 2.6 Boundary conditions

In every numerical simulations a proper boundary condition is essential to represent the physics of the flow correctly. This section represents the different types of boundary conditions.

### 1. Inflow (Dirichlet type)

For inflow boundaries, it is assumed that the spatial and temporal distributions of the main unknowns are known. These unknowns can be either instantaneous averaged or filtered quantities.

### 2. Outflow (von Neumann type)

For outflow boundaries it is assumed that for all quantities, the gradients normal to the outflow plane are taken to be zero. The exit mass flow is fixed from overall continuity consideration. For the momentum equation, this “free out-stream” condition is assured by an imposed pressure.



### 3. Symmetry

This condition denotes a surface at which the normal velocity and the normal gradients of all other variables are zero. There is no flux across the surface.

### 4. Periodic Boundaries

This boundary condition refers to a pair of surfaces at which the flow repeats itself either in terms of some variables or all variables.

The source term for velocity and temperature in the momentum and energy equation is necessary with stream wise periodic condition to maintain the flow and energy balance in the periodic domain. If there is no external momentum source term in Navier-Stokes equation then the periodic flow will undergo friction loss at the walls repeatedly at each transit that will finally diminish the flow with flow velocity going to zero. The additional momentum source term compensates for these frictional losses to maintain the flow. Similarly, if there is no source term in the energy equation (transport equation of temperature) to withdraw the extra energy deposited in the flow at each transit of the computational domain then with the fluid will get continuously heated up and the temperature field will never stabilize. Thus, while using the periodic flow boundary condition in the computational domain extra source term for momentum and energy equations is indispensable.

The source term (represented by  $f_i(t)$ ) used for the momentum equation in the periodic direction (say  $i$ ) is defined as follows (Ackerman, 2000):

$$f_i^{n+1} = f_i^n - \frac{2}{\rho A_f \Delta t} (\dot{m}^{n+1} - \dot{m}^0) + \frac{1}{\rho A_f \Delta t} (\dot{m}^n - \dot{m}^0) \quad (2.123)$$

Where  $\Delta t$  is the time step,  $A_f$  is the flow area of the periodic surface,  $\dot{m}^n$  is the flow rate at time  $n$  normalized by density and  $\dot{m}^0$  is the desired flow rate.

The source term for energy equation  $s_T(t)$  is defined below:

$$s_T(x, y, z, t) = -\frac{q_w}{\rho C_p V u_b} v(x, y, z, t) \quad (2.124)$$

Where  $v(x, y, z, t)$  is the velocity according to the periodic direction,  $V$  is the volume of the fluid,  $q_w$  is the heat flux imposed on the periodic channel walls and  $u_b$  is the bulk velocity.

The formulation of this expression comes from the energy balance on the periodic domain.

The heating condition imposed on the wall implies a linear increase of the time averaged temperature in the direction of the flow. For the fully developed flows, the following equalities are satisfied (Redjem-Saad, 2007),

$$\frac{\partial T}{\partial z} = \frac{\partial T_b}{\partial z} \quad (2.125)$$

Where  $T_b$  represents the bulk temperature and  $T$  is the temperature at a local position averaged in time and space in the homogeneous direction. The flow is assumed to be statistically homogeneous in the axial direction, with axial periodicity (direction  $z$ ) of velocity, pressure and temperature fields. So the axial temperature gradient should be corrected in order to make the rate of change of ensemble-average temperature invariant at any location.

Figure 2.3 shows a rectangular computational domain periodic in  $z$  with only one heated wall (area,  $A_w$ ) at the bottom. The flow is periodic with bulk velocity  $u_b$  and a constant heat flux of  $q_w$  is imposed on the wall. The temperature variation in this domain can be written as

$$T(z) = T_0 + \frac{dT_b}{dz} z \quad (2.126)$$

Where  $T_0$  is the constant periodic temperature.

Consider a small domain  $dz$  then the energy entering the domain  $dz$  in time  $t_1$  is given by  $E$ :

$$E = q_w A_w t_1 = q_w A_w \frac{dz}{u_b} \quad (2.127)$$

Energy balance on domain  $dz$  is gives that:

$$E = mC_p T_b(z + dz) - mC_p T_b(z) = mC_p dT_b \quad (2.128)$$

Equating the two equations (2.127) and (2.128) and put mass of the fluid,  $m=\rho V$  with  $V$  representing the volume of the domain we have

$$\frac{dT_b}{dz} = \frac{q_w A_w}{\rho V C_p u_b} \quad (2.129)$$

From (2.126) and (2.129) we have

$$T = T(z) = T_0 + \frac{q_w A_w}{\rho V C_p u_b} z \quad (2.130)$$

The conservation of energy equation without any source term is written as

$$\frac{\partial T}{\partial t} + u_i \frac{\partial T}{\partial x_i} = \alpha \frac{\partial^2 T}{\partial x_i \partial x_i} \quad (2.131)$$

Using (2.130) in (2.131) we have

$$\frac{\partial T_0}{\partial t} + u_i \frac{\partial T_0}{\partial x_i} = \alpha \frac{\partial^2 T_0}{\partial x_i \partial x_i} - \frac{q_w A_w}{\rho V C_p u_b} u_z \quad (2.132)$$

Thus, the equation for temperature can be reduced to equation for constant periodic temperature  $T_0$  with an external source term defined as  $S_T$  given as

$$S_T = -\frac{q_w A_w}{\rho V C_p u_b} u_z \quad (2.133)$$

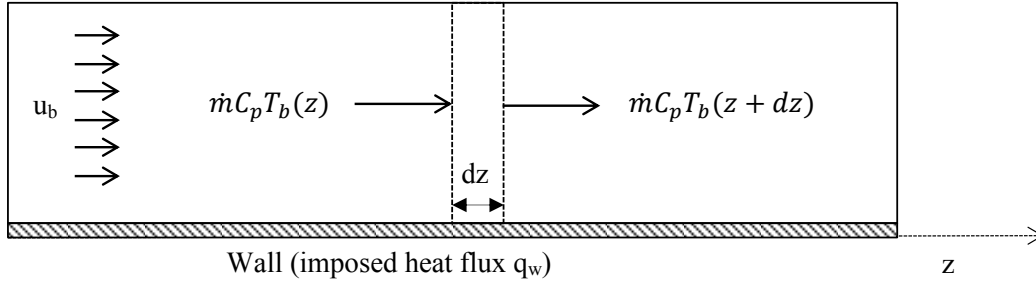


**Figure 2.3-Energy balance on a periodic domain (z) with a heated wall**

Another formulation for source term of energy is on a similar basis to (2.123) describing the source term for velocity. It implies that the time variation of bulk temperature inside the periodic computational domain is set to zero. Therefore, the source term is dynamically set to difference in the bulk temperature at two instant of time  $n$  and  $n+1$ .

Define the temperature variation in the periodic domain

$$s_T^{n+1} = s_T^n - \frac{2}{\Delta t} (T_b^{n+1} - T_b^0) + \frac{1}{\Delta t} (T_b^n - T_b^0) \quad (2.134)$$

Where superscript  $n$  denotes the time and  $T_b^0$  is the desired value of bulk temperature that is generally set to zero. This procedure is used in the DNS code.

## 2.7 Wall treatment

The profile of velocity near the wall in wall-bounded fully turbulent flows has been discussed in Chapter 1 (section 1.2.4.1). The velocity profile has three zones-linear viscous sub-layer, buffer layer and logarithmic zone (Figure 1.6). In order to capture the wall shear stress correctly the viscous sub-layer needs to be resolved completely i.e. the size of first mesh cell near the wall should be in this zone with non-dimensional distance from the wall,  $y^+ < 5$ . The viscous sub-layer gets thinner when the Reynolds number is increased and so the numerical simulation of the commonly encountered engineering flows with high Reynolds number needs to have very small size of the first mesh cell near the wall. This often leads to a too large number of mesh cells for the interested computational domain to produce adequate resolution along the wall.

In DNS approach this layer has to be well resolved to capture correctly the flow features that leads to large number of mesh cells. However, in case of RANS and LES methods the number of the mesh cells can be limited by the choice of a wall treatment method- wall functions. A

wall function is empirically derived algebraic model that can capture correctly the wall normal velocity or longitudinal velocity of the fluid which varies near wall region boundary layer.

If the required mesh resolution in the viscous-layer is not respected nor the wall functions are used then the numerical simulation gives wrong velocity gradient near the wall. Figure 2.4 shows that a mesh too coarse (with the first mesh cell at  $y^+=100$ ) without any modelling with wall functions leads to a poor estimation of the gradient of the variables transported. Thus, the correct turbulent profiles cannot be estimated by the numerical scheme (regardless of the order of accuracy) because a simple extrapolation process is not enough. Indeed for a good prediction of the wall gradients, the extrapolation process must account for the physics contained in the Navier-Stokes equation. This is the principle of wall function. Thus, use of wall functions allows us to have a comparatively coarser mesh near the wall and reduces the number of cells in the mesh and consequently the computational cost and time.

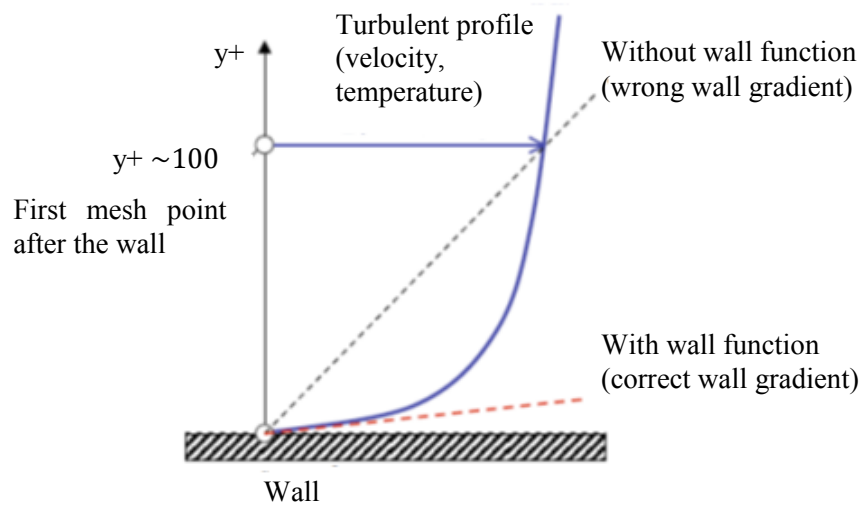


**Figure 2.4-Velocity gradient near the wall with and without wall function for a mesh with first mesh cell from wall at a distance,  $y^+$  of 100**

Wall functions provide the boundary layer information to mean flow of Navier-Stokes equations at first point close to the wall. At a distance less than the first point of wall, the physical quantities are modelled using analytical expressions for velocity profiles in lower part of boundary layer and turbulent transport quantities at first point of wall. It assumes that the wall shear stress, wall heat flux and pressure are constant in the lower boundary layer.

The wall functions for velocity is the Riechardt correlation that is the blended function well-adapted to capture the linear region, logarithmic region and the transition zone. It is given as follows:

$$u^+ = F_{Rei}(y^+) \quad (2.135)$$

Where  $F_{Rei}(y^+)$  is given by:

$$F_{Rei}(y^+) = \frac{\ln(1 + 0.4y^+)}{\kappa} + 7.8 \left( 1 - e^{-\frac{y^+}{11}} - \frac{y^+}{11} e^{-\frac{y^+}{3}} \right) \quad (2.136)$$

The wall function used for temperature should be able to reflect well the effect of Prandtl number on the thickness of thermal boundary layer. In simple words, it should account for the differences in the velocity and thermal layer i.e. at  $y^+ = 30$  if velocity profile follows the logarithmic law then it does not implies that temperature also follows the logarithmic law however it depends on the function of Prandtl number. Kader law (Kader, 1981) takes in to account the molecular Prandtl number and thus reflects well the physics of the flow and thermal behavior for different ranges of Prandtl number (Kawamura, 1999). Kader law is given as follows:

$$T^+(y^+, Pr) = Pr y^+ e^\Gamma + (2.12 \ln(1 + y^+)) e^{-1/\Gamma} \quad (2.137)$$

Where  $\Gamma$  is defined below:

$$\Gamma = \frac{0.01 (Pr y^+)^4}{1 + 5 Pr^3 y^+} \quad (2.138)$$

In the two CFD tools – STAR-CCM+ used for RANS based simulations and TRIO\_U used for LES based simulations, the wall functions used are Reichardt and Kader for velocity and temperature field respectively.

## **2.8 Summary**

In this chapter the three major families- RANS, LES and DNS of CFD method are presented along with their principle and mathematical formulations. The different turbulence models used to close the set of time averaged RANS and space filtered LES equations are discussed. The choice of turbulence model made for the study in next chapters are- realizable k- $\epsilon$  model to perform RANS study and WALE model to perform LES study. The numerical tool used to for RANS study is STAR-CCM+ code and LES study is TRIO\_U code. The code used to perform DNS calculation is University in-house code that is capable of treating cylindrical flow with homogeneous azimuthal direction. In the context of this thesis the code has been modified to treat the case of obstacle leading to non-homogeneous azimuthal direction. The old and the new version of the DNS in-house code have been described. In the next two chapters, the DNS, LES and RANS study are presented to study the heat transfer in in sodium and hot-spots in sub-assembly.

# CHAPTER 3

---

## *Numerical study of turbulent heat transfer in liquid sodium*

*In this chapter both Direct Numerical Simulation (DNS) and Large Eddy Simulation (LES) approaches are used to study the heat transfer between the cylindrical fuel pin and turbulent flow of liquid sodium at very low Prandtl number ( $\sim 10^{-3}$ ). This chapter is divided in to three parts. The first part deals with the validation of DNS code by comparing the results for the turbulent flow and heat transfer in air with the available data in the open literature. The second part gives the thermal statistics for heat transfer in sodium by DNS approach showing the effect of three parameters- low Prandtl number, effect of Reynolds number and curved surface of the wall. In the last section the results from DNS study of sodium are used as a reference for comparison with the LES approach.*

## 3.1 Introduction

Direct Numerical Simulation (DNS) is an essential tool to examine turbulence phenomena and study the turbulent heat transfer. DNS of turbulent heat transfer are now widely performed for various configurations to gain significant insight into the physics of wall-bounded turbulent flow and heat transfer. Among various configurations studied in the past, it is seen that the turbulent flow inside the rectangular channel is the most widely studied geometry due to its simplicity and fundamental nature to understand the convective heat transfer between fluid and solid wall. The DNS study for turbulent flow inside pipe and concentric annular pipe are however limited due to peculiar numerical difficulties associated with the cylindrical coordinate system (Ould-Rouiss, 2010).

Turbulent heat transfer is characterized not only by the Reynolds number ( $Re$ ) but also by the Prandtl number ( $Pr$ ) of the fluids. Many attempts have been made to explore the effect of Prandtl number on turbulent heat transfer in channel flows with DNS (Kawamura, 1998, 1999; Na and Hanratty, 2000; Abe, 1998, 2002, 2004). The study has been done for fluids with a wide range of Prandtl number varying from 0.025 to 10. However, the heat transfer in liquid sodium with Prandtl number  $\sim 10^{-3}$  has not been studied yet.

Table 3.1 gives overview of the turbulent heat transfer in wall bounded flows at  $Pr \sim 0.025$  at different thermal boundary conditions. The majority of the studies in the channel flow geometry have been done for a fixed friction Reynolds number. The effect of Reynolds number has been studied for low Prandtl number in channel flow geometry by Kawamura et al (Kawamura, 1999, 2002, 2004), Kawamoto et al (Kawamoto, 1999b) and Abe et al (1998, 2002, 2004). The various friction Reynolds number ( $Re_\tau$ ) for which thermal statistics have been evaluated are 180, 395, 640, 1020. These studies have been done for mixed boundary condition where the temperature fluctuations at the wall are zero. These studies show that the time average temperature is almost independent of Reynolds number but the temperature fluctuations and turbulent heat flux have strong dependence on the Reynolds number. The temperature fluctuations and turbulent heat flux increases with the increase in Reynolds number. The effect of Reynolds number is stronger for fluids with  $Pr < 0.2$  and almost negligible for fluids with higher Prandtl number (Kawamura, 1999).



$Re_{\tau}$ ( $Re_{Dh}$ )	DNS Publication	Boundary conditions					Geometry
		UTD <sup>1</sup>	MBC <sup>2</sup>	SMTG <sup>3</sup>	IWHF <sup>4</sup>	CF <sup>5</sup> / PF <sup>6</sup>	
150	Piller et al. (2002)	•				PF	Channel flow
180	Kawamura et al. (1997)		•			PF	
180, 395	Abe et al. (1998)		•			PF	
180	Kawamura et al. (1998a)		•			PF	
180	Kawamura et al. (1998b)		•			PF	
180	Kawamoto and Kawamura (1998)			•		PF	
180	Kawamoto and Kawamura (1999a)	•	•			PF	
180, 395	Kawamoto and Kawamura (1999b)		•			PF	
180, 395	Kawamura et al. (1999)		•			PF	
180, 395	Kawamura et al. (2000)	•	•			PF, CF	
180, 395, 640	Kawamura and Abe (2002)		•			PF	
180, 395, 640	Abe and Kawamura (2002)		•			PF	
180, 395, 640, 1020	Abe et al. (2004)		•			PF	
180, 395, 640, 1020	Kawamura et al. (2004)		•			PF	
186 (5500)	Redjem-Saad et al. (2007)		•			PF	Pipe flow
170 (8825)	Saha et al. (2010)		•			PF	
	Ould-Rouiss, 2010				•	PF	Annulus

<sup>1</sup>UTD-Uniform temperature difference, <sup>2</sup>MBC-Mixed boundary Condition, <sup>3</sup>SMTG-Spanwise mean temperature gradient, <sup>4</sup>IWHF-Ideal iso-flux boundary condition, <sup>5</sup>PF-Poiseuille flow, <sup>6</sup>CF-Couette flow

**Table 3.1-Overview of DNS calculations for Pr=0.025**

In the open literature, the DNS study for flow in pipe and concentric annulus are very scarce. The effect of Prandtl number has been studied for pipe (Redjem-Saad, 2007) and concentric annular pipe (Ould-Rouiss, 2010) for a fixed value of Reynolds number ( $Re_{Dh}$ ) based on hydraulic diameter  $D_h$  and bulk velocity  $u_b$  equal to 5500 and 8825 respectively. The effect of heat flux ratio (Ould-Rouiss, 2009) and radius ratio (Chung, 2002, 2003) on the thermal statistics has been studied for the turbulent flow of air (Pr=0.7) in concentric annular pipe.

However, the effect of Reynolds number on the heat transfer characteristics in pipe or annular cylinder at Prandtl number of 0.025 has not been studied.

The Prandtl number of 0.025 ( $\sim 10^{-2}$ ) corresponds to the lead-bismuth eutectic (LBE), sodium potassium (NaK) fluids. However the liquid sodium used as coolant in sub-assembly of SFRs has Prandtl number of 0.004 ( $\sim 10^{-3}$ ). Therefore there exists a difference of order of magnitude of 1 between Prandtl number for which thermal statistics are available in the literature and the desired value. The studies have shown that with decrease in Prandtl number the near wall structures become more elongated and a much longer computational domain is required. Saha et al. (Saha, 2011) have shown that for fluid with Prandtl number 0.025 in pipe of radius  $\delta$  the pipe length should be at least  $8\pi\delta$  or 4300 in wall units to have convergence for various thermal turbulence statistics. The larger computational domain implies that the computational cost is higher in terms of computer memory and CPU-time. This can be a plausible reason that why the lowest Prandtl number studied in the literature is limited to 0.025.

For the thermal hydraulic study of sub-assembly, it is inevitable to understand the heat transfer phenomena in liquid sodium with  $Pr \sim 10^{-3}$  and to characterize the flow and thermal statistics. This is done by academic calculation of a simple geometry using DNS approach. The objective is to add in the existing literature the heat transfer characteristics at  $Pr \sim 10^{-3}$  and see the effect of Reynolds number on turbulent thermal statistics. In addition to this an industrial LES calculation is performed for the same geometry and same data set in order to compare with the DNS results.

## 3.2 Data set

The following section presents a simple geometry for studying the heat transfer in fully developed turbulent liquid sodium flow. It is beyond the capabilities of the code to model a complex geometry of wire wrapped sub-assembly. Hence, a simplification of the geometry of the sub-assembly is required for the DNS calculation of turbulent sodium flow.

The computational domain is shown in Figure 3.1. The wire wrapped sub-assembly with 217 fuel pins has been simplified to a concentric annulus for DNS study. The inner radius of the annulus represented by  $R_{int}$  is equal to radius of the fuel pin of SFR ( $R_{int}=4.285$  mm). The dimension of the radius of the fuel pin is taken from the core design of ASTRID. The CFV version 2 of the core specifies the diameter of fuel pin  $D_p$  equal to 8.57 mm. Therefore the radius of the inner cylinder of the annulus is set to  $D_p/2$ .

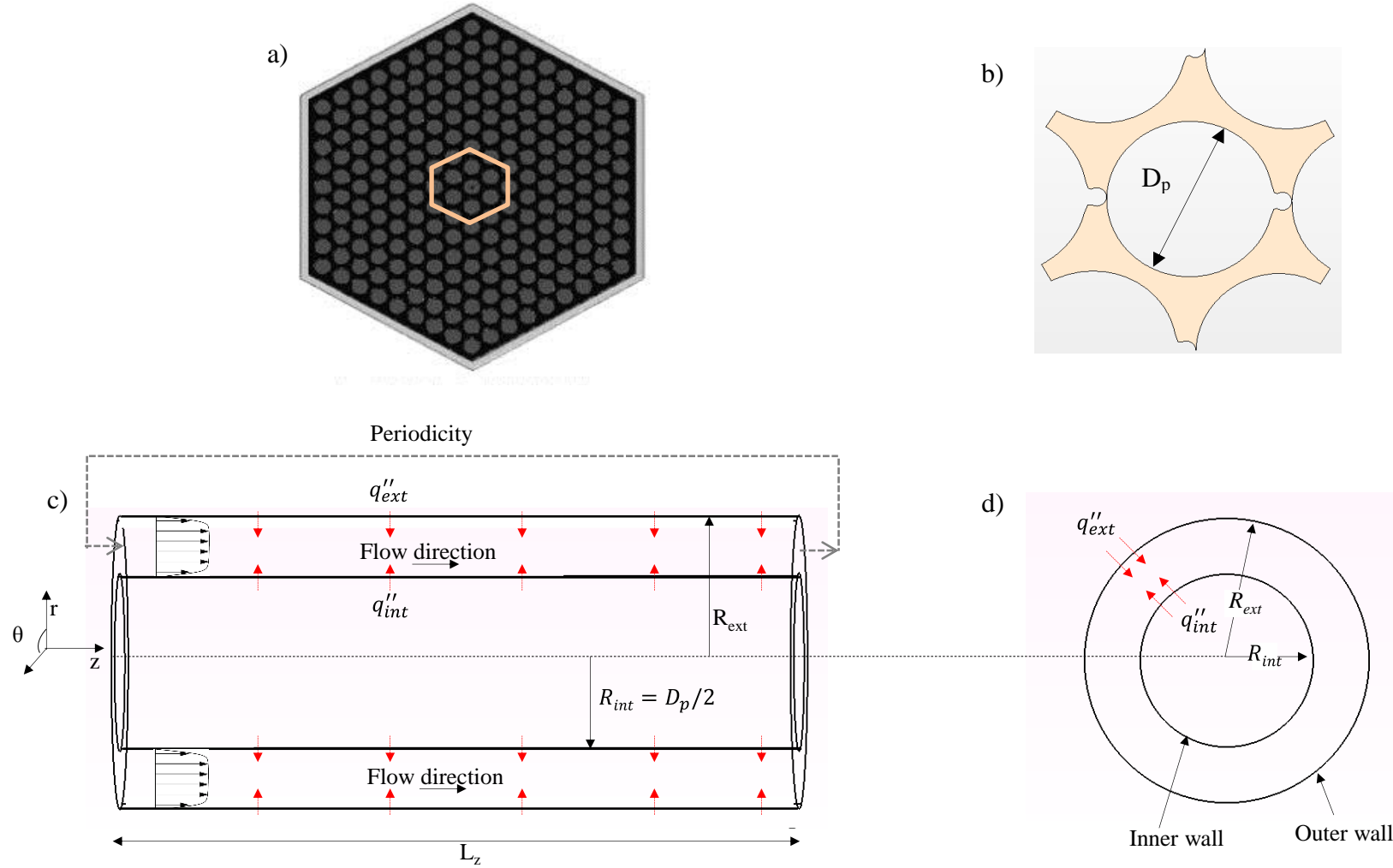


**Figure 3.1- Schematic representation of the simplified geometry for DNS study- a) Sub-assembly with 217 fuel pins (top view), b) Central region of sub-assembly with 217 fuel pins (top view), c) Simplified representation-concentric annulus (side view), d) top view of the concentric annulus**

The radius of outer cylinder,  $R_{ext}$ , is calculated such that the volume of sodium inside central pin of sub-assembly is same. This gives  $R_{ext}=7.055$  mm. The spacer wire present in the sub-assembly is currently not represented in the simplified geometry due to current capabilities of the In-house University DNS code (version 1 represented by V1). The azimuthal direction ( $\theta$ ) has to be homogeneous and an obstacle like spacer wire around the inner wall of the annulus will destroy this homogeneity of the flow in azimuthal direction. So the spacer wire is not taken in to consideration in the simplified geometry. The objective of this study is to capture correctly the heat transfer phenomena in sodium with curvature and so the proposed simplified geometry is capable of meeting the current objective.

However, a new version of the In-house University DNS code (version 2 represented by V2) has been developed in the context of this thesis. The V2 of the DNS code can have a straight obstacle around the inner cylinder aligned in the axial direction. Due to time limitation the version V2 of the code has not been used for studying the flow around the obstacle but in this chapter the new version as well as the old version of the code has been used to study the turbulent air flow in concentric annulus and compare the results to the results available in open literature.

The characteristic parameters of the concentric annulus are radius ratio  $R^*=R_{int}/R_{ext}$  and hydraulic diameter,  $D_h=2(R_{ext}-R_{int})$ . These parameters for the different DNS calculations have been summarized in Table 3.2. The computational domain for the DNS calculation of turbulent flow in air is same as Chung et al. (Chung 2002, 2003) in order to compare the results for the validation of the DNS code used for the study (V1 and V2). The Radius ratio,  $R^*$  is 0.5. Similar to Chung et al., the computational domain in azimuthal direction contains only  $\pi/2$  region with periodic conditions at the boundary. The DNS calculation for air done with version 1 of the code is represented as AIR-V1 and the one done with version 2 of the code is represented as AIR-V2 in the subsequent sections.

For the thermal-hydraulic study of the liquid sodium flow, the same computational domain with  $\pi/2$  region in azimuthal direction is used except the radius ratio is slightly changed to 0.6 and Reynolds number ( $Re_{Dh}$ ) is increased from 8900 to 16000 in order to be coherent with the dimensions of the inner and outer cylinder obtained from the simplification of the sub-assembly geometry and have higher turbulence. This simulation will be referred as Na-16K-V1 in the following sections where Na stands for sodium and 16000 represents the Reynolds number done with version 1 of the code. However, the auto-correlation (presented in section 3.5.3) shows that domain size has to be longer in axial and azimuthal direction.

- 1) **Insufficient domain size in axial direction**-The axial length of  $7.5D_h$  that is sufficient to simulate the thermal structures in air is not sufficient for sodium. The domain was increased stepwise and finally  $25D_h$  axial length was found to be sufficient to capture the large thermal structures in liquid sodium flow.
- 2) **Insufficient domain in azimuthal direction**- The  $\pi/2$  domain in azimuthal direction was found to be insufficient for the large thermal structures even with sufficiently long axial domain of length  $25D_h$ . The thermal structures in sodium are longer in axial as well as in azimuthal direction. Therefore, complete  $2\pi$  domain in azimuthal direction is necessary to simulate the thermal field in liquid sodium. However, with the increase in domain size by a factor of 4 (from  $\pi/2$  to  $2\pi$ ) the memory requirements are also increased. This is because number of mesh cells is also increased by the factor 4. The refinement of mesh cannot be change without decreasing the Reynolds number. Therefore, the Reynolds number for  $2\pi$  domain is reduced back to 8900 similar to that studied by Chung et al. (Chung, 2003) in order to reduce the mesh refinement and consequently the computational cost. This DNS simulation will be represented by Na-8.9K-V2.

Parameter	Formula	Chung, 2003	AIR-V1	AIR-V2	Na-16K-V1	Na-8.9K-V2
$R^*$	$R_{int}/R_{ext}$	0.5	0.5	0.5	0.6	0.5
$Pr$	$\nu/\alpha$	0.7	0.7	0.7	0.004	0.004
$q^*$	$q''_{ext}/q''_{int}$	1	1	1	1	1
$D_h$ (mm)	$2(R_{ext} - R_{int})$	8.57	8.57	8.57	5.54	8.57
$\delta$ (mm)	$D_h/4$	2.14	2.14	2.14	1.385	2.14
$Re_{D_h}$	$u_b D_h / \nu$	8900	8900	8900	16000	8900
$u_b$ (m/s)		0.3145	0.3145	0.3145	0.8744	0.3145
$\theta$	-	$\pi/2$	$\pi/2$	$\pi/2$	$\pi/2$	$2\pi$
$L_z$	-	$7.5D_h$	$7.5D_h$	$7.5D_h$	$25D_h$	$7.5D_h$

**Table 3.2-Computational domain and data set for different DNS calculations**

### 3.3 Numerical method

The DNS calculation is done using two versions of the in-house University code. The two versions are based on pseudo-spectral scheme that has accuracy of order two in time and order four in space. The first version denoted by V1 is the old version that uses Fourier method in azimuthal direction and finite difference in axial, radial direction. The second version denoted by V2 is the new modified version of the code that uses Fourier method in axial direction and finite difference method in azimuthal direction. The advantage of V2 of the code over V1 is that the computational domain need not be homogeneous in azimuthal direction. The two versions (V1 and V2) of the code are presented in Chapter 2.

### 3.4 Meshing

A structured mesh is generated with specified number of points –  $N_r$  in radial,  $N_\theta$  in azimuthal and  $N_z$  in axial direction. The mesh is staggered with velocity components  $u_r$ ,  $u_\theta$  and  $u_z$  located at nodes  $((i + \frac{1}{2})\Delta r, j\Delta\theta, k\Delta z)$ ,  $(i\Delta r, (j + \frac{1}{2})\Delta\theta, k\Delta z)$  and  $(i\Delta r, j\Delta\theta, (k + \frac{1}{2})\Delta z)$  respectively, while the pressure and temperature nodes are located at  $(i\Delta r, j\Delta\theta, k\Delta z)$  where  $\Delta r$ ,  $\Delta\theta$  and  $\Delta z$  are corresponding grid spacing in  $r$ ,  $\theta$  and  $z$  directions. The meshing is uniform in axial and azimuthal direction i.e.  $\Delta\theta$  and  $\Delta z$  is constant but non-uniform in radial direction. In order to capture correctly the steep velocity gradients near the wall the mesh size near the wall has to be very small such that the non-dimensional distance from the wall i.e.  $y^+$  is less than unity. The mesh refinement in radial direction is achieved by using a hyperbolic transformation defined below (Vedy, 2003):

$$r_j = \frac{\delta}{\gamma} \tanh \left[ \frac{R_j}{\delta} \tanh^{-1}(\gamma) \right] \quad (3.1)$$

Where  $\delta$  is the half width between interior and exterior walls and  $R_j$  is given as follows:

$$R_j = \delta + \Delta x(i - 1) \quad (3.2)$$

And,

$$\Delta x = \frac{R_{ext} - R_{int}}{(N_r - 1)} \quad (3.3)$$

The value of  $\gamma$  for current mesh refinement is set to 0.98346 for the two meshes corresponding to the computational domain with size  $\pi/2$  and  $2\pi$  in azimuthal direction Figure 3.2 and Figure 3.3. The two meshes have the same mesh refinement near the wall.

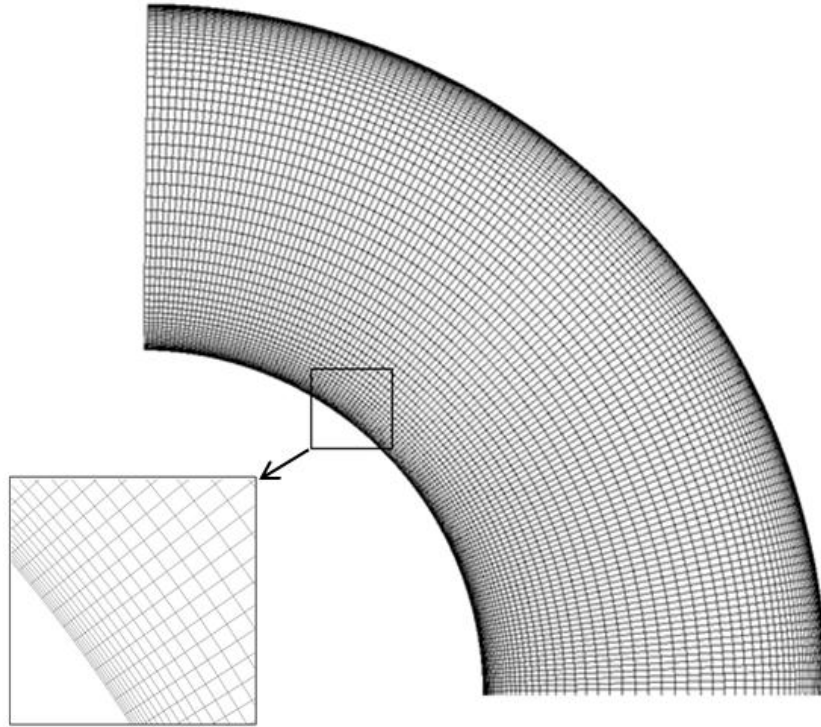


**Figure 3.2-Mesh of the computational domain with size  $\pi/2$  in azimuthal direction and zoom view to show the mesh refinement near the wall in radial direction**

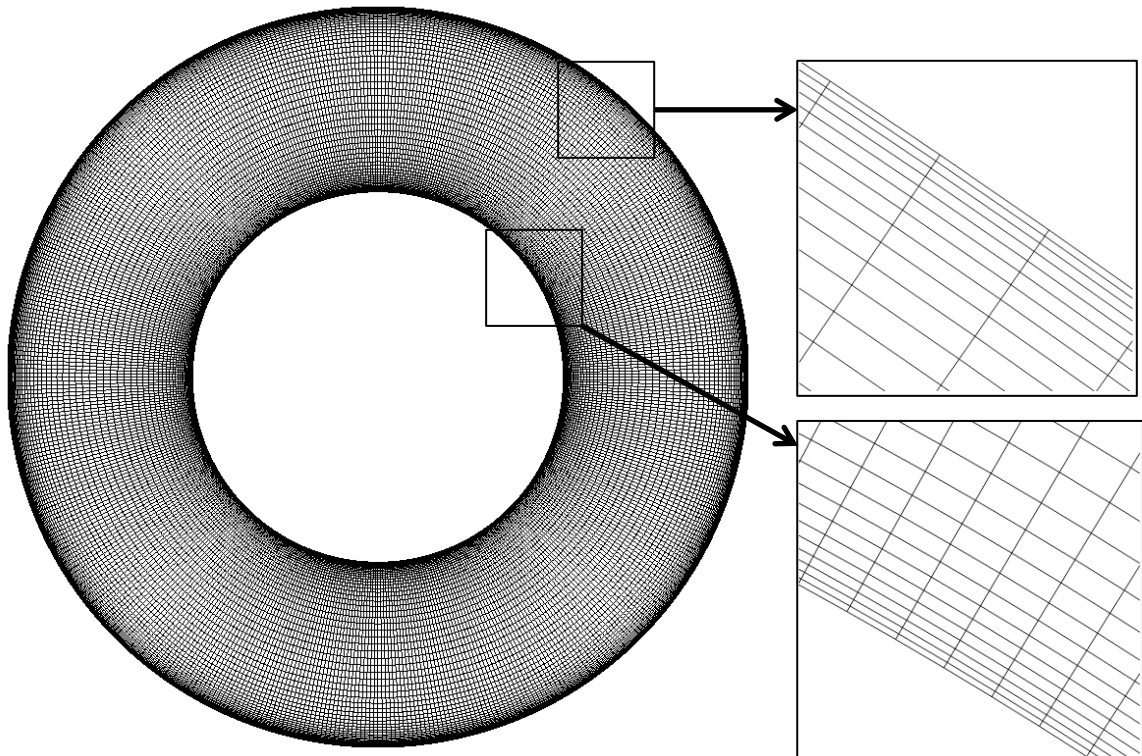


**Figure 3.3-Mesh of the computational domain with size  $2\pi$  in azimuthal direction and zoom view to show the mesh refinement near the wall in radial direction**

Parameter	Formula	Chung, 2003	AIR-V1	AIR-V2	Na16000	Na8900
Pr	$\nu/\alpha$	0.7	0.7	0.7	0.004	0.004
$\Delta z_{int}^+$	$\Delta z \cdot \frac{u_{\tau-int}}{\nu}$	14.23	14.12	32.63	24.81	32.36
$\Delta r_{int}^+ _{min}$	$\Delta r _{min} \frac{u_{\tau-int}}{\nu}$	0.13	0.41	0.38	0.71	0.39
$\Delta r_{ext}^+ _{min}$	$\Delta r _{min} \frac{u_{\tau-ext}}{\nu}$	0.12	0.39	0.36	0.66	0.37
$(r_{int}\Delta\theta)^+$	$R_{int}\Delta\theta \frac{u_{\tau-int}}{\nu}$	3.73	3.7	3.59	9.55	3.52
$(r_{ext}\Delta\theta)^+$	$R_{ext}\Delta\theta \frac{u_{\tau-ext}}{\nu}$	7.10	7.06	6.94	15.45	6.72
$\Delta r_{max}^+$	$\Delta r _{max} \frac{u_{\tau-int}}{\nu}$	12.89	4.6	4.44	8.01	5.53
$N_r$	-	65	65	65	65	65
$N_\theta$	-	128	128	128	128	256
$N_z$	-	320	324	130	1028	130
Time step (s)	-	-	$7.10^{-5}$	$7.10^{-5}$	$7.10^{-6}$	$5.3.10^{-5}$
Total averaging time(s)	-	-	7.632	7.6503	0.4536	1.1905
Number of cells	-	$2.7 \cdot 10^6$	$2.7 \cdot 10^6$	$1.1 \cdot 10^6$	$8.5 \cdot 10^6$	$2.2 \cdot 10^6$
Version of the DNS code	-	-	V1	V2	V1	V2

**Table 3.3- Data set and grid resolution for the different DNS calculations**

The mesh size and grid refinement for the four DNS calculations is shown in Table 3.3. The time step of the all the calculation is small enough such that the maximum value of CFL number around 0.25. In the DNS calculation for air, the number of grid points in radial direction is same as that in Chung et al. (Chung, 2003) but the radial refinement factor are different. The radial refinement factor used in Chung et al. (Chung, 2003) has not been indicated. However with the radial refinement factor used to perform DNS study we have slightly less refinement near the walls as compared to Chung et al. (Chung, 2003) but we have comparatively more refined mesh in the center of the domain with  $\Delta r_{max}^+$  around 4.

Another important point is that in liquid sodium (Pr=0.004) the ratio of thermal boundary layer to dynamic boundary layer varies as  $Pr^{-1/2}$  (equation 1.15). Therefore, a larger grid resolution will be sufficient for thermal conduction region (Montreuil, 2000). Thus, DNS of turbulent heat transfer for sodium is done with coarser mesh in axial direction with care that



the computation domain is enlarged to capture larger thermal scales as shown by auto-correlation presented later in section 3.5.3. Moreover the above grid was found to provide a good agreement for temperature field with slight differences in velocity field with the available data in literature for air (AIR-V2). Thus, it gives a good compromise between required CPU time and accuracy.

## 3.5 Boundary and initial conditions

DNS calculation is performed for incompressible, single phase, fully developed turbulent flow of air and sodium.

The Navier-Stokes equations have Dirichlet boundary condition and Energy equation uses Neumann boundary condition.

Dirichlet boundary condition prescribes the value of velocity field at the boundary. The velocity field is required to stick at the inner and outer walls i.e. no-slip boundary condition:

$$\vec{u}(r = R_{int}, \theta, z, t) = 0 \quad (3.4)$$

$$\vec{u}(r = R_{ext}, \theta, z, t) = 0 \quad (3.5)$$

The Neumann boundary condition prescribes the derivatives of temperature at boundaries given below:

$$q'' = -\nabla T \quad (3.6)$$

The boundary condition has an important effect on the turbulence heat transfer quantities. A constant heat flux is imposed on the walls instead of constant temperature to capture the temperature fluctuations at the wall. Kong et al. (Kong, 2000) studied the effect of iso-thermal and iso-flux boundary condition on the development of the thermal boundary condition. Kasagi, 1989 mentioned that in order to accurately solve the thermal boundary layer one has to accurately solve the conjugate heat transfer problem by specifying the thickness of solid wall, property of solid wall and property of fluid. They studied air flow over wall made up of metal, glass and plastic and determined the temperature fluctuations at wall for iso-thermal and iso flux conditions. The temperature fluctuations are almost zero and independent of wall thickness when iso-thermal boundary condition is used. With iso flux boundary condition at the wall the temperature fluctuations are not negligible when the wall is extremely thin.

In this study the wall is assumed to be extremely thin and iso-flux boundary condition is used to have non zero temperature fluctuations.

The inner and outer wall has equal heat flux. Thus, the ratio of heat flux on two walls,  $q^* = 1$ . The value of  $q'' = 9.11427 \cdot 10^5 \text{ W/m}^2$  comes from the approximation that the energy developed in the nuclear reactor fuel pin by fission can be considered equally distributed and carried to the metallic liquid which flows around the fuel pin in sub-assembly (Piller 2005). The heat flux is uniform along the wall and constant with time.

$$q''_{int} = q''_{ext} = q'' \quad (3.7)$$

In Chapter 2 it is shown that the computational requirements for DNS calculation vary as  $Re^{11/4}$  to capture the Kolmogorov length and time scales. Thus DNS study at Reynolds number around 50000-70000 corresponding to liquid sodium flow in SFR sub-assembly is not achievable with the current computational power. Hence the DNS calculation is performed at Reynolds number 8900 and 16000.

To simulate an infinite domain for the flow in axial direction periodicity is used in the axial domain over the length  $L_z$ . This condition is described as follows:

$$\vec{u}(r, \theta, z) = \vec{u}(r, \theta, z + L_z) \quad (3.8)$$

As the flow is considered periodic in axial direction so the temperature field also has to be periodic.

$$T(r, \theta, z) = T(r, \theta, z + L_z) \quad (3.9)$$

Periodic boundary conditions are also used in azimuthal direction when only quarter of the domain ( $\pi/2$ ) is studied.

### 3.5.1 Source term for periodic flow in axial direction

When periodic boundary conditions are used in axial direction for velocity and temperature then in order to maintain the flow in the periodic boundary conditions and energy balance in the domain external source terms are necessary. The momentum source term,  $F$  has non zero value only in the periodic direction  $z$  (represented as  $f_z$ ) and it is zero in other two directions. The expressions for these source terms-  $f_z$  in momentum equation and  $S_T$  in the temperature equation are recalled from chapter 2 and given below:

$$f_z^{n+1} = f_z^n - \frac{2}{\Delta t} (u_b^{n+1} - u_b^0) + \frac{1}{\Delta t} (u_b^n - u_b^0) \quad (3.10)$$

$$S_T^{n+1} = S_T^n - \frac{2}{\Delta t} (T_b^{n+1} - T_b^0) + \frac{1}{\Delta t} (T_b^n - T_b^0) \quad (3.11)$$

Where superscript  $n$  denotes the time,  $\Delta t$  is the time step,  $u_b^n$  is the bulk velocity at time  $n$  and  $u_b^0$  is the desired bulk velocity deduced from the Reynolds number and  $T_b^0$  is the desired value of bulk temperature that is taken to be zero in this study.

The two versions of the DNS code-V1 and V2 uses the same source term for temperature (3.10) and the source term for velocity is different, however. Momentum source shown in equation (3.9) is used in DNS V2. In DNS V1, there is no explicit source term and the flow in periodic direction is maintained by correction in provision velocity  $U^*$  denoted as  $U_{corrected}^*$  at each iteration to have desired mass flow rate (Chapter 2-section 2.5.3):

$$U_{corrected}^* = U^* \frac{u_b^0}{u_b^n} \quad (3.12)$$

### 3.5.2 Initial condition

The velocity field at time  $t=0s$  is initialized with the bulk velocity corresponding to desired Reynolds number. When laminar flow has been established, the velocity field is perturbed with random fluctuations that have magnitude ranging from 0% to 15% of the bulk velocity. This helps the flow to undergo transition to turbulence. The temperature is initialized with 0 °C and the source term is also initialized to zero. The fluid is heated up with the imposed heat flux at the wall and temperature at the wall and bulk domain increases. The source term adjusts itself at each iteration to have bulk temperature equal to zero.

### 3.5.3 Auto-correlation in periodic directions

The auto-correlation is traced in periodic direction to determine if spatial resolution is sufficient for thermal and flow structures of the turbulent flow. The auto-correlation for fluctuations of a variable  $\varphi$  (representing temperature or velocity) in direction  $x_i$  is defined as follows:

$$R_\varphi(l, t) = \frac{\overline{\varphi'(x_i, t)\varphi'(x_i + l, t)}}{\overline{\varphi'^2(x_i)}} \quad (3.13)$$

Where  $\overline{\varphi(x_i, t)}$  represents the time averaged quantity and  $\varphi'(x_i, t)$  is the fluctuations with respect to time given below:

$$\varphi'(x_i, t) = \varphi(x_i, t) - \overline{\varphi(x_i, t)} \quad (3.14)$$

The auto-correlation curve is symmetric for the total domain so it is traced only for half of the complete domain in axial and azimuthal direction. The auto-correlation of velocity is

calculated at a radial distance of  $y^+ \sim 5$  from the inner and outer wall. At this distance the structures are more elongated and have maximum turbulent kinetic energy. The temperature auto-correlation in space is calculated at the inner and outer wall. Figure 3.4 and Figure 3.5 shows the auto-correlation for the fluctuations of axial velocity and temperature for air ( $Pr=0.7$ ) and sodium ( $Pr=0.004$ ) in both axial direction ( $z$ ) as well as azimuthal direction ( $\theta$ ). These figures show the effect of Prandtl number on the required computational length in axial direction  $L_z$  and in azimuthal direction ( $\theta$ ).

#### i. Auto-correlation for air

The DNS calculation of air has been performed with the two versions of the code V1 and V2 represented as AIR-V1 and AIR-V2. The auto-correlations in axial and azimuthal directions for the two simulations have been traced and they show similar behavior. Therefore for simplicity the auto-correlation for only one calculation (AIR-V1) has been presented.

Figure 3.4a shows that the auto-correlation for velocity fluctuations in axial direction vanishes at the center of the domain ( $3.75D_h$ ) implying that the total domain of  $7.5D_h$  (twice of  $3.75D_h$ ) is sufficiently long in axial direction to capture the largest flow structures for air. However for temperature fluctuations the auto-correlation do not decay completely to zero. The minimum value obtained for temperature is 0.04. Chung et al. (Chung, 2003) and Ould-Rouiss et al. (Ould-Rouiss, 2009) also observed same behavior with constant value equal to 0.04 and 0.09 respectively. Tiselj et al. (Tiselj, 2001) showed that the auto-correlation of fluctuating temperature does not vanish for this kind of boundary conditions even if the domain is enlarged.

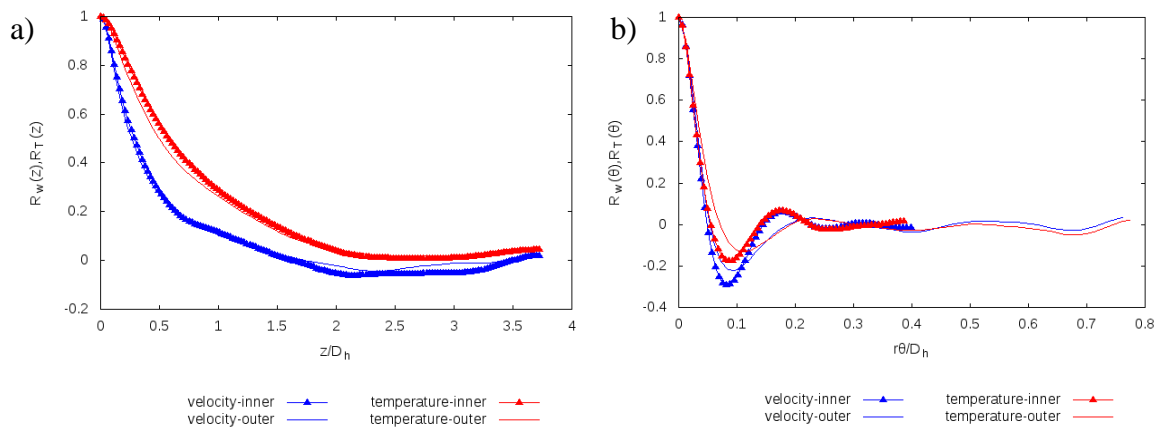


**Figure 3.4-Auto-correlation for fluctuations in axial velocity and temperature in a) axial direction b) azimuthal direction**

The auto-correlation for velocity and temperature fluctuations in azimuthal direction goes to zero for both inner and outer wall (Figure 3.4b). There is a slight deviation between the negative peaks of fluctuating temperature and axial velocity, due to the difference in the boundary conditions for the temperature field and velocity field. Thus, in case of air with Prandtl number equal to 0.7, only  $\pi/2$  domain with periodic condition in azimuthal direction is sufficient to study the turbulent velocity and thermal structures in azimuthal direction.

## ii. Auto-correlation for sodium

In this section, we refer to the DNS calculation of sodium (Na-16K-V1) with  $\pi/2$  domain size in the azimuthal direction. The auto-correlation for velocity fluctuations in axial as well as azimuthal direction (Figure 3.5) shows similar behavior as for air. However, it is not true for thermal structures.

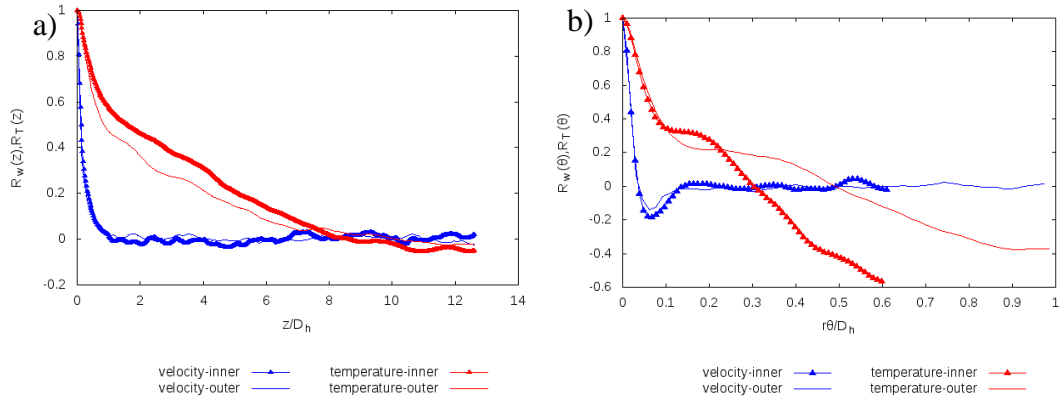


**Figure 3.5-Auto-correlation for fluctuations in axial velocity and temperature in sodium (Na-16K-V1) a) axial direction and b) azimuthal direction**

The domain size of at least  $8\pi\delta$  (corresponding to  $2\pi D_h$ ) given by Saha et al. (Saha, 2011) for convergence of higher order temperature fluctuations in fluids with  $Pr=0.025$  in pipe flow is not applicable for sodium with  $Pr=0.004$  in concentric annulus. We observe that computational domain with length  $7.5D_h$  (more than  $8\pi\delta$ ) in axial direction and  $\pi/2$  in azimuthal direction is sufficient to capture the turbulent velocity structures. The auto-correlation of temperature fluctuations does not decay to zero for axial height of  $7.5D_h$  and are far from zero at mid-height of  $3.25D_h$  shown in Figure 3.5a. In the same figure we can see that auto-correlation of temperature fluctuations decays to a small value around zero at  $12.5D_h$  and  $25D_h$  (Figure 3.5a). Thus a much longer domain in axial direction is required for sodium. This is due to the difference in the Prandtl number for air and sodium. The low Prandtl number of sodium leads to larger thermal structures as compared to the size of

velocity structures. Thus, the computational domain has to be large enough to capture these large thermal structures in sodium. In air, with Prandtl number of 0.7, the velocity and thermal structures are of the same size and they are smaller than that of thermal structures in sodium so a smaller computational domain is required.

Thus, the size of the computational domain for sodium is determined by thermal field i.e. it should be long enough to capture the largest thermal structures and size of the mesh is determined by the velocity field as the mesh size has to be small enough to capture the smallest length scale of the eddies (Kolmogorov scale,  $\eta$ ). This imposes a challenge to have number of mesh cells within the range that can be solved in reasonable time with the currently available powerful computers. Therefore, the refinement of mesh in z direction,  $\Delta z_1^+$  for the DNS of sodium (Na-16K-V1) is much larger than that of air to limit the number of mesh cells. Similar behavior is observed for the domain size in azimuthal direction. The auto-correlation for temperature fluctuations for the domain size  $\pi/2$  does not decay to zero (Figure 3.5b). Currently with axial height of  $25D_h$  and  $\pi/2$  domain size the number of mesh cells already around 8.5 million. The increase of domain in azimuthal direction to  $\pi$  and  $2\pi$  will need much larger no of mesh cells of about 17 million and 34 respectively. This is too heavy to run sequentially on any computer. This could be possible only with the parallelization of the DNS code and not feasible currently.

Therefore, the Reynolds number of the calculation with sodium was reduced to 8900 with domain  $2\pi$  in azimuthal direction represented by Na-8.9K-V2. The increase in domain size was compensated by decrease in required grid resolution at low Reynolds number. Figure 3.6b shows that the auto-correlation for only temperature fluctuations in azimuthal direction goes to zero for domain size  $2\pi$ . Another important point to mention here is that with domain  $2\pi$  the axial length required to have thermal structures is now reduced as seen from Figure 3.6a. We know that auto-correlation in axial direction doesn't decay to zero for this domain but to a constant negative value (-2 and -4 for inner and outer cylinder, respectively). However, comparing the two curves Figure 3.5a and Figure 3.6a we see that in the former at height of  $2D_h$  the auto-correlations were positive with a value of 5 whereas in the latter the auto-correlations at this height are zero. Implying that the sufficiently long computational domain in axial direction for sodium thermal structures will be more than  $7.5D_h$  but less than  $25D_h$ . There are two possible explanations for this behavior-

- 1) It is possible that in the DNS calculation of sodium (Na-16K-V1) with domain size  $\pi/2$  in azimuthal direction, the insufficient domain in azimuthal direction forced the

thermal structures to be much more elongated in axial direction. This leads to have a domain size of  $25D_h$  in axial direction so that the auto-correlation falls off to zero. However, with domain size  $2\pi$  in azimuthal direction this phenomenon is not observed as the azimuthal direction is sufficiently large and doesn't induce any elongation of the thermal structures. This reduces the axial domain size to around  $7.5D_h$  with auto-correlations for temperature fluctuations going to zero.

- 2) Secondly this can also be an effect of Reynolds number on the size of thermal structures. In the open literature it is seen that the effect of Reynolds number on the thermal statistics is much stronger for fluids with Prandtl number around 0.025 and almost negligible for fluids with  $Pr \geq 0.2$  (Kawamura 1999; Abe, 2004). Therefore the effect of Reynolds number on the thermal field for the fluid with Prandtl number of 0.004 will be even more predominant than at Prandtl number equal to 0.025. Thus probably the size of thermal structures in DNS calculation of sodium at Reynolds number 16000 represented by Na-16K-V1 are much larger than that in DNS calculation of sodium at Reynolds number 8900 represented by Na-8.9K-V2.

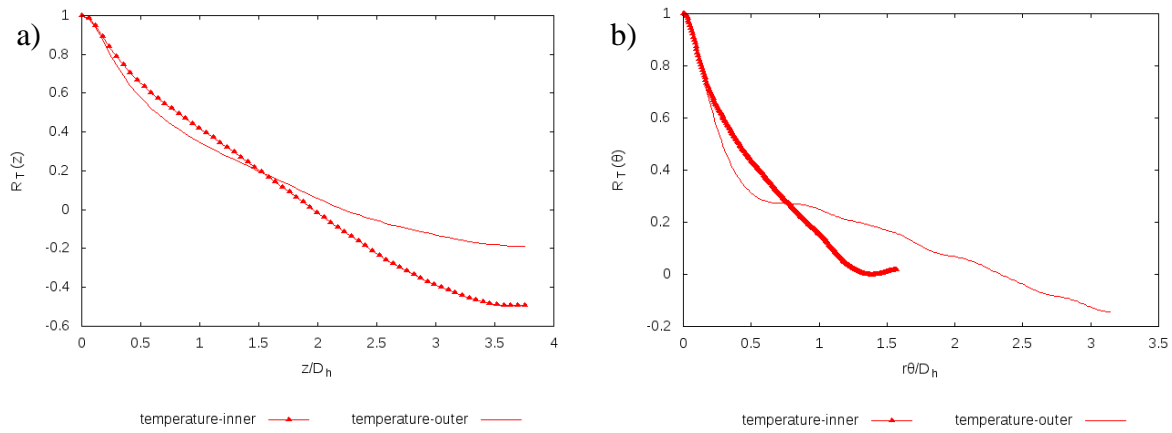


**Figure 3.6-Auto-correlation for fluctuations in temperature in sodium (Na-8.9K-V2) a) axial direction and b) azimuthal direction**

In order to confirm which of the aforementioned arguments is correct another DNS calculation with azimuthal domain of  $2\pi$  and Reynolds number 16000 is necessary. However with the high computational cost (in terms of time) this calculation has not been performed in the restricted time of the thesis.

### 3.6 Validation with DNS of air (Pr-0.7)

Before presenting the results of DNS calculation for low Prandtl number fluids it is important to ascertain the reliability and accuracy of the used numerical procedure by comparing the results to the DNS data of fluid flow and heat transfer in the publication Chung, 2002 and Chung, 2003 respectively. The mean flow and thermal properties are listed in Table 3.4 and compared with Chung et al.

In the simulation the Reynolds number  $Re_{Dh}$  (based on bulk velocity  $u_b$  and hydraulic diameter  $D_h$ ) is fixed to 8900 same as that of Chung et al. The friction Reynolds number based on friction velocity are comparable to that obtained by Chung et al. with slight under prediction for simulation AIR-V2. The skin friction coefficient  $C_f$  of the inner wall is higher than that of the outer wall due to the curvature effect. The value of  $C_f$  according to empirical relation of Nouri et al. (Nouri, 1993) is given below:

$$C_f = 0.36 Re^{-0.39} \quad (3.15)$$

This relation gives a value of 0.01038 for Reynolds number 8900. Chung et al. (Chung, 2002) obtained a value of 0.0088 for average skin friction coefficient  $C_f$  that is defined as follows:

$$C_f = \frac{R_{int}}{R_{int} + R_{ext}} C_{f-int} + \frac{R_{ext}}{R_{int} + R_{ext}} C_{f-ext} \quad (3.16)$$

The value of  $C_f$  in our simulation is 0.00867 and 0.00803 for DNS V1 and AIR-V2 respectively. The value is smaller than that of Chung et al. and Nouri, 1993. The friction velocity obtained from simulation AIR-V1 is same as Chung, 2003 and that for AIR-V2 is slightly under predicted.

The non-dimensional pressure gradient, denoted as  $K_p$ , is defined as (Patel, 1965)

$$K_p = \frac{\nu}{u_\tau^3} \frac{dp}{dz} \quad (3.17)$$

Where  $dp/dz$  is the pressure gradient normalized by density of the fluid and it is equivalent to the momentum source term,  $f_z$  in the axial direction. In the simulation by Chung, 2002 only hydraulic calculation was performed and so the axial length ( $L_z$ ) is  $18\delta$  whereas in Chung, 2003 and our simulation thermal hydraulic calculation is performed with longer domain that has axial length of  $30\delta$ . Therefore in, order to compare the non-dimensional pressure drop from our simulation with Chung, 2002 the normalization factor of  $L_z$  in terms of  $\delta$  has been used i.e. the results of Chung, 2002 has been normalized with 18 and our simulation results have been normalized with 30. With this normalization and comparing our results to that of



Chung et al. we see that non-dimensional pressure for inner wall is slightly under predicted in AIR-V1 with respect to Chung, 2002 whereas slightly over predicted in AIR-V2. However, the difference is not very large. The friction temperature is almost the same. The Nusselt number is however slightly over predicted in the two versions of the DNS code.

### 3.6.1 Mean velocity

The mean velocity field  $U$  can be decomposed in to three components- radial, azimuthal and axial represented by  $u$ ,  $v$  and  $w$  respectively. Figure 3.7 shows non-dimensional mean axial velocity ( $w^+$ ) profiles versus distance from wall in wall units ( $y^+$ ) in logarithmic scale for air ( $Pr=0.7$ ) with two versions of the DNS code. The time averaged axial velocity represented by  $w$  is normalized by friction velocity for inner and outer wall,  $u_{\tau-int}$  and  $u_{\tau-ext}$  respectively to give  $w^+$ . The distance normal to the wall in dimensionless units,  $y^+$  is defined for the inner and outer wall as follows:

$$y^+ = (r - R_{int}) \frac{u_{\tau-int}}{\nu} \quad \text{inner wall} \quad (3.18)$$

$$y^+ = (R_{ext} - r) \frac{u_{\tau-ext}}{\nu} \quad \text{outer wall} \quad (3.19)$$

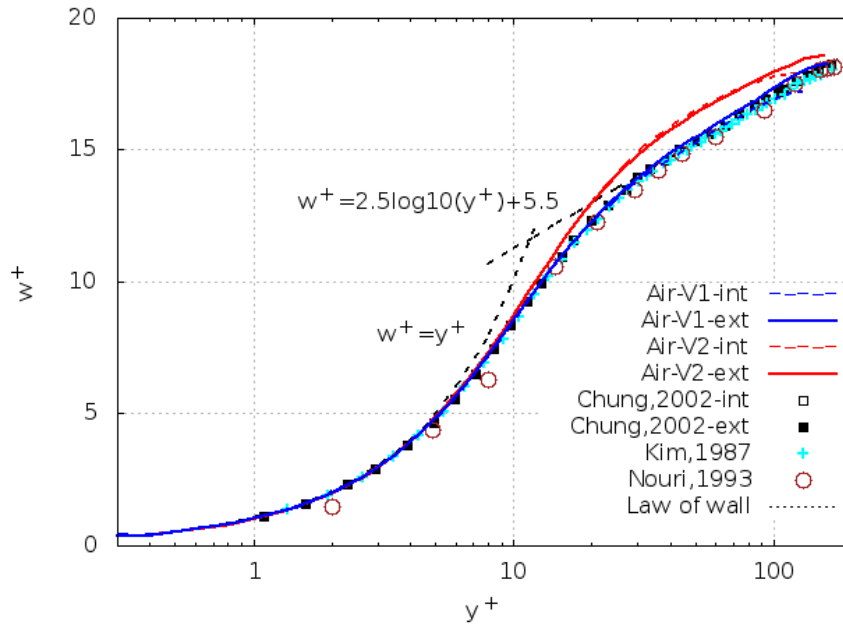


Figure 3.7-Mean velocity profile normalized by the friction velocity at each wall

The predicted profile for AIR-V1 simulation coincides with the numerical data from Chung et al. (2002). The viscous sub-layer and buffer layer are well resolved in present DNS. It follows the universal profile for velocity showing viscous sub-layer that follows linear law of velocity profile at  $y^+ < 5$  and logarithmic region at  $y^+ > 30$  following the log law  $u_z^+ = 2.5 \log(y^+) + 5.5$ . The difference in the velocity profile at inner and outer layer is almost negligible and a slight discrepancy exists in logarithmic region at  $y^+ \sim 100$ . This deviation depends on the radius of curvature and it becomes more dominant if radius ratio,  $R^*$ , is decreased to 0.1 (Chung, 2002). For radius ratio of 0.5, the mean velocity distribution is almost similar to that of flow in rectangular channel as results of Kim et al., 1987 completely coincides with the profile at outer wall.

The agreement with the experimental data of Nouri et al. (1993) is satisfactory with slight deviation in the center region at  $y^+ \sim 10$ . This difference also exists in the results from Chung et al. and they mentioned that the measured profiles in radial direction does not yield a value of unity while that of the numerical profiles shows 1.0 (Azouz, 1998).

The result of AIR-V2 simulation coincides with that of Chung et al. up till  $y^+$  around 10 and over predicts for  $y^+ > 30$ . The lower mesh resolution in the axial direction (Table 3.2) can probably lead to this result. But a test was done with higher axial refinement and we found the same difference in the velocity profile with respect to Chung et al. does not improve. Therefore the difference in velocity field is due to another reason that can be the momentum source term or modified numerical scheme.

### **3.6.2 Root-mean-square velocity fluctuations and Reynolds shear stresses**

The root mean square (r.m.s) of velocity fluctuations normalized by friction velocity are shown in figure 3.8 for simulation AIR-V1 and AIR-V2 along with the results of Chung et al. (2002). We observe that the fluctuations on inner wall are always smaller than fluctuations on outer wall. This is because of the transverse curvature effect. Since the surface area of the inner wall is smaller than that of the outer wall, the inner wall supplies less turbulent kinetic energy than the outer wall to the same volume of flow. This is the effect of curvature of the wall. The effect is stronger if radius ratio is smaller and as the radius ratio is increased the profile at inner and outer wall becomes similar and finally approach to the case of channel flow. The turbulent flow in channel is limiting case of annular cylinder when the radius of the cylinder tends to infinity.

The predicted velocity fluctuations in AIR-V1 simulation shows good agreement with the simulation of Chung et al. (2002) for radial direction (Figure 3.8a) and azimuthal direction (Figure 3.8b). However, the predicted fluctuations in axial (Figure 3.8c) are slightly over predicted at the peak but the position of the peak ( $y^+ \sim 15$ ) is well determined by the current DNS calculation. Overall agreement between present predictions by AIR-V1 and those obtained by Chung et al. is satisfactory. In AIR-V2 simulation the fluctuations in radial and azimuthal directions are under predicted with respect to Chung et al. (2002). However, they show good agreement in the center of the domain at  $y^+ \sim 100$ . The fluctuations in axial direction are in good agreement until  $y^+ \sim 10$  but the peak value is over predicted.

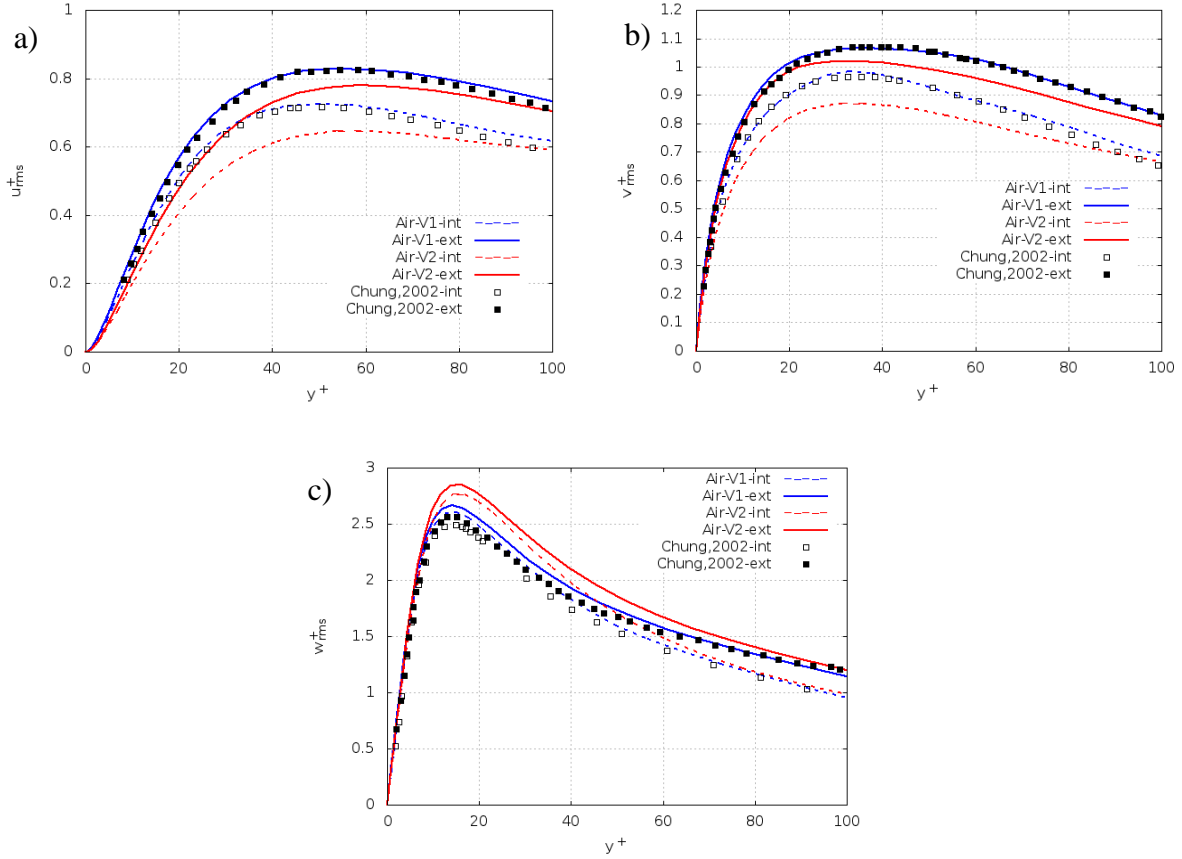


**Figure 3.8-Root mean square velocity fluctuations (a) Wall- normal (radial) velocity, (b) Azimuthal velocity, (c) Axial velocity**

The Reynolds shear stress ( $-w'u'$ ) is shown in Figure 3.9. It compares the position of maximum velocity scaled by bulk velocity (Figure 3.9a) and the position of zero total shear stress (Figure 3.9b). The turbulent shear stress at the wall is zero because they are stationary. The Reynolds shear stress is asymmetric like the velocity profile. The maximum of the velocity and position of zero total shear stress is closer to inner wall at position  $0.89\delta$  and  $0.88\delta$ . The result of AIR-V1 and AIR-V2 agree well with the findings of Chung et al.

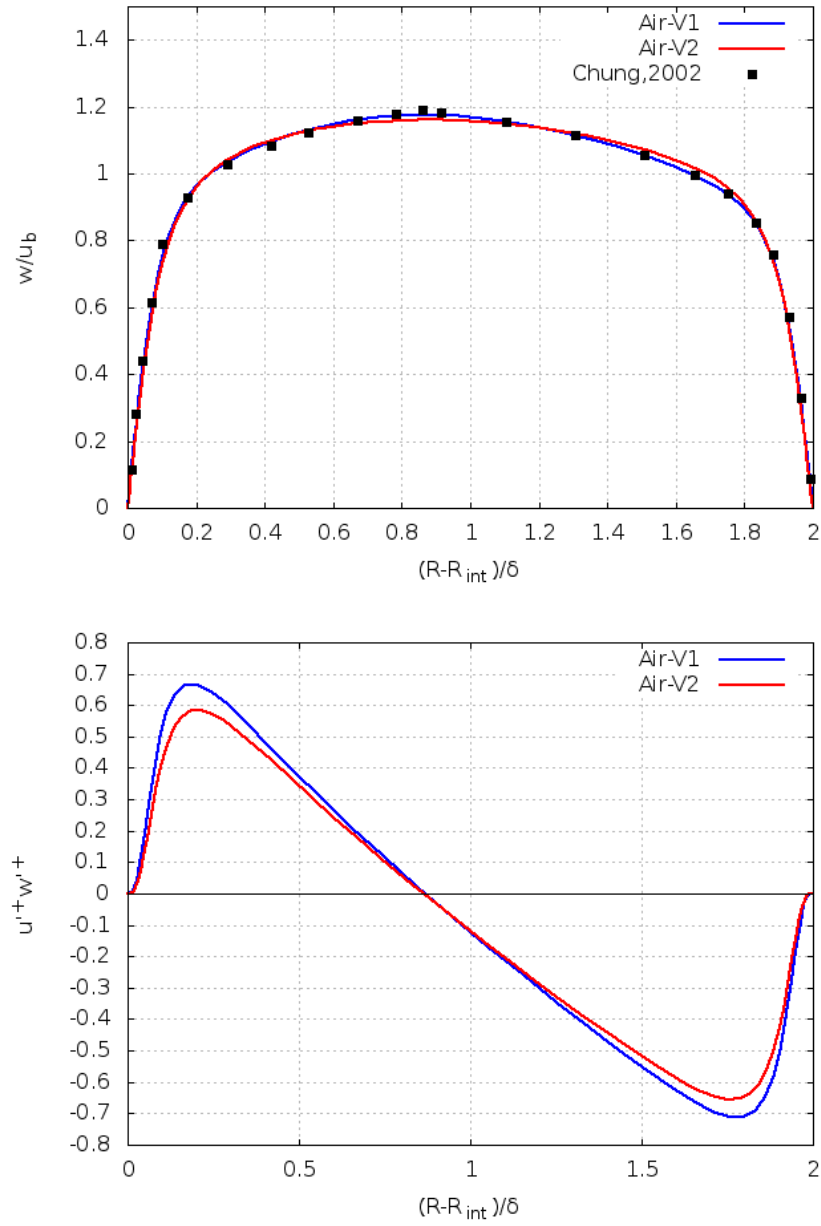
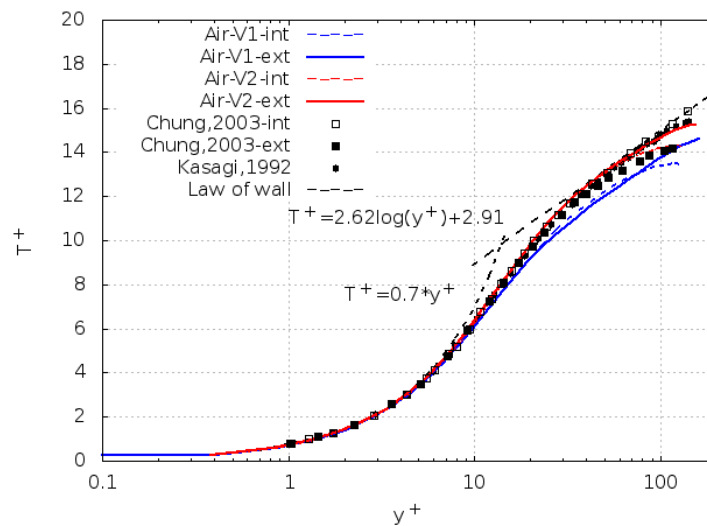


Figure 3.9-Position of a) maximum velocity and b) zero total shear stress

### 3.6.3 Mean temperature

Figure 3.10 depicts the semi-log plot of mean temperature distributions non-dimensionalized by the friction temperature at each wall versus the distance to the inner or outer annulus wall in wall units. It shows that the DNS results for air are in good agreement with Chung et al. (Chung, 2003). The thermal resistance is mainly concentrated in the conductive sub-layer and the thickness of conductive sub-layer is similar to viscous sub-layer (extending up to  $y^+ \sim 5$ ). Beyond the conductive sub-layer there is a rapid transport of heat in the logarithmic region. The results for our simulations AIR-V1 and AIR-V2 are compared with the results from Chung et al., Kasagi et al. (Kasagi, 1992). An excellent agreement exists between AIR-V2 and Chung, 2003. This shows the coarse mesh refinement in axial direction does not affect the mean temperature. The profile at outer wall is similar to the profile obtained by Kasagi et al. for channel flow. The effect of curvature is seen in the logarithmic zone at  $y^+ \sim 70$  where the profiles of inner wall are smaller than that of outer wall. The profile of AIR-V1 simulation is similar to Chung et al., 2003 except that the logarithmic zone is slightly under defined. However, the slope of logarithmic zone is same as of Chung, 2003. This difference is attributed to the implementation of temperature source term in the version 1 that is not as accurate as in version 2. However, the comparison shows that the results are satisfactory with slight difference in logarithmic region.



**Figure 3.10-Mean temperature distributions**

### 3.6.4 Root-mean-square temperature fluctuations and turbulent heat flux

The r.m.s. of temperature fluctuations ( $T_{rms}$ ) normalized by friction temperature of each wall is compared with the results from Chung et al. calculation in Figure 3.11. The value of  $T_{rms}$  at wall is non-zero due to iso-flux boundary condition. Similarly to velocity fluctuations, the intensity of temperature fluctuations at outer wall is larger than that at inner wall due to curvature effects. The temperature fluctuation at the wall has a constant value ranging from 2.2 to 2.4. These values are independent of the Reynolds number when iso-flux boundary condition is applied at the walls (Chung, 2003). The profile of temperature fluctuations from the two simulations- AIR-V1 and AIR-V2 are almost similar. The profile at the inner wall shows slight variation with Chung et al. near the wall up till  $y^+ \sim 14$  and beyond the two results show good agreement. The temperature fluctuation at outer wall is over predicted than Chung et al. up till  $y^+ \sim 10$  and beyond this the fluctuations are under predicted with respect to Chung et al. and coincides with the results of Tiselj, 2001 for channel flow at  $y^+ > 14$ . The differences with respect to Chung et al. may be due to different grid size in radial direction. We are slightly less refined near the wall than Chung et al. but on the contrary the mesh refinement in the center of the domain is higher than Chung et al. as the number of points in the radial direction are kept same as that of Chung et al.

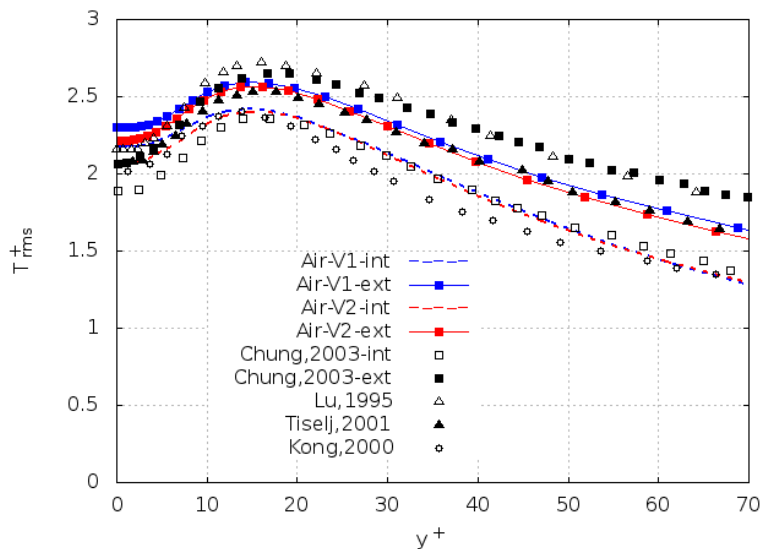
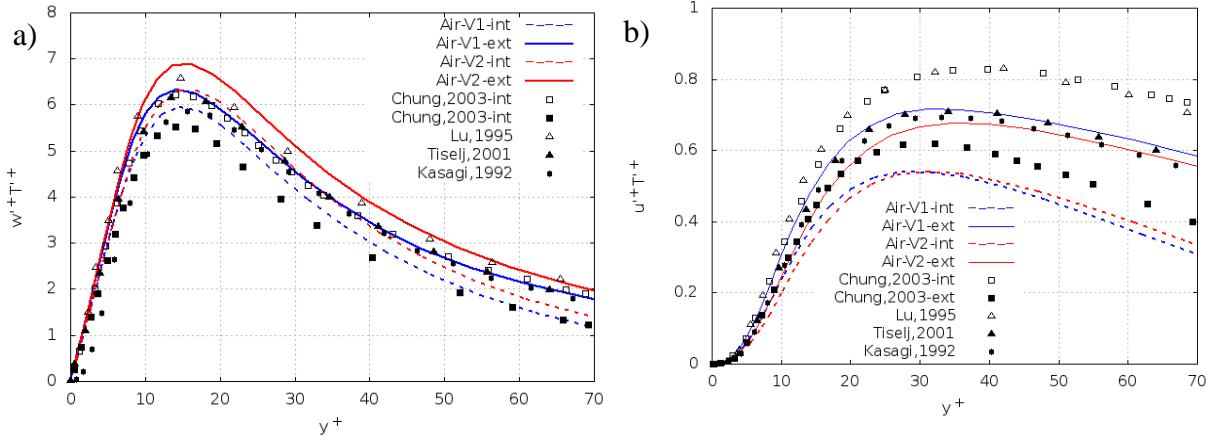


Figure 3.11-Root mean square temperature fluctuations

The axial and wall normal turbulent heat fluxes normalized by the friction velocity and friction temperature are displayed in Figure 3.12. The turbulent heat fluxes near the outer wall are larger than those near the inner one, like the r.m.s. of temperature fluctuations.



**Figure 3.12-Turbulent heat flux (a) Axial direction (b) Wall- normal (radial) direction**

The turbulent heat flux in axial direction for outer wall from AIR-V1 simulation is in good agreement with the Chung et al. simulation. The profile from AIR-V2 is slightly higher than that of AIR-V1. This may be due to over prediction of axial velocity fluctuations. The turbulent heat flux at inner wall is over predicted than Chung et al. for the two simulations. The position of peak turbulent heat flux in axial direction at  $y^+ \sim 14$  is more or less correctly predicted by the two simulations.

The wall normal turbulent heat flux from the two DNS simulations is under predicted with respect to Chung et al. The profile at the outer wall agrees fairly well the results from Tiselj, 2001 and Kasagi, 1992 with slight discrepancy at the  $y^+ \sim 20 - 30$ .

Figure 3.13 depicts the wall normal turbulent heat flux and the total heat flux. The distributions of wall-normal heat flux and total heat flux are asymmetric and curvilinear like total shear stress. This is the curvature effect of the cylindrical walls and iso-flux boundary conditions. The position of zero wall normal turbulent heat flux is  $0.84\delta$  closer to the inner wall than zero position of total shear stress ( $0.88\delta$ ).



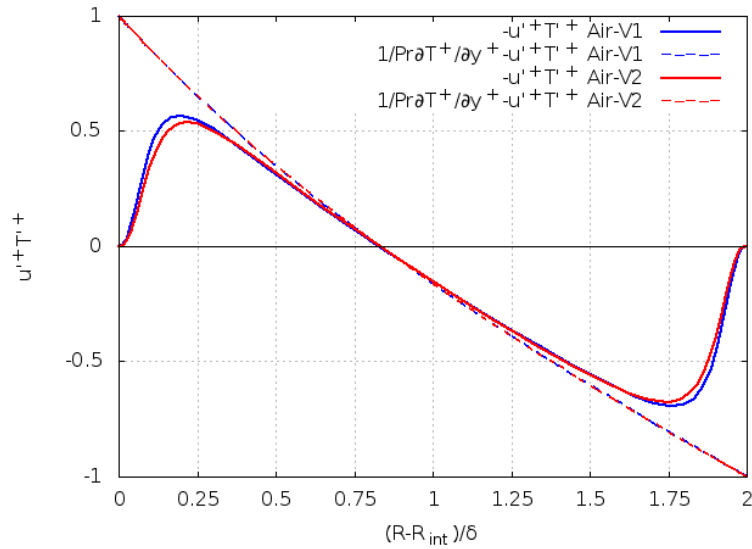


Figure 3.13-Distribution of turbulent wall normal heat flux and total heat flux

### 3.7 Results for DNS of sodium (Pr=0.004)

In this section the results for the DNS calculation of turbulent liquid sodium flow at two Reynolds number 8900 and 16000 are presented. The objective of this section is to understand the heat transfer phenomena at Prandtl number as low as 0.004 that has not yet studied in the literature. This will present the effect of low Prandtl on the thermal statistics and the effect of Reynolds number at this low Prandtl number.

Table 3.5 summarizes the mean parameters for flow and temperature for simulation Na-8.9K-V2 and Na-16K-V1. The friction velocity  $u_\tau$  at inner and outer wall are higher with higher Reynolds number and consequently the friction temperature  $T_\tau$  is lower for high Reynolds number. The skin friction coefficient for Na-8.9K-V2 simulation is similar to that obtained for AIR-V2 simulation for air because the Reynolds number is same. The effect of Prandtl number is seen in the value of friction temperature that is increased from 0.27 for air to 41.46 for sodium at same Reynolds number. The Nusselt number is lower than that obtained for air because for sodium the heat transfer by conduction is much more dominant than in air.

The skin friction coefficient  $C_f$  obtained the relation of Nouri et al. 1993 for Reynolds number equal to 16000 (equation 3.15) is 0.00825. The mean value of  $C_f$  (equation 3.16) obtained for Na-16K-V1 simulation is 0.00877. We see slight over prediction in the value between our simulation and Nouri et al. 1993 contrary to the under predicted value obtained at Reynolds

number 8900 for air. The non-dimensional axial pressure gradient  $K_p$  defined in equation 3.17 normalised by axial length in units of  $\delta$  is more for Na-16K-V1 than Na-8.9K-V2. The higher Reynolds number leads to higher friction loss and higher pressure gradient.

Parameters	Formulae	Na-8.9K-V2	Na-16K-V1
$Re_{Dh}$	$\frac{u_b D_h}{\nu}$	8900	16000
$u_{\tau-int}$	$\sqrt{\frac{1}{\nu} \left( \frac{\partial w}{\partial r} \right)_{int}}$	$2.04 \cdot 10^{-2}$	$5.69 \cdot 10^{-2}$
$u_{\tau-ext}$	$\sqrt{\frac{1}{\nu} \left( \frac{\partial w}{\partial r} \right)_{ext}}$	$1.97 \cdot 10^{-2}$	$5.30 \cdot 10^{-2}$
$Re_{\tau-int}$	$\frac{u_{\tau-int} \delta}{\nu}$	144.65	260
$Re_{\tau-ext}$	$\frac{u_{\tau-ext} \delta}{\nu}$	138.09	242
$C_{f-int}$	$\frac{2\nu u_{\tau-int}^2}{u_b^2}$	$8.45 \cdot 10^{-3}$	$8.45 \cdot 10^{-3}$
$C_{f-ext}$	$\frac{2\nu u_{\tau-ext}^2}{u_b^2}$	$7.70 \cdot 10^{-3}$	$7.34 \cdot 10^{-3}$
$\frac{K_{p-int}}{L_z(\delta)}$	$\frac{\nu}{u_{\tau-int}^3} \frac{f_z}{L_z(\delta)}$	$2.13 \cdot 10^{-4}$	$3.9 \cdot 10^{-5}$
$\frac{K_{p-ext}}{L_z(\delta)}$	$\frac{\nu}{u_{\tau-ext}^3} \frac{f_z}{L_z(\delta)}$	$2.46 \cdot 10^{-4}$	$4.07 \cdot 10^{-5}$
$T_{\tau-int}$	$\frac{q''}{\rho C_p u_{\tau-int}}$	41.46	15.50
$T_{\tau-ext}$	$\frac{q''}{\rho C_p u_{\tau-ext}}$	43.55	16.16
$Nu_{int}$	$\frac{q'' D_h}{\lambda(T_b - T_{int})}$	20.35	17.19
$Nu_{ext}$	$\frac{q'' D_h}{\lambda(T_b - T_{ext})}$	9.50	10.28

**Table 3.4-Mean flow and thermal parameters for the DNS study of sodium at two different Reynolds number**

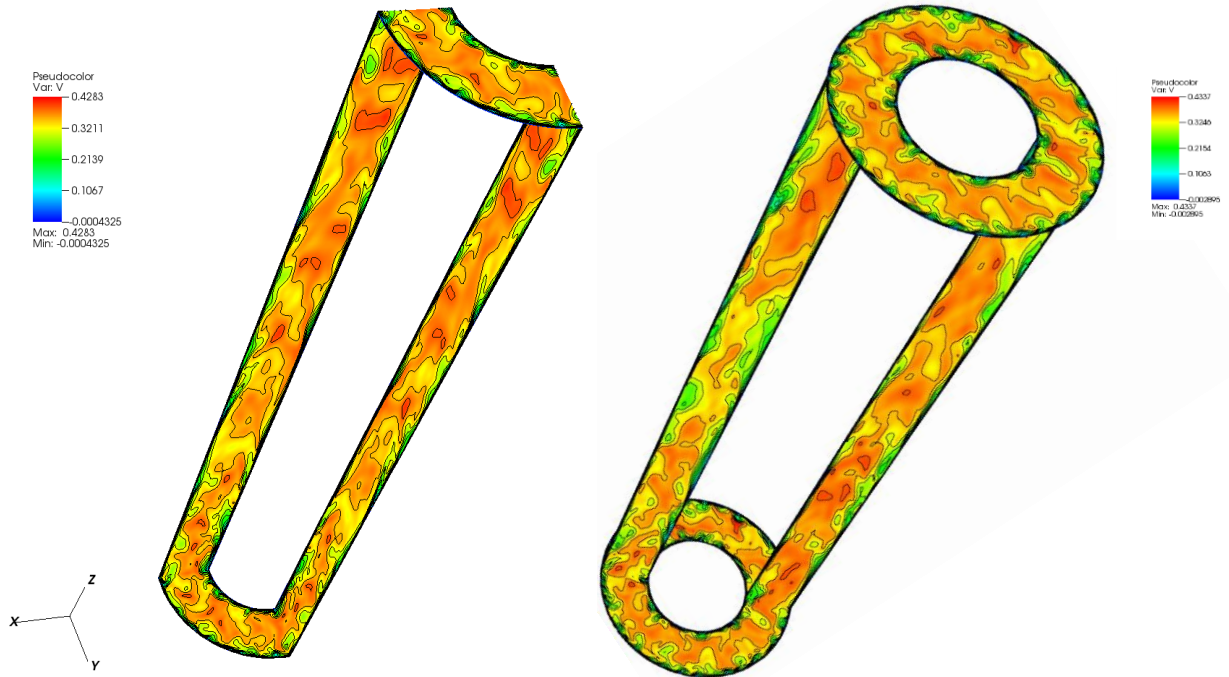
### **3.7.1 Instantaneous flow and temperature fields**

In this section the instantaneous structures for temperature and velocity field are shown for air with  $Pr=0.7$  (AIR-V2 simulation) and liquid sodium with  $Pr=0.004$  at Reynolds number 8900 (Na-8.9K-V2 simulation). Figure 3.14a shows the instantaneous axial velocity for air and sodium. The velocity fields for liquid sodium and air are same as the Reynolds number is same for two calculations. The effect of Prandtl number is not seen in axial velocity because temperature behaves as a passive scalar. Figure 3.14b shows the Iso surface of the  $Q$  criteria for a constant value equal to 10000. The streaky structures aligned in direction of the flow can be seen. The size and intensity of these structures is also a function of only Reynolds number and hence it is same for air and sodium.

However, the temperature field for the two fluids is very different due to the difference in the Prandtl number (Figure 3.15a). In case of air, with  $Pr=0.7$ , the velocity field is similar to temperature field. However, for liquid sodium the Prandtl number is much lower than 1 and thermal diffusivity is very high. Therefore even if the velocity field is turbulent still the temperature field is homogeneous without any strong turbulent motion. Low Prandtl number implies that the thermal conductivity is very high leading to thicker thermal boundary layer as compared to velocity boundary and the dominant mode of heat transfer is conduction rather than convection. This leads to a uniform and homogeneous thermal field even if the velocity field is fully turbulent because the conductive sub-layer is very large. The conductive region becomes thinner with increase in Prandtl number leading to a reduction of the molecular heat flux and an enhancement of the turbulent heat flux normal to the wall. Therefore, the iso-surfaces of temperature for air shown in Figure 3.14b shows turbulent structures in between the walls whereas in case of liquid sodium, concentric cylindrical surfaces due to thermal stratification.

Air,  $Pr=0.7$ Sodium,  $Pr=0.004$ 

## a) Instantaneous Axial velocity



## b) Iso surfaces of Q criteria (10000)

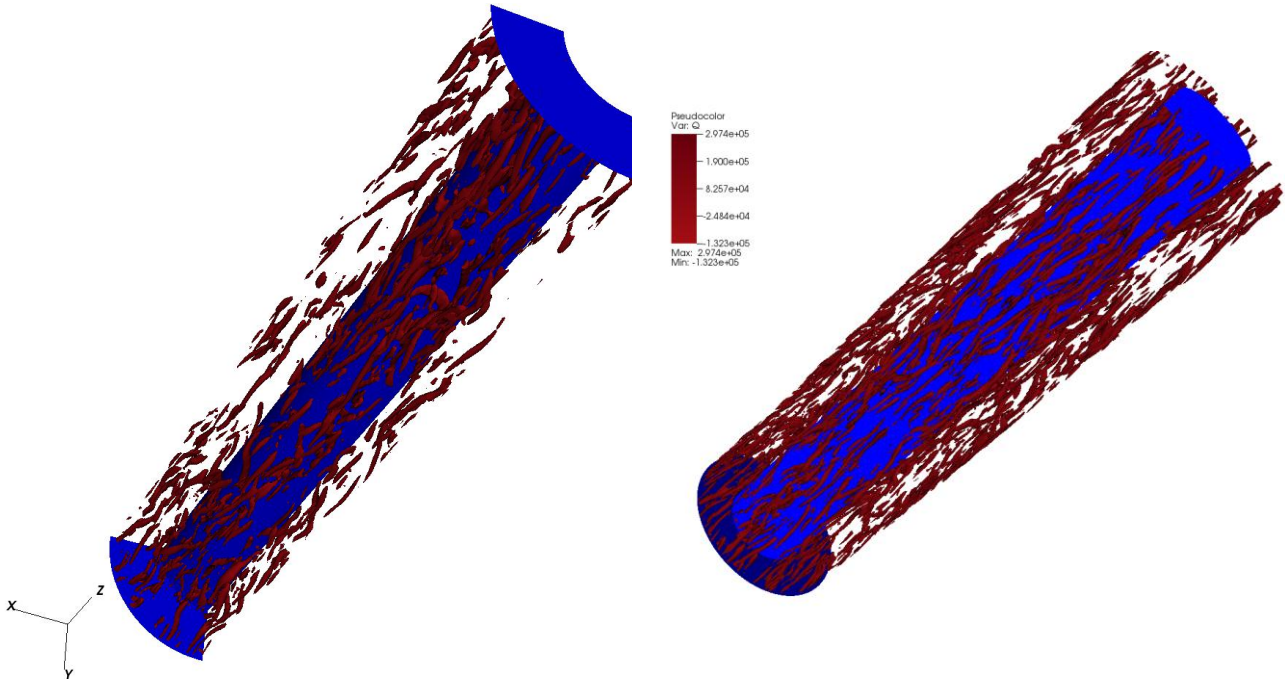
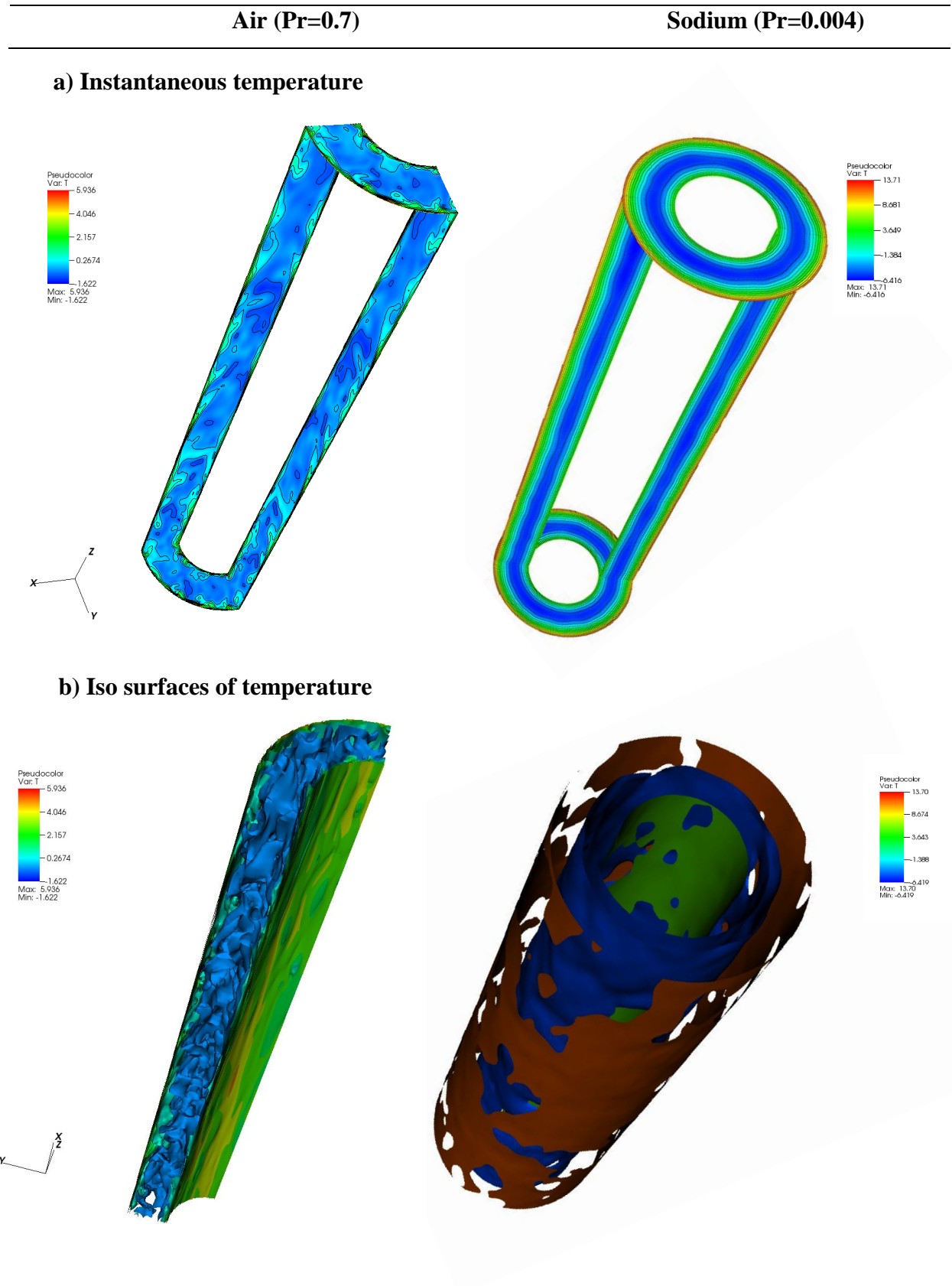


Figure 3.14-a) Instantaneous axial velocity and b) Iso surface of Q criteria from DNS calculation for air (AIR-V2) and sodium (Na-8.9K-V2) at Reynolds number 8900



**Figure 3.15-a) Instantaneous temperature and b) Iso surface of temperature from DNS calculation for air (AIR-V2) and sodium (Na-8.9K-V2) at Reynolds number 8900**

### 3.7.2 Mean Temperature profile

The mean temperature profile is shown in Figure 3.16 where the temperature is plotted with reference to the temperature at the inner wall. The temperature gradient is much steeper near the walls for air as compared to that for sodium. The temperature for air becomes flatter at the middle of the domain with constant value of about -4 whereas for low Prandtl number fluids it continues to decrease to a minimum value at a unique position. This is because the linear conduction sub-layer in the thermal boundary layer for sodium extends to a much larger distance than that for air.

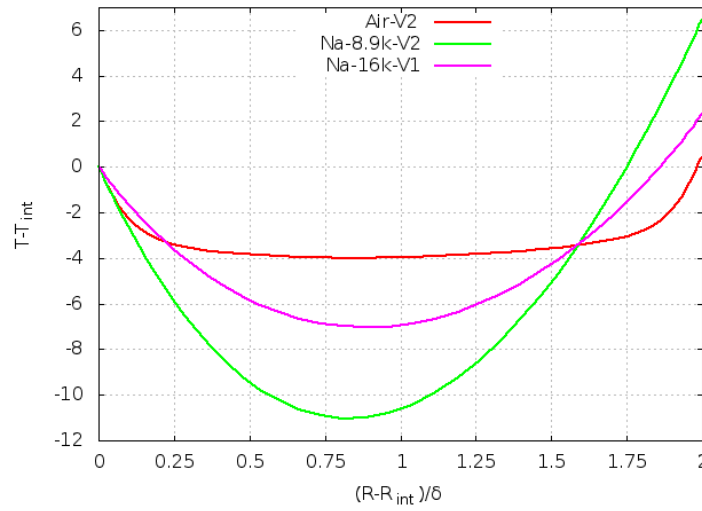


**Figure 3.16-Mean temperature profile for air and sodium at  $Re=8900$  and sodium at  $Re=16000$**

The difference between minimum temperature and temperature at inner wall is more for sodium than that for air. In case of sodium, we observe that with decrease in the Reynolds number, the difference between maximum temperature and minimum temperature also increases. However, the effect of Reynolds number is not present in the mean non-dimensional temperature as the effect of Reynolds number is taken in to account by the normalization factor of friction temperature.

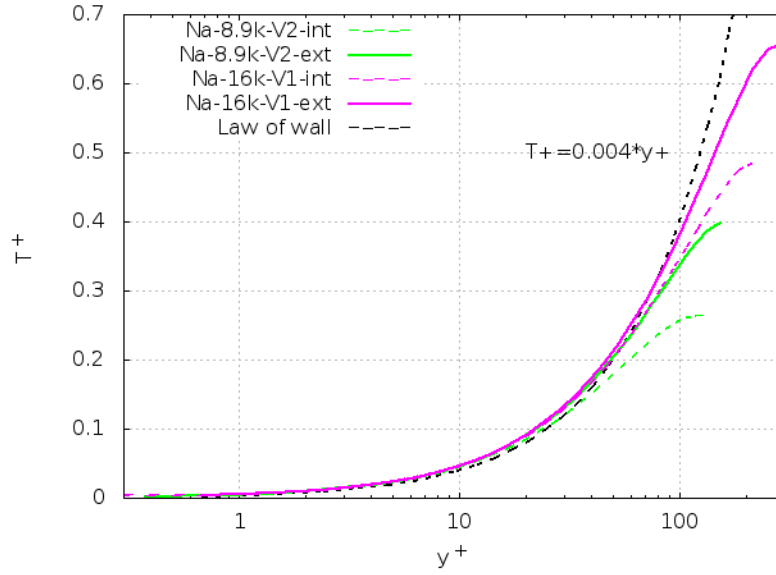


**Figure 3.17-Mean Temperature profile normalized by friction temperature versus  $y^+$**

Figure 3.17 depicts the mean temperature distributions in dimension-less units. The mean temperature is normalized by the friction temperature of each wall and it is plotted against the dimensionless distance to wall denoted by  $y^+$ . We see that the decrease in Prandtl number from 0.7 to 0.004 leads to spread of conductive sub-layer from the wall to the central region. It indicates that molecular heat transfer dominates for low Prandtl number fluids.

The logarithmic part of the temperature profile does not exist for low Prandtl number fluids. Kawamura et al., 1999 showed that the logarithmic region of the temperature can be better distinguished from the wake region with increase in Reynolds number in Prandtl number. In our simulations at Reynolds number of 8900 and 16000 the logarithmic region is not observed. With increase in Reynolds number, the linear zone also extends to a larger distance from wall. At Reynolds number 8900, the linear zone extends until  $y^+ \sim 60$  and at Reynolds number 16000 it extends until  $y^+ \sim 100$ .

### 3.7.3 Root-mean-square of temperature fluctuations

The r.m.s. of temperature fluctuations ( $T_{rms}$ ) are shown in Figure 3.18 for sodium. Figure 3.18a shows the fluctuations of temperature with dimensions and Figure 3.18b depicts the non-dimensional ( $T_{rms}^+$ ) temperature fluctuations normalized by the friction temperature of each wall.

The intensity of the temperature fluctuations at the outer cylinder is larger than that at the inner cylinder due to curvature effects. The r.m.s of temperature fluctuations yield non-zero values at the walls due to the iso-flux boundary conditions. As the Prandtl number is reduced, the position of the peak of r.m.s. of temperature fluctuations ( $T_{rms}$ ) moves away from wall and the magnitude decreases.

At same Reynolds number (equal to 8900), the r.m.s. of temperature fluctuations ( $T_{rms}$ ) at the inner wall are smaller in sodium by a factor of 2 with respect to air. However, the difference in non-dimensional units is much larger as friction temperature takes in to account the effect of high thermal diffusivity of sodium.

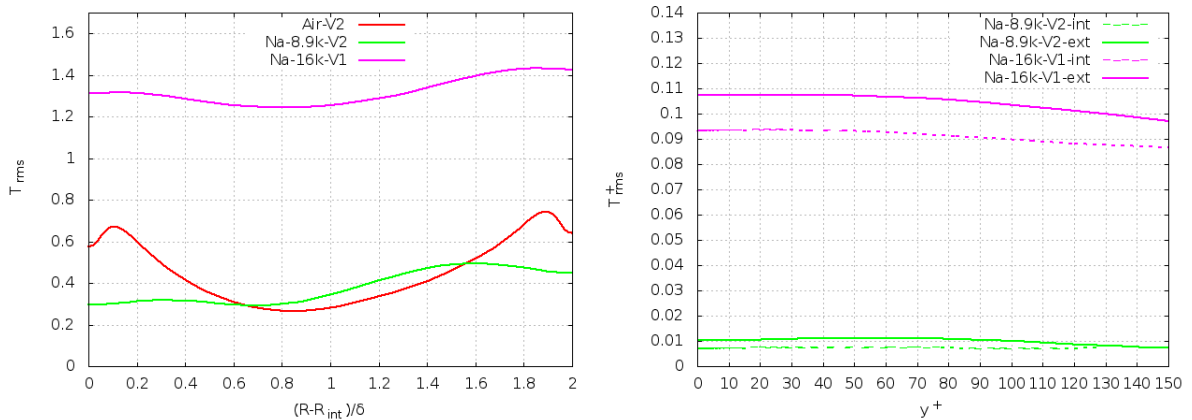


**Figure 3.18- Root mean square temperature fluctuations a) with dimensions for sodium and air and b) non-dimensional normalized by friction temperature versus  $y^+$  for sodium at different Reynolds number**

The r.m.s. of temperature fluctuations depends on the Reynolds number for liquid sodium as the Prandtl number is lower than 0.2 (Kawamura, 1999; Abe 2004). When the Reynolds number is increased from 8900 to 16000 we notice that the r.m.s. temperature fluctuations

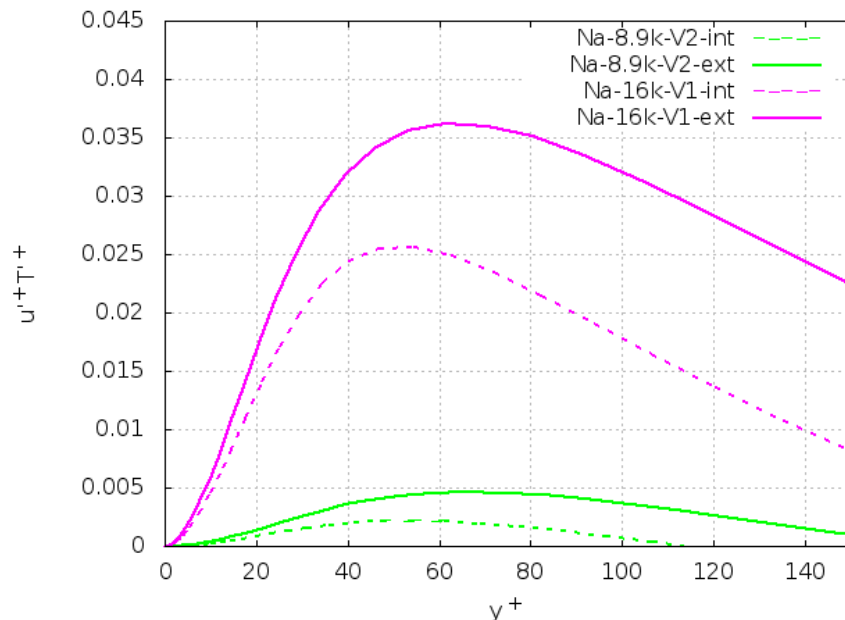


( $T_{rms}$ ) at the wall are increased by a factor of 4.3 (Figure 3.18a) and non-dimensional temperature fluctuations ( $T_{rms}^+$ ) increases by factor 10 (Figure 3.18b).

In the open literature, only two studies are found that study the effect of Reynolds number on the temperature field for low Prandtl number ( $\sim 10^{-2}$ ). The first one is by Kawamura, 1999 and second one is by Abe, 2004. They studied LBE flow in rectangular channel with mixed boundary conditions so the temperature fluctuation at wall is always zero irrespective of the Reynolds number. To the best of our knowledge, this is the first study in annular cylinder where the effect of Reynolds number has been studied on the temperature fluctuations at the wall with iso-flux boundary conditions that too at a Prandtl number of  $\sim 10^{-3}$ .

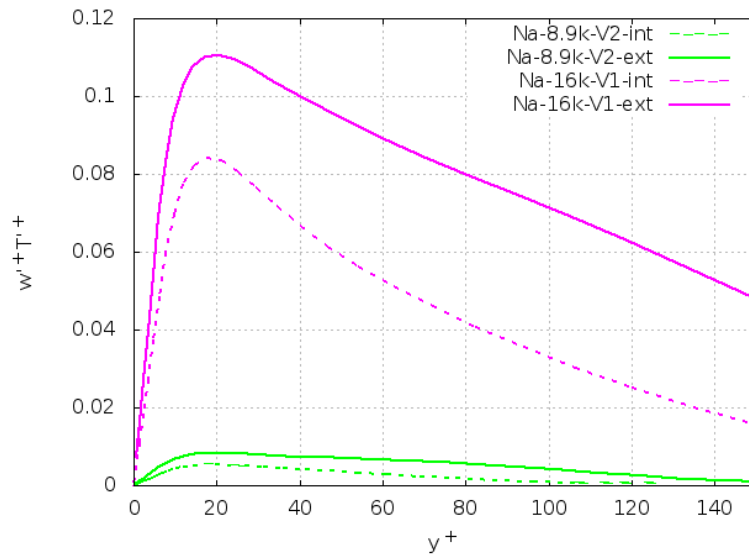
### 3.7.4 Turbulent heat flux

Figure 3.19 shows the wall-normal turbulent heat flux normalized by friction velocity and friction temperature. As the Prandtl number is reduced the conductive sub-layer increases and the turbulent wall –normal heat flux decreases and moves away from to inner and outer wall surfaces. The results for inner walls are smaller than that of outer walls like the r.m.s. distribution of fluctuating temperature in Figure 3.18. The effect of Reynolds number on turbulent heat flux is strong. As the Reynolds number is increased the wall-normal turbulent heat flux also increases.



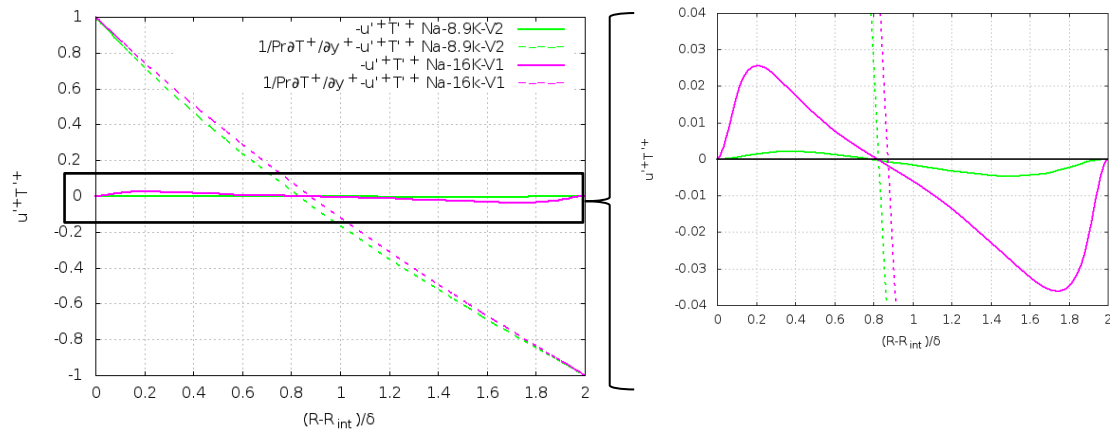
**Figure 3.19- Wall-normal turbulent heat flux normalized by friction temperature and friction velocity versus  $y^+$  for sodium at different Reynolds number**

Figure 3.20 shows the distribution of the axial turbulent heat flux normalized by friction temperature and friction velocity. It shows similar behavior to wall normal turbulent heat flux with decrease in Prandtl number. The position of the peak moves slightly away from the wall with decrease in Prandtl number. The position of the peak for air is at  $y^+ \sim 15$  whereas in case of sodium the position of the peak is at  $y^+ \sim 20$ . The position of the peak for sodium is however independent of the Reynolds number. Only the intensity of the axial turbulent heat flux is reduced with lowering of Reynolds number by a factor of about 10.



**Figure 3.20- Axial turbulent heat flux normalized by friction temperature and friction velocity versus  $y^+$  for sodium at different Reynolds number**

Figure 3.21 illustrates the distribution of wall normal (radial) turbulent heat flux normalized by friction velocity and friction temperature for sodium at two Reynolds number 16000 and 8900. The wall normal turbulent heat flux is asymmetric due to more energy from outer wall with more surface area. The position of zero wall normal heat flux is at  $0.82\delta$  and  $0.84\delta$  and it is close to inner surface. The wall normal turbulent heat flux increases strongly with increase in Reynolds number. The position of zero turbulent shear stress is slightly different due to slight difference in radius ratio for the two cases.



**Figure 3.21-Distribution of turbulent wall normal heat flux and total heat flux (a) with zoom to see the effect of Reynolds number (b)**

### 3.7.5 Energy and temperature spectra

The one dimensional axial energy spectrum is defined as Fourier transform of the corresponding self-correlation functions evaluated at  $y^+=5$  where the turbulent kinetic energy is maximum. The spectrum is normalized by their mean square values. The energy spectra in axial direction indicates an adequate space resolution of the present simulations, since the spectra drop by several orders of magnitude (Figure 3.22). The energy spectra show a decrease in energy density when the wave number is increased. There has been no accumulation of energy in the domain.

The temperature spectrum normalized by mean square values is nearly same to axial energy spectra for air with  $Pr=0.7$ . In case of sodium with  $Pr=0.004$ , the energy spectra still drop several orders of magnitude and thus the resolution is adequate. In the axial direction, the spectra increase significantly with increase in Prandtl number at intermediate and high wave numbers. This shows that the contribution of small and intermediate scales to mean square value decreases in the near wall region with decrease in Prandtl number. The small scale structures are also highly damped due to the enhanced conductive effect with the decrease in Prandtl number (Abe, 2004; Redjem-Saad, 2007). This trend can be seen in the instantaneous temperature field presented in Figure 3.15. Therefore the contribution of high wave numbers to the mean square value decreases with decreasing Prandtl number.

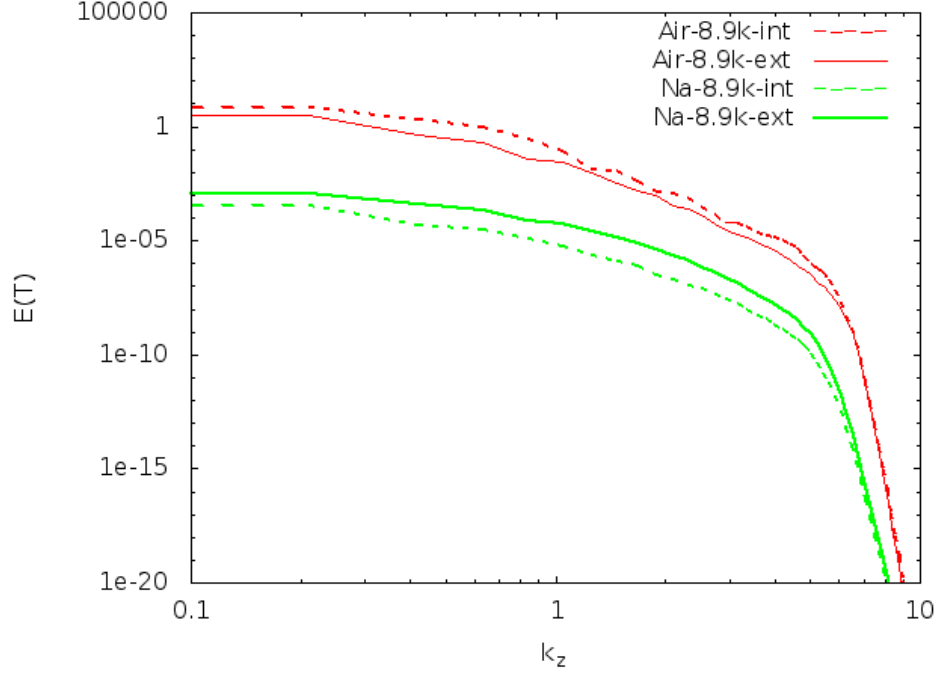


Figure 3.22-Energy spectra in axial wave number for air and sodium

## 3.8 Asymptotic behavior

In this section the effect of Prandtl number on the asymptotic behavior of the turbulent thermal statistics is studied. The near wall asymptotic behavior of the turbulent thermal statistics is done by expanding the mean and fluctuating quantities by Taylor series (Kong, 2000). Considering the continuity and momentum equations under no-slip conditions the velocity and velocity fluctuations are expressed in following form:

**Non-dimensional axial velocity,  $w^+$ :**

$$w^+ = a_1 y^+ + a_4 y^{+4} + \dots \quad (3.20)$$

**Non-dimensional axial velocity fluctuations,  $w'^+$ :**

$$w'^+ = b_1 y^+ + b_2 y^{+2} + \dots \quad (3.21)$$

**Non-dimensional radial velocity fluctuations,  $u'^+$ :**

$$u'^+ = c_2 y^{+2} + c_3 y^{+3} + \dots \quad (3.22)$$

The Taylor series expansion of thermal field depends on the thermal boundary condition. In case of isothermal boundary condition- the root mean square temperature fluctuations, the turbulent axial and wall-normal fluxes develop as  $y^+$ ,  $y^{+2}$  and  $y^{+3}$  respectively (Kong, 2000).

However, in case of iso-flux boundary condition the behavior is different and is presented below:

$$T^+ = d_0 + d_2 y^{+2} + d_3 y^{+3} + \dots \quad (3.23)$$

The first term in mean temperature expansion and temperature fluctuations is constant independent of  $y^+$ .

$$T'^+ = \text{Pr}(e_0 + e_1 y^+ + e_3 y^{+3} + \dots) \quad (3.24)$$

Note that second order term is absent in temperature fluctuations while it exist in case of iso-thermal condition (Kawamura, 1998; Redjem-Saad, 2007). This gives near wall limiting behavior of the temperature fluctuation as

$$\frac{T'^+}{\text{Pr}} \approx e_0, \quad y^+ \rightarrow 0 \quad (3.25)$$

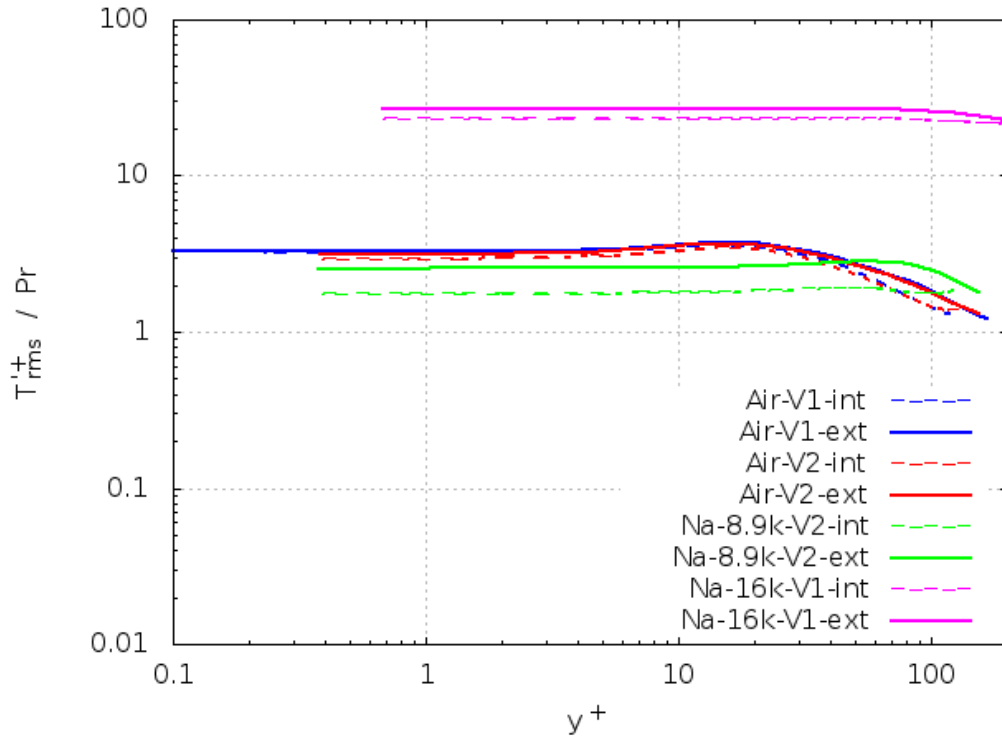


**Figure 3.23-Asymptotic behavior of the temperature fluctuations for air and sodium**

Figure 3.23 displays clearly the asymptotic behavior of the r.m.s of temperature fluctuations when the inner and outer walls are approached. For  $\text{Pr}=0.7$ , the  $T'^+ / \text{Pr}$  is constant up to  $y^+ \approx 3$  near the inner wall and the outer wall which corresponds to the conductive sub-layer's thickness. When Prandtl number is decreased to 0.004 then the conductive sub-layer thickness increases. Hence the quantity  $T'^+ / \text{Pr}$  is constant up to  $y^+ \approx 50$  for inner wall and  $y^+ \approx 30$

for outer wall. The constant  $a_T$  increases from has a strong dependence on Reynolds number at low Prandtl number. The constant  $a_T$  increases from 2 to 25 when Reynolds number is increased from 8900 to 16000.

The asymptotic behavior of turbulent axial heat flux and turbulent wall normal heat flux can be obtained from the expansion of axial velocity fluctuations ( $u'_z$ ) and wall normal velocity fluctuations ( $u'_r$ ). Therefore, using the expansion for axial velocity fluctuations (3.20) and temperature fluctuations (3.23) the asymptotic behavior of the turbulent axial heat flux is given as:

$$w'^+ T'^+ = \text{Pr}(b_1 e_0 y^+ + (b_2 e_0 + b_1 e_1) y^{+2} + \dots) \quad (3.26)$$

This gives

$$\frac{w'^+ T'^+}{\text{Pr}} \approx b_1 e_0 y^+, \quad y^+ \rightarrow 0 \quad (3.27)$$

Figure 3.24 shows the asymptotic behavior of turbulent axial heat fluxes in the vicinity of the both inner and outer wall that varies linearly with  $y^+$  as expected from equation (3.25).

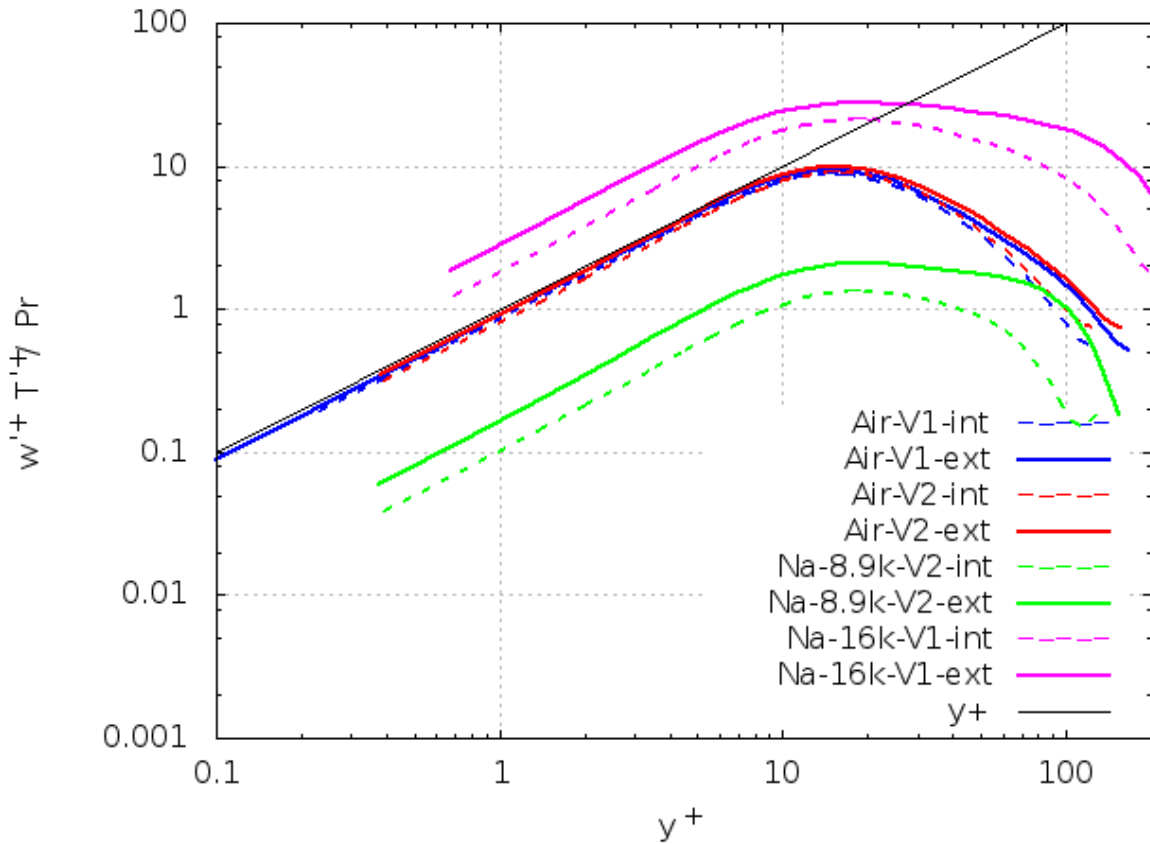


**Figure 3.24-Asymptotic behavior of the turbulent axial heat flux for sodium and air**

Similarly, using the expansion for wall normal velocity (3.21) and temperature fluctuations (3.23) the asymptotic behavior of the turbulent wall normal heat flux is given as:

$$u'^+ T'^+ = \text{Pr}(e_0 c_2 y^{+2} + (c_3 e_0 + c_2 e_1) y^{+3} + \dots) \quad (3.28)$$

Which yields that

$$\frac{u'^+ T'^+}{\text{Pr}} \approx e_0 c_2 y^{+2}, \quad y^+ \rightarrow 0 \quad (3.29)$$

The asymptotic behavior of turbulent wall normal heat flux in Figure 3.25 confirms that it varies as a function of  $y^{+2}$  near the wall.

Ould-Rouiss, 2010 studied the asymptotic behavior for Prandtl number ranging from 0.025 to 7 and found that the coefficients  $b_1 e_0$  and  $e_0 c_2$  are independent of Prandtl number. However, in our case with Prandtl number even one order of magnitude lower than 0.025 the coefficients  $b_1 e_0$  and  $e_0 c_2$  are no more independent of Prandtl number.

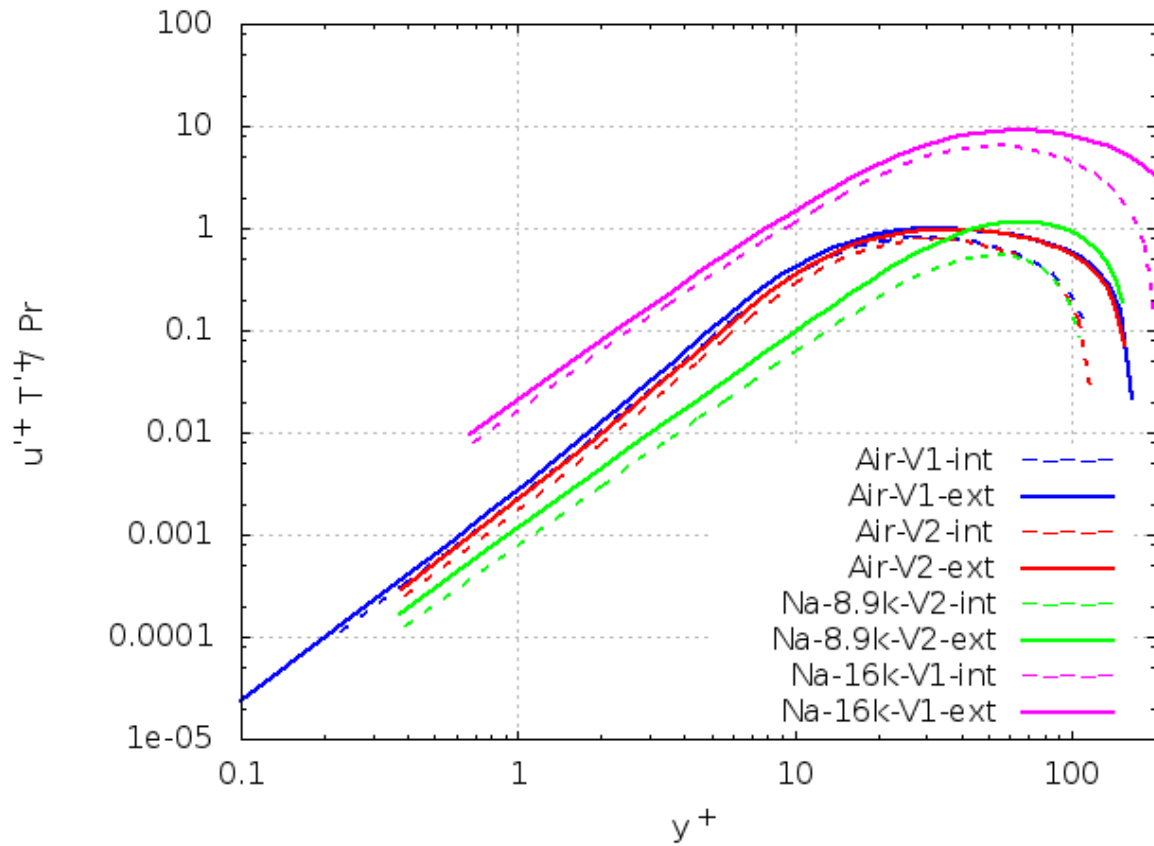


**Figure 3.25- Asymptotic behavior of the turbulent wall normal heat flux for sodium and air**

The near wall behavior of turbulent viscosity and turbulent diffusivity are determined for the iso-flux boundary condition. The turbulent viscosity,  $\nu_t$  is defined as

$$\nu_t = \frac{-u'^+ w'^+}{\partial w^+ / \partial y^+} \quad (3.30)$$

Using the Taylor series expansion for  $w^+$ ,  $u'^+$  and  $w'^+$  from equations 3.20, 3.21 and 3.22 respectively, the near wall expansion of turbulent viscosity is given as

$$\nu_t = -\frac{b_1 c_2}{a_1} y^{+3} + \dots \quad (3.31)$$

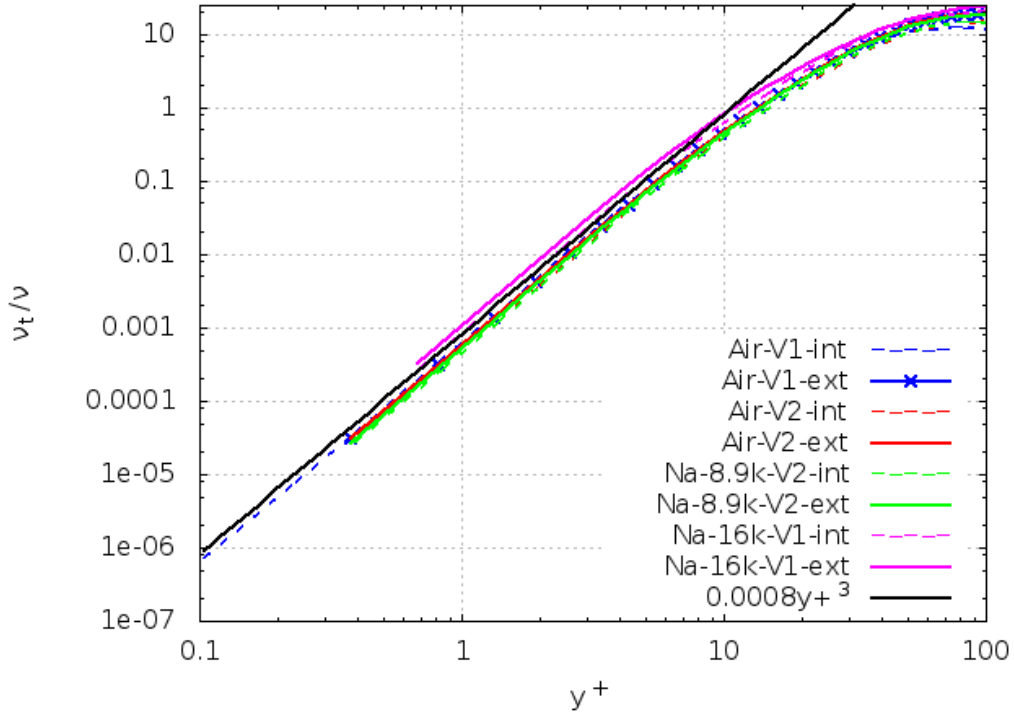


**Figure 3.26-Near-wall behavior of turbulent viscosity**

Figure 3.26 shows that for all the DNS simulations the turbulent viscosity varies as  $y^{+3}$ . It confirms the asymptotic behavior found in the literature.

Similarly, for turbulent thermal diffusivity  $\alpha_t$  is defined as

$$\alpha_t = \frac{-u'^+ T'^+}{\partial T^+ / \partial y^+} \quad (3.32)$$

Using the Taylor series expansion for  $u'^+$ ,  $T^+$  and  $T'^+$  from equations 3.22, 3.23 and 3.24 respectively, the near wall expansion of turbulent thermal diffusivity is given as

$$\alpha_t = -\frac{e_0 c_2}{d_0} y^{+2} + \dots \quad (3.33)$$



This indicates that near the wall when  $y^+ \rightarrow 0$  the turbulent viscosity is proportional to  $y^{+3}$  and turbulent thermal diffusivity is proportional to  $y^{+2}$ . This behavior is predicted well for turbulent viscosity for both air and sodium (Figure 3.27). However, the constant  $\frac{e_0 c_2}{d_0}$  is a function of Prandtl number and Reynolds number. The value of this coefficient changes to 0.025, 0.0008 and 0.02 for air, sodium with  $Re=8900$  and sodium with  $Re=16000$  respectively.

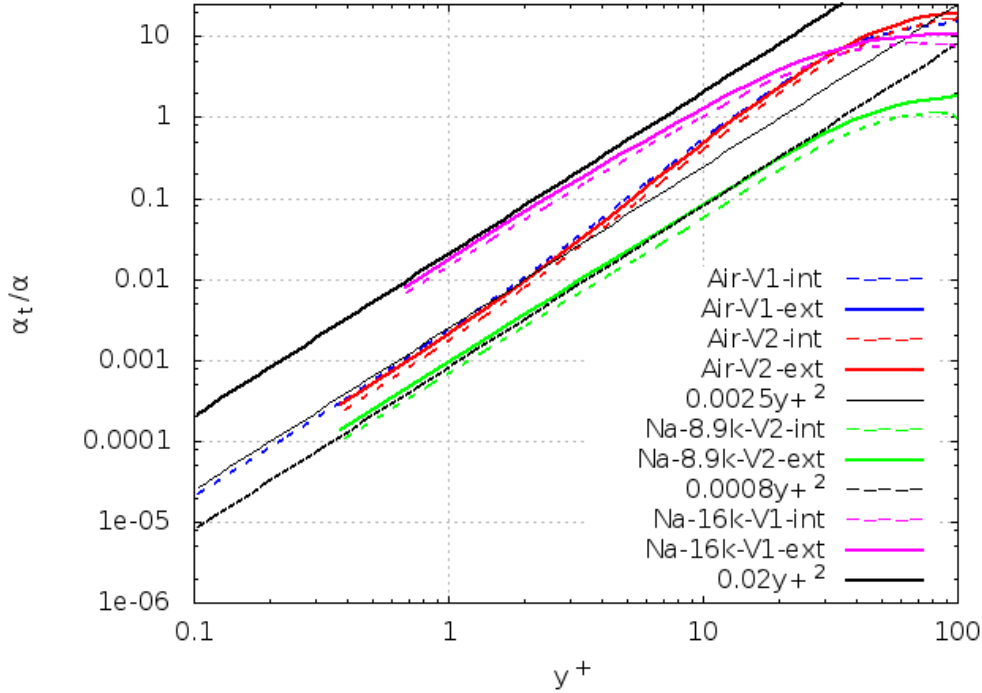
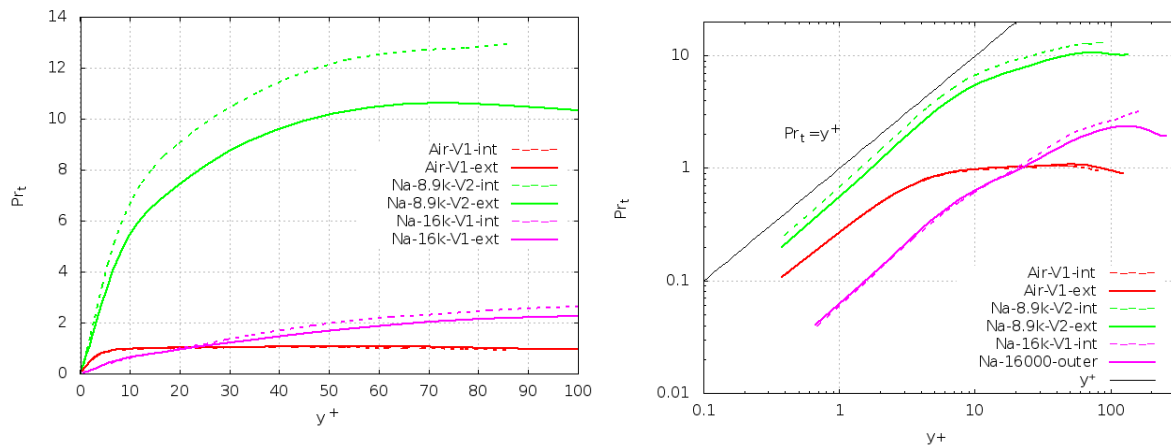


Figure 3.27-Near wall behavior of turbulent thermal diffusivity

### 3.8.1.a Turbulent Prandtl number

We recall the definition of turbulent Prandtl number as ratio of turbulent viscosity and turbulent thermal diffusivity, given as  $Pr_t = \frac{\nu_t}{\alpha_t}$ . It plays an important role in prediction of the near wall heat transfer using turbulence models. Hence, it is a sensitive parameter for the study of peak fluid temperatures (hot-spots). The near wall behavior for the turbulent Prandtl number can be written using equation (3.31) and (3.33) for turbulent viscosity and turbulent thermal diffusivity as shown below

$$Pr_t = \frac{\nu_t}{\alpha_t} = \frac{\frac{b_1 c_2}{a_1} y^{+3}}{\frac{e_0 c_2}{d_0} y^{+2}} + \dots = \frac{b_1 c_2 d_0}{e_0 c_2 a_1} y^+ + \dots \quad (3.34)$$



**Figure 3.28-Turbulent Prandtl number variation near the wall for sodium at different Reynolds number and compared with air as a function of  $y^+$  (a) and log-log scale (b)**

The turbulent Prandtl number varies as a function of  $y^+$  near the wall as shown in Figure 3.28. The effect of Reynolds number on the turbulent Prandtl number can be clearly seen from these figures. The Reynolds number has stronger effect on the turbulent thermal statistics. At low Reynolds number the turbulent heat flux is very small and as a consequence the asymptotic value of turbulent Prandtl number of about 10 is obtained. With increase in Reynolds number the turbulent heat flux increases and the asymptotic value of turbulent Prandtl number decreases to 3.5.

Thus, at low Reynolds number flow of sodium one has to be careful with the value of turbulent Prandtl number. The turbulent Prandtl number given by different correlations presented in Chapter 1 have been determined for LBE and NaK fluids with Prandtl number 0.025. They show strong discrepancy when traced for low Reynolds number and Prandtl number of sodium equal to 0.004. Thus, new correlations and new experiments are envisaged to have turbulent Prandtl number correlation in the lower range of Reynolds number.

### 3.9 LES study for sodium

The objective of this section is to compare the results from an industrial LES calculation with DNS results. The LES method will be used in next chapter to study the thermal hydraulics in sub-assembly of SFR. This comparison with the reference results from the DNS calculation will serve as a validation of the numerical schemes and model parameters used for LES method. Table 3.6 shows the data set for the LES calculation. The LES calculation is performed with the same data set as of the DNS simulation Na-16K-V1 except that the domain in azimuthal direction is  $2\pi$  as the LES code works with cartesian mesh and it will not be possible to reproduce the periodicity in azimuthal direction.

Parameter	Formula	DNS (Na-16K-V1)	LES
$R^*$	$R_{int}/R_{ext}$	0.6	0.6
Pr	$\nu/\alpha$	0.004	0.004
$q^*$	$q''_{ext}/q''_{int}$	1	1
$D_h$ (mm)	$2(R_{ext} - R_{int})$	5.54	5.54
$\delta$ (mm)	$D_h/4$	1.385	1.385
$Re_{D_h}$	$u_b D_h / \nu$	16000	16000
$u_b$ (m/s)		0.8744	0.8744
$\theta$	-	$\pi/2$	$2\pi$
$L_z$	-	$25D_h$	$25D_h$

**Table 3.5-Data set for LES calculation compared with the DNS calculation**

### **3.9.1 Numerical method**

The LES calculation has been performed using thermal-hydraulic code TRIO\_U (Trio\_U, v1.6.8). Table 3.7 summarizes the numerical scheme used for LES calculation. A more detailed description of the numerical schemes can be found in Chapter 2-Numerical methods and tools.

An important point to note is this is not a wall resolved LES but rather an industrial LES calculation where the cells near the wall are not fine enough to capture the wall profiles instead wall functions are used. This is because wall resolved LES calculation that is possible for this simple geometry would not be feasible later on for the complex geometry of the sub-assembly. The small size of the tetrahedral meshes near the wall will reduce the calculation time making the calculation very slow and time consuming. The objective of performing LES calculation is to compare the results of the current LES methodology (numerical schemes) with the obtained DNS results and then use the same numerical scheme for LES calculations of the sub-assembly.

Therefore the wall normal distance of the first cells near the wall in wall units,  $y^+$  is more than 1 and so wall functions have been used for momentum equation. However, for the energy equation the mesh is refined enough to resolve completely the thermal conductive sub-layer near the wall. This is because of the large thermal conductivity of the sodium. Therefore no wall functions have been used for energy equation. The turbulent Prandtl number is set to constant value of 3.5 that has been obtained by DNS calculation (Figure 3.28).

<b>Meshing</b>	Tetrahedrons	At least 12 calculation point between pins
<b>Discretization</b>	Finite Volume Elements	P0/P1 for the pressure P1-non conform for velocity and temperature
<b>Time scheme</b>	Scheme	Semi-implicit
	Solver	3 <sup>rd</sup> order Adams Bashforth scheme
	Facsec	0.5
<b>Momentum transport</b>	Convection	Stabilized centered scheme (Ef_stab with $\alpha=0.2$ )
	Diffusion	2 <sup>nd</sup> order centered scheme
	Wall treatment	Wall law Riechardt
	Turbulence	LES with WALE sub-grid model
	Diffusive time step	$9.23 \cdot 10^{-6}$
	Convective time step	$1.24 \cdot 10^{-5}$
<b>Mass conservation</b>	Incompressible fluid	Pressure projection method: petsc cholesky
<b>Energy equation</b>	Convection of temperature	Ef_stab with alpha 1
	Diffusion of temperature	Centered
	Wall treatment	No wall law
	Treatment of turbulence	Turbulent Prandtl number, $Pr_t=3.15$
	Diffusive time step	$3.67 \cdot 10^{-5}$
	Convective time step	$1.19 \cdot 10^{-6}$
<b>Final Time step</b>	dt	$6 \cdot 10^{-6}$

Table 3.6-Numerical schemes for LES calculations

### 3.9.2 Meshing

The computational domain is meshed using ICEM tool. An unstructured cartesian tetrahedral mesh has been created with two prism layers around the inner and outer cylindrical wall. Figure 3.29 is a shows the mesh at the inner wall and outlet. The two prism layers around the wall can be seen clearly. The prism layers are cut in to into tetrahedral before exporting the mesh in Trio-U format. The size of the first mesh cell from the wall is around 4 wall units for majority of the cells (Figure 3.30). Therefore the thermal conductive sub-layer is well resolved but the velocity sub-layer is not completely resolved and hence Riechardt wall function is used for the velocity field. The generated mesh is identical at inlet and outlet to respect the periodic boundary condition. The total number of the tetrahedral for this domain is approximately 15 million. The size of the cells near the wall is given in Table 3.8. The calculation is launched on curie-cluster (TGCC, CEA) using 512 processors that gives around 30000 tetrahedral per processor.

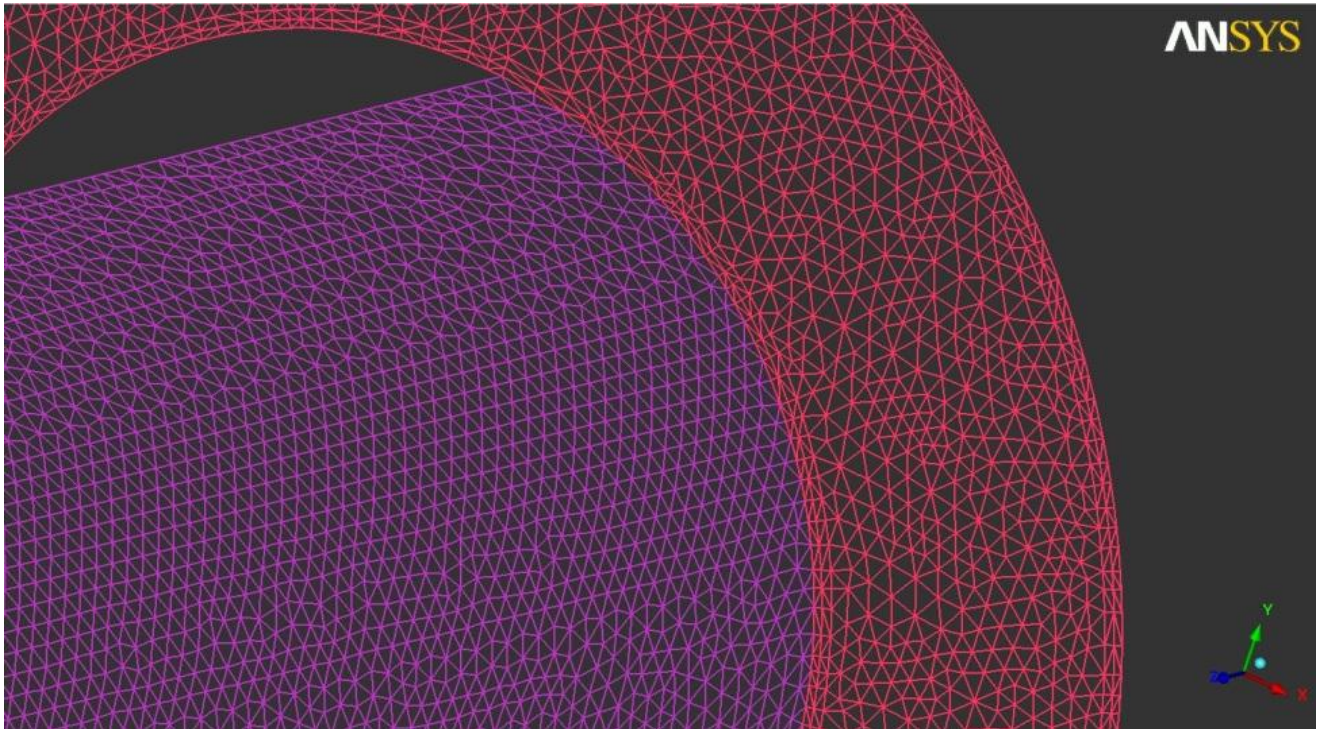


**Figure 3.29-2**Dimensional view of the tetrahedral mesh created by ICEM tool

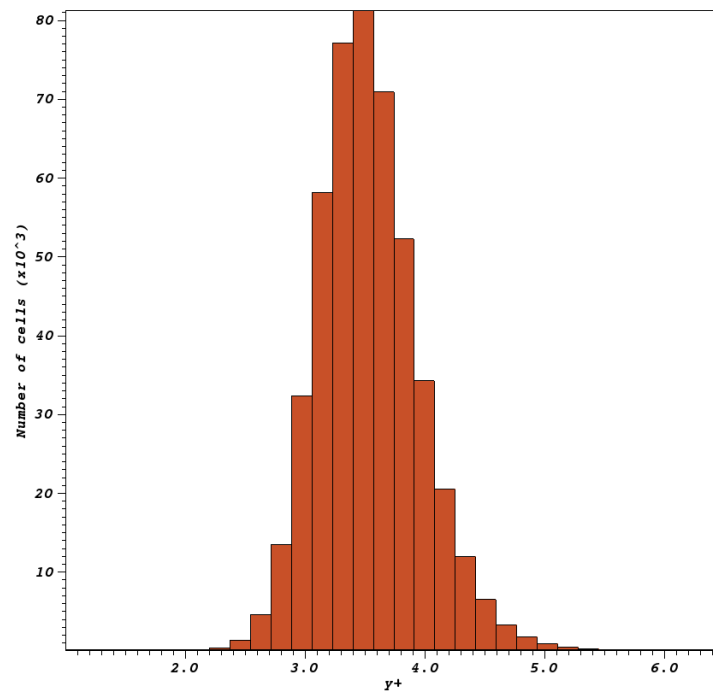


**Figure 3.30-**Histogram showing distance of the first cell from wall in wall units

Mesh Layer near the wall	$\Delta r^+$	$\Delta \theta^+$	$\Delta z^+$
Prism layer	5	2.5	14.5
First tetrahedral layer after prism layer	13	15.5	14.5
Tetrahedral layer following the tetrahedral layer 1	10.5	16.5	14.5

**Table 3.7-Grid resolution of tetrahedral mesh for the first three layers around the wall**

### 3.9.3 Boundary condition

The boundary condition for the LES study and Na-16K-V1 DNS simulations are the same and are described below. The only difference in the two studies is the domain size in azimuthal direction. The DNS calculation uses periodic condition in azimuthal direction whereas in LES calculation the complete  $2\pi$  domain in azimuthal direction is studied.

The Navier-stokes equation has Dirichlet boundary condition and Energy equation uses Neumann boundary condition.

Dirichlet boundary condition prescribes the value of velocity field at the boundary. The velocity field is required to stick at the inner and outer walls i.e. no-slip boundary condition (equation 3.4 and 3.5).

A constant heat flux equal to  $9.11427 \cdot 10^5 \text{ W/m}^2$  is imposed on the two walls instead of constant temperature to capture the temperature fluctuations at the wall.

The periodicity in axial direction is maintained for the flow and thermal field with external source term in momentum and energy equation.

The source term for velocity and temperature in the momentum and energy equation is necessary with axial periodic condition to maintain the flow and energy balance in the periodic domain. In Chapter 2, a detailed description of the different source terms used below is given.

The source term  $f(t)$  used for the momentum equation in the periodic direction ( $z$ ), is defined as follows:

$$f_z(t) = \frac{2(\dot{m}_0 - \dot{m}(t)) - (\dot{m}_0 - \dot{m}(t - dt))}{coeff \, dt \, Area} \quad (3.35)$$

Where *coeff* is damping coefficient, *dt* is the time step, *Area* represents the area of periodic boundary and  $\dot{m}(t)$  is the flow rate at time *t*. This source term imposes a constant pressure gradient of 152,828 Pa in axial direction.

The source term for energy equation has two different formulations the first one  $S_T^1$  does not take in to account the effect of velocity on the temperature and hence temperature fluctuations are damped. This is the older formulation present in TRIO-U and is defined below:

$$S_T^1 = \frac{q_w}{\rho C_p V} \quad (3.36)$$

Where  $V$  is the volume of the fluid,  $q_w$  is the heat flux imposed on the periodic channel walls  $\rho$  is the density of the fluid and  $C_p$  is the specific heat capacity.

The second formulation is the modified source term that now takes in to account the velocity fluctuations. This modification was done after the first comparison of the temperature fluctuations with the DNS results. The effect of the two source terms will be presented later in section (3.9.8).

$$S_T^2(x, y, z, t) = \frac{q_w}{\rho C_p V u_b} w(x, y, z, t) \quad (3.37)$$

Where  $w(x, y, z, t)$  is the axial velocity in the periodic direction  $z$  and  $u_b$  is the bulk velocity.

### 3.9.4 Initial conditions

In order to perform LES calculation it is necessary to have a turbulent velocity field at the inlet. The flow is initialized with constant initial velocity of 0.8744 m/s corresponding to Reynolds number of 16000 and 472°C. The initial flat velocity profile undergoes acceleration in the bulk region of the flow and decelerates to zero near the wall developing the laminar parabolic profile of velocity. The flow undergoes transition to turbulence at around 0.3s. The velocity field maintains the turbulent oscillations (Figure 3.31a) with time. The temperature field undergoes sharp decreases in the first 0.1s to adjust the temperature to a constant mean value according to imposed temperature source term. The random turbulent fluctuations in temperature field can also be seen in (Figure 3.31b).



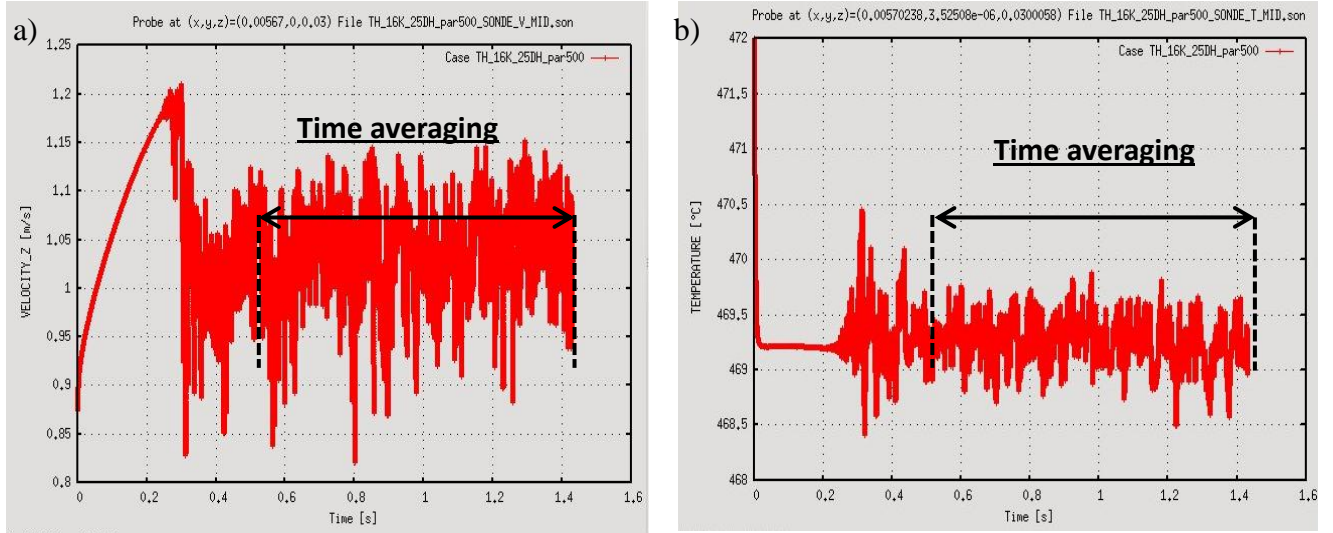


**Figure 3.31-Time variation of axial velocity and temperature at a local point**

The Fourier transform of the turbulent velocity and temperature signal is shown in Figure 3.32. The spectrum shows that the temperature and velocity oscillations follow the Kolmogorov 5/3 law as the slope in inertial region is  $-5/3$ . Thus, the required turbulent velocity and temperature field for LES calculation is obtained by this method. The time averaging is done from 0.6 s to 1.44s (0.2 million time steps). This corresponds to 5 complete traversals in the axial direction (0.15 s) that is long enough to capture all the physical phenomena.

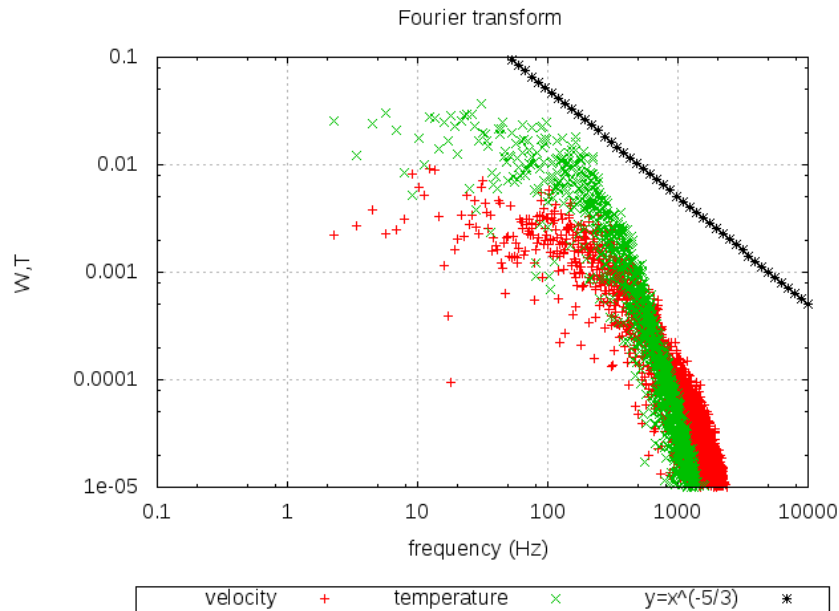


**Figure 3.32-Fourier transform of velocity and temperature signal showing that the temperature fluctuations follow Kolmogorov law**

### 3.9.5 Post processing tool for time averaged results

The time averaged velocity and temperature field in the DNS calculations are averaged in the homogenous axial and azimuthal direction where the turbulence is homogeneous. This is easier in structured mesh of DNS calculation but challenging for unstructured tetrahedral mesh used in LES calculation. However in order to compare the results with DNS same post processing has to be used.

The space averaging in axial and azimuthal direction has been performed by defining 39 cylinders of different radius. These different cylinders contain the tetrahedral mesh cells within  $\pm 0.1\text{mm}$  range of the specified radius of the cylinder.

The Trio-U code performs weighted mean of the time averaged quantities over the integration volumes i.e. volume around the faces for velocity and temperature to give a unique value for each cylinder. Thus 1-D profile for time and space averaged velocity and temperature statistics is obtained as a function of radius of the cylinder.

Table 3.9 shows the difference between friction velocity and the momentum source term between DNS and LES calculation. LES calculation under predicts the value with respect to DNS. We observe a difference of about 25% in the friction velocity and around 30% in the momentum source term. We note that the flow near the wall is not completely resolved in the LES calculation and wall functions are used to model the velocity gradient near the wall. This might be one of the reasons for under prediction of the friction velocity. Secondly the formulation of momentum source term in the LES and DNS code is the same but the implementation is done with a numerical scheme having different accuracy. The accuracy of the LES code is order 2 in space and time whereas DNS code has accuracy of order 4 in space. Therefore the momentum source term has difference of about 30% leading to different friction velocity.

Due to existing differences in friction velocity between DNS and LES simulations the results of LES calculations are not normalized by friction velocity. The comparison of physical quantities from DNS and LES results is made with dimensions without using any normalization.

Parameter	Units	LES	DNS	Relative error
$u_{\tau-int}$	m/s	0.042586	0.056922	~25%
$u_{\tau-ext}$	m/s	0.04089	0.005301	~25%
$f_z$	m/s <sup>2</sup>	1.446	2.14082	~30%

**Table 3.8-Mean flow parameters for LES and DNS calculation with sodium at Reynolds number 16000**

### 3.9.6 Mean velocity and turbulent statistics

In this section the results for the time and space averaged velocity field and velocity fluctuations are evaluated as a function of distance from the wall. The distance from the wall is expressed in terms of  $\delta$  that represents half of the distance between the two walls. Figure 3.33 depicts the profile of time and space averaged axial velocity with distance from the wall. The axial velocity in LES simulation under predicts the wall gradients with respect to DNS (Na-16K-V1) results and as a consequence the axial velocity at the center of the domain is over predicted. However the position of the peak of the axial velocity is well determined by LES method with slight discrepancy. The peak is closer to the inner wall at distance of  $0.884\delta$  in DNS and  $0.89\delta$  in LES.

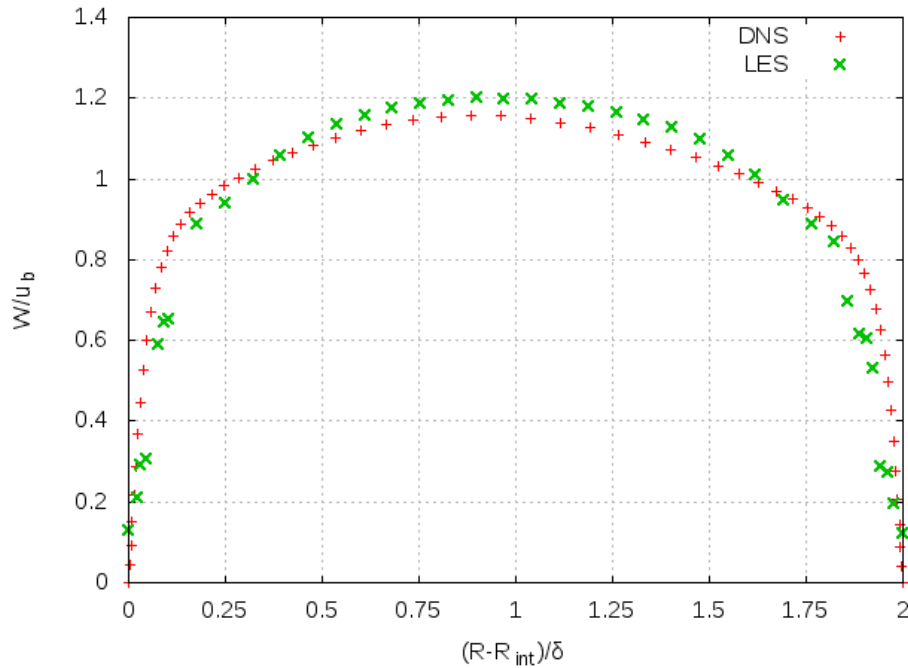


**Figure 3.33-Comparison of mean axial velocity normalized with bulk velocity between DNS (Na-16K-V1) and LES**

The comparison of r.m.s velocity fluctuations is shown in Figure 3.34. In general LES calculation predicts well the position of the maximum fluctuations near the wall with slight shift away from the wall. However the magnitude of the peak fluctuations is under estimated. For the fluctuations of velocities in radial and azimuthal direction (Figure 3.34a and Figure 3.34b) the LES calculation follows the same variation as in DNS calculation with under estimation of the magnitude.

The fluctuations of velocity in axial direction (Figure 3.34c) are under predicted near the wall and over estimated at the center of the domain.

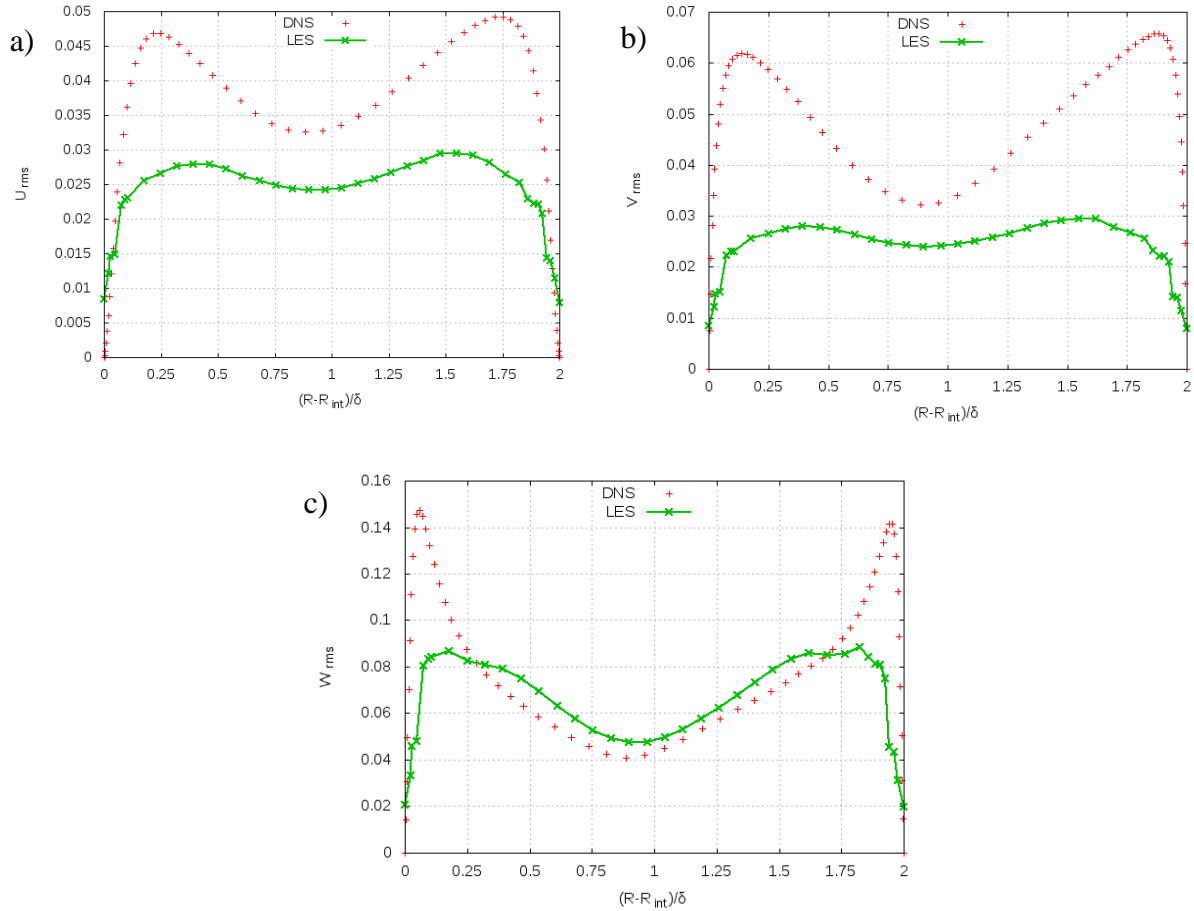


**Figure 3.34-Comparison of root mean square velocity fluctuations between DNS (Na-16K-V1) and LES (a) Wall- normal (radial) velocity, (b) Azimuthal velocity, (c) Axial velocity**

The turbulent kinetic energy variation near the wall is given in Figure 3.35. The most of the turbulent kinetic energy is present near the wall where the flow structures are highly elongated and contains maximum energy. In LES simulation the position for maximum

turbulent kinetic energy is slightly shifted away from the wall and the maximum production of turbulent kinetic energy is under predicted with respect to DNS simulation.

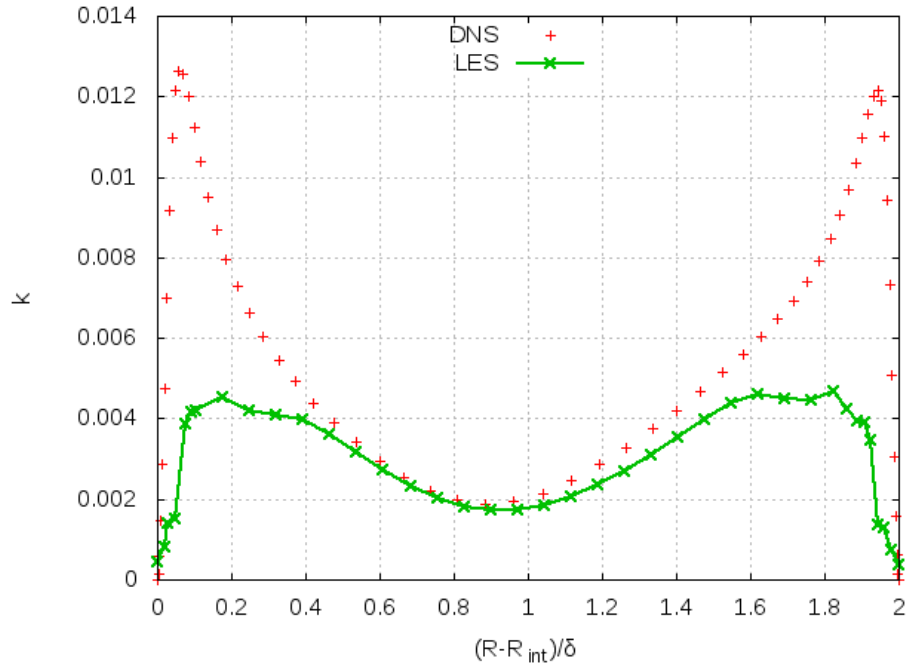
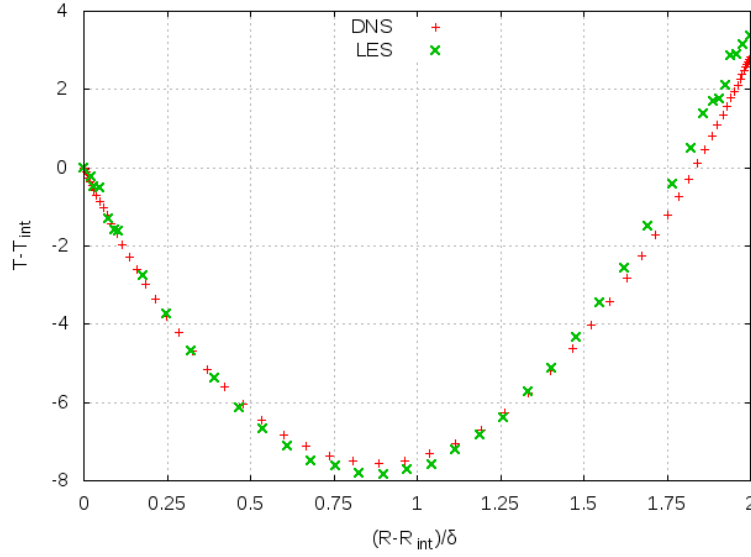


Figure 3.35-Turbulent kinetic energy comparison between DNS (Na-16K-V1) and LES

### 3.9.7 Mean temperature and thermal statistics

The profile of average temperature between the two walls of concentric annular cylinder showed good agreement for LES and DNS methods. Figure 3.36 shows the variation of temperature profile with respect to the temperature at inner wall. In sodium conduction is the dominant mode of heat transfer because of low Prandtl number. It is because of this reason that even if the wall gradients of axial velocity are not well determined by LES but still the temperature profile is shows good agreement with DNS results.



**Figure 3.36-Comparison of mean temperature profile between DNS (Na-16K-V1) and LES**

However, the magnitude of temperature fluctuations was observed to be very small as compared to that given by DNS method. The amplitude of temperature fluctuations from LES simulations is found to be around 6.5 times less than that from DNS simulations. In Figure 3.37 the temperature fluctuations from LES code without any modifications are represented by “LES\_old.” The small magnitude of temperature fluctuations in LES method is due to the non-physical numerical dissipation coming mainly from two reasons.

Firstly, the formulation of temperature source term (equation 3.36) that does not take in to account the effect of velocity. This source term stabilizes the temperature field quickly to a periodic temperature but it imposes a non-physical dissipation of the temperature fluctuations that decreases the magnitude of temperature fluctuations.

Secondly, the convection scheme used for the temperature equation is Ef\_stab in the upwind mode (with parameter  $\alpha=1$ ). This scheme is very dissipative. The energy centered scheme used for momentum equation (with parameter  $\alpha=0.2$ ) when used for temperature equation gives very large temperature oscillations and lead to divergence of the calculation.

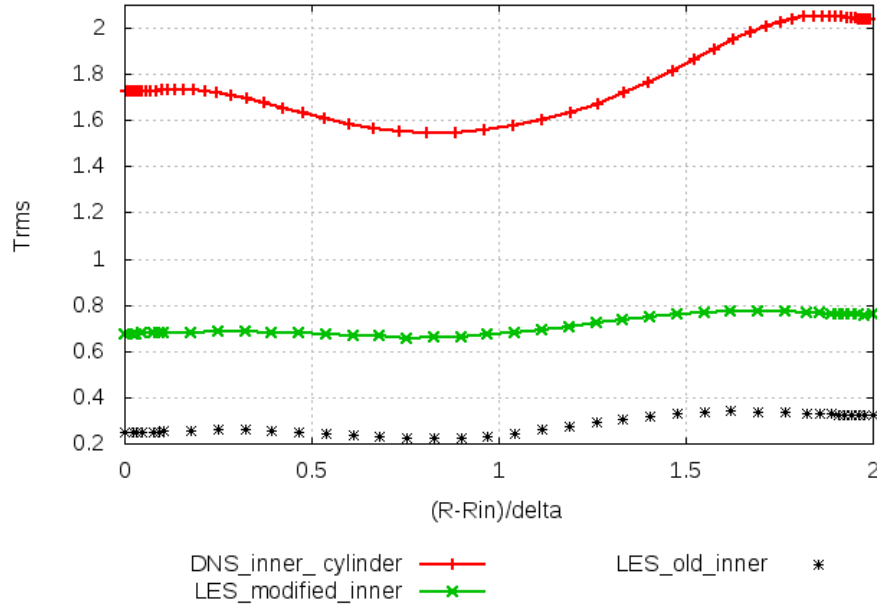


**Figure 3.37-Root-mean-square temperature fluctuations**

Thus, the temperature source term was reformulated which takes in to account the velocity variations (equation 3.37) and the convection scheme was changed to less dissipative formulation (Ef\_stab with parameter  $\alpha=0.5$ ). The convection scheme could not be changed to completely non-dissipative energy centered scheme because the temperature field diverges to non-physical limits.

Using these changes in the numerical method and temperature source term the magnitude of temperature oscillations in LES was increased around 4 times. However, the magnitude of temperature oscillations from LES methods is still less than that from DNS methods by a factor of around 2.5.

This difference is mainly because of the difference in convection scheme for the two codes. In pseudo-spectral DNS method with accuracy of order 4 in space the temperature equation uses energy centered scheme for convection term without encountering any numerical problems. But in finite element volume based LES method with accuracy of order 2 in space, a combination of energy centered and upwind scheme is used in order to avoid the numerical divergence caused by use of energy centered scheme.

Therefore, in this study the comparison between the results obtained through DNS and LES methods shows that the numerical scheme used in LES methods gives accurately the mean temperature field but the temperature fluctuations are underestimated by a factor of around 2.5. This difference is acceptable considering the difference in the numerical schemes and order of accuracy but while applying this LES method on the complex sub-assembly

geometry it is important to take into account this difference in the results as the uncertainty in the obtained results for temperature fluctuations.

## 3.10 Summary

In the present work, DNS of turbulent heat transfer for fully developed flow in concentric annulus under iso-flux conditions have been performed for liquid sodium with  $Pr=0.004$  at two Reynolds number-8900 and 16000 using the in-house University DNS code.

The concentric annulus is a simplification of the complex geometry of the sub-assembly so that DNS can be performed. The concentric annulus permits us to see the effect of curvature of the wall on the turbulent flow and thermal quantities. It is observed that all the thermal statistics at outer wall are larger than that at the inner wall and this difference is a function of the radius ratio between the two walls.

The DNS code has two versions- the first one that already existed (V1) and is capable of modeling any cylindrical domain with homogenous azimuthal direction and the modified version (V2) that can model in homogenous azimuthal direction like a straight obstacle present along the axial direction on the inner cylinder of the concentric annulus. These two versions have been validated by studying the turbulent heat transfer in air at 8900 Reynolds number for iso-flux conditions and comparing the results to those available in literature. Over all agreement between the two versions of the code and result from literature was acceptable with slight differences.

The two DNS simulations for the liquid sodium at different Reynolds number allow us to see 2 effects- firstly the effect of reducing the Prandtl number to as low as 0.004 that has not been studied in the open literature for annulus or other geometries. The lowest Prandtl number that has been studied in the past has been limited to 0.025 corresponding to lead bismuth eutectic flow. Secondly the effect of Reynolds number on the thermal field with iso-flux boundary condition has been studied. This is interesting phenomena because up till now the effect of Reynolds number with low Prandtl number has been studied only for lead that too only in channel flow.

The mean temperature profile for liquid sodium shows that the conductive sub-layer extends to larger distance from wall ( $y^+$ ) as compared to that in air. The logarithmic region is absent for until Reynolds number 16000. With increase in Reynolds number the conductive sub-layer gets thicker and molecular conduction dominates. The fluctuations in temperature and turbulent heat flux show strong dependence on the Reynolds number for sodium flow. The



consequence of this is that the turbulent Prandtl number for sodium flow shows strong variation for the two Reynolds number. We obtain a value of turbulent Prandtl number equal to 10 for Reynolds 8900 and 3.5 for Reynolds number 16000. The variation in turbulent Prandtl number with further increase in Reynolds number could not be verified by DNS because of computational limitations which vary  $Re^{11/4}$ . However the study of the turbulent Prandtl number evaluated for Prandtl number 0.025 shows that with increase in Reynolds number the turbulent Prandtl number shows less variation and achieve an asymptotic value. Therefore for sodium flow with  $Re > 16000$  we assume that the turbulent Prandtl number is constant to a value of 3.5.

At the end an industrial LES method with wall functions for velocity that will used for study of sub-assembly in chapter 4 has been used to study the sodium flow in concentric annulus at  $Re=16000$  in order to make a comparison with DNS results. We observe that the unstructured tetrahedral mesh with wall functions under predicts the gradient of velocity near the wall. The profile of turbulence intensities is well traced with slight shift in the radial position away from the wall. The results are however in good agreement for mean temperature as for low Prandtl fluids thermal conduction dominates over convection. However temperature fluctuations in LES are under predicted. Initially a factor of 6 was observed which was reduced to a factor of 2.5 by optimizing the temperature source term. This is because of the numerical dissipation of the dissipative and lower order accuracy of the convection scheme in LES code. But the factor difference of 2.5 cannot be reduced further as temperature field diverges with the use of energy centered convection scheme.

After this comparison between the LES and DNS method for sodium flow in concentric annulus we will now use this LES method along with the widely used RANS method to study the sodium flow in sub-assembly in Chapter 4.

# CHAPTER 4

---

## *Thermal-hydraulic studies of sub-assembly by CFD*

*In this chapter the RANS and LES approach that have been compared with the results of DNS calculation in Chapter 3 have been used to perform thermal-hydraulic study of the sub-assembly of SFR. The objective of the study is to identify and investigate the region peak fluid temperature, referred to as hot spot that are important concern from the safety point of view. The RANS method is used at first to give information about the steady state velocity, pressure and temperature field in the complete sub-assembly with 217 fuel pins. The information about higher order statistics of these physical quantities is then obtained by performing LES calculation on the local region of the sub-assembly with appropriate boundary conditions.*

## 4.1 RANS

In Reynolds Averaged Navier-Stokes (RANS) is a time averaging method that removes the necessity of simulating all the scales of the turbulence spectrum. The details of this method can be found in chapter 2. RANS method is computationally less demanding than LES method. Thus, RANS have been widely applied in many engineering problems. We also start by using the RANS method as the first approach for thermal-hydraulic study of sub-assembly.

### 4.1.1 Computational domain

Figure 4.1 shows the top view of the computational domain. It represents the fluid domain contained in the sub-assembly with 217 wire wrapped fuel pins inside a hexagon duct wall. The diameter of the fuel pin ( $D_p$ ) is 9.7 mm and the diameter of spacer wire ( $D_w$ ) is 1.1 mm. Thus, the minimum distance between two fuel pins of the sub-assembly (also known as pitch) is 10.8 mm. The distance between the two parallel walls of hexagonal duct also called as plate-to-plate distance ( $e$ ) is 161.5 mm and the gap,  $g$  that is the distance between the center of the fuel pin in the last ring and hexagonal wall is equal to 10.44 mm. There are 8 rings ( $N_{rings}$ ) of the fuel pins around the central fuel pin. The dimensions of the sub-assembly have been summed up in table 4.1. In the axial direction the height of sub-assembly is 800 mm with 4 helical wraps of the spacer-wire. The pitch of the spacer wire is 180 mm.

Variable	Description	Value	Units
$D_p$	Diameter of fuel pin	9.7	mm
$D_w$	Diameter of spacer wire	1.1	mm
$P$	Pitch of the fuel pin	10.8	mm
$L_z$	Total axial height	800	mm
$H$	Helical pitch of wire	180	mm
$N_{rings}$	Number of rings	1+8	-
$N_{pins}$	Number of fuel pins	217	-
$g$	gap	10.44	mm
$L$	side of hexagonal duct wall	93.24	mm
$e$	plate to plate distance	161.5	mm

**Table 4.1-Geometrical parameters of the sub-assembly**

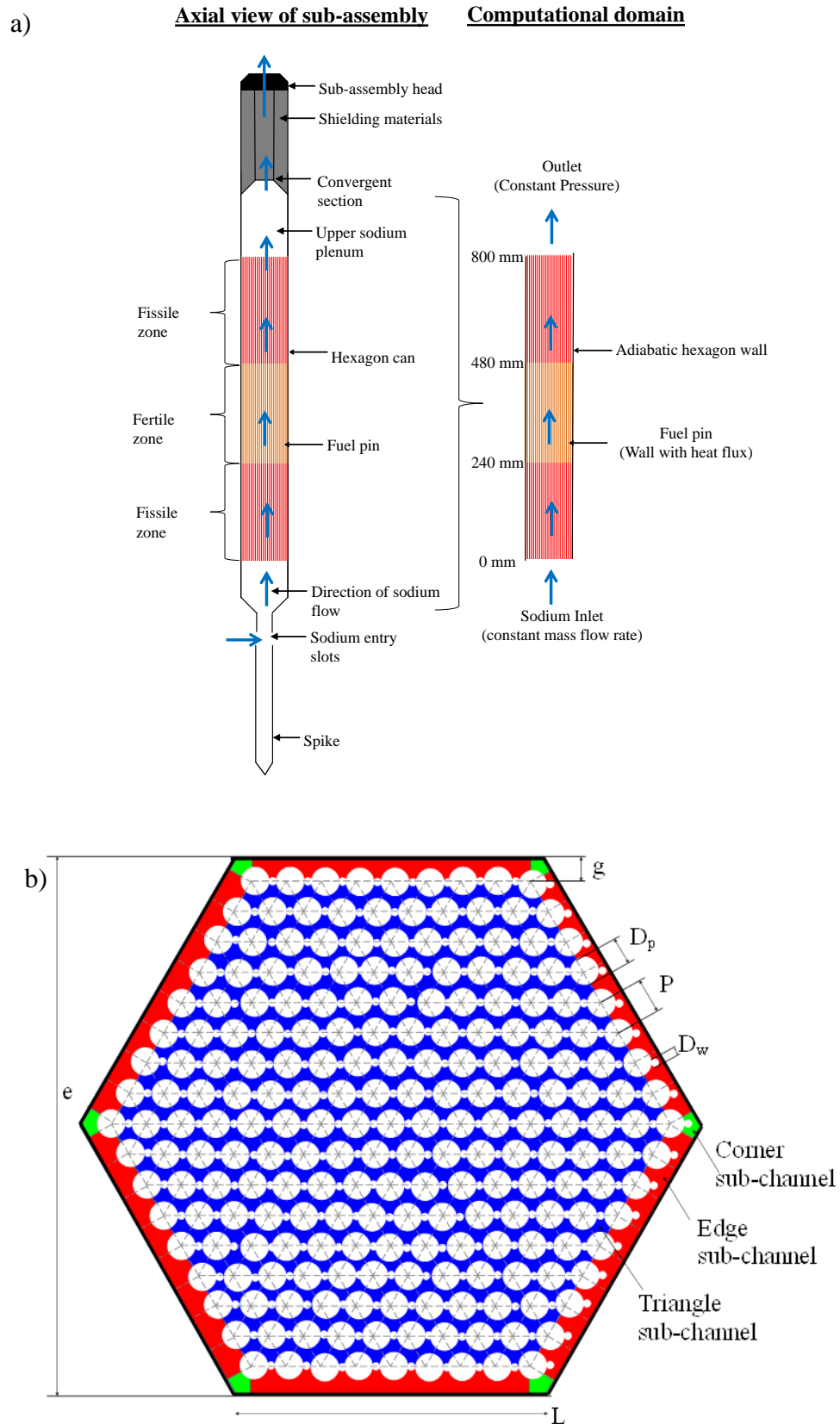


**Figure 4.1-Schema of 217-fuel pin sub-assembly showing geometry parameters and boundary conditions a) axial view and b) transversal view**

The hydraulic diameter of the sub-assembly is defined as

$$D_h = \frac{4A_f}{P_w} \quad (4.1)$$

Where  $A_f$  is the flow area of the sub-assembly and  $P_w$  is the wetted perimeter by the flow in the transverse direction. If the spacer wire is considered tangent to the fuel pin then we have

$$A_f = \underbrace{\frac{3\sqrt{3}}{2}L^2}_{\text{surface area of hexagon}} - \underbrace{N_{pins} \frac{\pi}{4}(D_p^2 + D_w^2)}_{\text{surface area of fuel pins and wires}} \quad (4.2)$$

And

$$P_w = \underbrace{6L}_{\text{Perimeter of hexagon}} + \underbrace{N_{pins}\pi(D_p + D_w)}_{\text{Perimeter of fuel pins and wires}(P_{w-pins})} \quad (4.3)$$

Therefore,

$$D_h = \frac{6\sqrt{3}L^2 - N_{pins}\pi(D_p^2 + D_w^2)}{6L + N_{pins}\pi(D_p + D_w)} \quad (4.4)$$

Thus, the total hydraulic diameter of the sub-assembly is 3.20mm. However, the triangular lattice arrangement of the fuel-pins inside the hexagonal can forms three different types of sub-channels in which coolant circulates. These 3 sub-channels are triangular, edge and corner sub-channel. The grey line in Figure 4.1 represents the different sub-channels and distinguishes them in three colors - blue for triangular, red for edge and yellow for corner sub-channels. These sub-channels have different hydraulic diameter. Table 4.2 gives information about number and hydraulic diameter of these sub-channels.

Types of sub-channel	Number of sub-channels		Hydraulic diameter
Triangular	$N_1=6 N_{rings}^2$	384	$D_{h1}=3.29\text{mm}$
Edge	$N_2=6 N_{rings}$	48	$D_{h2}=3.96\text{mm}$
corner	$N_3$	6	$D_{h3}=4.75\text{mm}$

**Table 4.2-Flow parameter for different kinds of sub-channels in sub-assembly**

### 4.1.2 Numerical tool

The CFD code used for the RANS study is STAR-CCM+. The turbulence model, wall treatment and other conditions for the calculation are given below and have been described before in chapter 2.

- The resolution of the Navier -Stokes equations is based on an integral approach in finite volume
- The SIMPLE algorithm is used by the solver
- The turbulence model k-  $\epsilon$  of Launder and Spalding (1974) is used
- The model law of wall is treated by the model All y +
- The turbulent Prandtl number is assumed to be constant and equal to 0.85
- Gravity is not taken into account for the forced convection

### 4.1.3 Meshing

In the sub-assembly, the wire-spacers and fuel rods are in point contact in two dimensions and in line contact in three dimensions. The pitch between two adjacent fuel pins is very small so every time when the wire of the fuel pin turns helically it comes almost in contact with the surrounding pins. Thus, it is not possible to obtain a volume mesh for this kind of geometry with the available resources and a simplification of the contact point between fuel pin and spacer wire is required. In the following section we first present the different ways to represent the contact point between fuel pin and spacer wire and then present the meshing method for the selected computational domain.

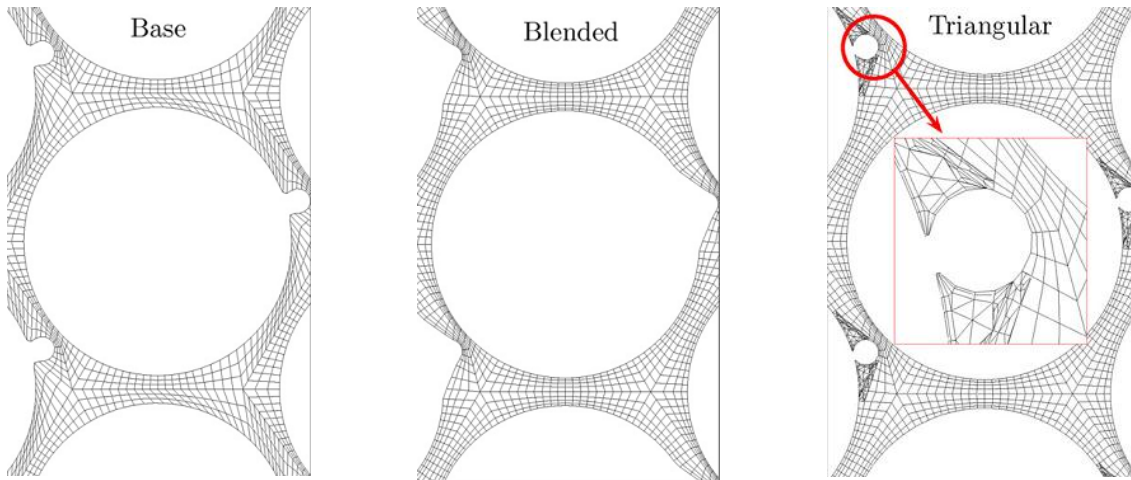
#### 4.1.3.1 Representation of fuel pin –wire line contact

Many representations of wire-fuel pin contact have been studied in the open literature to obtain a good quality volume mesh. Raza et al. (Raza, 2008) studied three different shapes of spacer wire - circle, hexagon and rhombus and concluded that the circular shape of spacer wire is the best representation with respect to other two shapes due to overall pressure drop, maximum temperature, and uniformity of temperature. Rolfo et al. (Rolfo, 2012) studied the circular shaped spacer wire and shows three different configurations- base, blended and triangular (Figure 4.2) to simplify the meshing. The three configurations are as follows:

- i. In the base configuration the wire surface is connected to the pin surface at a right angle. This representation has also been used by Pointer et al. (Pointer, 2009) and

using this simplification the author was able to reduce the mesh size for 217 fuel sub-assembly from 44 million to 10 million cells.





- ii. The blended configuration has a very smooth transition as the wire has a large blending with the attached pin.
- iii. The triangular configuration has a very detailed discretization of the singularity between wire and pin, obtained with an unstructured mesh of the area.



**Figure 4.2-Meshing of three different representations of wire-pin contact (Rolfo, 2012)**

The effect of the three configurations on the velocity is very small with the maximum difference of friction factor below 4% but the effect on heat transfer is very large. Rolfo et al. found variation of the Nusselt number of the order of 10–15% with respect to the value given by the most detailed geometrical representation i.e. triangular. The area around the wire is the one that is characterized by the highest wall temperature (imposed  $q_w$ ) and wall heat fluxes (imposed  $T_w$ ) so for hot-spot studies the triangular configuration is the best representation.

Bieder et al. (Bieder, 2010) summarized the different possible representations of wire with the ability to study the hot-spot (Table 4.3). It is clear from the table that only two representations are capable of predicting the hot-spots at the contact zone. The first is with radial displacement of wire into the rod and second is open wire representation.

Contact between the rod and wire	Characterization	Meshing	Temperature in contact zone
	Reality	Almost impossible to mesh due to tangencies	Can be calculated correctly
	Radial displacement of the circular wire into the rod for about 5% of the wire diameter	Homogeneous meshing with only some degraded tetrahedrons	Possible hotspots between rod and wire cannot be predicted
	Blending which can be degraded to large radii (so called open wires)	Very small meshes in the contact zone might be created	Possible hotspots between rod and wire can be predicted with some uncertainty
	Square wire of equivalent surface as the wire	Easy to mesh	Possible hotspots between rod and wire cannot be predicted

**Table 4.3-Summary of different ways to represent the contact point between fuel pin and spacer wire (Bieder, 2010)**

The representation of spacer wire that is used for this RANS takes the radial displacement of  $0.10D_w$  where  $D_w$  is diameter of circular wire into the fuel pin.



### 4.1.3.2 Meshing tool

The meshing tool used to create the volume mesh has been developed by the supervisor of the thesis, Thierry Cadiou and is based on NASA work (Thompson et al., 1977). The advantage of this tool is that it allows optimizing the mesh size. The user has control over the desired number of mesh cells needed to properly represent the space wire mesh in each mesh plane and finally to control mesh size between the two pins. The meshing generation is based on a multi-bloc elliptic meshing technique (Appendix A). As a first step, the sub-assembly is subdivided into axial slices in order to perform a 2D meshing of the region comprised between the external contour of the pins and the external hexagonal box. The idea behind this meshing technique consists of determining the streamlines between two contours: the pin contour and the hexagonal box contour. The sub-assembly meshing is finally built by assembling the 2D meshing. The final 3D mesh of the sub-assembly contains 150 axial layers and giving a mesh with 15 million cells (Figure 4.3). The mesh resolution has been verified by checking the value of non-dimensional distance from wall ( $y^+$ ). It gives an idea that the first point after the wall is placed correctly to have physical value of the velocity and wall shear stress. In the current mesh, there are 4 million cells on the wall of fuel pins and out of these 3 million cells have non dimensional distance normal to wall ( $y^+$ ) values in the range 5 to 100. The remaining 1 million cells are present around the helical turning spacer wire that shows some degradation but it is sufficient to see the tendency of the global flow features.

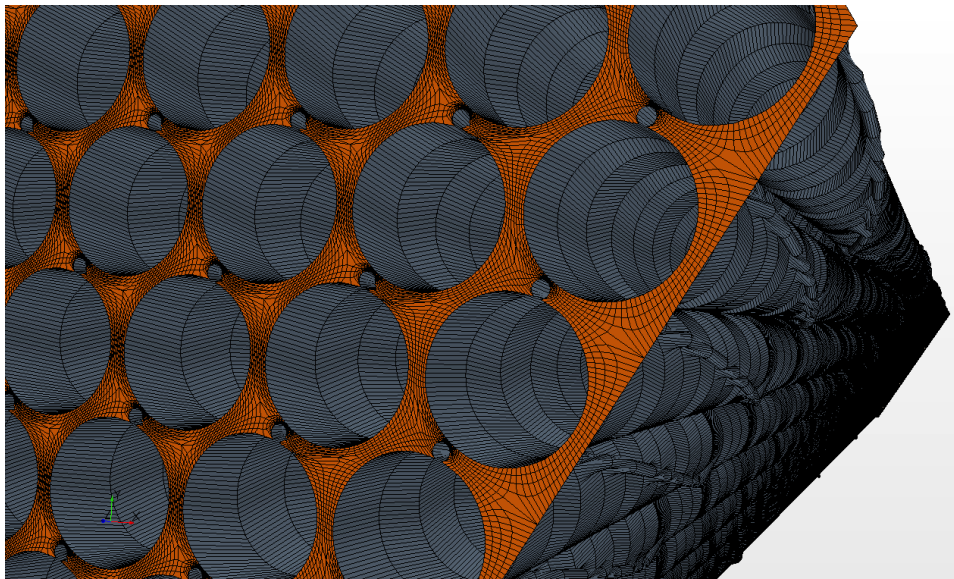


**Figure 4.3-Three dimensional meshing of the computational domain**

## 4.1.4 Boundary and initial conditions

In the current modelling the solid part is not accounted for and only the fluid domain inside the sub-assembly has been considered for modelling. Thus, most appropriate boundary conditions have to be applied on the domain to well represent the actual flow conditions. The boundary conditions used in this calculation are listed below:

### i. Hexagonal duct wall

The outer most hexagonal can is fixed wall with no slip boundary condition for velocity i.e. velocity at the wall is equal to zero and it is thermally adiabatic.

### ii. Fuel pins and spacer wire

Like hexagonal duct wall, the fuel pins and spacer wire are also fixed walls with no slip boundary condition but they are not adiabatic. The energy produced in the fuel pins by fission reaction is modeled by imposing uniform heat flux on the fuel pins. The surface heat flux emitted by the fuel pin is considered azimuthally uniform. The fuel pins have uniform heat flux in the radial direction and varies in the axial direction. The fuel pin consists of both fissile and fertile material and therefore the power deposited in the fissile and fertile part are not the same. Therefore an axial variation of the heat flux has been imposed as shown in Figure 4.4. This represents the power profile in the maximum heated sub-assembly inside the inner core at the end of irradiation cycle. The total nuclear power generated by the pins is 6MW. The spacer wire is considered adiabatic representing the ideal conditions in the reactor sub-assembly.

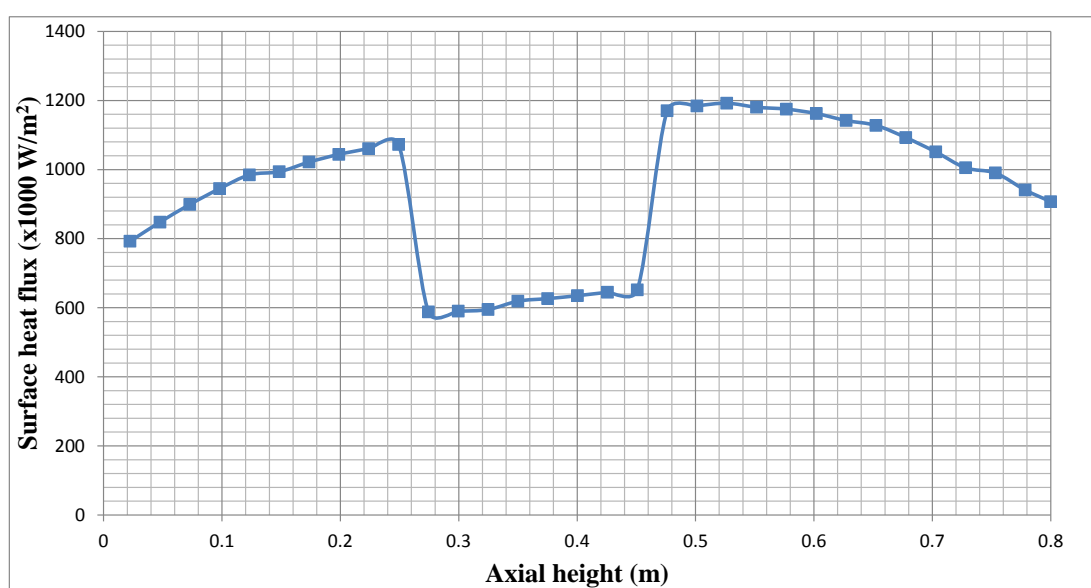


**Figure 4.4-Heat flux imposed on the fuel pins as a function of axial height**

### iii. Inlet and outlet

The sodium flow is considered incompressible. A constant mass flow rate boundary condition has been imposed at the inlet and the outlet of the sub-assembly has constant pressure as the boundary condition.

### iv. Fluid properties and flow conditions

The different thermo-physical properties of sodium varies with temperature (T) according to equation 4.5 to 4.8 which are valid for the range 200 to 600 °C.

**Density** (kg/m<sup>3</sup>)

$$\rho(T) = 1008.575 - 0.213445 \cdot T - 1.75 \cdot 10^{-5} \cdot T^2 \quad (4.5)$$

**Thermal conductivity** (W/m/K)

$$\lambda(T) = 103.85 - 0.04859 \cdot T \quad (4.6)$$

**Specific heat** (J/kg/K)

$$C_p(T) = 1595.34 - 0.8329 \cdot T - 4.6229 \cdot 10^{-4} \cdot T^2 \quad (4.7)$$

**Dynamic viscosity** (Pa.s)

$$\mu(T) = \rho(T) \cdot 1.2162 \cdot 10^{-5} \cdot e^{0.6979 \cdot \frac{\rho(T)}{T}} \quad (4.8)$$

Thus, the Prandtl number of sodium varies from 0.01 to 0.005 in the range 200 to 600 °C. The order of magnitude of the physical properties at the average temperature of 470°C in the sub-assembly is given in Table 4.4. These values have been used in the RANS study.

Properties	Symbol	Value	Units
Density	$\rho$	838.79	kg/m <sup>3</sup>
Thermal conductivity	$\lambda$	68.18	W/m/K
Specific heat	$C_p$	1268.4	J/kg/K
Dynamic viscosity	$\mu$	$2.54 \cdot 10^{-4}$	Pa.s

**Table 4.4-Thermo-physical properties of sodium at 470 °C**

The flow conditions are varied to study the flow at different Reynolds numbers and the heat flux has been changed accordingly in order to have the same desired elevation in temperature,  $\Delta T$  of 149 °C. It is based on the energy balance equation given below

$$Q = \dot{m} C_p \Delta T \quad (4.9)$$

A summary of flow conditions for different calculations has been shown in Table 4.5.

Variable	Units	Reference	C1	C2	C3	C4	C5
Power, $Q$	MW	6.00	1.05	2.1	4.2	5.18	6.45
Mass flow rate, $\dot{m}$	kg/s	31.25	5.6	11.22	22.4	27.6	33.6
Temperature difference, $\Delta T$	°C	149	149	149	149	149	149
Reynolds number	-	54831	9138	18277	36554	49402	58954

**Table 4.5-Flow conditions for different calculations**

#### v. Initial conditions

The flow in the computational domain has been initialized with temperature 400°C and velocity of 0 m/s. The flow develops itself with time according to the imposed mass flow rate at the inlet.

The RANS study gives the result about global flow features for variation of pressure, temperature and velocity in the sub-assembly. A steady state solution is achieved when the surface average pressure and temperature at the outlet is constant i.e. they do not vary change with the time.

### 4.1.5 Pressure drop

The pressure loss due to friction is defined as

$$\Delta P = \frac{1}{2} \frac{f \rho u^2 L_z}{D_h} \quad (4.10)$$

Where  $f$  represents the friction factor,  $u$  represents the velocity,  $L_z$  is the total height of the channel and  $D_h$  is the hydraulic diameter. The friction factor has been estimated in the past by various empirical and semi-empirical correlations. The different correlations are listed in Appendix B.

The result of the pressure drop from the simulations for different flow Reynolds number listed in table 4.5 has been compared to the available correlations in Figure 4.5. The pressure drop maintains the quadratic variation with the Reynolds number. The correlations and simulation results have good agreement for low Reynolds numbers up to 20000. When the Reynolds number is increased further then there exist some discrepancy between the correlations and simulation results. In the current study, the Cheng and Todreas correlation (Cheng, 1984) well represent the sodium flow in sub-assembly with 217 fuel pins.

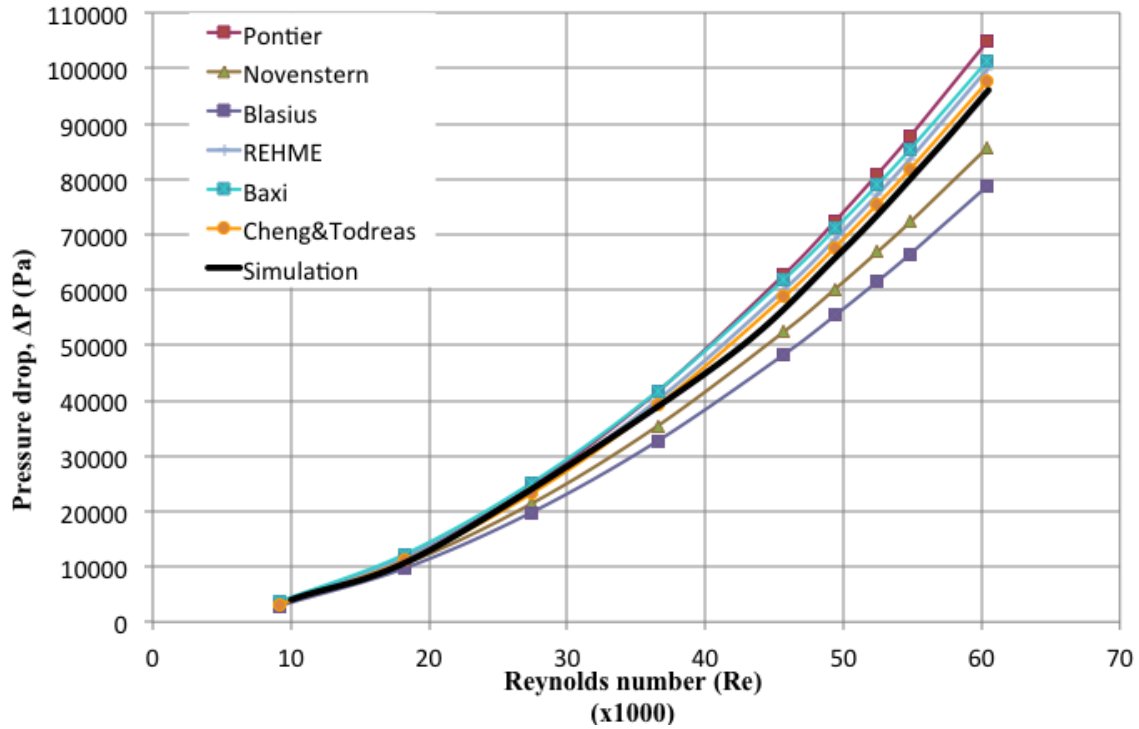
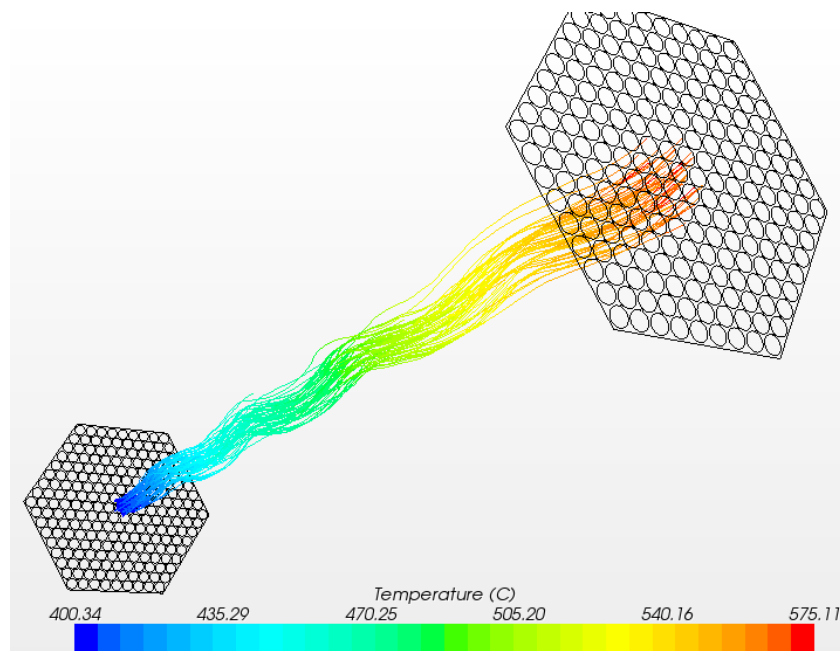


**Figure 4.5-Pressure drop variation with Reynolds number for different correlations and simulation**

### 4.1.6 Velocity

The velocity streamlines for reference calculation (in Table 4.5) is shown in Figure 4.6. The velocity distribution shows a different behavior between the central portion and the peripheral portion of the sub-assembly. In the central part, the sodium follows a helical movement along the spacer wire (Figure 4.6) whereas in the periphery the fluid rotates around the hexagonal duct wall. This is called as the swirl flow occurring in the peripheral sub-channels. Furthermore, the speed of the sodium is greater in this area due to comparatively higher hydraulic diameter of the peripheral sub-channels as compared to the interior sub-channels.

a)



b)

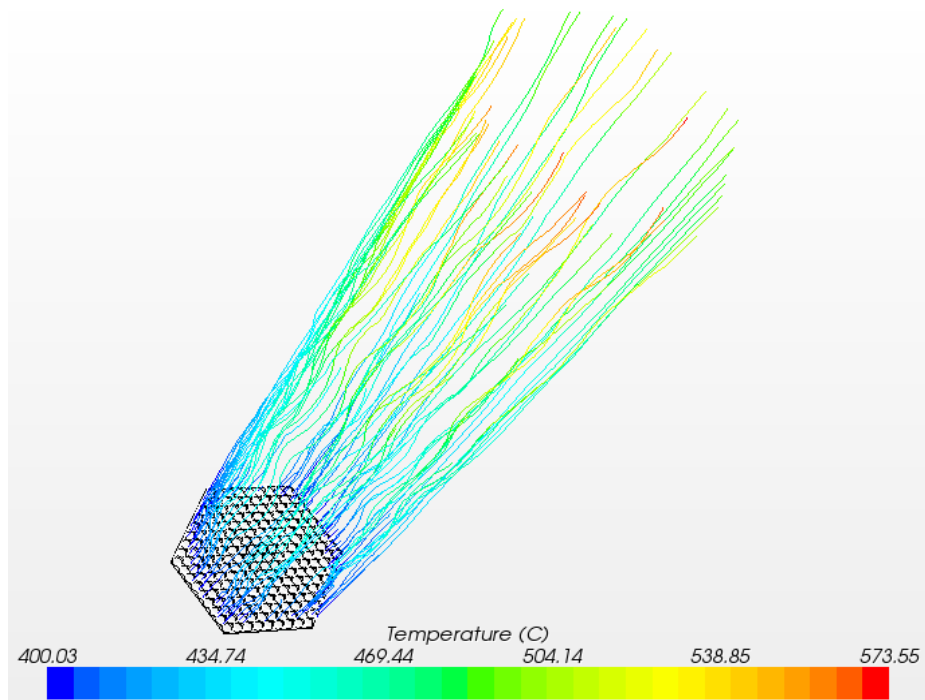


**Figure 4.6-Streamlines of the flow with evolution of temperature a) Around the central fuel pin and b) Around the hexagonal can**

## 4.1.7 Temperature

The axial temperature distribution in the sub-assembly is shown in Figure 4.7 and Figure 4.8 for the reference calculation. It follows the linear increase in temperature from the inlet to the outlet except at the region of fertile blanket from 0.26 mm to 0.48 mm. The temperature difference between the average inlet and outlet temperature is 150 °C as imposed in the calculation corresponding to mass flow rate and power (given by energy balance equation 4.9).

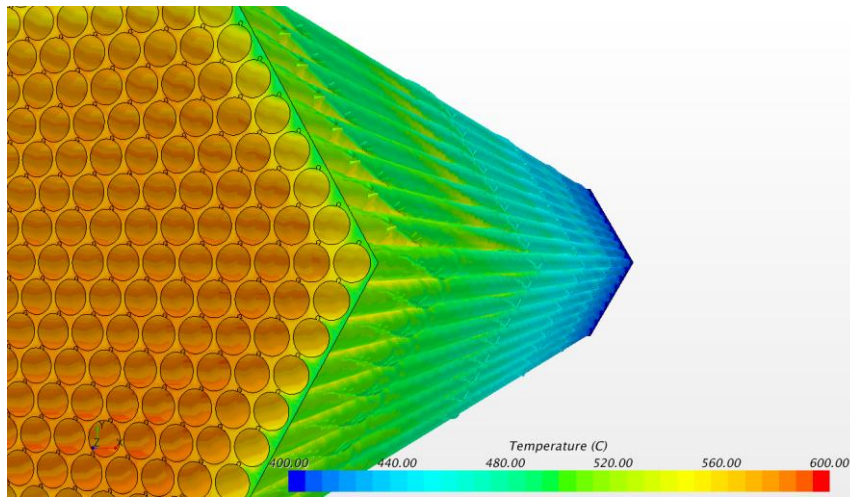


**Figure 4.7-Axial distribution of temperature in 3-D**

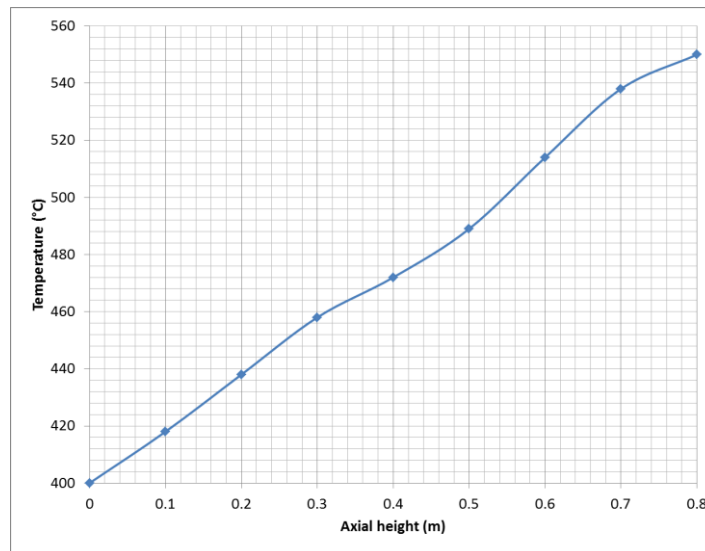


**Figure 4.8- 1-D profile of temperature variation with respect to axial height**

Figure 4.9 shows the radial distribution of the temperature near the outlet where two distinct regions are clearly visible- the central heated region and the comparatively colder region in



the periphery around the hexagonal wall. The temperature difference between these two zones is around 100 °C. There are two reasons for the periphery to be colder than the central region. The first explanation comes from the geometry of the sub-channels in the periphery that have higher hydraulic diameter than the central triangular sub-channel. This leads to high axial velocity of the fluid and more extraction of heat energy. The second reason is that the fluid in this region is heated by only two fuel pins unlike the central region where the fluid is heated up three neighboring pins which makes the fluid cooler than the central region. Thus, the periphery has higher mass flow rate and less power which gives lower value of the ratio of power to mass flow rate. We see from equation (4.9) that this ratio is proportional to temperature difference giving lower value of temperature difference in the periphery of the sub-assembly.

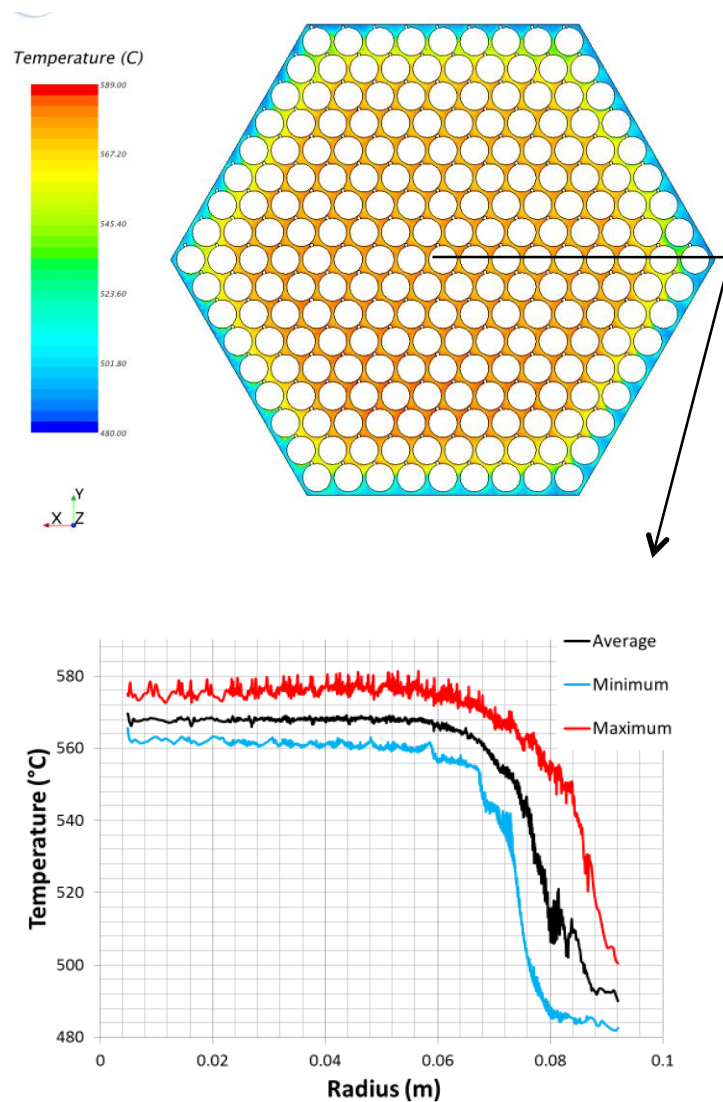


**Figure 4.9-Radial distribution of temperature in 2-D plane near the outlet plane and the curve showing temperature variation with respect to radius**



### 4.1.8 Nusselt number

The Nusselt number is defined as

$$Nu = \frac{q_w}{(T_w - T_b)} \frac{D_h}{C_p \lambda} \quad (4.11)$$

Where  $T_b$  is the bulk temperature of sodium,  $T_w$  is the temperature at the surface of the fuel pin.

The axial variation of the Nusselt number on the central fuel pin of the sub-assembly is shown in Figure 4.10. The Nusselt number is very high at the inlet and as the flow develops it decreases and achieves a constant value at the outlet. It is seen that after 2 helical turns of the spacer wire the thermal field is fully developed and the Nusselt number is approximately constant.

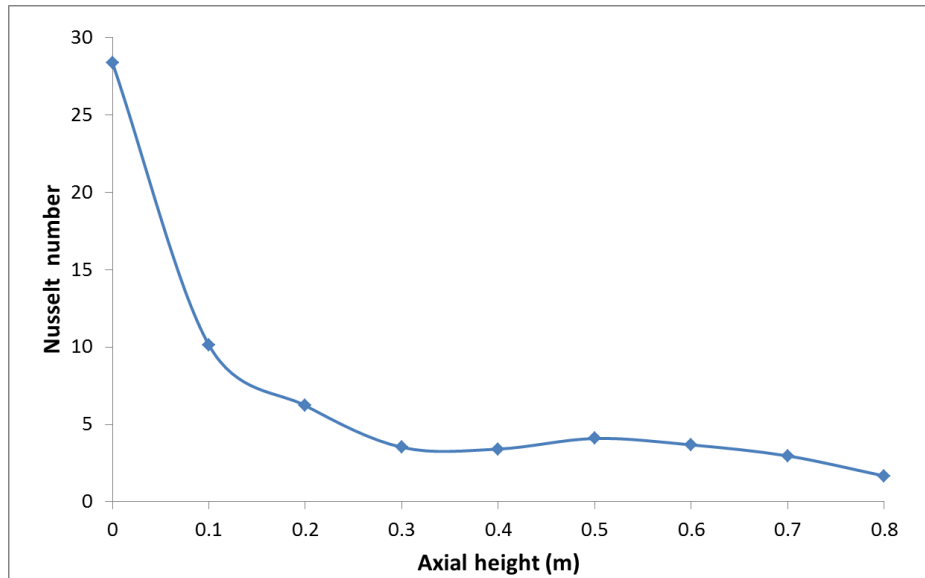


**Figure 4.10-Variation of Nusselt number at the central fuel pin with axial height**

### 4.1.9 Summary

The RANS study of 217 fuel pins sub-assembly gives information about global flow in the steady state. It shows the two regions within the sub-assembly that have different velocity and temperature distributions. The inner central region that is characterized by the higher temperature and the peripheral region around the hexagonal wall where the axial velocity is higher and swirl flow exists leading to lower temperature. The central zone and the periphery region do not have any inter-mixing of the flow. Thus, the sodium flow follows the spacer wire. The mixing effect of the spacer wire is a local phenomenon not a global phenomenon. We also determine the region of local hot-spot at the wake of spacer wire with temperature elevation of about 20°C with respect to the bulk. This study permits us to extract a smaller region of the sub-assembly which has maximum deposition of heat and the flow streamlines confined to this domain.

Therefore, as next step more accurate LES method is used to study the central region of the sub-assembly that has the hottest region and has more possibility of having the hot-spots. The hottest region is identified as central pin with one third of neighboring pins represented by a red hexagon in Figure 4.11. This region will be referred as unit cell. The unit cell represents the central core flow in the sub-assembly and not the peripheral flow near the wall. The central region of the sub-assembly is more heated than the periphery so for hot-spot studies only the central flow is considered.

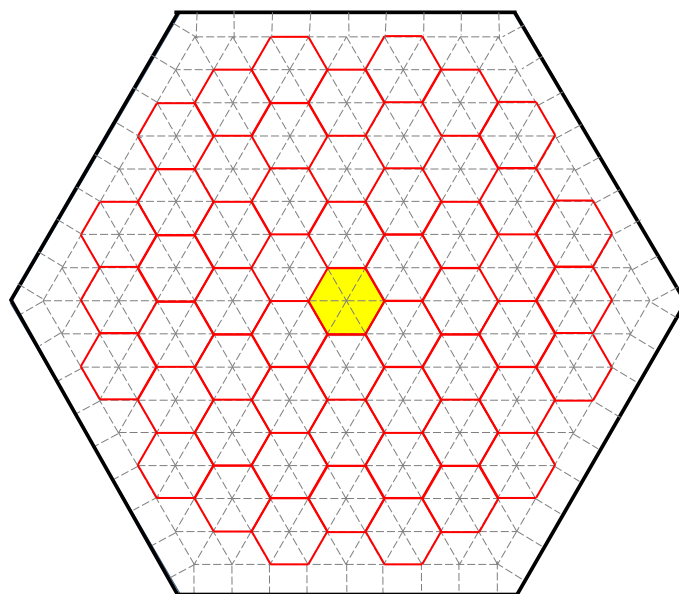


**Figure 4.11-Representation of the selected unit cell (red hexagon) inside the complete 217 fuel pin sub-assembly**

## 4.2 LES

Large Eddy Simulation (LES) method is based on a space filtering method that resolves the large scales of motions and models the small scales of motions. The idea of LES is based on the Kolmogorov theory of self-similarity: large eddies of the flow are dependent on the flow geometry, while smaller eddies are self-similar and have a universal character. In more detail, the large eddies are usually rotational, but their shapes and strengths are flow dependent and highly anisotropic, while the small eddies are much more nearly isotropic and hence easier to model.

LES resolve the large-scale motions of the flow by solving the spatial-filtered Navier-Stokes equations while the effect of the smaller universal scales, the sub-grid scales (SGS), are modelled (Chapter 2). The main advantage of LES over the computationally more efficient RANS approach is the increased level of detail it can deliver. The ability to predict instantaneous flow characteristics and turbulent flow structures is particularly important in simulations of transient phenomena like that of hot-spot studies which have been presented in the following sections.

### 4.2.1 Numerical tool

The LES calculation has been performed using thermal-hydraulic code Trio\_U (Trio\_U, v1.6.8). More information on the code and the discretization can be found in chapter 2. Table 4.6 summarizes the numerical scheme used for LES calculation. An important point to note is that this is not a wall resolved LES but rather an industrial LES calculation (with majority of cells with  $y^+$  around 15) and so wall functions have been used for momentum equation. However, for the energy equation the mesh is refined enough to resolve completely the conductive sub-layer near the wall. This is because of the large thermal conductivity of the sodium that the LES for heat transfer is almost close to a DNS of heat transfer. Therefore no wall functions have been used for energy equation and the turbulent Prandtl number is set to constant value of 3.5 that has been obtained by DNS calculation of sodium at 16000 in Chapter 3. The turbulent Prandtl correlations of Jischa, 1979, Reynolds, 1975 and Cheng, 2006 also gives turbulent Prandtl number of about 4 for sodium at Reynolds number 50000 (Figure 1.13).

<b>Meshing</b>	Tetrahedrons	At least 12 calculation point between pins
<b>Discretization</b>	Finite Volume Elements	P0/P1 for the pressure P1-non conform for velocity and temperature
<b>Time scheme</b>	Semi-implicit	3 <sup>rd</sup> order Adams Bashforth scheme with Facsec=0.8
<b>Momentum transport</b>	Convection	Stabilized centered scheme (Ef_stab with $\alpha=0.5$ )
	Diffusion	2 <sup>nd</sup> order centered scheme
	Wall treatment	Reichardt correlation
	Turbulence	LES with WALE sub-grid model
	Diffusive time step	$8.20352 \cdot 10^{-8}$ s
	Convective time step	$8.75684 \cdot 10^{-7}$ s
<b>Mass conservation</b>	Incompressible fluid	Pressure projection method: petsc cholesky
<b>Energy equation</b>	Convection of temperature	Ef_stab with alpha 1
	Diffusion of temperature	centered
	Wall treatment	No wall law
	Treatment of turbulence	Turbulent Prandtl number, $Pr_t=3.15$
	Diffusive time step	$4.34547 \cdot 10^{-9}$ s
	Convective time step	$8.75684 \cdot 10^{-7}$ s
<b>Final Time step</b>	dt	$7 \cdot 10^{-7}$ s

Table 4.6-Numerical schemes for LES calculations

## 4.2.2 Computational domain

The LES calculation needs very high spatial resolution than RANS so the mesh size and consequently the computational requirements to model sub-assembly with LES approach will be enormous. Therefore, it is not feasible to perform LES calculation of complete sub-assembly and a smaller domain within the sub-assembly has to be identified to perform the LES study. The RANS study presented in section 4.2 helps us to determine a local region of the sub-assembly that with proper boundary conditions is capable of reproducing the flow inside full sub-assembly. This local region is a small regular hexagon with side length equal to pitch of the sub-assembly, P. This will be referred to as a unit cell of the sub-assembly from now onwards. The unit cell shown in Figure 4.9 contains the fluid region around the central pin with one third of each of the 6 neighboring pins so that the 6 triangular sub-channels of the sub-assembly are present in the computational domain. A similar geometry has also been used in the literature for both wire wrapped and bare rod bundles (Fischer, 2007; Ninokata, 2009).

When the unit cell is repeated periodically then it is capable of reproducing the flow in the center of the sub-assembly (Figure 4.11). In axial direction the unit cell contains only one

helical pitch of the spacer wire, H. This is a common approach that has been used in the past to minimize the mesh size and limit the computational resources (Raza, 2008; Natesan, 2010). The geometrical parameters of the selected domain are summarized in Table 4.7. The CAD modelling of this unit cell has been done by solid works (SolidWorks, 2010).

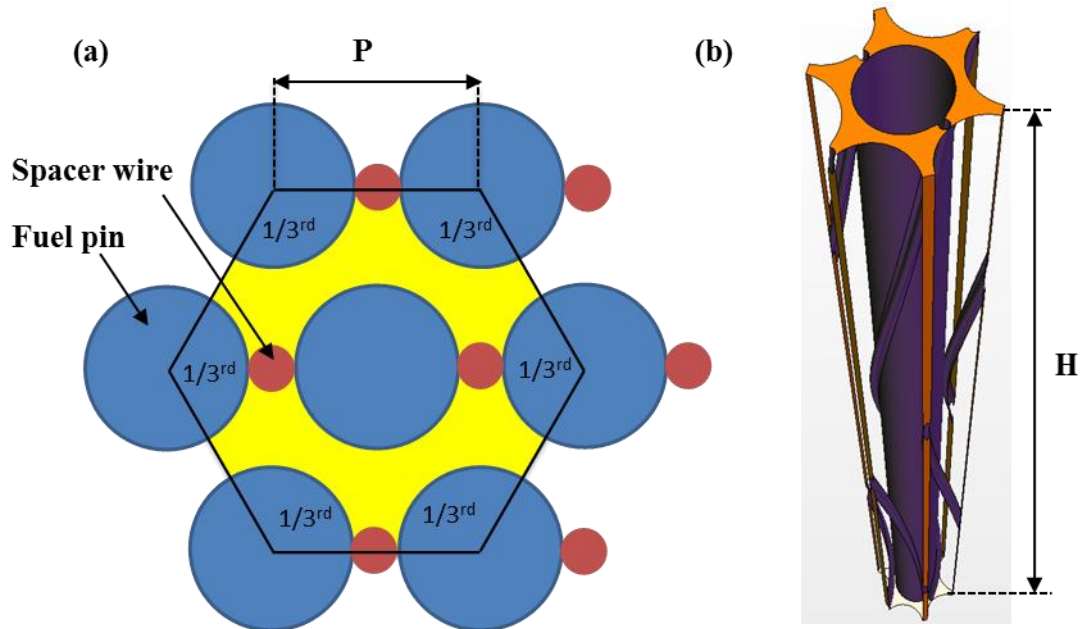


**Figure 4.12-Schematic representation of the unit cell of sub-assembly (a) Transverse cut plane showing the solid part (fuel pin +spacer) and the fluid part (in yellow). (b) Axial view of the fluid domain**

Variable	Description	Value	Units
$D_p$	Diameter of fuel pin	8.57*	mm
$D_w$	Diameter of spacer wire	1	mm
P	Pitch of the fuel pin	9.57	mm
$L_z$	Total axial height	180	mm
$N_{pins}$	Number of pins	$1+6*1/3=3$	
H	Wire-wrapping pitch	180	mm
$A_f$	Flow area	62.905	$mm^2$
$P_w$	Wetted perimeter	85.653	mm
$D_h$	Hydraulic diameter	2.9386	mm

**Table 4.7-Geometrical parameters of the unit cell of sub-assembly for LES calculation**

\* The diameter of fuel pin is slightly smaller than that treated in RANS method because of the evolution of the version of the pre-conceptual design of ASTRID. The LES study has been performed on version 2 CFV core and RANS on CFV version 3.

### 4.2.3 Meshing

The meshing of the unit cell is even more challenging than that of the full sub-assembly because of the following reasons:

- i. The unit cell contains  $1/3^{\text{rd}}$  of the wire wrapped neighboring pins so the boundary wall of the unit cell cuts the spacer wire at an inclined angle as it turns helically. This creates a domain that is very small to mesh and may produce distorted tetrahedral.
- ii. The domain is periodic in axial and radial direction so the mesh has to be identical on the corresponding periodic faces. Also, where the spacer wire cuts the domain at the periodic interface.
- iii. Another challenge is to add prism layers around the wall (fuel pin + spacer wire) to have small sized and uniform cells in order to capture more accurately the wall profile for temperature and velocity. In order to read this mesh in Trio U the prism cells have to be cut in to tetrahedral.
- iv. The cutting of prisms in to tetrahedral should maintain the periodicity i.e. the mesh should remain identical at the periodic faces.

Using the Centaur mesh generator (Centaur\_v.5.1) the above challenges in meshing have been achieved and finally a tetrahedral mesh for the unit cell, containing 4 million cells and 2 prism layers cut in to tetrahedral has been created. There are at least 11 points between the two walls as per the recommendation by Trio U (Figure 4.13) and the presence of prism layers keeps the wall normal distance,  $y^+$  in the range 4 to 40 with majority of the cells having  $y^+ \sim 15$ . The total numbers of nodes in the mesh are 770,000 with 105,000 nodes per wire wrapped fuel pin.

The meshing of unit cell also uses simplification to represent the fuel pin and spacer wire contact point (section 4.2.2). It is a combination of the two methods. Firstly, the radial displacement of wire in to the fuel pin by a distance of  $0.05D_w$  where  $D_w$  is diameter of circular wire into the rod and secondly, blending of the sharp edges with a small radius. This method does not lead the degraded tetrahedrons and reduces the uncertainty in hotspot prediction present in the open wire representation.

The calculation is launched on curie-cluster (TGCC, CEA) using 100 processors that give around 40000 tetrahedral per processor.

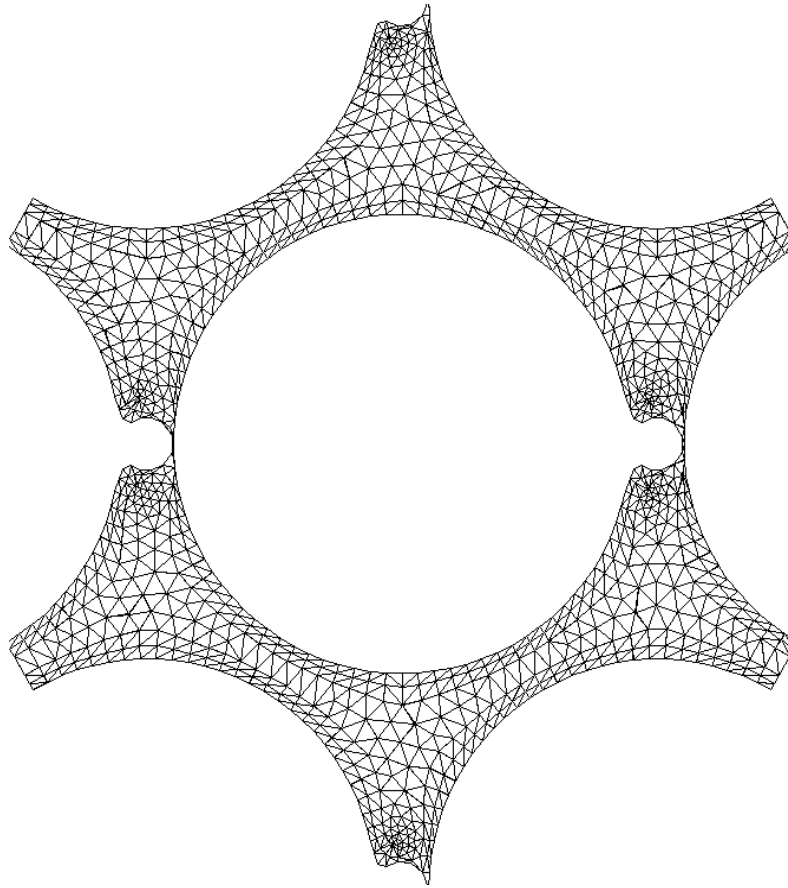


**Figure 4.13-2-Dimensional view of the tetrahedral mesh created by centaur tool**

## **4.2.4 Boundary conditions**

Periodic boundary condition has been used in the transverse and axial direction of the unit cell of sub-assembly. The axial height of 180mm is around 61 times the hydraulic diameter that is large enough to have fully developed turbulent flow. The inlet and outlet of the unit cell has periodic conditions that help to reproduce an infinite domain without the entry and exit effects.

The concept of tri-periodicity is used in the radial direction. It means that the 6 faces in the transverse direction are periodic to their parallel faces giving three periodic faces (Figure 4.14). This condition has also been used in the past by Ninakota et al (Ninakota, 2009) for bare rod bundles and has been recommended by Rolfo et al (Rolfo, 2012) for future DNS/LES calculations. In this study the tri periodicity concept has been used not on one fuel pin but extended over a larger domain containing a section of neighboring pins.

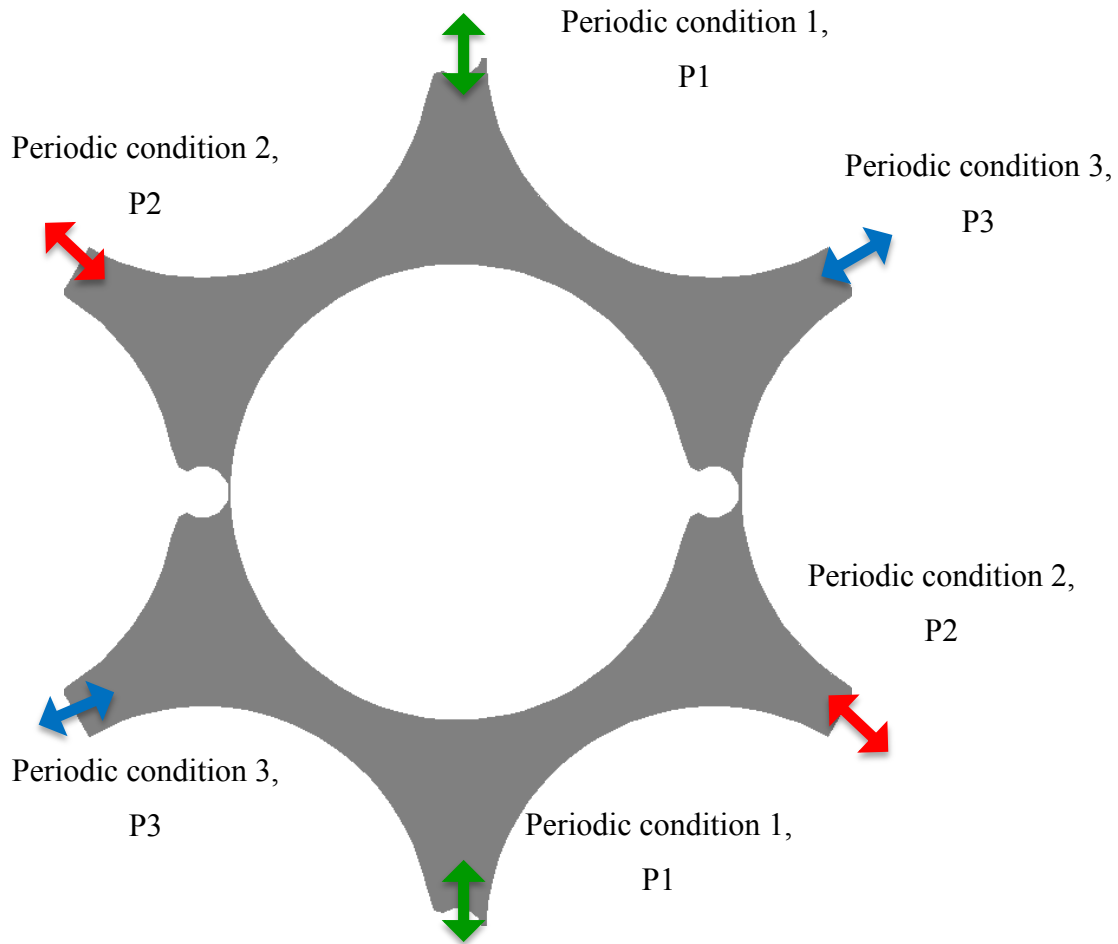


**Figure 4.14-Representation of periodic boundary conditions in radial direction**

A constant heat flux of  $911,427 \text{ W/m}^2$  is imposed on the outer surface of fuel pins and spacer-wire. The same temporally and spatially constant heat flux density is imposed on each rod independently from its axial and radial location. In RANS study, we use the ideal conditions by imposing adiabatic boundary condition. In reality the spacer wire conducts some heat from the fuel pin. An exact estimation of this heat conducted in the wire is difficult. Thus, in order to have safety margin a conservative approach with equal heat flux is imposed on wire. This is an over estimation of real condition in order not to underestimate the value of temperature difference at the hot-spot and temperature fluctuations.

Constant physical properties of the fluid are considered and thermal feedback effects on the flow are neglected. The fluid properties are same as those used in RANS and summarized in Table 4.4.



#### 4.2.4.1 Source term for periodic boundary conditions

The source term for velocity and temperature in the momentum and energy equation is necessary with axial periodic condition to maintain the flow and energy balance in the periodic domain. In Chapter 2, a detailed description of the different source terms used below is given.

The source term  $f(t)$  used for the momentum equation in the periodic direction (z), is defined as follows:

$$f_z(t) = \frac{2(\dot{m}_0 - \dot{m}(t)) - (\dot{m}_0 - \dot{m}(t - dt))}{\rho \text{coeff} dt \text{Area}} \quad (4.12)$$

Where *coeff* is damping coefficient, *dt* is the time step, *Area* represents the area of periodic boundary and  $\dot{m}(t)$  is the flow rate at time *t*. This source term imposes a constant pressure gradient of 152,828 Pa in axial direction.

The source term for energy equation  $S_T(t)$  is defined below:

$$S_T(x, y, z, t) = \frac{q_w}{\rho C_p V u_b} v(x, y, z, t) \quad (4.13)$$

Where  $v(x, y, z, t)$  is the velocity according to the periodic direction, *V* is the volume of the fluid,  $q_w$  is the heat flux imposed on the periodic channel walls and  $u_b$  is the bulk velocity.

#### 4.2.5 Initial conditions

In order to perform LES calculation it is necessary to have a turbulent velocity field at the inlet. Therefore, the calculation has been done progressively in two steps:

- i. Firstly only a hydraulic calculation is launched with constant initial velocity of 4.5853 m/s corresponding to Reynolds number of 41000. The initial flat velocity profile undergoes acceleration in the bulk region of the flow and decelerates to zero near the wall developing the laminar parabolic profile of velocity. The acceleration of the flow at a local point in the center of sub-channel is seen in Figure 4.15. Velocity increases from 4.5 m/s to 6 m/s and then the flow undergoes transition to turbulence at 0.02s (after 28000 time steps). The turbulent flow field is let to be established for another 2 complete axial flow traversals.

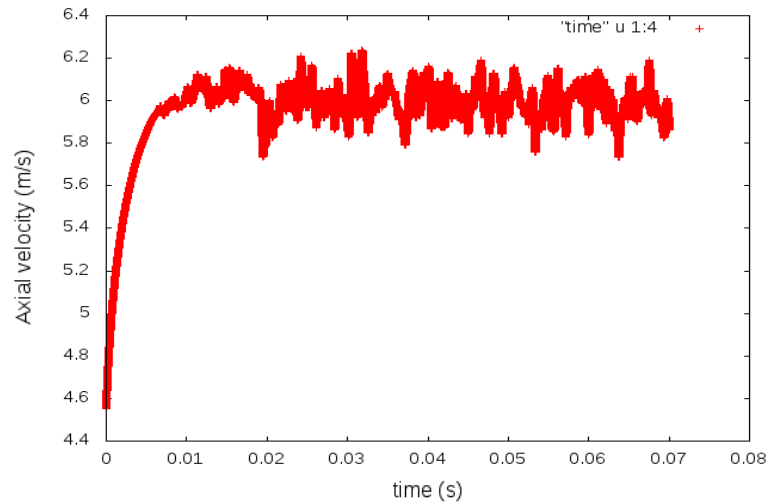


**Figure 4.15-Variation of velocity with time showing transition to turbulence at 0.02s at point (0, -0.005, 0.09) in the center of sub-channel**

- ii. Secondly thermal-hydraulic calculation is launched where the velocity field is initialized with the turbulent velocity of the hydraulic calculation and the temperature field is initialized to 472 °C. The velocity field maintains the turbulent oscillations (Figure 4.16a) and the temperature decreases with time until 0.1s to adjust itself to a constant mean value according to imposed temperature source term (equation 4.7). The random turbulent fluctuations in temperature field can also be seen in (Figure 4.16b). The initial boundary conditions and the final values after turbulence are summarized in Table 4.8.

Thus, the required turbulent velocity and temperature field for LES calculation are obtained by this method.

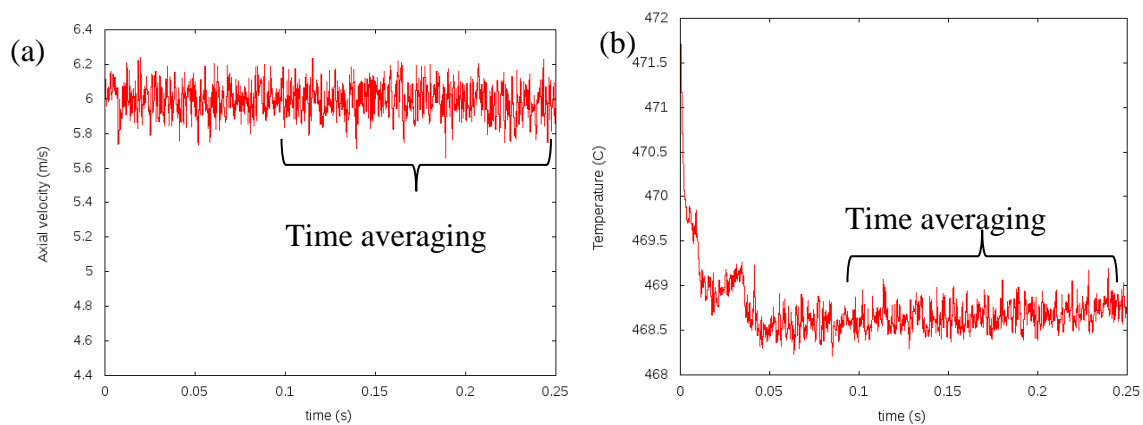


**Figure 4.16-Variation of (a) axial velocity and (b) temperature with time at a local point (0, -0.005, 0.09) in the center of sub-channel**

Variable	Description	Value	Units
$\vec{u}_0$	Initial velocity	(0,0,4.5853)	m/s
$Re_0$	Initial Reynolds number	41,820	
$Re_t$	Final Reynolds number	54,723	
$\overline{w}_t$	Time averaged axial velocity after transition	6	m/s
$t_{transit\_0}$	Initial time for one traversal	0.039	s
$t_{transit\_t}$	Final time for one traversal	0.03	s
$\dot{m}$	Final mass flow rate	0.2415	kg/s
$T_0$	Initial temperature	472	°C
$\overline{T}_t$	Time averaged final temperature for periodic flow	468.5	°C

**Table 4.8-Initial conditions for the thermal-hydraulic LES simulation**

The time averaging is done from 0.1 s to 0.25 s (0.2 million time steps) to obtain higher order statistics. This corresponds to 5 complete traversals in the axial direction (0.15s) that is long enough to capture all the physical phenomena. The results of the LES calculations are presented in the following sections. In the first part, the instantaneous flow field is visualized. After that the time averaged LES results are compared with the RANS results of the complete sub-assembly by extracting the unit cell. Then, axial distribution of temperature in a sub-channel is presented to determine plane with high temperature and then develop the statistical analysis at the desired locations.

## 4.2.6 Flow visualization

The three dimensional view of the turbulent axial velocity can be seen in Figure 4.17. This is extracted on a cylindrical plane at a distance of about 5 mm from the wall. The velocity field clearly shows that the velocity decreases in the wake of spacer wire that acts as an obstacle to the flow. The flow follows the swirling motion of the spacer wire as seen in the streamlines of the flow in Figure 4.18. This phenomenon has been also seen in RANS simulation. The temperature at the central fuel pin surface shows clearly the presence of high temperature zone at the wake of spacer wire. When the spacer wire is very close to the neighboring fuel pin a much more localized high temperature zone of liquid sodium is observed. This is called as hot-spot. We clearly see the hot-spot on the cylindrical fuel pin and the 2-D cut plane.

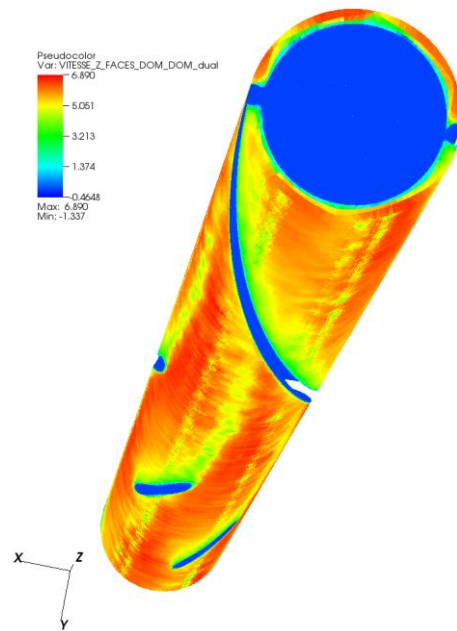


**Figure 4.17-Instantaneous view of axial velocity at 5mm from the central fuel pin**

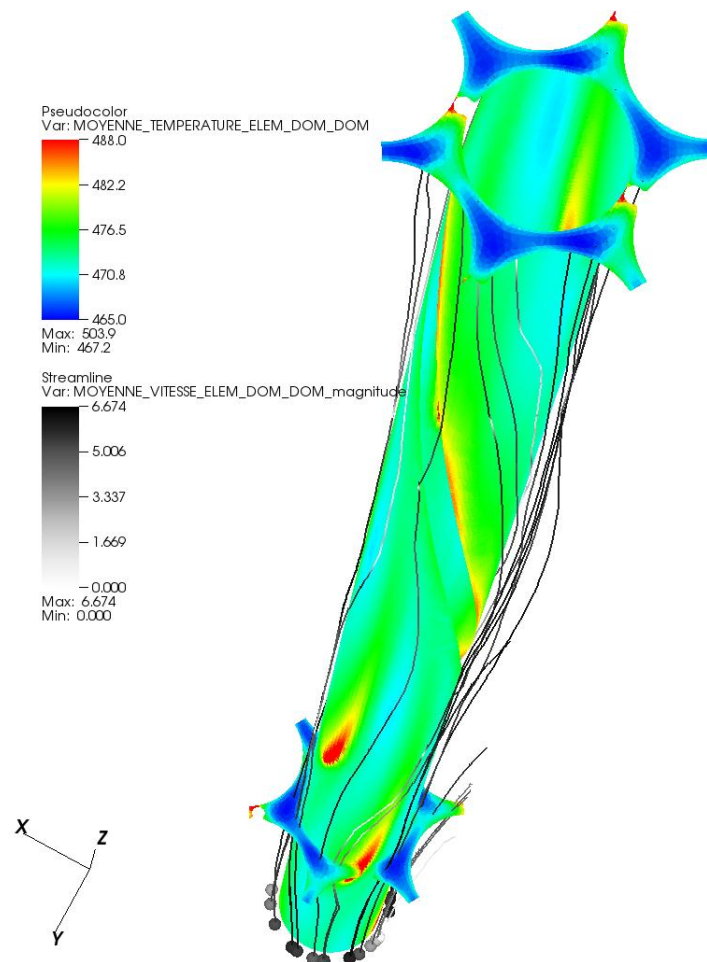


**Figure 4.18-Streamlines of the flow along with time averaged temperature distribution around the central fuel pin**

We will evaluate the thermal characteristics of this hot-spot in the following sections but before that time averaged flow field is compared with the steady state RANS results.

## 4.2.7 Time averaged results – Comparison with RANS study

In the following section, the steady state velocity and temperature field from RANS are compared with time averaged results from LES. This comparison will determine if the flow in complete sub-assembly is well captured by the tri-periodicity in the unit cell studied by LES. In LES we study only one helical pitch of the spacer wire with periodicity in axial direction. In order to make the comparison with RANS study we extract the unit cell domain from the complete sub-assembly near the outlet with same position of the spacer wire. This axial position is equal to  $0.38H$  where  $H$  is the helical pitch of wire in LES. In RANS calculation, the corresponding position is near the outlet at the last helical turn of the wire corresponding to the axial height of 688.4 mm.

### i. Axial velocity distribution

The results from RANS and LES calculation are made by normalizing the axial velocity with the maximum axial velocity (Figure 4.19). The flow fields are similar with the sub-channels in the front of wire with higher axial velocity as compared to the sub-channels behind the wire. The flow field at the periodic boundaries P1, P2 and P3 are also similar.

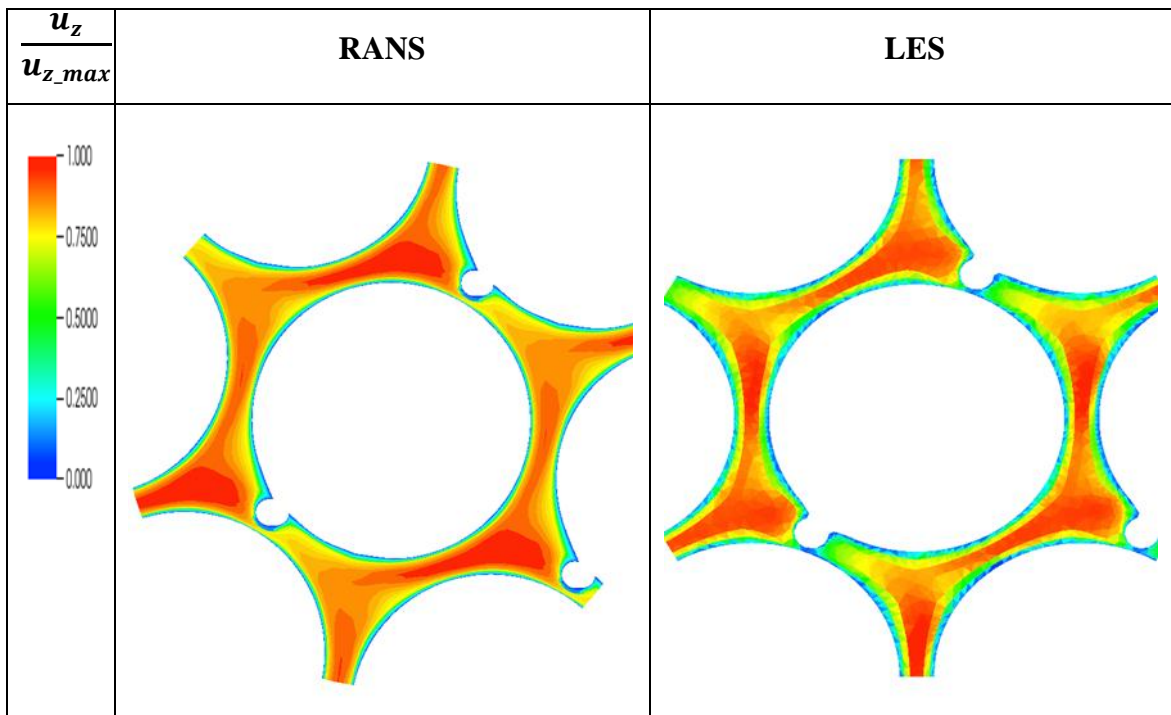
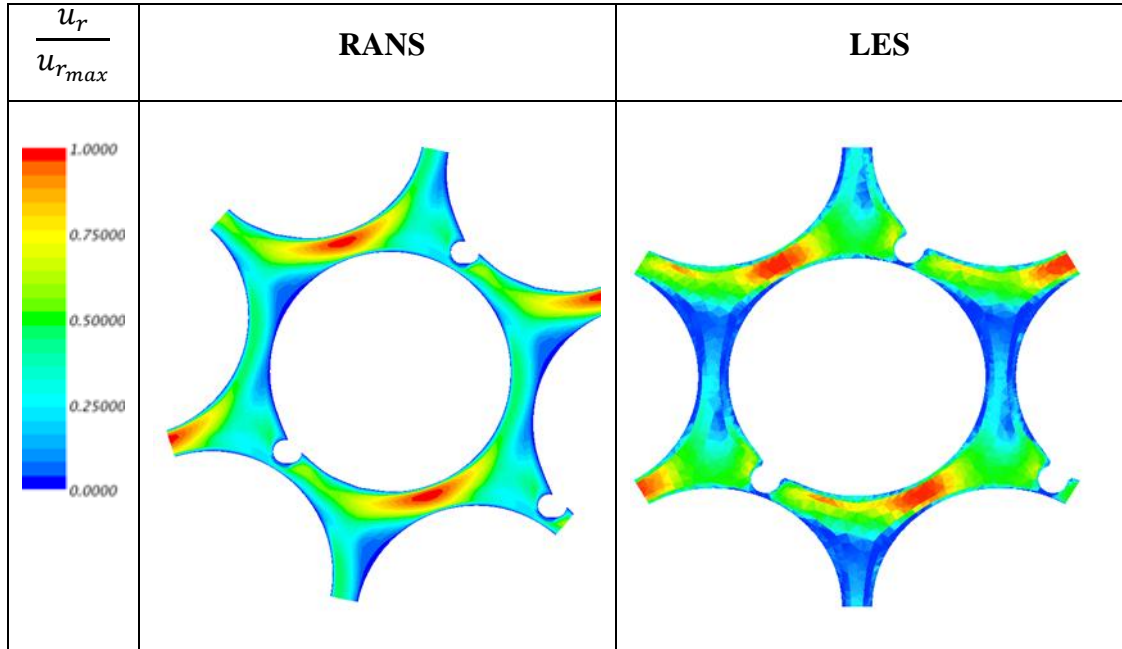


Figure 4.19-Comparison of axial velocity magnitude between RANS and LES

## ii. Transverse velocity

The transverse velocity,  $u_r$  is defined as the velocity in the plane (x-y) perpendicular to the axial direction (z).

$$u_r = \sqrt{u_x^2 + u_y^2}$$



**Figure 4.20-Comparison of transverse velocity magnitude between RANS and LES**

In this case the radial velocity is normalized with the maximum radial velocity (Figure 4.20). The position of maximum transverse velocity is when the two fuel pins are at the minimum distance from each other. The RANS and LES methods give similar distribution of transverse velocity in the plane and at the boundaries. The vector plot of the transverse velocity and the zoom of the region near space wire are shown in Figure 4.21. The region behind the spacer wire shows recirculation zone because the spacer wire obstructs the flow field.

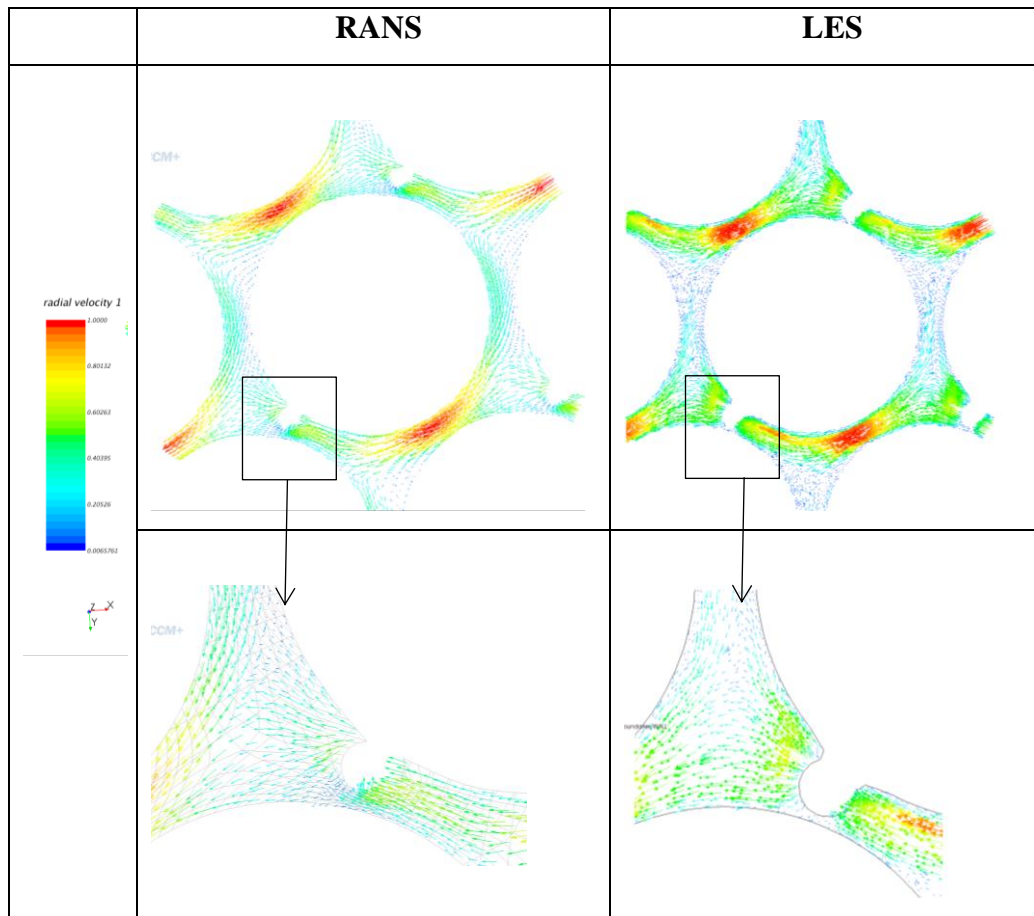


**Figure 4.21-Comparison of transverse velocity (vector) between RANS and LES and zoom over the spacer wire**

### iii. Temperature hot-spot

The hot-spot is the region of maximum fluid temperature near the wall. The region of hot-spot is similar in RANS and LES (Figure 4.22). In LES, the region of hot-spot is extending to larger region than RANS and also the magnitude of maximum temperature differs by  $\sim 2^{\circ}\text{C}$  because of two reasons:

- i. Effect of geometry: The distance between spacer wire and the neighboring pin is around  $0.05 D_w$  in LES and  $0.10 D_w$  in RANS. The wire is much closer to the neighboring fuel pin in LES
- ii. Effect of boundary condition: The wire is adiabatic in RANS calculation and has imposed heat flux in LES calculation. Hence, the fluid near the wire experience more heat energy and more rise in temperature.

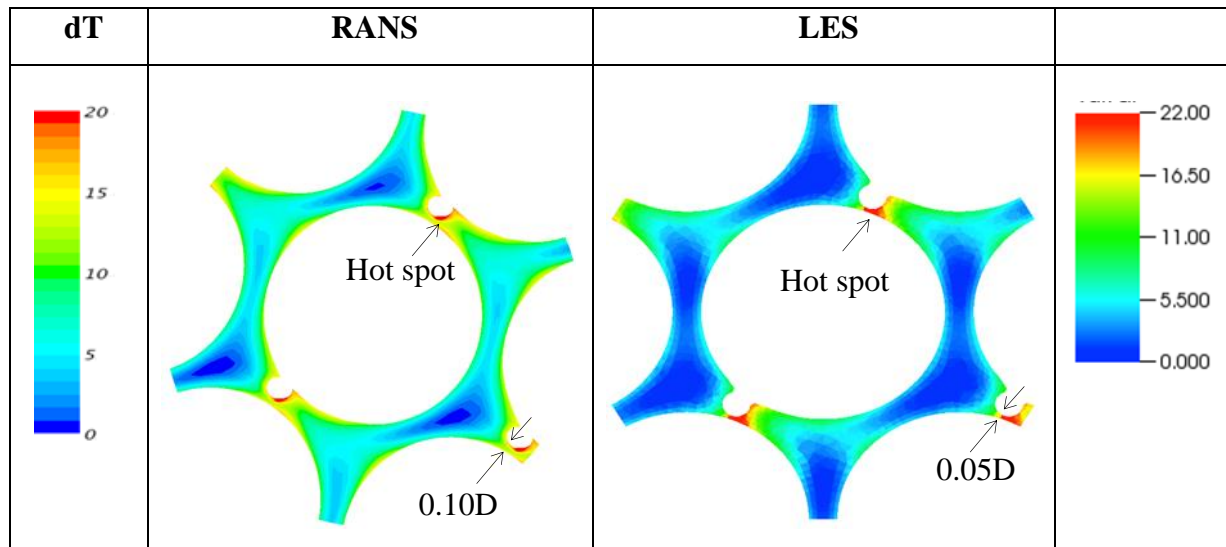


**Figure 4.22-Comparison of temperature drop between RANS and LES**

The above comparison between RANS and LES shows that the selected unit cell with tri-periodic boundary conditions is able to represent the steady state flow in the center of 217 fuel pin sub-assembly. Now in the following sections the LES results will be examined further to have more information about the thermal statistics around the hot-spot which cannot be determined by RANS method.

### 4.2.8 Time averaged results – Axial distribution

The objective of this section is to present the axial distribution of the temperature. The spacer wire is turning helically in the axial direction so in order to determine the position of maximum heating of liquid sodium in the sub-channel. The axial profile of the flow variables has been extracted at the center of each sub-channel. The position and numbering of these sub-channels is shown in 2-D plane in Figure 4.23. The time averaged temperature fields are plotted as a function of ratio of axial distance,  $z$  and helical pitch of the wire,  $H$ .



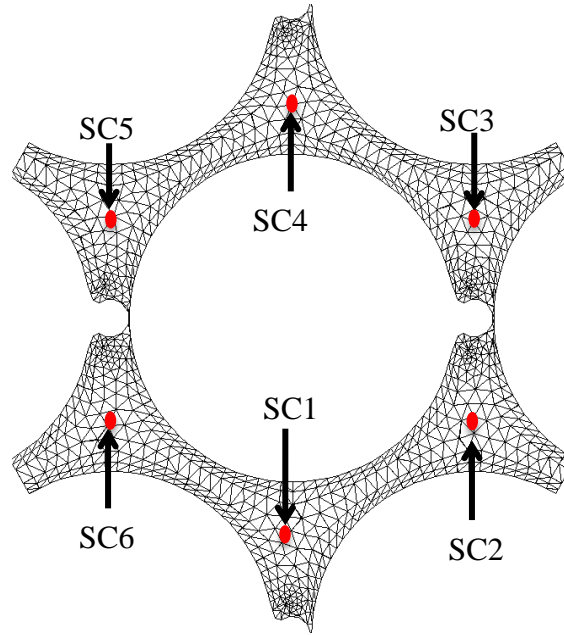


**Figure 4.23-Position and numbering of axial probe in the center of sub-channel referred as SC**

The SC1, SC3 and SC5 are located in the sub-channels that are behind the spacer wire and the SC2, SC4 and SC6 are located in front of the spacer wire at  $z=0$ . Figure 4.24 shows the axial variation of temperature in the sub-channels. In one helical turn of the spacer wire there are total six axial positions of high temperature at  $0.18H$ ,  $0.50H$ ,  $0.80H$  and  $0.03H$ ,  $0.30H$ ,  $0.70H$  from Figure 4.24a and Figure 4.24b respectively. The decrease in the temperature occurs due to helical movement of spacer-wire in the sub-channel. The temperature statistics are now extracted at these planes to study the hot-spots.

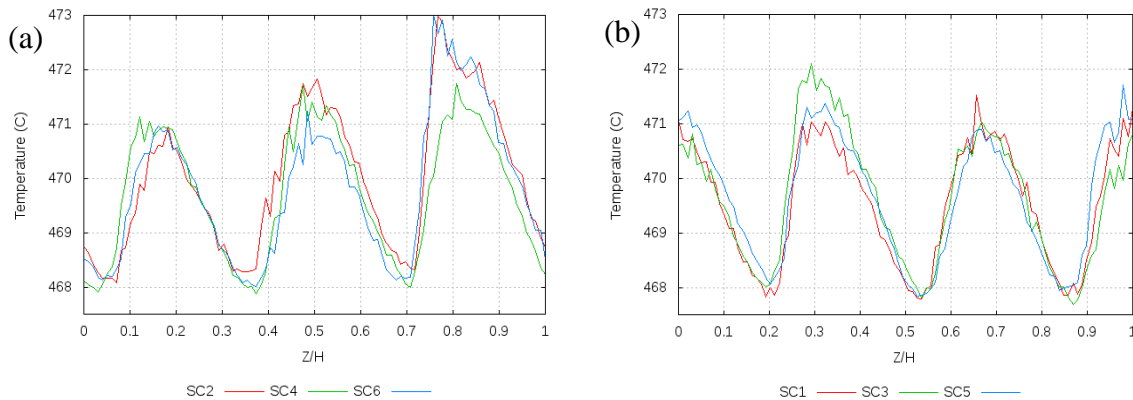


**Figure 4.24-Axial variation of temperature in the sub-channel probes (a) Sub-channel probe 2,4,6 and (b) sub-channel probe 1,3,5 (refer to figure 4.20 for labels SC)**

The axial probes at center of the sub-channel give the height,  $H$  at which maximum temperature was observed. We define 2-D planes at these axial positions to obtain time averaged values of maximum temperature and average temperature in these planes. Table 4.9 shows the values obtained at these planes.

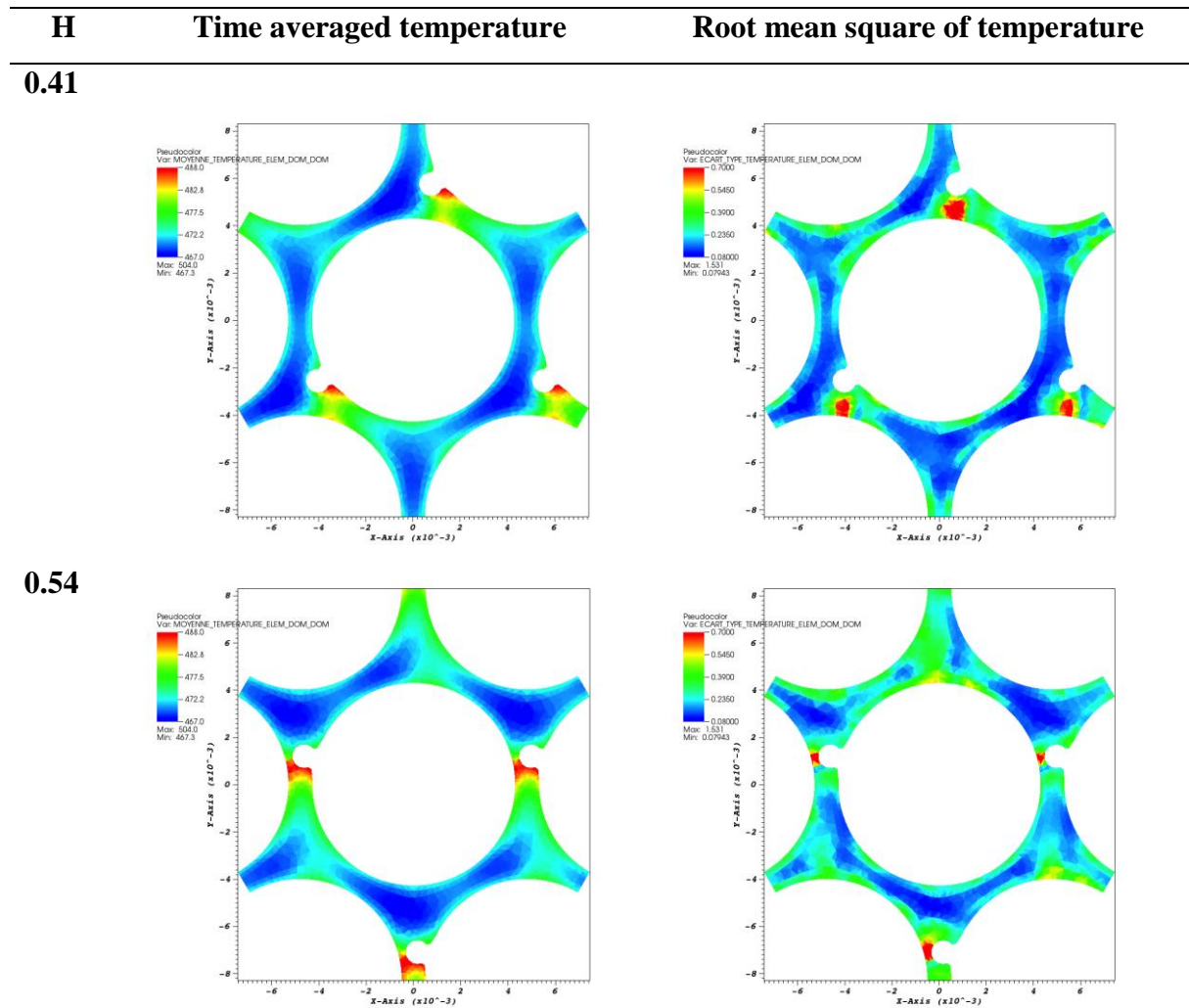
$H$	$T_{\text{maximum}}$	$T_{\text{average}}$	$\Delta T$
0.04H	490.3	472.10	18.2
0.20H	489.62	472.24	17.38
0.36H	489.12	472.18	16.94
0.52H	488.40	472.46	15.96
0.68H	489.48	472.33	17.15
0.84H	490.01	472.34	18

**Table 4.9-Space and time averaged temperature at different plane to estimate the hot-spot temperature**

The difference between maximum and average temperature in the plane gives an estimation of the peak sodium temperature in the central sub-assembly that is called as hot-spot temperature. With the axial height we do not observe a big difference in the hot-spot temperature. The hot-spot has temperature elevation of around  $17^{\circ}\text{C}$  with respect to the bulk average temperature.

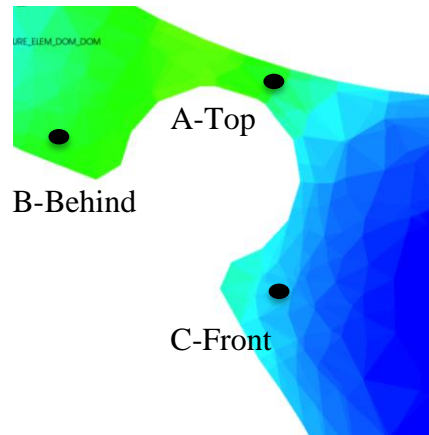
### 4.2.9 Statistics of order 1: Root mean square values

Figure 4.25 shows the root mean square of the temperature field at two different heights 0.41H and 0.54H along with the time-averaged temperature. The maximum value of temperature root mean square ( $T_{\text{rms}}$ ) is  $0.7^{\circ}\text{C}$  and maximum value of temperature is around  $21^{\circ}\text{C}$ . The distribution of root mean square temperature in the plane shows that region of high fluctuation of temperature is present around the spacer wire and they move to different locations at different height. At height equal to 0.41H the region of high temperature fluctuations is behind the spacer wire and at height 0.54H the region of high temperature fluctuations is in top of the wire.



**Figure 4.25-Time averaged temperature and root mean square of temperature at different planes**

Therefore, in order to estimate the fluctuations of temperature around the spacer wire 3 positions are identified: top of spacer wire (A), behind the spacer wire (B) and in front of spacer wire (C) as shown in Figure 4.26.



**Figure 4.26-Three positions around the spacer wire to determine the temperature fluctuations**

Point probes are placed at these three positions around the spacer wire at different axial height. The root mean square of temperature is evaluated at these positions as a function of axial height. Figure 4.27 shows that the maximum temperature fluctuations are present at the top position of the spacer wire and the order of magnitude is around twice to the value at the position behind the spacer wire. The front position of the wire facing the flow has minimum temperature fluctuations.

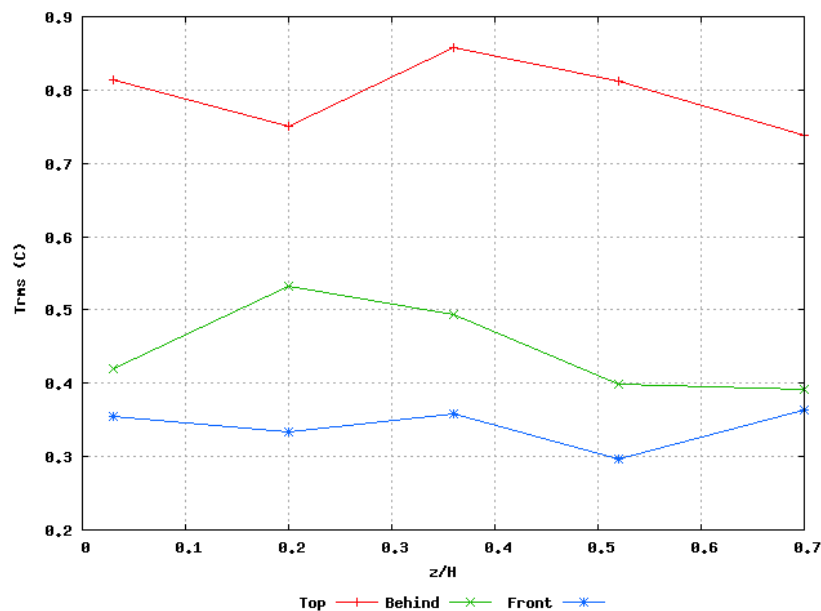


**Figure 4.27-Temperature fluctuations as a function of axial position for three positions around the spacer wire**

Therefore, the hot-spot at the position top and behind the spacer wire has temperature elevation of about 18°C and the root mean square of temperature fluctuations of around 0.8 °C. By taking in to account the difference of factor of 2.5 between the temperature fluctuations evaluated by LES and DNS methods in Chapter 3 we obtain maximum order of temperature fluctuations of about 2°C. The magnitude of temperature oscillations is not very high to induce the safety risk from the point of view of mechanical strength of clad (Chellapandi, 2009). However even with lower magnitude of the temperature oscillations we can obtain dominant frequency of oscillations that can degrade mechanical strength. Therefore the Power spectra is analyzed in next section to evaluate the frequency of temperature oscillations.

#### 4.2.10 Power spectral density

Power spectra density (PSD) is invaluable tool to interpret the turbulent mixing in the context of thermal fatigue problem. Thermal fatigue is defined as cyclic temperature fluctuations at the walls leading to crack initiations and growth. Most common example of thermal fatigue problem in Nuclear Power Plants (NPP) are T junctions in the primary circuit piping. The problem arises when the side flow of the fluid at higher temperature merges with the main fluid flow at lower temperature leading to temperature fluctuations. These temperature fluctuation leads to variable thermal loading in the pipe walls creating the problem of thermal fatigue. The same problem may or may not arise at the region of the hot-spot present at the wake of spacer wire. It is possible that the scalar fluctuations in magnitude are not threatening at the first glance but they have a frequency that can lead to problem like thermal fatigue in the clad.

The PSD of the temperature fluctuations (denoted by  $x$ ) is defined as follows:

$$PSD = |\hat{x}(\omega)|^2 = \frac{\left| \int_0^T x(t) e^{-i\omega t} dt \right|^2}{x} \quad \text{where } x = T - \bar{T} \quad (4.14)$$

The most damaging high cycle fluctuation frequencies have been determined to be between 0.1 to 10 Hz (Noda, 2003; Hannik, 2011; Radu, 2007). Figure 4.24 shows the PSD for the frequencies in this range obtained from the publication of Chellapandi et al (Chellapandi, 2009). The frequencies greater than 10 Hz not produce significant temperature gradient in the wall profile and the frequencies lower than 0.1 Hz give the wall sufficient time to relieve the internal stress caused by the constrained thermal expansion.

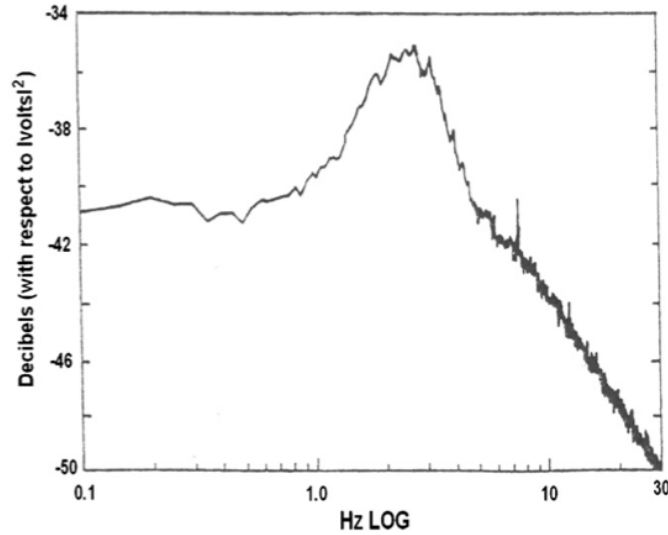


**Figure 4.28-Power spectral density of a typical thermal stripping (Chellapandi, 2009)**

In order to evaluate the frequency of temperature oscillations in the hot-spot region the PSD is performed at the three positions around the spacer wire. The three positions are front, top and behind the spacer wire at 6 different axial locations. The PSD is independent of the size of time window thus the signal is random and sufficiently long for PSD.

The spectra are same at different axial height. The mean of the PSD at different height is compared at the three different positions around the spacer wire with a point far from the spacer wire to see how the spacer wire affects the PSD. It is shown in Figure 2.29. We observe that follow the universal Kolmogorov 5/3 law. The amplitude of energy spectra is higher around the spacer wire as compared to the position far from the spacer wire. The spectrum at three different positions around the spacer is almost the same except in the low frequency range. It does not show a dominant low frequency oscillation peak.

The ratio of thermal effusivity between the effusivity of solid and solid clad material plays an important role to determine if these oscillations propagate in solid or not. The effusivity of a material  $E_f$  is defined as ability to exchange the thermal energy with the surroundings. It is given as square root of product of thermal conductivity  $\lambda$ , density,  $\rho$  and heat capacity,  $C_p$ .

$$E_f = \sqrt{\rho \lambda C_p} \quad (4.15)$$

The ratio of effusivity of fluid and wall determines the interface temperature. If the effusivity of solid wall is very low as compared to that of liquid sodium ( $E_f=8516$ ) is large then the interface temperature is determined by fluid and temperature fluctuations can propagate the wall (Manod, 2012).

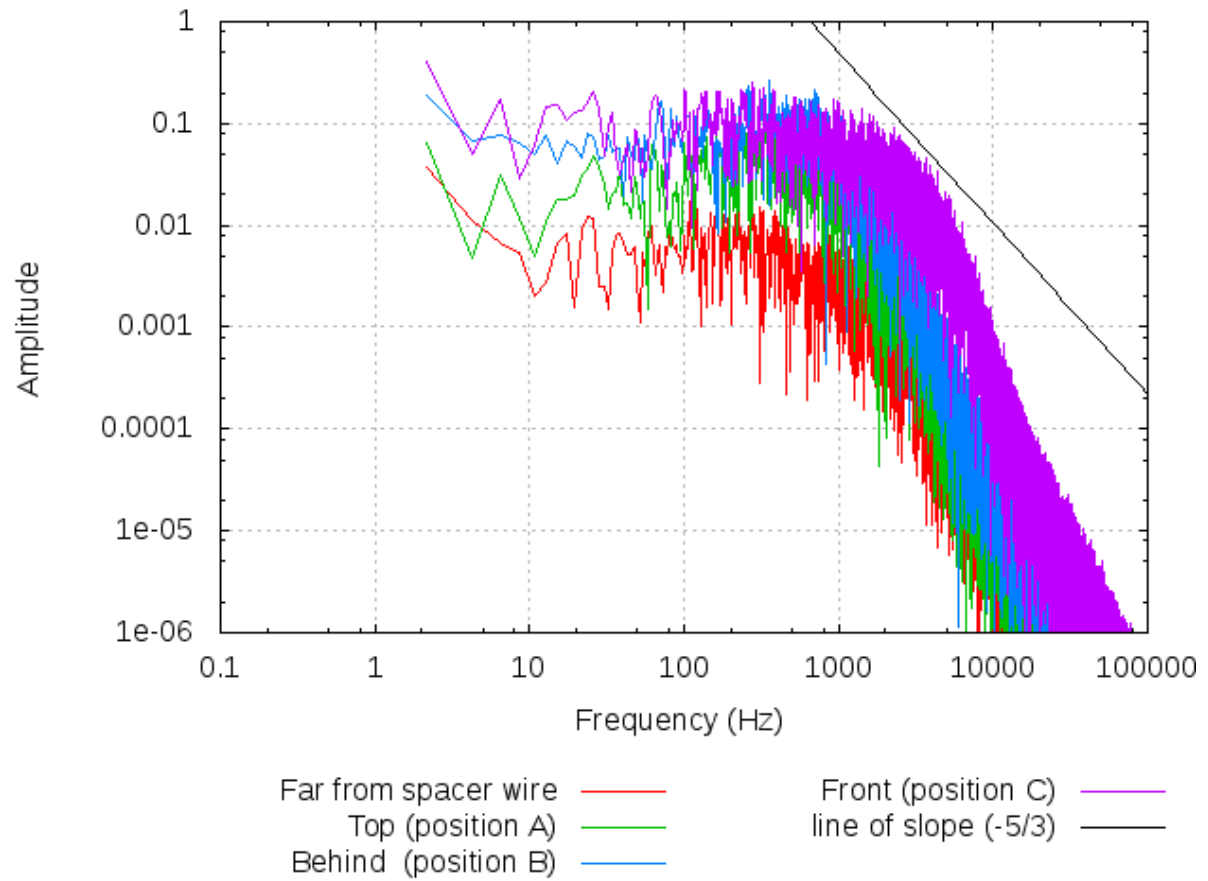


**Figure 4.29-Comparison of power spectra density at three positions around the wire and distance away from spacer wire**

## 4.3 Summary

The LES study of the unit cell of the sub-assembly shows that it well represents the flow in sub-assembly. The peak fluid temperature is present at two locations. The first position is behind the spacer wire and second position is at the top of spacer wire when it comes close to neighboring fuel pin. This peak fluid temperature is called as region of hot-spot. The temperature difference between the hot-spot and bulk temperature at the plane is around 17 °C. The fluctuations of temperature at the hot-spot are about 0.5°C to 0.8°C depending on their position. Taking in to account the difference of factor 2.5 the magnitude of temperature fluctuations are about 1°C to 2°C. The high thermal conductivity of sodium and conduction as the dominant mode of heat transfer transfers quickly the heat deposited in a region with low velocity. The Power Spectra Density (PSD) shows absence of low frequency peak in the range 2 to 10Hz. The mechanical study using this PSD can give an idea whether it poses a threat of thermal fatigue problem.



# CONCLUSIONS

---

The main objective of the thesis is to perform thermal hydraulic study of the turbulent sodium flow inside the sub-assembly of Sodium-cooled Fast Reactor, such as the ASTRID prototype. A correct evaluation of thermal as well as hydraulic characteristics at a local region around the spacer wire in the sub-assembly is important for the safety of the reactor. The study has been performed using Computational Fluid Dynamics (CFD) at nominal conditions for the single phase flow of liquid sodium.

The state of art for the current knowledge of heat transfer in sodium and thermal hydraulic studies of sub-assembly is presented in Chapter 1.

Liquid sodium is characterized by very low Prandtl number ( $Pr \sim 0.001$ ) as compared to water ( $Pr \sim 1$ ). The DNS studies for low Prandtl number fluids available in the open literature for the academic test cases like turbulent channel flow, pipe flow and flow in concentric cylindrical pipe have been limited to  $Pr \sim 0.01$ . These studies show that for low Prandtl number fluids the temperature field is much smoother than the velocity field, and for moderate Reynolds number (around 50000 to 70000) the heat transfer at the wall could be essentially molecular conduction while the flow is fully turbulent. The classical Reynolds analogy hypothesis that is used in RANS and LES methods introduces the concept of turbulent Prandtl number ( $Pr_t$ ). The default value of  $Pr_t \sim 1$  cannot determine the thermal field in low Prandtl number fluids correctly. The lowest Prandtl number studied in the open literature is limited to 0.01 and effect of lowering the Prandtl number from 0.01 to 0.001 on thermal fields is missing. Therefore, we first evaluate the heat transfer characteristics of liquid sodium ( $Pr \sim 0.001$ ) using DNS method.

The DNS study is performed using University in-house code to model the turbulent heat transfer in fully developed turbulent flow of liquid sodium in concentric annulus with iso-flux walls. This is a simplified geometry that is representative of the sodium flow in sub-assembly. This geometry is also encountered in other engineering applications like control rods and heat exchangers.

This study gives insight to the thermal field of sodium and the main learning from this study is listed below:

- i) **Computational domain:** The thermal structures in sodium are very large in axial and azimuthal direction. Thus, a longer computational domain is required to capture these thermal structures.
- ii) **Thermal Turbulence:** The temperature field in sodium can remain homogeneous even if the flow field is turbulent. The temperature field evolves very smoothly along the wall because in sodium molecular conduction dominates the heat transfer at the wall unlike for the fluids like water or air where convection dominates over conduction. As a result, the thermal field for sodium shows stratification in radial direction. The thermal stratification is a beneficial effect in sub-assembly as sodium can provide effective cooling even at low velocity.
- iii) **Temperature fluctuations:** The magnitude of temperature oscillations is very low in sodium as compared to that in air or water. We observe that in case of sodium at Reynolds number 8900, the non-dimensional r.m.s. of temperature fluctuations are smaller by a factor of around 200 in magnitude as compared to that in air and the position of maximum temperature fluctuations moves away from the wall for sodium.
- iv) **Effect of Reynolds number on thermal field:** A stronger effect of Reynolds number is observed on the thermal field of sodium. This is mainly because the reduction in Reynolds number has stronger effect on the temperature fluctuations and turbulent heat fluxes. The mean non-dimensional temperature, however, remains unaffected.
- v) **Turbulent Prandtl number:** The value of turbulent Prandtl number ( $Pr_t$ ) for sodium is more than 1 and it shows high sensitivity to Reynolds number for low turbulent flow. With the decrease in Reynolds number from 16000 to 8900, the  $Pr_t$  increase from 3.5 to 10. The correlations for  $Pr_t$  in the open literature shows large variation of Prandtl number from 2.5 to 15 at 16000 and 8900 Reynolds number. These correlations have been developed for fluids with  $Pr \sim 0.01$ . Therefore, we need new correlations to determine correctly the turbulent Prandtl number.

As a next step we study the same domain as in above DNS study by LES approach that can be used later to study the sub-assembly. Thus LES approach uses wall function for velocity and unstructured tetrahedral mesh with prism layers.

Comparison between DNS and LES results shows that the velocity gradients near the wall are under predicted in LES but the overall profile of r.m.s velocity fluctuations and turbulent kinetic energy is well predicted. But the peak values are under predicted because in LES we model small scale structures by sub-grid scale model. This however does not affect the temperature field as we found an excellent agreement between DNS and LES results for the mean temperature. This is mainly due to heat transfer dominated by molecular conduction in liquid sodium. Therefore, in liquid sodium flow even if velocity field is not captured correctly still the temperature field can be well predicted by LES. This probably may not be true for water or air.

However, the temperature fluctuations are under estimated in LES. With optimization of the temperature source term the difference in temperature fluctuations was reduced to a factor around 2.5 but could not be reduced further. This is due to numerical dissipation coming from the use of upwind convection scheme unlike in DNS that uses non-dissipative energy-centered scheme. We take into account this difference of factor 2.5 in the results of temperature fluctuations while working with sub-assembly geometry.

The DNS calculation and comparison with LES approach is followed by the thermal-hydraulic study of the SFR sub-assembly in Chapter 4. The RANS study of 217 fuel pins sub-assembly gives information about global flow in the steady state. It shows the two regions within the sub-assembly that have different velocity and temperature distributions. The inner central region of the sub-assembly has comparatively higher temperature whereas the peripheral region around the hexagonal wall with higher axial velocity has lower temperature. The flow remains confined to the spacer wire creating local mixing of the flow but the intermixing of the flow between the two different regions of sub-assembly is not observed. It also identifies the hot-spot (region of peak fluid temperature) present behind the spacer wire at temperature difference of around 20°C from the minimum value.

The widely used RANS approach is simple and less time consuming but it involves modelling of all length and time scales of turbulent motion and gives steady state flow features. Therefore, as next step, LES calculations are performed that have higher accuracy in terms of resolution of turbulent structures. They can give details about the temperature oscillations and frequency spectra at these hot-spot.

The LES study is performed on a small unit cell that can represent the flow in the complete sub-assembly with periodic conditions. This unit cell contains the central fuel pin that is the hottest region with one third of neighboring 6 pins and studied for one helical pitch of the spacer wire. The LES calculation performed in the thesis respects the real geometry of sub-assembly and flow conditions of sodium with  $Pr=0.001$  and  $Re=50000$ . This calculation being close to reactor conditions helps us to characterize the flow around spacer wire and answer the questions of existence of “hot-spot” in sodium cooled wire-wrapped fuel sub-assembly.

The LES study of the unit cell shows that the hydraulic and thermal fields are well represented by periodic conditions. We observe that the peak fluid temperature is present at two locations. The first position is behind the spacer wire as found in RANS study and second position is at the top of spacer wire when it comes close to the neighboring fuel pin. The temperature difference between the hot-spot and bulk temperature at the plane is around  $18^{\circ}\text{C}$ . The statistics obtained at these hot spots gives r.m.s of temperature fluctuations of about  $1^{\circ}\text{C}$  to  $2^{\circ}\text{C}$  depending on their position by taking in to account the difference of factor 2.5.

The high thermal conductivity of sodium transmits these temperature fluctuations quickly to the solid wall. The ratio of thermal effusivity between the effusivity of solid and solid clad material determines if these oscillations propagate in solid or not. If the effusivity of solid clad material is very high than that of fluid then the solid wall will not see these fluctuations. However, in the contrary case, the fluctuations in fluid will be transferred to the solid wall.

Apart from the amplitude of the temperature oscillations, the frequency of temperature oscillations plays an important role in characterizing the mechanical strength. The Power Spectra Density (PSD) of the temperature fluctuations evaluated at different regions around the spacer wire shows absence of any dominant peak for frequency lower than 10Hz. Whether this PSD poses a threat of thermal fatigue problem and affect the mechanical strength of clad can be determined only by using this PSD as the input for further mechanical analysis. In this thesis we have given the input required for future mechanical analysis.

# FUTURE PERSPECTIVES

---

There are numerous future perspectives of this study.

A more accurate estimation of the temperature oscillations can be given by DNS method where the small length and time scales of the flow and thermal structures are completely resolved with numerical schemes having higher order of accuracy. This study can show the effect of an obstacle on the thermal stratification in sodium flow.

Another perspective of this work is the representation of solid fuel pin and wire in the computational domain. In the current study, we focused only on the hot-spot in the fluid domain of the sub-assembly and the effect of solid fuel pin and wire was represented with constant heat flux boundary condition. However, a more accurate estimation of the hot-spot, which can probably affect the mechanical integrity of the clad, should include the solid part of the sub-assembly representing the fuel pellets, spacer wire and cladding that can take into account the anisotropy of heat flux.

In the LES study of the sub-assembly we focused on the central fuel pin for the thermal-hydraulic analysis under forced convection in nominal conditions. At the scale of single fuel pin this study does not show any strong consequences of the existing hot-spot. However, there are other aspects to this problem:

- The sub-assembly during the life of nuclear reactor undergoes deformation due to irradiation. This results in phenomena like bowing and swelling of the fuel pin leading to loss of symmetry in the sub-assembly. The thermal-hydraulics will change substantially in this condition and may impose threat due to insufficient cooling by sodium.
- The thermal-hydraulics of the sub-assembly are strongly dependent on the geometrical parameters like ratio of fuel pin diameter to diameter of spacer wire ( $D_p/D_w$ ) and ratio of helical pitch to fuel pin diameter ( $H/D_p$ ). For instance the THERMOS experiment performed in CEA in 1980's in Rapsodie reactor shows that slight variation in geometrical parameters can lead to elevation in temperature. After 270 days of

irradiation, one of the sub-assemblies with modified geometrical parameters underwent clad failure near the outlet leading to emergency shutdown of the reactor. The source of this clad failure is not well known. It can have both mechanical as well as thermal hydraulic reasons. The thermal-hydraulic studies performed in the past used empirical correlations and now with the advent of CFD techniques, new thermal-hydraulic analysis of this problem is essential at the scale of sub-assembly.

These are few inevitable studies to ensure the structural integrity of ASTRID CVF-v3 sub-assembly.

# BIBLIOGRAPHY

---

- Abe, H., Kawamura, H. and Matsuo, Y. (2004).** “Surface heat-flux fluctuations in a turbulent channel flow up to  $Re_\tau = 1020$  with  $Pr = 0.025$  and  $0.71$ ”, *Int. J. of Heat and Fluid Flow*, Vol. 25, 2004, pp. 404-419.
- Abe, H. and Kawamura, H. (2002).** “A study of turbulence thermal structure in a channel flow through DNS up to  $Re_\tau = 640$  with  $Pr = 0.025$  and  $0.71$ ”, *9th European Turbulence Conference*, pp. 399–402.
- Abe, H., Kawamura, H. and Matsuo, Y., (1998).** “DNS of turbulent heat transfer in channel flow: near-wall turbulence quantities”, *In: Proceedings of the 13th Australasian Fluid Mechanics Conference*. Melbourne, Australia, pp. 849–852 (13–18 December).
- Abide, S. and Viazzi, S. (2005).** “A 2D compact fourth-order projection decomposition method”, *Journal of computational physics*, Vol. 206, 2005, pp. 252–276.
- Ackerman, C. (2000).** «Développements et validation de simulation des grandes échelles d’écoulement turbulents dans un code industriel», *Ph.D. thesis*, Institut National Polytechnique de Grenoble, 2000.
- Aloki, S., (1963).** “A consideration on the heat transfer in liquid metal”, *Bull. Tokyo Institute of Technology*, Vol. 54, 1963, pp. 63–73.
- Arwika, K. F. (1979).** “Heat transfer, momentum losses and flow mixing in a 61-tube bundle with wire-wrap”, *Nuclear Engineering and Design*, Vol. 55, 1979, pp. 403-417.
- Azer, N.Z. and Chao, B.T. (1960).** “A mechanism of turbulent heat transfer in liquid metals”, *Int. J. of Heat Mass Transfer*, Vol. 1, 1960, pp. 121–138.
- Azouz, I. and Shirazi, S.A., (1998).** “Evaluation of several turbulence models for turbulent flow in concentric and eccentric annuli”, *ASME J. Energy Resour. Technol.* Vol. 120, 1998, 268–275.
- Baglietto, E. and Ninokata, H. (2003).** “Turbulence model evaluation for heat transfer simulation in tight lattice fuel bundles”, *In: Proceedings of the NURETH-10*. South Korea.

- Baglietto, E. and Ninokata, H. (2005).** “A turbulence model study for simulating flow inside tight lattice rod bundles”, *Nuclear Engineering and Design*, Vol. 235, 2005, pp. 773-784.
- Baglietto, E. (2007).** “RANS and URANS Simulations for Accurate Flow Predictions Inside Fuel Rod Bundles”, *In: Proceedings of the ICAPP'07*, Nice, France.
- Berger, R. and Lapie, J. (1975).** «CFNa II - Détection d'ébullition par analyse des bruits de température», *Compte rendu d'essais du 25 Juin et du 1er Juillet 75*. C.E.A.
- Berthou, M. and Carenza, A. (2008).** “Pressure loss and heat exchange in a rod bundle representative of ETDR start-up core: ESTHAIR experiment in hot air similarity”, *In: Proceedings of the NUTHOS-7*, Seoul, Korea, October 5–9.
- Bieder U. (2010).** “CFD Calculations Of wire wrapped fuel bundles: modelling and validation strategies”, *CEA-Grenoble, DEN/DER/SSTH/LDAL*.
- Bieder U., Fauchet G., Bégin S., Kolev N. and Popov D. (2005).** “Simulation of mixing effects in a VVER-1000 reactor”, *In: Proceedings of the 11<sup>th</sup> International Topical Meeting on Nuclear Reactor Thermal-Hydraulics-NURETH-11*, Avignon, France, October 2–6, 2005.
- Bieder U., Calvin Ch. and Mutelle H. (2003).** Detailed thermal hydraulic analysis of induced break severe accidents using the massively parallel CFD code Trio U [Conference] *In: Proceedings of the International Conference on Supercomputing in Nuclear Applications*. - Paris, France, September 22–24, 2003.
- Bieder U., Calvin Ch. and Emonot P. (2000).** Priceless: an object oriented code for industrial large eddy simulations. *In: proceedings of 8<sup>th</sup> annual conference of the CFD society of Canada*. Montreal, Canada, June 11–13, 2000.
- Bishop, A.A, and Todreas N. (1980).** “Hydraulic characteristics of wire-wrapped rod bundles.” *Nuclear Engineering and Design* Vol. 62, 1980, pp. 271-293.
- Bricteux, L., Duponcheel, M., Winckelmans, G., Tiselj, I. and Bartosiewicz, Y. (2012).** “Direct and large eddy simulation of turbulent heat transfer at very low Prandtl number: Application to lead–bismuth flows”, *Nuclear Engineering and Design*, Vol. 246, 2012, pp. 91–97.
- Bubelis, E. and Schikorr, M. (2008).** “Review and proposal for best fit of wire-wrapped fuel bundle friction factor and pressure drop predictions using various



- existing correlations”, *Nuclear Engineering and Design*, Vol. 238, 2008, pp. 3299–3320.
- Calvin, Ch., Cueto, O. and Emonot, P. (2002).** “An object-oriented approach to the design of fluid mechanics software”, *Mathematical Modelling and Numerical Analysis*, Vol. 36, 2002, pp. 907 - 921.
- Cebeci, T. and Bradshaw, P. (1984).** “Physical and Computational Aspects of Convective Heat Transfer”, Berlin, Germany Book published by Springer, 1984.
- Centaur, (2014).** 3D hybrid mesh generator. [www.centaursoft.com](http://www.centaursoft.com).
- Chang, D. and Tavoularis, S. (2007).** “Numerical simulation of turbulent flow in a 37-rod bundle”, *Nuclear Engineering and Design*, Vol. 237, 2007, pp. 575–590.
- Chang, D. and Tavoularis, S. (2008).** “Simulations of turbulence, heat transfer and mixing across narrow gaps between rod-bundle subchannels”, *Nuclear Engineering and Design*, Vol. 238, pp. 109-123.
- Chabard, J. (2000).** «Transferts thermiques dans les processus énergétiques», ENSTA, EOLSS 2000.
- Châtelain, A. (2004).** «Simulation des Grandes Echelles d’écoulements turbulents avec transferts de chaleur», *Ph.D. thesis*, Institut National Polytechnique de Grenoble.
- Chellapandi, P., Chetal, S. C. and Baldev, R. (2009).** “Thermal stripping limits for components of sodium cooled fast spectrum reactors”, *Nuclear Engineering and Design*, Vol. 239, 2009, pp. 2754-2765.
- Cheng, S.K., (1984).** “Constitutive correlations for wire-wrapped sub-channel analysis under forced and mixed convection conditions”, *Ph.D. Thesis*. Nuclear Engineering Department, MIT, August, 1984.
- Cheng, X. and Tak, N. (2006).** “CFD analysis of thermal-hydraulic behaviour of heavy liquid metals in sub-channels”, *Nuclear Engineering and Design*, Vol. 236, pp. 1874–1885.
- Chiu, C. (1979).** “Pressure drop measurements in LMFBR wire-wrapped blanket bundles”, *American nuclear society*, Vol. 22, 1979, pp. 541-543.
- Choi et al. (2003).** “Measurement of pressure drop in a full-scale fuel assembly of a liquid metal reactor”, *Journal of pressure vessel technology*, Vol. 125, 2003, pp. 233-238.

- Chun M.H. and Seo K.W. (2001).** “An experimental study and assessment of existing friction factor correlations for wire-wrapped fuel assemblies”, *Annals of nuclear energy*, Vol. 28, 2001, pp. 1683-1695.
- Chung, S.Y. and Sung, H.J. (2003).** “Direct numerical simulation of turbulent annular concentric pipe flow Part 2: Heat transfer”, *Int. J. Heat Fluid Flow*, Vol. 24, 2003, pp. 399–411.
- Chung, S.Y., Rhee, G.H. and Sung, H.J. (2002).** “Direct numerical simulation of turbulent concentric annular pipe flow. Part I: Flow field”, *Int. J. Heat Fluid Flow*, Vol. 23, 426– 440.
- Collingham, R.E., Thorne, W.L. and McCormack, J.D. (1971).** “217-pin wire wrapped bundle coolant mixing test”,doi:10.2172/4725044.  
<http://www.osti.gov/scitech/servlets/purl/4725044>.
- Deardoff J.,W. (1973).** “The use of subgrid transport equations in three -dimensional model of atmospheric turbulence”, *ASME Journal of Fluid Engineering*, 1973, pp. 429-438.
- Dorey, L.H. (2012).** «Modélisation des phénomènes couplés combustion-formation des suies-transferts radiatifs dans les chambres de combustion de turbine à gaz», *P.hD thesis*, Ecole centrale de Paris, 2012.
- Ducros, F. (2010).** “Verification and validation considerations regarding the qualification of numerical schemes for LES for dilution problems”, *Nuclear Engineering and Design*, Vol. 240, 2010, pp. 2123-2130.
- Engel, F.C., et al., (1979).** “Laminar, transition and turbulent parallel flow pressure drop across wire-wrap-spaced rod bundles”, *Nuclear Science and Engineering*, Vol. 69, 1979, pp. 290–296.
- Fanning, T., Pointer, D. and Thomas (2009).** “Multi-resolution modeling of subassembly pin bundles for advanced fast reactor safety simulations”, *International Conference on Mathematics, Computational Methods and Reactor Physics (MandC 2009)*. New York: American Nuclear Society, Saratoga Springs.
- Fernandez, et al., (2000).** “Static pressure and wall shear stress distributions in air flow in a seven wire-wrapped rod bundle”. *Journal of the Brazilian Society of Mechanical Sciences*, Vol. 22, 2000, pp 291 - 302.

- Ferziger J. and Peric M. (2001).** “Computational methods for fluid dynamics”, *Book*, published by Springer, 2001.
- Fischer, P. F., Lottes, J., Siegel, A. and Palmiotti, P. (2007).** “Large eddy simulation of wire- wrapped fuel pins I: Hydrodynamics in a periodic array”, *Proc. of M and C + SNA 2007*, Monterey, California, 2007.
- Fontana, M., MacPherson, R. E., Gnadt, P., Parsly, L. and Wantland, J. (1973).** “Temperature Distribution in a 19-Rod Simulated LMFBR Fuel Assembly in a Hexagonal Duct (Fuel Failure Mockup Bundle 2A) – Record of Experimental Data”, *Oak Ridge National Laboratory, Oak Ridge, TN*, 1973.
- Fricano, J. M. and Baglietto, E. (2014).** “A quantitative CFD benchmark for Sodium Fast Reactor fuel assembly modelling”, *Annals of Nuclear Energy*, Vol. 64. Pp. 32–42.
- Fuchs, H. (1973).** “Heat transfer to flowing sodium: Theoretical and experimental study of excess temperature profiles and turbulent temperature fluctuations in tube geometry (in German)”, *P.hD thesis*, ETH Zürich, EIR- Bericht Nr. 241, Würenlingen.
- Gajapathy, R., Velusamy, K., Selvaraj, P., Chellapandi, P. and Chetal, S. (2007).** “CFD investigation of helical wire-wrapped 7-pin fuel bundle and the challenges in modeling full scale 17 pin bundle”, *Nuclear Engineering and Design*, Vol. 237, pp. 2332–2342.
- Gauché, F. (2011).** “The French Prototype of 4th Generation Reactor: ASTRID.” *Annual meeting on Nuclear Technology*, 2011.
- Ghoshal, S. (1999).** “Mathematical and physical constraints on Large-Eddy Simulations of turbulence”, *AIAA Journal*, Vol. 37 (4), 1999, pp. 425-433.
- GIF. International Generation IV Forum. 2000.** <http://www.gen-4.org/>.
- Grötzbach, G. (2013).** “Challenges in low-Prandtl number heat transfer simulation and modelling”, *Nuclear Engineering Design*, Vol. 264, 2013, pp.41-55.  
<http://dx.doi.org/10.1016/j.nucengdes.2012.09.039>.
- Grötzbach, G. (2011).** “Revisiting the resolution requirements for turbulence simulations in nuclear heat transfer”, *Nuclear Engineering Design*, Vol. 241, 2011, pp. 4379–4390.

- Grötzbach, G. (2003).** “Turbulence modelling issues in ADS thermal and hydraulic analyses”, *IAEA Technical Meeting on Theoretical and Experimental Studies of Heavy Liquid Metal Thermal Hydraulics*, Karlsruhe, Germany.
- Grötzbach, G. (2007).** “Anisotropy and Buoyancy in Nuclear Turbulent Heat Transfer—Critical Assessment and Needs for Modelling”, *Institut für Reaktorsicherheit*, FZKA 7363.
- Grötzbach, G. (1981).** “Numerical simulation of turbulent temperature fluctuations in liquid metals”, *Int. J. of Heat and Mass Transfer*, Vol. 24, 1981, pp. 475-490.
- Hamman, K. D. and Berry, R. A. (2010).** “A CFD simulation process for fast reactor fuel assemblies”, *Nuclear Engineering and Design*, Vol. 240, 2010, pp. 2304-2312.
- Heib (2003).** «Nouvelles discrétisations non structures pour des écoulements de fluides à incompressible renforcée». *Ph.D. thesis*. University Paris 6, 2003.
- Hirt C.V., Nichols B.D. and Romero N.C. (1975).** “SOLA-A numerical solution algorithm for transient flow”, Report Los Alamos National Lab, 1975, LA-5852.
- Hinze, J. O. (1975).** “Turbulence”, *Book*, New York: McGraw-Hill, 1975.
- Husson, S. (2007).** «Simulations des grandes échelles pour les écoulements turbulents anisothermes», *Ph.D. thesis*. INSA de Lyon, 2007.
- ICEM.** ANSYS ICEM CFD meshing software.  
<http://www.ansys.com/Products/Other+Products/ANSYS+ICEM+CFD>
- Ikeno, T. and Kajishima, T. (2007).** “Analysis of Dynamical Flow Structure in a Square Arrayed Rod Bundle”, *NURETH12*, Paper 86, Pittsburg, USA.
- Jischa, M. and Rieke, H.B. (1979).** “About the prediction of turbulent Prandtl and Schmidt numbers from modelled transport equations”, *Int. J. of Heat Mass Transfer*, Vol. 22, pp 1547–1555.
- Kasagi N. and Iida O. (1999).** “Progress in direct numerical simulation of turbulent heat transfer”, *In: Proceedings of the 5th ASME/JSME Joint Thermal Engineering Conference*.- San Diego. 1999.
- Kasagi, N. and Shikazono, N. (1995).** “Contribution of Direct Numerical Simulation to Understanding and Modeling Turbulent Transport”, *In Proceedings R. Soc. Lond. A.*, Vol. 45, pp. 257-292.

- Kasagi, N., Kuroda, A. and Hirata, M. (1989).** “Numerical investigation of near-wall turbulent heat transfer taking into account the unsteady heat conduction in the solid wall”, *J. Heat Trans. (ASME)*, Vol. 111(2), 1989, pp. 385-392.
- Kawamoto, N. and Kawamura, H. (1999a).** “DNS of turbulent heat transfer in a channel flow for different thermal boundary conditions”, *Transaction of JSME*, Vol. 65 (637), pp. 181–188.
- Kawamoto, N. and Kawamura, H. (1999b).** “Turbulent heat flux model in consideration of Reynolds and Prandtl number effects”, *Transaction of JSME*, Vol. 65 (638), pp. 194–202.
- Kawamoto, N. and Kawamura, H. (1998).** “DNS and modelling of turbulent heat transfer in channel flow with a spanwise mean temperature gradient”, *In: 13th Australasian Fluid Mechanics Conference*. Melbourne, Australia, pp. 611–614 (13–18 December).
- Kawamura, H., Abe, H. and Matsuo, Y. (2004).** “Very large-scale structures observed in DNS of turbulent channel flow with passive scalar transport”, *In: 15th Australasian Fluid Mechanics Conference*, Sydney, Australia (13–17 December).
- Kawamura, H. and Abe, H. (2002).** “DNS of turbulent scalar transport in a channel flow up to  $Res = 640$  with  $Pr = 0.025$  and  $0.71$ ”, *In: Seventh TRA Conference*. Seoul Nat’l Univ., Seoul, Korea, pp. 65–79 (27 April).
- Kawamura, H., Abe, H. and Shingai, K. (2000).** “DNS of Turbulence and Heat Transport in a Channel Flow with Different Reynolds and Prandtl Numbers and Boundary Conditions”, *In: Nagano et al.(Eds.), Proc. of 3rd Int. Symp. Turbulence, Heat and Mass Transfer*, pp. 15–32.
- Kawamura, H., Abe, H. and Matsuo, Y. (1999).** “DNS of turbulent heat transfer in channel flow with respect to Reynolds and Prandtl number effects”, *Int. J.of Heat and Fluid Flow*, Vol. 20, pp. 196–207.
- Kawamura, H., Kawamoto, N., Abe, H., Matsuo, Y. and Yamamoto, K. (1998a).** “DNS and modeling of turbulent heat transfer in channel flow with various Prandtl numbers”, *In: 11th International Heat Transfer Conference*, vol. 4. Kyongju, Korea, pp. 193–198 (23–28 August).
- Kawamura, H., Ohsaka, K., Abe, H. and Yamamoto, K. (1998b).** “DNS of turbulent heat transfer in channel flow with low to medium-high Prandtl number fluid”, *Int. J.of Heat and Fluid Flow*, Vol. 19 (5), pp. 482–491.

- Kawamura, H., Ohsaka, K. and Yamamoto, K., (1997).** “DNS of turbulent heat transfer in channel flow with low to medium-high Prandtl number fluid”, *In: 11th Symposium Turbulent Shear Flows*, vol. 1, Grenoble, pp. 8.7–8.12.
- Kays, W. M. and Crawford, M. E. (1993).** “Convective Heat and Mass Transfer (3rd ed.)”, New York, U.S.A: McGraw-Hill.
- Kim, A. and Ahmad, K. (2005).** “Three-dimensional analysis of flow and heat transfer in a wire-wrapped fuel assembly”, *ICAPP' 05*. Seoul, Korea.
- Kim, W.S. and Kim Y.G. (2002).** “A subchannels analysis code MATRA-LMR for wire wrapped LMR sub-assembly”, *Annals of Nuclear Energy*, Vol. 29, 2002, pp. 303–321.
- Kim, S. E., Choudhury, D. and Patel, B. (1997).** “Computations of Complex Turbulent Flows Using the Commercial Code ANSYS FLUENT”, *In Proceedings of the ICASE/LaRC/AFOSR Symposium on Modeling Complex Turbulent Flows*. Hampton, Virginia, 1997.
- Kim, J., Moin, P. and Moser, R., 1987.** “Turbulence statistics in fully developed channel flow at low Reynolds number”, *J. Fluid Mech.* 177, 133–166.
- Kong, H., Choi, H. and Lee, J.S., 2000.** “Direct numerical simulation of turbulent thermal boundary layers”, *Phys. Fluids*, Vol. 12, 2000, pp. 2555–2568.
- Kirillov, P.L., (1963).** “Generalization of experimental data on heat transfer in molten metals”, *Atomic Energy*, Vol. 13, 1963, pp. 1103–1106.
- Kolmogorov, A. N. (1941).** “Dissipation of energy in locally isotropic turbulence”, *Doklady Akademii Nauk SSSR*, Vol. 32, 1941, pp. 19-21.
- Lafay, J., Menant, B. and Barroil, J. (1975).** “Local pressure measurements and peripheral flow visualisation in water 19-rod bundle compared with FLICA II B calculations”, Influence of helical wire-wrap spacer system”, *Heat Transfer Conference*. San Francisco, USA.
- Launder, B. E., Reece, G. J. and Rodi, W. (1975).** “Progress in the Development of a Reynolds-Stress Turbulence Closure”, *J. Fluid Mech.*, Vol. 68(3), 1975, pp. 537–566.
- Launder, B. E. and Spalding, D. B. (1972).** “Lectures in Mathematical Models of Turbulence”, *Academic Press*, London, England. 1972.
- Leonard, A.** “Energy cascade in large eddy simulations of turbulent fluid flows”, *Advances in Geophysics*”, Vol. 18A, 1974, pp. 237.

- Lilly, D. K., 1996.** “On the application of the eddy viscosity concept in the inertial subrange of turbulence”, *NCAR Manuscript 123*, 1996.
- Macdougall, J.D. and Lillington, J.N. (1984).** “The SABRE code for fuel rod cluster thermo- hydraulics”, *Nuclear Engineering and Design*, Vol. 82, 1984, pp. 91-407.
- Marten, K., Yonekawa, S. and Hoffmann, H. (1982).** “Experimental investigation on pressure drop in tightly packed bundles with wire wrapped rods”, *Rome: IAHR Second International Specialists Meeting on Thermal-hydraulics in LMFBR Rod Bundles*, 1982.
- Martinelli, R. (1947).** “Heat transfer to Molten metals”, *Trans. Am. Soc. Mech. Engr.*, Vol. 69, 1947, pp. 947-959.
- Menant, B. (1976).** «Quelques particularités des écoulements de sodium bouillant dans les grappes d’aiguilles chauffantes», *Ph.D. thesis*, Institut Polytechnique de Grenoble.
- Menter, F.R. (1994).** “Two-Equation Eddy-Viscosity Turbulence Models for Engineering Applications”, *AIAA Journal*, Vol. 32(8), 1994, pp. 1598–1605.
- Métais, O. (2002).** «Modélisation et simulation numérique». *In cours de DEA Mécanique des Fluides et Transferts*, INPG, 2002-03.
- Merzari, E., Pointer, W., Smith, J.G., Tentner, A. and Fischer, P. (2012).** “Numerical simulation of the flow in wire-wrapped pin bundles: Effect of pin-wire contact modeling”, *Nuclear Engineering and Design*, Vol. 253, 2012, pp. 374–386.
- Merzari, E., Ninokata, H. and E. B. (2008).** “Numerical simulation of flows in tight-lattice fuel bundles”, *Nuclear Engineering and Design*, Vol. 2382, 2008, pp. 1703-1719.
- Merzari, E., Ninokata, H. and Baglietto, E. (2007).** “Unsteady Reynolds Averaged Navier–Stokes Simulation for an Accurate Prediction of the Flow Inside Tight Rod Bundles”, *NURETH12*. Pittsburg, USA.
- Mikityuk, K., (2009).** “Heat transfer to liquid metal: review of data and correlations for tube bundles”, *Nuclear Engineering and Design*, Vol. 239 (4), 2009, pp 680–687.
- Montreuil, E. (2000).** «Simulation numérique pour l’aérothermique avec des modèles de sous-maillages», *Ph.D. Thesis*, Université Pierre et Marie Curie, France.

- Na, Y. and Hanratty, T. (2000).** “Limiting behavior of turbulent scalar transport close to a wall”, *Int. J. of Heat and Mass Transfer*, Vol. 43 (10), 1749–1758.
- Namekawa, F., Ito, A. and Mawatari, K. (1984).** “Buoyancy effects on wire-wrapped rod bundle heat transfer in an LMFBR fuel assembly”, *AIChE Symposium Series Niagra Falls*, pp. 128-133.
- Natesan, K., Sundarajan, T., Narasimhan, A. and Velusamy, K. (2010).** “Turbulent flow simulation in a wire-wrap rod bundle of an LMFBR”, *Nuclear Engineering and Design*, Vol. 240, 2010, pp. 1063–1072.
- Nicoud F. and Ducros F. (1999).** “Subgrid-scale modelling based on the square of the velocity gradient”, *Flow, Turbulence and Combustion*, Vol. 62, 1999, pp. 183-200.
- Ninokata, H., Merzari, E. and Khakim, A. (2009).** “Analysis of low Reynolds number turbulent flow phenomena in nuclear fuel pin”, *Nuclear Engineering and Design*, Vol. 239, 2009, pp. 855–866.
- Nouri, J.M., Umur, H. and Whitelaw, J.H. (1993).** “Flow of Newtonian and non-Newtonian fluids in concentric and eccentric annuli”, *J. Fluid Mech.*, Vol. 253, 1993, pp. 617–641.
- Novendstern, E.H. (1972).** “Turbulent flow pressure drop model for fuel rod assemblies utilizing a helical wire-wrap spacer system”, *Nuclear Engineering and Design*, Vol. 22, 1972, pp. 19.
- OECD/NEA. (2007).** “Handbook on Lead-bismuth Eutectic Alloy and Lead Properties, Materials Compatibility, Thermal-hydraulics and Technologies”, *Nuclear Energy Agency*, ISBN 978-92-64-99002-9.
- Ould-Rouiss, M., Redjem-Saad, L., Lauriat, G. and Mazouz, A. (2010).** “Effect of Prandtl number on the turbulent thermal field in annular pipe flow”, *International Communications in Heat and Mass Transfer*, Vol. 37, 2010, pp. 958–963.
- Patel, V.C. (1965).** “Calibration of the Preston tube and limitations on its use in pressure gradients”, *J. Fluid Mech.*, Vol. 23, 1965, pp. 185–208.
- Patera, A.T. (1984).** “A spectral element method for fluid dynamics: laminar flow in a channel expansion”, *Journal of Computational Physics*, Vol. 54, 1984, pp. 468–488.



- Péniguel, P., Rolfo, S. and Guillaud, M. (2010).** “Thermal-Hydraulics and Conjugate Heat Transfer Calculation in a Wire Wrapped SFR Assembly”, *ICAPP'10*. San Diego, CA, USA.
- Pfrang, W. and Struwe, D. (2007).** “Assessment of Correlations for Heat Transfer to the Coolant for Heavy Liquid Metal Cooled Core Designs”, *Institut für Reaktorsicherheit*, FZKA 7352.
- Piettre, C. (1985).** «*Compte rendu des essais GR19 BP*», C.E.A.
- Piettre, C. and Rameau, B. (1987).** «*ECONA. Grappe à profil axial de flux constant. Annexes du compte rendu des essais de convection naturelle simple phase et d'ébullition. Tome 2*», C.E.A.
- Piller, M. (2005).** “Direct numerical simulation of turbulent forced convection in a pipe”, *Int. J. for Numerical Methods in Fluids*, Vol. 49, 2005, pp. 583–602.
- Piller, M., Nobile, E. and Hanratty, T.J. (2002).** “DNS study of turbulent transport at low Prandtl numbers in a channel flow”, *Journal of Fluid Mechanics*, Vol. 458, 2002, pp. 419–441.
- Pointer, D.W., Thomas, J., Fanning, T., Fischer, P. and Siegel, A. (2009).** “RANS-based CFD simulations of sodium fast reactor wire-wrapped pin bundles”, *In: International Conference on Mathematics, Computational Methods and Reactor Physics*. New York: American Nuclear Society, Saratoga Springs.
- Pointer, W., Fischer, P., Siegel, A. and Smith, J. (2008).** “RANS-based CFD Simulations of Wire Wrapped Fast Reactor Fuel Assemblies”, *ICAPP '08*. Anaheim, CA.
- Pope, S. (2000).** “*Turbulent Flows*”, Cambridge university press.
- Popov, M., Tzanos, C. and Mendonça, F. (2008).** “Large-Eddy simulation of turbulent flow in a rod cluster”, *ANS Annual Meeting 2008*. Anaheim, USA.
- Poitou, D. (2009).** «Modélisation du rayonnement dans la simulation aux grandes échelles de la combustion turbulente», *Ph.D. thesis*. Institut National Polytechnique de Toulouse, 2009.
- Ould-Rouiss, M., Redjem-Saad, L. and Lauriat, G. (2009).** “Direct numerical simulation of turbulent heat transfer in annuli: effect of heat flux ratio”, *Int. J. Heat Fluid Flow*, Vol. 30, 2009, pp. 579–589.
- Rameau, B. (1982).** «*FETUNA GR 91 - Resultats d'essais et interpretation à l'aide du code*», CEA.

- Ranjan, R., Fischer, P. and Pantano, C. (2011).** Direct simulation of turbulent heat transfer in swept flow over a wire in a channel. *Int. J. of Heat and Mass Transfer*, Vol. 54, 2011, pp. 4636 - 4654.
- Ranjan, R., Pantano, C. and Fischer, P. (2010).** Direct simulation of turbulent swept flow over a wire in a channel. *Journal of Fluid Mechanics*, Vol. 651, 2010, pp. 165–209.
- Raza, W. and Kim, W. (2008).** “Effects of wire-spacer shape in LMR on thermal–hydraulic performance”, *Nuclear Engineering and Design*, Vol. 238., 2008, pp. 2678–2683.
- Redjem-Saad, L., Ould-Rouiss, M. and Lauriat. G. (2007).** “Direct numerical simulation of turbulent heat transfer in pipe flows: Effect of Prandtl number.” *Int. J. of Heat and Fluid Flow*,: Vol. 28, 2007, pp. 847-861.
- Rehme, K. (1973).** “Pressure drop correlations for fuel element spacers”, *Nuclear Technology*, Vol.17, 1973, pp. 15-23.
- Reynolds., O. (1895).** “The dynamical theory of incompressible viscous fluids and the determination of the criterion”, *The Royal Society’s Philosophical Transactions A*, Vol. 186, 1895, pp. 123–164.
- Reynolds, A.J., (1975).** “The prediction of turbulent Prandtl and Schmidt numbers”, *Int. J. Heat Mass Transfer*, Vol. 18, 1975, pp. 1055–1069.
- Richardson, L. F. (1992).** “Weather prediction by numerical process”, Cambridge university press (cambridge).
- Roidt, R., Carelli, M. and Markley, R. (1980).”** Experimental investigations of the hydraulic field in wire-wrapped LMFBR core assemblies”, *Nuclear Engineering and Design*, Vol. 62, 1980, pp. 295–321.
- Rolfo et al, (2012).** “Thermal-hydraulic study of a wire spacer fuel assembly”, *Nuclear Engineering and Design*, Vol. 243, 2012, pp. 251-262.
- Saha, S., Chin, C., Blackburn, H., Ooi, A. (2010).** “Numerical study of heat transfer in a fully developed turbulent pipe flow”, *In: 17th Australasian Fluid Mechanics Conference*, Auckland, New Zealand (5–9 December) 2010.
- Saha, S., Chin, C., Blackburn, H.M. and Ooi., A. (2011).** “The influence of pipe length on thermal statistics computed from DNS of turbulent heat transfer”, *Int. J. of Heat and Fluid Flow*, Vol. 32, 2011, pp. 1083–1097.

- Schulenberg, T. and Stieglitz. R. (2010).** “Flow measurement techniques in heavy liquid metals”, *Nuclear engineering and design*, Vol. 240, 2010, pp. 2077-2087.
- Shih T.H., Liou W.W., Shabbir A., Yang Z. and Zhu. J. (1995).** A New \_Eddy-Viscosity Model for High Reynolds Number Turbulent Flows - Model Development and Validation". *Computers Fluids*. Vol. 24(3), 1995, pp. 227–238.
- Simoneau, J., Champigny, J. and Gelineau, O. (2010).** “Applications of large eddy simulations in nuclear field”, *Nuclear Engineering and Design*, Vol. 240, 2010, pp. 429-431.
- Smagorinsky. J. (1963).** “General Circulation Experiments with the Primitive Equations. I. The Basic Experiment”, *Monthly Weather Review*, 1963. - 3 : Vol. 91, 1963, pp. 99–164.
- Smith, G., J., Tokuhiko, Akira, W.David, P., Fischer, et al. (2009).** “Predictions in CFD simulations of wire-wrapped SFR fuel assemblies”, *Proceedings of ICAPP '09*, Tokyo, Japan.
- Smith, G., J., Babin, B. R., Pointer, W., D., Fischer, et al. (2008).** “Effects of mesh density and flow conditioning in simulating 7-pin wire wrapped fuel pins”, *Proceedings of the 16th International Conference on Nuclear Engineering; Orlando, Florida, USA*. pp. 1-9.
- SolidWorks, (2010).** 3D CAD modelling software. <http://www.solidworks.fr/>
- Spalart, P. (1988).** “Direct simulation of a turbulent boundary layer up to  $Re=1410$ ”, *Journal of Fluid mechanics*, Vol. 187, 1988, pp. 61-88.
- STAR-CCM+ Version 9.02**, CFD code developed by Cd-Adapco. User guide, [www.cd-adapco.com](http://www.cd-adapco.com)
- Tennekes, H. and Lumley, L. (1972).** “A First Course in Turbulence”, *Cambridge*, U.S.A.: MIT Press.
- Tenchine, D. (2010)** “Some thermal hydraulic challenges in sodium cooled fast reactors”, *Nuclear Engineering and Design*, Vol. 240, 2010, pp. 1195-1217.
- TGCC, CEA.** Très Grand Centre de calcul du CEA, <http://www-hpc.cea.fr/fr/complex/tgcc.htm>
- Thompson, J et al. (1977).** “Boundary-fitted curvilinear coordinate systems for solution of partial differential equations on fields containing any number of arbitrary two-dimensional bodies”, *NASA contractor CR 2729* - July 1977.

- Tiselj, I., Pogrebnyak, E., Li, C., Mosyak, A. and Hetsroni, G. (2001).** “Effect of wall boundary condition on scalar transfer in a fully developed turbulent flume”, *Phys. Fluids*, Vol. 13, 2001, pp. 1028–1039.
- Tong, L.S. (1968).** “Pressure drop performance of a rod bundle, in Heat transfer in rod bundle”, *In: ASME Winter Annual Meeting*, 1968, NY.
- Trio\_U**, Version 1.6.8, <http://www-trio-u.cea.fr>.
- Vanderhaegen, M. and Belguet, A. L. (2014).** “A Review on Sodium Boiling Phenomena in Reactor Systems”, *Nuclear Science and Engineering*, Vol. 176, 2014, pp. 115-137.
- Vanetin, B. (2000).** “The thermal hydraulics of a pin bundle with a helical wire wrap spacer. Modelling and qualification for a new sub-assembly concept”, *In: LMFR Core Thermohydraulics: status and prospects*, Vienna, Austria: IAEA-TECDOC-1157, 2000, pp. 269-280.
- Vedy, E., Viazzo, S. and Schiestel, R. (2003).** “A high-order finite difference method for incompressible fluid turbulence simulations”, *Int. J. Numer. Meth. Fluids*, Vol. 42, 2003, pp. 1155–1188.
- Vijayan, P.K et al. (1999).** “Experimental studies on the pressure drop across the various components of a PHWR fuel channel”, *Experimental Thermal and Fluid science*, Vol. 20, 1999, pp. 34-44.
- Waltar, A. and Reynolds, A. (1981).** “Fast breeder reactors”, *Pergamon press*.
- Weigand, B., Ferguson, J.R. and Crawford, M.E. (1997).** “An extended Kays and Crawford turbulent Prandtl number model”, *Int. J. of Heat Mass Transfer*, Vol. 40, 1997, pp. 4191–4196.
- Wheeler, C.L., Stewart, C.W., Cena, R.J., Rowe, D.D. and Sutey, A.M. (1976)** “COBRA-IV-I: An interim version of COBRA for thermal-hydraulic analysis of rod bundle nuclear fuel elements and cores”, *BNWL-1962*, 1976.
- Wikstrom, P. (1998).** “Measurements, direct numerical simulation and modeling of passive scalar transport in turbulent flows”, *P.hD Thesis*. Sweden, Stockholm: Royal Institute of Technology.
- Wilcox, D. (1988).** “Reassessment of the scale determining equation for advanced turbulence models”, *AIAA J*, Vol. 26, 1988, pp. 1299.



# APPENDIX A

---

## *Meshing Tool*

The meshing generation is based on a multi-bloc elliptic meshing technique consisting of solving two differential equations (Thompson, 1977).

For this purpose, the sub-assembly is subdivided into axial slices in order to perform, as a first step, a 2D meshing of the region present between the external contour of the pins and the external hexagonal wrapper tube. The meshing technique consists of determining the streamlines between two contours: the pin contour and the hexagonal box contour (Figure A.1). By assembling the 2D meshing, the sub-assembly meshing is finally built.

Mathematically, the 2 function  $\varepsilon(x, y)$  and  $\eta(x, y)$  representing the equations of the orthogonal streamlines check the following system:

$$\Delta\varepsilon(x, y) = 0 \quad (\text{A.1})$$

$$\Delta\eta(x, y) = 0 \quad (\text{A.2})$$

These functions  $\varepsilon(x, y)$  and  $\eta(x, y)$  are completely determined by their values on the boundary, which are the pin contour and the hexagonal box contour.

The function  $\eta(x, y)$  is chosen to respect the condition  $\eta = 0$  around each pin and  $\eta = \eta_{\max}$  on the periphery of the hexagonal box.

The function  $\varepsilon(x, y)$  is defined from  $\varepsilon = 0$  and  $\varepsilon = \varepsilon_{\max}$  on an arbitrary line between the pin and the hexagonal box.

The solution of the problem is the couple  $(x,y)$  checking  $\varepsilon(x,y)=\text{constant}$  and  $\eta(x,y)=\text{constant}$ .

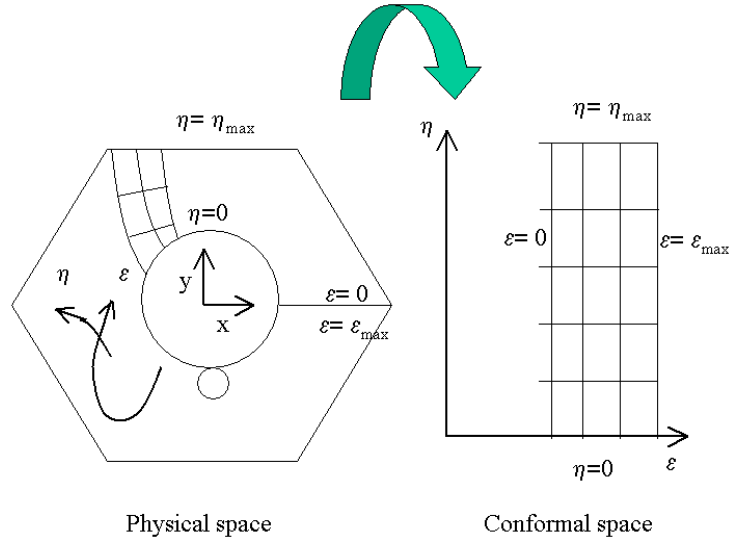


**Figure A.1-Physical space and conformal space**

Transforming the initial problem in the physical by an equivalent one in the conformal space, the problem is reduced to a mapping of a rectangular. This transformation is simply obtained by the inversion of the two functions  $\varepsilon(x,y)$  and  $\eta(x,y)$ . The two inverted functions are now dependent on  $(\varepsilon, \eta)$ :

$$x = x(\varepsilon, \eta) \quad (\text{A.3})$$

$$y = y(\varepsilon, \eta) \quad (\text{A.4})$$

The inversion of the 2 laplacians is written as:

$$\alpha x_{\varepsilon\varepsilon} - 2\beta x_{\varepsilon\eta} + \gamma x_{\eta\eta} = 0 \quad (\text{A.5})$$

$$\alpha y_{\varepsilon\varepsilon} - 2\beta y_{\varepsilon\eta} + \gamma y_{\eta\eta} = 0 \quad (\text{A.6})$$

Solving this system by the Gauss-Seidel method, the successive domains, which are obtained by a continuous deformation of their frontier, are meshed (Figure A.2). Finally one gets the 2D meshing for the region comprised between the pin and the hexagon contours.

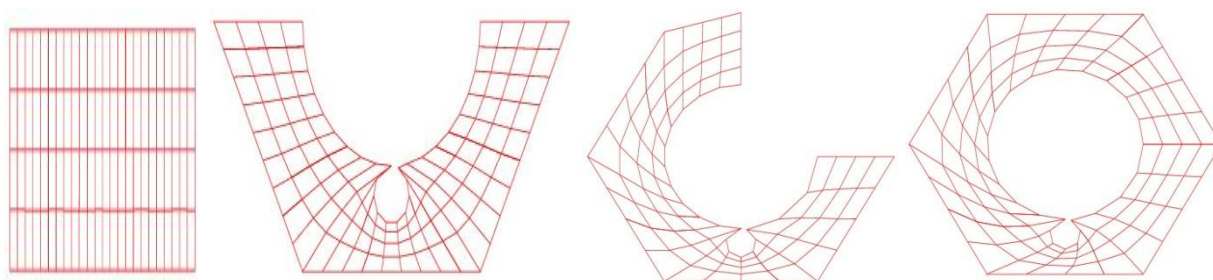


**Figure A.2-Meshing of domains that are continuously deformed from the rectangular domain to the final one**



# APPENDIX B

## *Pressure drop Correlations*

In the past, there have been different studies that recommend different correlations for reference. Bubelis and Schikorr (Bubelis, 2008) have reviewed the existing friction factor correlations for wire-wrap fuel bundles and found that Rehme (Rehme, 1973) and Baxi (Baxi, 1981) correlations are best suited for sodium flow through pin bundles with helical wire. Chun and Seo (Chun, 2001) studied the existing friction factor correlations to identify the best performing correlation for the sub-channel pressure drop analysis of a wire-wrapped fuel assembly. They found that the correlation proposed by Novendstern (Novendstern, 1972) agrees fairly well with experimental data in the turbulent region and Rehme's correlation (Rehme, 1973) consistently under predicts the friction factor for the entire Reynolds number regime studied.

Correlation	Formulae for friction factor, f
Cheng & Todreas, 1984	$\frac{\left(0.8063 - 0.9022 \cdot \log\left(\frac{H}{D}\right) + 0.3526 \cdot \log\left(\frac{H}{D}\right)^2\right) \cdot \left(\frac{P}{D}\right)^{9.7} \cdot \left(\frac{H}{D}\right)^{1.78-2 \cdot \frac{P}{D}}}{Re^{0.18}} \quad (B.1)$
Blasius	$f_{blasius} = \frac{0.316}{Re^{0.25}} \quad (B.2)$
Baxi (Engel, 1979)	$f_{blasius} \left( \frac{1.034}{\left(\frac{P}{D}\right)^{0.124}} + 29.6 \cdot \left(\frac{P}{D}\right)^{6.94} \cdot \frac{Re^{0.086}}{\left(\frac{H}{D+D_w}\right)^{2.239}} \right) \quad (B.3)$
Pontier	$\frac{0.12 \cdot e^{\left(1+4.6 \cdot \left(\frac{P}{D}-1\right)\right) \cdot \pi \cdot \frac{D}{H}}}{Re^{0.16}} \quad (B.4)$

Rehme (1973)	$f = \left( \frac{64}{Re'} \cdot F^{0.5} + \frac{0.0816}{Re'^{0.133}} \cdot F^{0.9335} \right) \cdot \frac{P_{w-pin}}{P_w} \quad (B.5)$ $\text{where } F = \left( \frac{P}{D} \right)^2 + \left( 7.6 \cdot \frac{D+D_w}{H} \cdot \left( \frac{P}{D} \right)^2 \right)^{2.16} \quad (B.6)$ $Re' = Re \cdot \sqrt{F} \quad (B.7)$
Novendsten, 1972	$f = \frac{0.316 M}{\left( X \frac{D_{h1}}{D_{h2}} Re \right)^{0.25}} X^2 \quad (B.8)$ $\text{where } M = \frac{1.034}{\left( \frac{P_w}{D_h} \right)^{0.124}} + \frac{29.7 \cdot \left( \frac{P_w}{D_h} \right)^{0.694} \cdot Re^{0.086}}{\left( \frac{H}{D_h} \right)^{2.239}}$ $X = \frac{A_T}{N_1 \cdot A_{f1} + N_2 \cdot A_{f2} \cdot \left( \frac{D_{h2}}{D_{h1}} \right)^{0.714} + N_1 \cdot A_{f1} \cdot \left( \frac{D_{h3}}{D_{h1}} \right)^{0.714}} \quad (B.9)$

**Table B.1-List of correlations to determine the pressure drop in the sub-assembly**

# APPENDIX C

---

## *Version Abrégée en Français*

### C.1.Introduction

Contrairement à la majorité des réacteurs nucléaires dans le monde refroidis à l'eau, les Réacteurs à Neutrons Rapides refroidis au sodium (SFR pour Sodium-cooled Fast Reactor en anglais) pourraient jouer un rôle important à l'avenir pour la production d'énergie nucléaire en raison de leur potentiel d'utilisation des ressources naturelles et de leur capacité à réduire le volume et la radio toxicité intrinsèque à long terme des déchets ultimes. Le projet ASTRID : Advanced Sodium Technological Reactor for Industrial Demonstration (Gauché, 2011) a pour origine la loi du 28 juin 2006 qui demande la mise en service d'un réacteur de quatrième génération à l'horizon 2020. Après 3 ans d'études et de R&D pour explorer des solutions innovantes, le projet ASTRID a été lancé fin 2009. Le choix a été fait d'une centrale électrogène à neutrons rapides refroidie au sodium. L'Avant-Projet Sommaire d'ASTRID est en cours au "Commissariat à l'Energie Atomique et aux Energies Alternatives" (CEA).

Depuis 2010, le concept de référence pour le cœur ASTRID est appelé CFV (qui signifie Cœur à Faible coefficient de vidange). L'optimisation du concept de cœur est en cours pour améliorer ses performances. Le cœur CFV présente la particularité d'avoir un coefficient de vidange global négatif, à l'inverse des cœurs homogènes de type SUPERPHENIX ou EFR qui présentent un coefficient de vidange positif de l'ordre de + 7\$. Le cœur CFV est caractérisé par une géométrie hétérogène radiale et axiale. L'hétérogénéité radiale peut être vue sur la Figure C.1a.

Le cœur en forme de creuset asymétrique est composé des assemblages du cœur interne et externe qui contiennent le combustible fissile. En plus des assemblages combustible, le cœur contient aussi des réflecteurs en acier, des protections neutroniques latérales, des barres de

contrôle et d'arrêt, et des Dispositifs Complémentaires de Sûreté de type Prévention et mitigation de la fusion généraliser du cœur.

Le cœur interne est composé axialement de deux zones fissiles séparées par une zone fertile (cf. Figure C.1b).

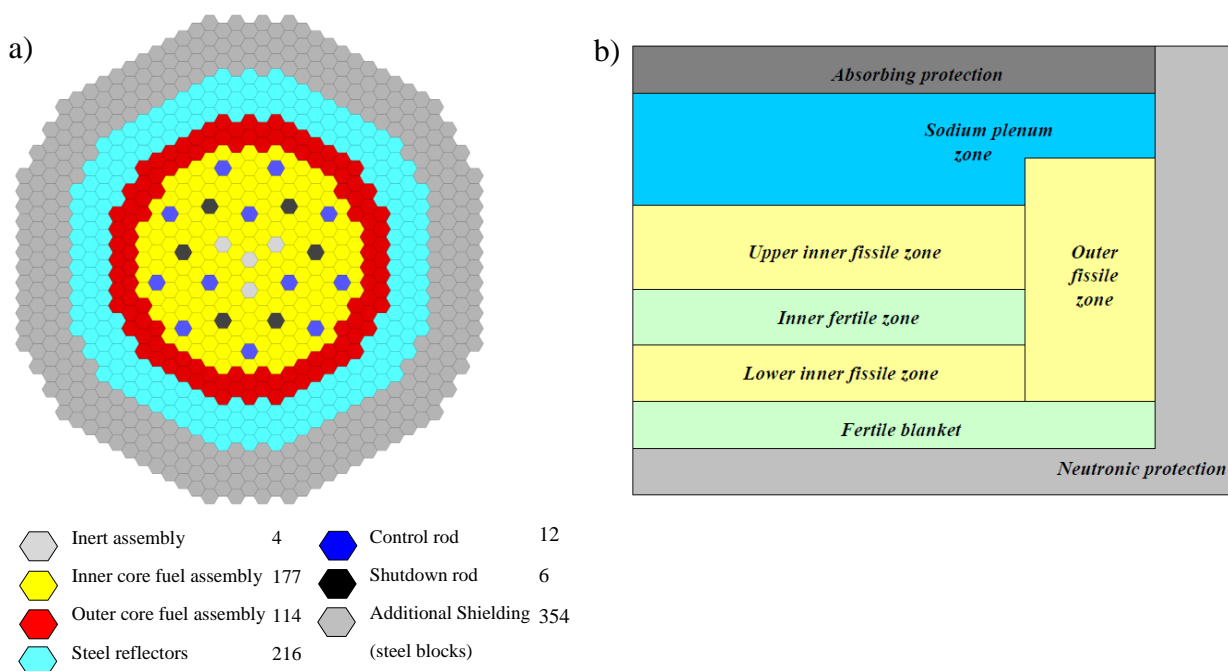


**Figure C.1-Cœur CFV ASTRID (a) Coupe radiale (b) Coupe axiale**

L'assemblage combustible se compose d'un tube hexagonal avec 217 aiguilles de combustible. Ces aiguilles cylindriques d'un diamètre  $D_p$  sont disposées en un réseau triangulaire avec un pas  $P$  qui représente la distance entre deux aiguilles adjacentes. Les aiguilles combustible sont séparées l'une de l'autre par un fil hélicoïdal enroulée autour d'elles. Le pas de l'hélice du fil espaceur est noté  $H$ . Le rôle du fil espaceur d'une aiguille est double :

- éviter le contact direct de la gaine avec une autre gaine,
- maintenir autour de chaque aiguille une veine de sodium suffisante pour éviter des surchauffes locales.

Le fil hélicoïdal agit aussi comme un dispositif de mélange qui améliore le transfert de chaleur. En contrepartie, il augmente aussi la perte de charge. La Figure C.2a présente la coupe transversale de l'assemblage avec 217 aiguilles et le schéma de principe d'une aiguille.

Les deux paramètres principaux caractérisant la géométrie de l'assemblage sont le rapport du pas au diamètre aiguille ( $P/D_p$ ) et le pas de l'hélice au diamètre aiguille ( $H/D_p$ ). Typiquement, la version 2 de cœur CFV est caractérisée par  $P/D_p = 1,11$  et  $H/D_p = 21$ . Il existe trois types de sous-canaux présents dans l'assemblage :

- i. **Canal central.** Sous-canal intérieur de forme triangulaire et présent au centre de l'assemblage.
- ii. **Canal externe.** Sous-canal présent aux bords le long de la paroi du canal hexagonal.
- iii. **Canal de coin.** Sous-canal présent dans les coins de l'assemblage.

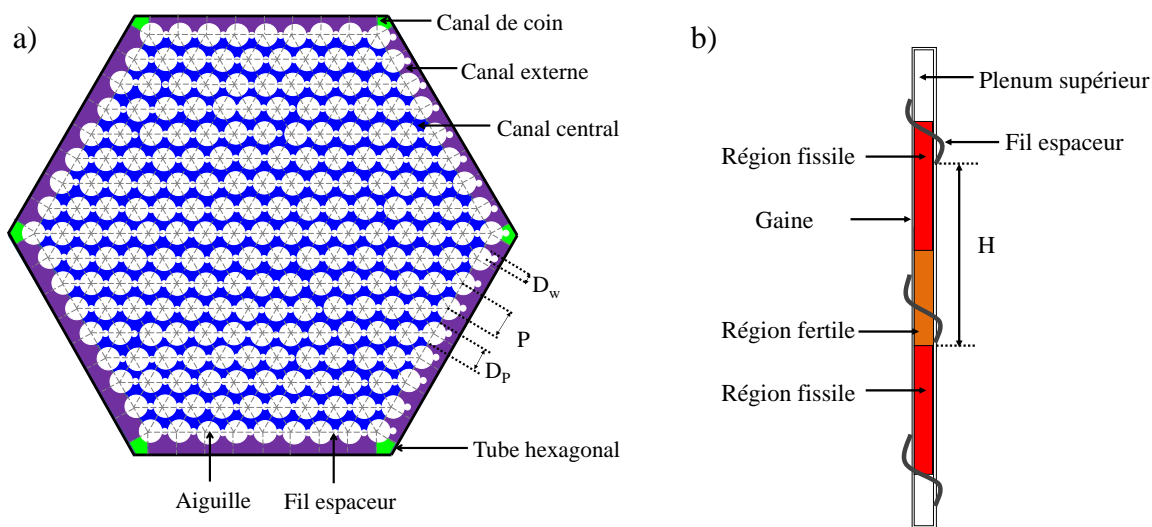


**Figure C.2-Représentation de (a) la coupe transversale de l'assemblage avec 217 aiguilles (b) une aiguille à fil espaceur enroulée hélicoïdalement**

La thermohydraulique est reconnue comme un sujet scientifique d'intérêt dans le développement des réacteurs à neutrons rapides à caloporteur sodium. Comme la géométrie de l'assemblage se différencie de celle du passé, de nouvelles études sont nécessaires pour étudier l'écoulement du sodium et caractériser le transfert de chaleur dans les faisceaux d'aiguilles. L'objectif de la thèse est de comprendre la thermohydraulique au niveau de l'assemblage et en particulier à proximité du fil espaceur.

Les principaux paramètres à évaluer dans toute étude thermohydraulique sont les distributions de pression, de température et de vitesse qui permettent de déterminer les quantités suivantes :

- La perte de charge totale de l'assemblage.
- La température de gaine et en particulier la température maximale en paroi.
- La température du tube hexagonal pour l'analyse thermomécanique.

- Les gradients de température et la température maximale du sodium. Des phénomènes localisés de points chauds éventuels ou de gradients thermiques entre le centre et la périphérie de l'assemblage peuvent être mis en évidence.

Ces paramètres précédents sont importants pour caractériser les situations de fonctionnement. La température maximale de la gaine nécessite une connaissance précise de la thermohydraulique globale et locale dans le faisceau d'aiguilles. L'écoulement transversal du sodium est induit par le fil espaceur qui impose un couplage thermohydraulique local entre les sous-canaux. Pour caractériser ces échanges, il est nécessaire de prendre en compte les trois types de sous-canaux représentés sur la Figure C.2a.

La simulation numérique (CFD pour Computational Fluid Dynamics en anglais) est un outil de calcul permettant l'étude des écoulements et des transferts de chaleur induits par les fils hélicoïdaux. La CFD résout les équations de conservation de la physique qui décrivent l'écoulement et le transfert de chaleur en utilisant une approche numérique. Ces équations sont les équations de Navier-Stokes (conservation de la quantité de mouvement), l'équation de continuité (conservation de la masse) et la conservation de l'énergie. Ainsi, un système de cinq équations composé de cinq variables (trois composantes de vitesse, de pression et de température) est obtenu. Cependant, les équations de Navier-Stokes sont des équations différentielles partielles non linéaires et fonction du temps ; il n'existe donc pas de solution analytique à l'exception de certains écoulements très simples. Ainsi, on doit résoudre les solutions des équations de Navier-Stokes numériquement.

Trois approches sont utilisées en CFD. Il s'agit des approches Reynolds-Averaged Navier-Stokes (RANS), Large Eddy Simulation (LES) et Direct Numerical Simulation (DNS). L'approche RANS est basée sur la moyenne temporelle des variables. La DNS se caractérise par une résolution complète des équations de Navier-Stokes sans modélisation, mais qui requiert d'importantes ressources informatiques. L'approche LES est basée sur la décomposition en fréquence du domaine spatial dans laquelle les grandes échelles de mouvement sont résolues et les petites échelles de mouvements sont modélisées.

Avec l'accroissement de la puissance de calcul ces dernières décennies, l'utilisation de approches précises en CFD a permis de traiter des géométries complexes. Par conséquent, ces

approches CFD sont utilisées dans cette thèse pour réaliser l'étude thermohydraulique de l'assemblage du réacteur à neutrons rapides à caloporteur sodium.

Le rapport de thèse est présenté en quatre chapitres :

- Le **chapitre 1** présente l'état de l'art des études thermohydrauliques relatives aux assemblages. Il est divisé en trois parties présentant l'état actuel des connaissances sur les transferts de chaleur en sodium, les expériences réalisées par le passé avec un nombre différent d'aiguilles dans l'assemblage et les études numériques utilisant les trois approches -RANS, LES et DNS.
- Le **chapitre 2** présente les lois fondamentales de la physique qui régissent l'écoulement du fluide et les transferts de chaleur. Les codes de CFD utilisés sont présentés.
- Le **chapitre 3** est consacré à l'étude du transfert de chaleur entre la paroi chauffée et le sodium en utilisant la DNS. Cette approche exige de grandes ressources de calcul, ce qui explique que l'étude actuelle a été faite sur une géométrie simplifiée, qui correspond à l'écoulement dans un cylindre annulaire concentrique. Cette géométrie est une représentation simplifiée de l'écoulement à l'intérieur de l'assemblage combustible du cœur. Cette approche a permis de valider l'approche LES pour les études hydrauliques et thermiques en sodium.
- Le **chapitre 4** présente l'utilisation des approches LES et RANS pour étudier la thermohydraulique de l'écoulement de sodium dans l'assemblage. L'approche RANS est mise en œuvre pour l'assemblage complet contenant 217 aiguilles avec fil espaceur. Cette étude donne les conditions aux limites pour l'étude LES sur la partie centrale de l'assemblage avec un seul pas d'hélice. En fin, le calcul LES donne des informations détaillées sur les points chauds.

## C.2. Etat de l'art

Le sodium liquide est caractérisé par un très faible nombre de Prandtl ( $Pr \sim 0,001$ ) par rapport à celui de l'eau ( $Pr \sim 1$ ). Les études DNS pour les faibles nombres de Prandtl sont disponibles dans la littérature pour les cas académiques, comme un écoulement turbulent dans un canal plan. Pour le canal cylindrique concentrique, les études sont limitées à un nombre de Prandtl

supérieur à 0.01. Ces études montrent que pour un faible nombre de Prandtl, le champ de températures est plus homogène que le champ de vitesses ; pour un nombre de Reynolds modéré (de l'ordre de 50000 à 70000), le transfert de chaleur à la paroi est essentiellement moléculaire tandis que l'écoulement est turbulent. L'analogie de Reynolds classique avec le concept de nombre de Prandtl turbulent ( $Pr_t \sim 1$ ) utilisé dans les approches RANS et LES ne permet donc pas de déterminer correctement le champ thermique à faible nombre de Prandtl.

Les études thermohydraulique de l'assemblage avec fil espaceur sont limitées et la plupart des expériences ont été réalisées dans les années 80. L'écoulement autour d'un fil espaceur est largement étudié avec l'air et le sodium comme caloporteurs. Pour le sodium, il existe des données expérimentales pour les faisceaux d'aiguilles et le sodium comme caloporteur en convection forcée. Ces essais sont les suivants :

- Oak-Ridge National Laboratory (ORNL) faisceau de 19 aiguilles (Fontana, et al., 1973) avec des mesures de températures en paroi et à la sortie d'un assemblage de combustible avec fil espaceur. Le point chaud a été identifié dans la zone de contact entre l'aiguille et le fil espaceur où la vitesse d'écoulement est réduite de manière significative.
- GR19-I (Berger, 1975) et GR19-BP (Piettre, 1985) avec des expériences sur un assemblage de 19 aiguilles en sodium.
- ECONA (Piettre, 1987) et Toshiba (Namekawa, 1984) avec un faisceau de 37 aiguilles.
- FETUNA (Rameau, 1982) avec un faisceau de 91 aiguilles.

L'approche RANS est une méthode largement utilisée en raison de sa simplicité de mise en œuvre. Elle a été utilisée pour étudier l'écoulement dans 7, 19, 37, 61 et 217 aiguilles de combustible. Les données expérimentales publiées à ce jour sont limitées et des résultats précis sont nécessaires en particulier pour l'obtention du champ thermique en sodium. L'étude RANS a été utilisée pour les études de sensibilité afin de comparer les effets de différents paramètres comme le modèle de turbulence, et les dimensions du faisceau d'aiguilles.

Le calcul LES de l'assemblage complet ne peut pas être réalisé car son coût est très élevé. L'approche la plus courante consiste à utiliser la périodicité axiale et à étudier un seul tour d'enroulement du fil espaceur. Fischer et al. (Fischer, 2007) ont utilisé la périodicité axiale et sélectionné la région centrale de l'assemblage pour effectuer les calculs hydrauliques LES.



Pointer et al. (Pontier, 2009) ont également utilisé la périodicité axiale et effectué un le calcul LES hydraulique avec 217 aiguilles en utilisant une représentation simplifiée du point de contact entre l'aiguille et le fil espaceur pour limiter le nombre de mailles. Cependant, les études thermohydraulique de l'assemblage avec fil espaceur en utilisant l'approche LES disponibles dans la littérature ouverte sont très souvent limitées à une géométrie simplifiée.

Merzari et al. (Merzari, 2012) ont effectué l'étude thermohydraulique LES avec un flux de chaleur imposée sur une paroi. Ce travail fait suite aux travaux DNS de Ranjan et al. (Ranjan, 2011) qui ont étudié le transfert de chaleur pour l'écoulement en canal avec fil espaceur. Les deux études ont contribué de manière significative à la connaissance du transfert de chaleur pour les métaux liquides, avec les limites suivantes :

- La géométrie simplifiée ne prend pas en compte l'effet de courbure des aiguilles de combustible.
- L'effet hélicoïdal du fil espaceur est modélisé artificiellement par un écoulement transverse.
- Le nombre de Prandtl est de 0,01.

Par conséquent, compte-tenu des lacunes dans les études thermohydraulique de l'assemblage avec fil espaceur, dans cette thèse les trois approches de CFD (DNS, RANS et LES) sont utilisées pour caractériser les points chauds en sodium.

## C.3. Méthodes et des outils numériques

Dans ce chapitre, les trois approches -RANS, LES et DNS de la CFD sont présentées avec leur principe et leurs formulations mathématiques. Les différents modèles de turbulence utilisés pour fermer le système d'équations pour les approches RANS et LES sont discutés. Le choix du modèle de turbulence utilisé pour l'étude est le modèle  $k-\varepsilon$  réalisable pour l'étude RANS et WALE pour l'étude LES. L'outil numérique utilisé pour les études RANS est le code industriel STAR-CCM+, et le code TRIO\_U utilisé pour l'approche LES développé au CEA. Le code utilisé pour les calculs DNS est développé au laboratoire M2P2 de l'Université d'Aix-Marseille permettant de traiter des géométries cylindriques avec direction azimutale homogène.

Il est usuel dans les approches LES et DNS d'utiliser des conditions aux limites périodiques pour la direction de l'écoulement. Pour ce faire, les termes sources sont utilisés pour la vitesse et pour la température dans l'équation de Navier-Stokes et d'énergie. Le terme source de quantité de mouvement de Navier-Stokes compense les pertes par frottement en frontière du domaine et le terme source d'énergie soustrait l'énergie supplémentaire déposée par le flux imposé aux parois.

Dans les deux chapitres suivants, les études DNS, LES et RANS sont présentées pour étudier le transfert de chaleur dans le sodium avec l'objectif de s'intéresser aux points chauds dans l'assemblage.

## **C.4. Etude numérique du transfert de chaleur turbulent en sodium**

Pour l'étude thermohydraulique de l'assemblage, il est nécessaire de comprendre les phénomènes de transfert de chaleur en sodium liquide avec un nombre de Prandtl de l'ordre de  $10^{-3}$ . On utilise l'approche DNS qui permet d'étudier les phénomènes de turbulence et de transfert de chaleur turbulent. Cependant, étant donné le temps de calcul élevé, l'approche ne peut donc pas être appliquée à des géométries complexes. Le domaine de calcul choisi pour l'étude DNS est un cylindre annulaire concentrique (cf. Figure C.3), avec un diamètre du cylindre intérieur identique à celui des aiguilles combustible de l'assemblage SFR. Cette configuration n'est pas seulement académique, mais est aussi rencontrée à d'autres endroits de la chaudière nucléaire, tel que les échangeurs de chaleur.

L'objectif de cette étude est de caractériser le transfert de chaleur et d'instruire l'effet du nombre de Reynolds sur les transferts thermiques en régime turbulent. Un calcul LES a aussi été effectué sur la même géométrie afin de comparer les résultats avec ceux de la DNS.

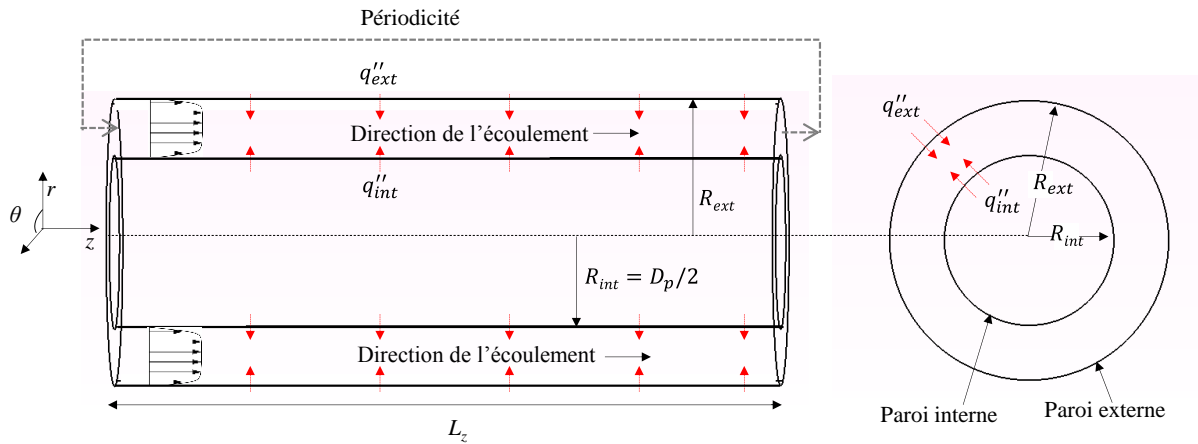


**Figure C.3-Géométrie du conduit annulaire concentrique utilisé pour l'étude DNS**

Un premier calcul destiné à se comparer à la littérature est réalisé avec de l'air et un nombre de Prandtl égal à 0,7. Le code de DNS est ensuite utilisé pour étudier l'écoulement turbulent en sodium liquide pour cette configuration.

Les résultats montrent que :

- i) Les structures turbulentes en thermique sont très grandes pour des fluides à faible nombre de Prandtl, ce qui nécessite un domaine de calcul étendu.
- ii) Le champ thermique est stratifié, même si l'écoulement est turbulent.

La Figure C.4 montre que les champs de vitesse et de débit pour l'air et le sodium sont identiques pour un même nombre de Reynolds (8900).

Les champs thermiques pour l'air et le sodium (Figure C.5) sont très différents dû au nombre de Prandtl. Dans le cas de l'air, le champ de températures est turbulent alors que pour le sodium, pratiquement aucune turbulence n'est observée. Le champ thermique en sodium évolue très lentement le long de la paroi. La conduction moléculaire est le mode prépondérant de transfert de chaleur à la paroi contrairement aux fluides avec un nombre de Prandtl proche de l'unité.

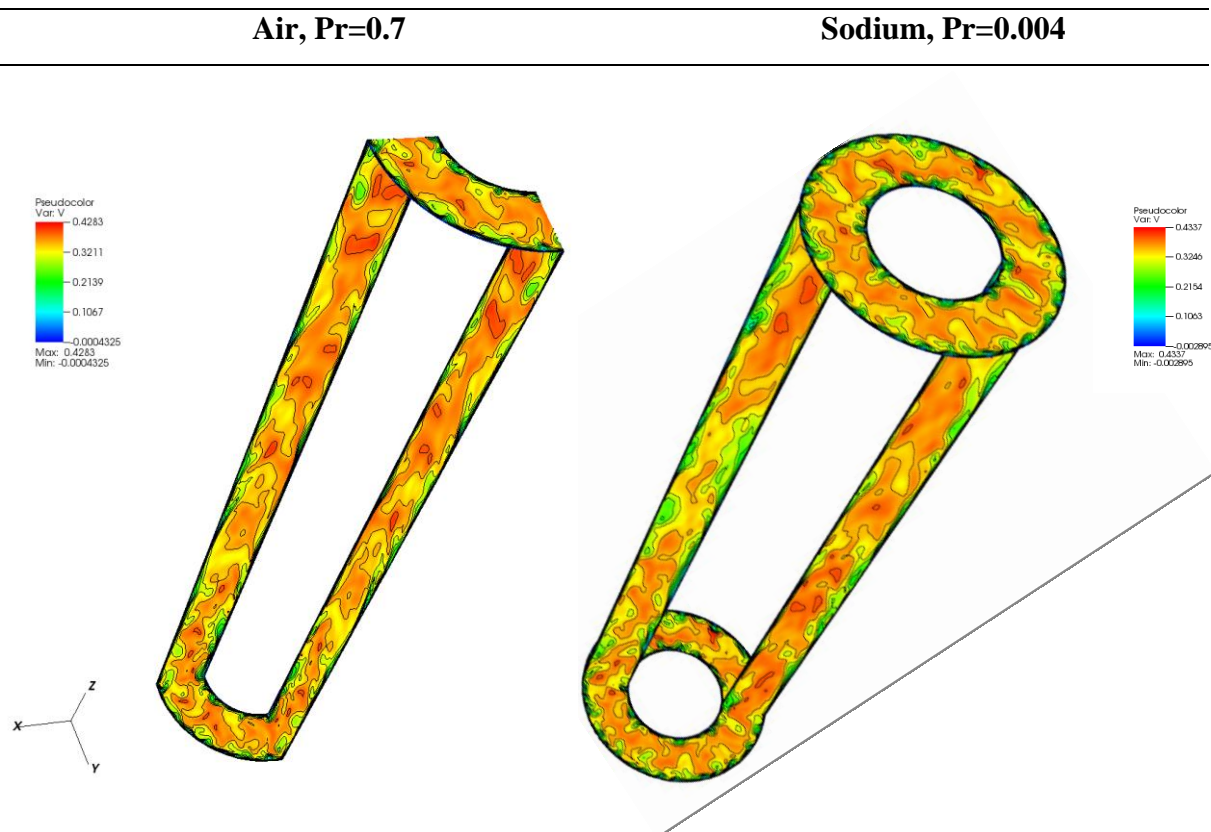


**Figure C.4-Vitesse axiale instantanée pour l'air (AIR-V2) et le sodium (Na-8.9K-V2)  
pour un nombre de Reynolds de 8900**

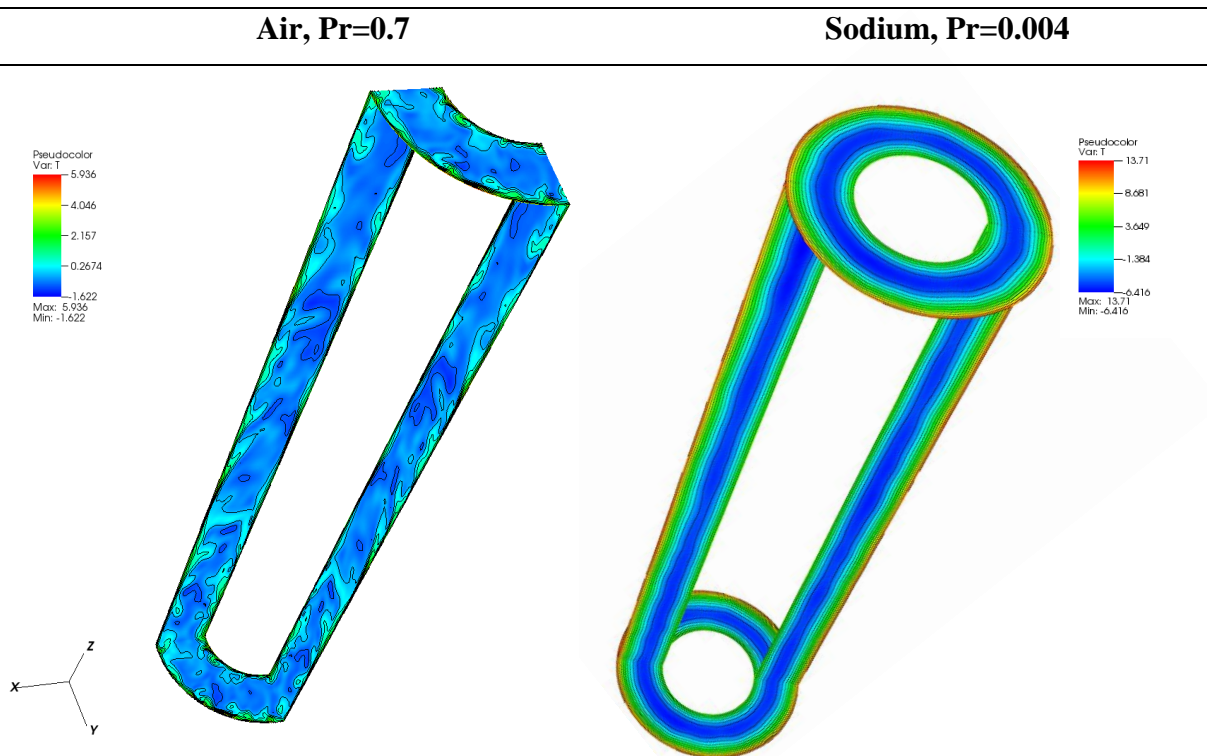


**Figure C.5- Température instantanée pour l'air (AIR-V2) et le sodium (Na-8.9K-V2)  
pour un nombre de Reynolds de 8900**

Le profil de température moyenne est représenté sur la Figure C.6a. Le gradient de température est beaucoup plus important à proximité des parois dans le cas de l'air. En effet, la sous-couche de conduction linéaire pour le sodium s'étend sur une distance plus grande que pour l'air.

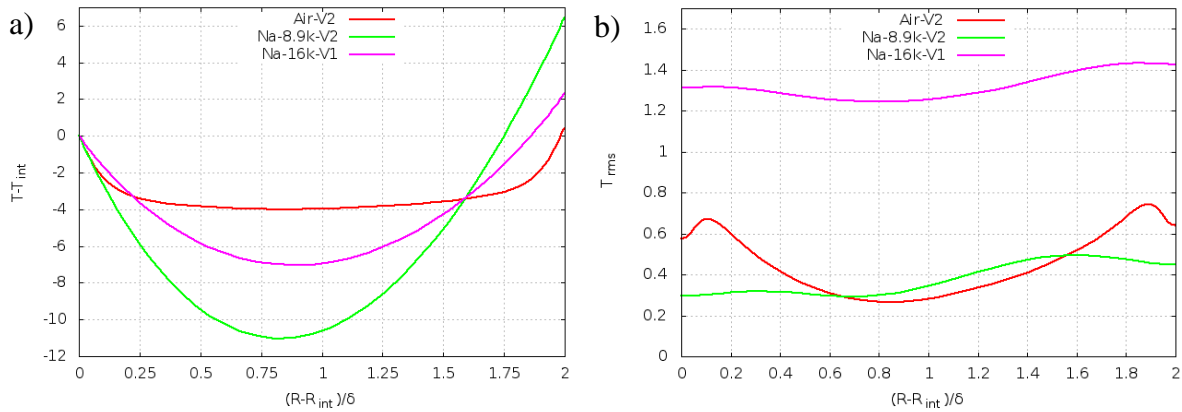


**Figure C.6-(a) Profil de température moyenne et (b) Racine carrée de la moyenne (r.m.s) de fluctuation de température pour l'air à  $Re=8900$  et le sodium à  $Re=8900$  et 16000**

La racine carrée de la moyenne (r.m.s) des fluctuations de température ( $T_{rms}$ ) est représentée sur la Figure C.6b pour l'air et le sodium. L'intensité de la variation de température au niveau du cylindre extérieur est plus grande que celle du cylindre intérieur en raison de l'effet de courbure. Les fluctuations de température donnent des valeurs non nulles sur les parois en raison des conditions aux limites imposées (iso-flux). Comme le nombre de Prandtl est réduit, la position du maximum des fluctuations en température ( $T_{rms}$ ) s'éloigne de la paroi et son amplitude diminue.

Les r.m.s des fluctuations de température dans le cas du sodium dépendent du nombre de Reynolds. Lorsque le nombre de Reynolds est augmenté de 8900 à 16000, la valeur efficace des variations de température ( $T_{rms}$ ) à la paroi est augmentée d'un facteur 4,3 (Figure C.6b). Dans la littérature, seules deux études évaluent l'effet du nombre de Reynolds sur le champ de températures à faible nombre de Prandtl ( $\sim 10^{-2}$ ). La première étude est celle de Kawamura, 1999 et la seconde d'Abe, 2004. Tous deux ont étudié l'écoulement du plomb-bismuth dans un canal rectangulaire. A notre connaissance, c'est la première étude réalisée en géométrie cylindrique annulaire où l'effet du nombre de Reynolds a été étudié sur les variations de

température paroi avec des conditions aux limites iso-flux avec un nombre de Prandtl de l'ordre de  $10^{-3}$ .

Le nombre de Prandtl turbulent ( $Pr_t$ ) est le rapport de la viscosité turbulente à la diffusivité turbulente. La variation de  $Pr_t$  en fonction de  $y^+$  près de la paroi est montré Figure C.7. Dans le cas de l'air,  $Pr_t$  est égal 1 comme attendu alors que pour le sodium  $Pr_t$ , il est plus grand que 1. Ceci montre que la valeur de  $Pr_t$  égal 1 utilisé par défaut dans les outils de CFD n'est pas correcte pour le sodium. De plus, le nombre de Reynolds a un effet sur le  $Pr_t$ . A faible nombre de Reynolds, le flux de chaleur turbulent est faible et par conséquent une valeur asymptotique du nombre de Prandtl turbulent de l'ordre de 10 est obtenue. Avec l'augmentation du nombre de Reynolds, le flux de chaleur turbulent augmente et la valeur asymptotique de nombre de Prandtl turbulent diminue à 3,5.

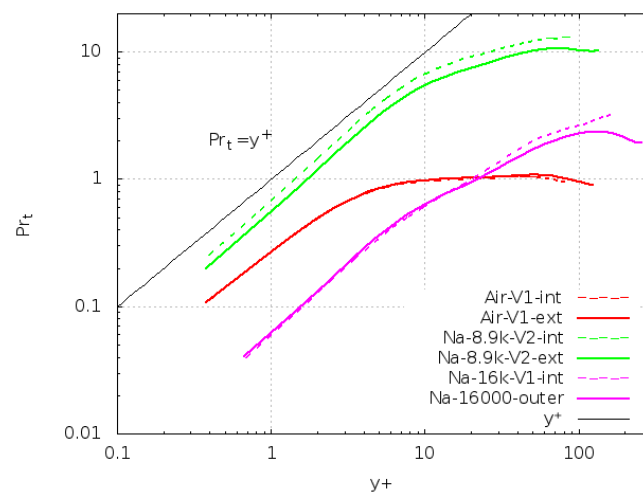


**Figure C.7-Evolution du nombre de Prandtl turbulent près de la paroi**

Ainsi, à faible nombre de Reynolds, il convient d'être prudent avec la valeur retenue pour le nombre de Prandtl turbulent. De nouvelles expériences sont nécessaires pour obtenir des corrélations du  $Pr_t$  pour des faibles nombres de Prandtl.

L'approche DNS aide à la compréhension du comportement thermohydraulique du sodium, mais est limitée à des géométries simples. Pour une géométrie complexe comme l'assemblage, nous utilisons l'approche LES. Nous avons d'abord étudié la même géométrie que celle du calcul DNS avec un flux thermique imposé pour un nombre de Reynolds égal à

16000. La valeur du nombre de Prandtl turbulent est fixée à 3,5 (valeur identique à celle obtenue par les calculs DNS). Le but de ce calcul est de comparer les approches DNS et LES.

La Figure C.8 montre la variation du profil radial de température. Les résultats LES et DNS montrent un bon accord pour la température moyenne.

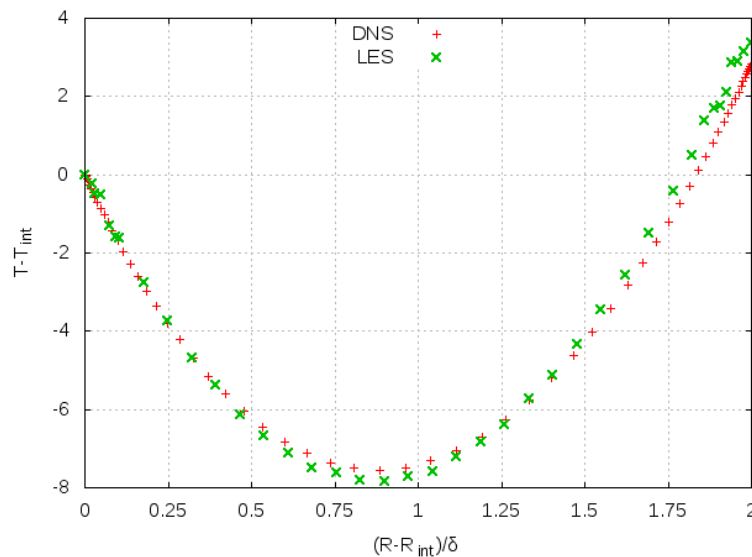


**Figure C.8-Comparaison de la température moyenne en DNS et LES**

L'amplitude des fluctuations de température obtenue par le calcul LES est environ 6,5 fois inférieure à celle des simulations DNS (Figure C.9 représenté par LES\_old\_inner). Cette faible amplitude est due à la dissipation numérique non physique. Ceci s'explique par :

- La formulation du terme source de température qui ne prend pas en compte l'effet de la vitesse. Ce terme source stabilise le domaine de température rapidement à une température périodique mais impose une dissipation non-physique des fluctuations de température qui diminue l'amplitude des fluctuations.
- Les schémas de convection utilisés pour les équations de température et de quantité de mouvement sont différents. L'approche DNS utilise le même schéma centré pour les deux équations alors que dans l'approche LES, le schéma centré n'est utilisé que pour l'équation de quantité de mouvement et un schéma upwind est choisi pour l'équation de la température.

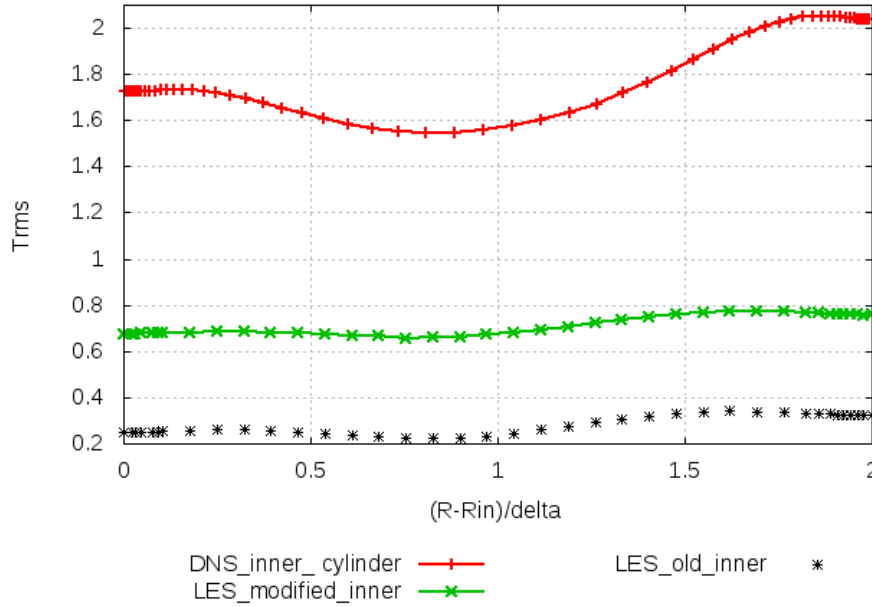


**Figure C.9- Comparaison des fluctuations de température en DNS et LES**

Les écarts sur les fluctuations de température ont été réduits en changeant le terme source et le schéma de convection de l'équation de température. Le terme source de température a été reformulé. Le schéma de convection a été changé pour réduire la dissipation (combinaison du schéma centré et du schéma upwind).

Avec les modifications du terme source et du schéma de convection, l'amplitude des oscillations de température dans LES a été augmentée. Toutefois, l'amplitude des variations de température en LES est encore inférieure celle la DNS par un facteur d'environ 2,5. Cet écart est principalement dû à la différence du schéma de convection entre les deux codes. Le code DNS est basé sur la méthode pseudo-spectrale avec une précision de l'ordre 4 en espace et utilise le schéma centré pour l'équation de la température. Le code TRIO\_U est basé sur la méthode aux éléments finis avec une précision de l'ordre de 2 en l'espace et utilise une combinaison du schéma centré et du schéma upwind.

En bilan, l'approche LES restitue avec précision le champ de température moyen, mais les variations de température sont sous-estimées d'un facteur de l'ordre de 2,5. Néanmoins, cet écart est jugé acceptable compte tenu de la différence entre les schémas et la précision numérique. Cette approche LES sera utilisée pour la suite pour l'étude de l'assemblage.



## C.5. Études thermohydrauliques de l'assemblage par la CFD

L'analyse thermohydraulique de l'écoulement dans l'assemblage est tout d'abord réalisée à l'aide de l'approche RANS qui permet d'étudier des géométries complexes avec des conditions aux limites idéales. Le maillage du domaine est effectué en utilisant la méthode de maillage par bloc permettant de limiter le nombre de mailles à 15 millions pour un assemblage de 217 aiguilles combustible entourées par un fil espaceur hélicoïdal. Le modèle de turbulence  $k-\varepsilon$  réalisable avec la loi de paroi est utilisé. Les fonctions de paroi utilisées pour modéliser l'effet de la paroi sur les gradients de température sont issues de la corrélation de Kader qui prend en compte l'effet du nombre de Prandtl sur le gradient de température à proximité de la paroi.

La perte de charge obtenue par l'étude RANS pour l'assemblage de 217 aiguilles est en accord avec la corrélation de Cheng-Todreas (Cheng, 1984). Les lignes de courant de l'écoulement (voir Figure C.10) montrent les deux régions à l'intérieur de l'assemblage pour lesquelles les distributions de vitesses et de températures sont différentes. La région centrale est caractérisée par une température élevée. La région périphérique hexagonale où la vitesse axiale est plus élevée conduit à une température plus faible. Le mélange de sodium se fait entre la zone centrale et périphérique. Ainsi, l'écoulement de sodium suit globalement le fil espaceur. Cette approche permet de caractériser la région du point chaud qui suit de près le fil espaceur avec une élévation de température d'environ 20°C par rapport à la moyenne.

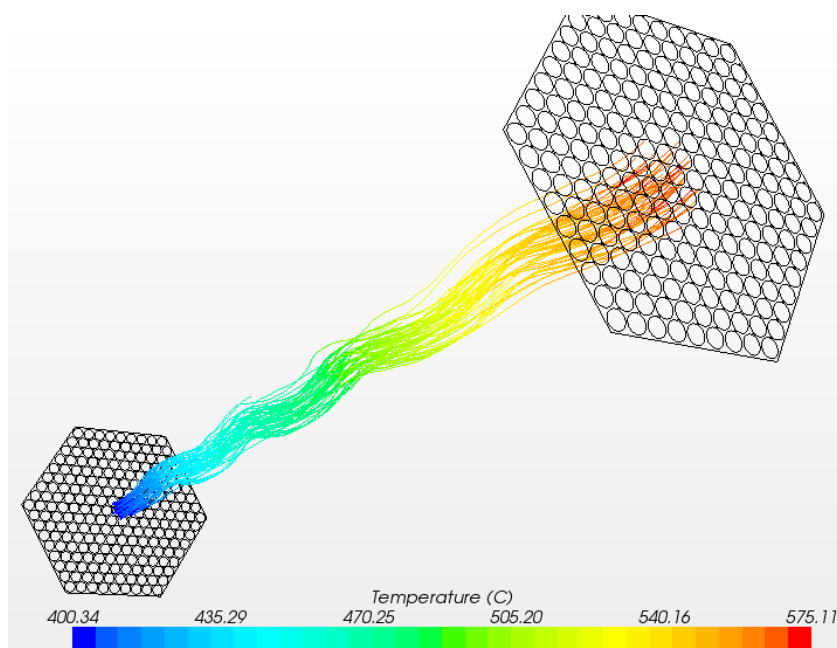


**Figure C.10-Lignes de courant de l'écoulement avec l'évolution de température autour de l'aiguille centrale**

L'étude RANS permet d'extraire un sous-domaine de l'assemblage représentatif de l'assemblage (Figure C.11). L'assemblage est constitué d'un ensemble de motifs élémentaires. Chaque motif comprend une aiguille avec son fil espaceur entouré de six tiers d'aiguille voisines.

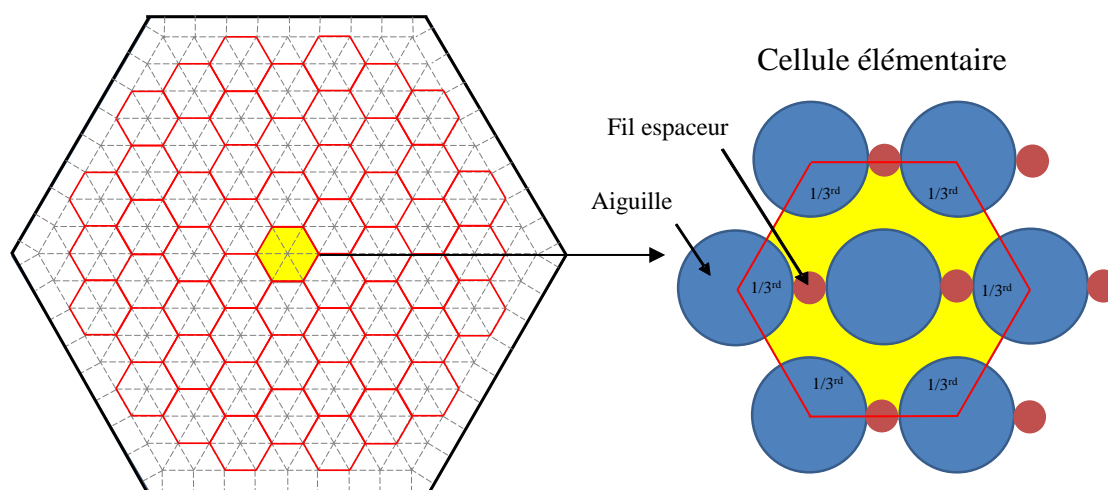


**Figure C.11-Représentation de la cellule élémentaire (hexagone rouge) à l'intérieur de l'assemblage complet**

L'étude LES restitue les phénomènes de turbulence et permet d'étudier l'effet de la forte diffusivité thermique du sodium sur les caractéristiques thermiques au point chaud. Les conditions périodiques axiales et radiales ont été utilisées pour l'écoulement. Une condition aux limites de flux est utilisée pour la thermique. Le flux sur le fil espaceur est le même que celui au niveau du combustible afin d'avoir une approche conservative. Ce calcul utilise les lois de paroi uniquement pour le champ de vitesse. En effet, la taille de la maille à proximité de la paroi est suffisamment petite pour capturer l'évolution thermique à proximité de la paroi. Ainsi, la précision des résultats pour le champ de températures en LES est proche celle de la DNS en termes de résolution près de la paroi. Avec cette étude, nous sommes en mesure de reproduire l'écoulement à l'état stationnaire et le champ thermique obtenu par l'approche RANS.

La position du point chaud et son amplitude sont similaires à celles obtenues pour l'approche RANS. La Figure C.12 montre l'évolution de la température le long des lignes de courant de l'écoulement. Elle indique aussi la position du point chaud de l'aiguille de combustible le long du fil espaceur.

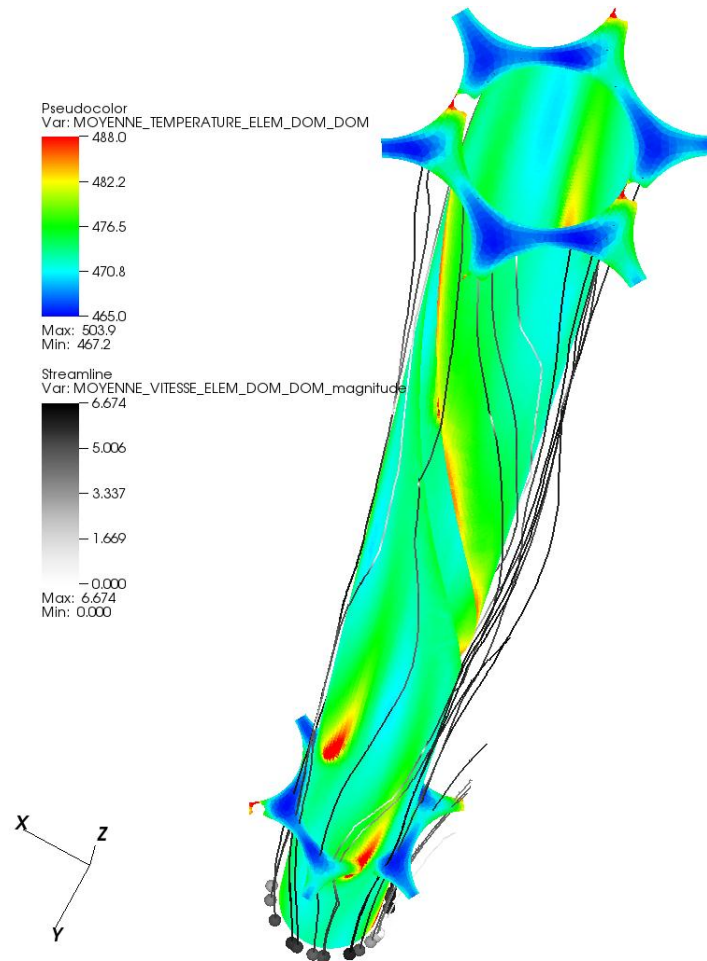


**Figure C.12- Lignes de courant de l'écoulement avec l'évolution de la température moyenne**

L'approche LES donne des informations sur l'amplitude des oscillations de température des points chauds. La valeur maximale de la racine carrée moyenne des oscillations de température est d'environ  $0,8^{\circ}\text{C}$  avec l'incertitude du facteur 2,5 issue de l'étude de validation sur le cylindre annulaire concentrique. Ainsi, l'amplitude maximale des oscillations de température dans l'assemblage au point chaud est d'environ  $2^{\circ}\text{C}$ , ce qui devrait être sans conséquences sur la tenue des matériaux de gainage.

Un autre paramètre qui influe sur la résistance mécanique est lié aux oscillations rapides temporelles de température correspondant aux basses fréquences comprises entre 0,1 et 10 Hz (Noda, 2003 ; Hannik 2011 ; Radu, 2007). Les spectres de température sont comparés à trois positions différentes (sommet du fil espaceur, en aval et amont du fil espaceur). D'après la Figure C.13, la distribution des spectres de température suit la loi universelle de Kolmogorov

en puissance  $-5/3$  dans la zone inertielle. L'amplitude du spectre de température est plus élevée autour du fil espaceur par rapport à celle mesurée sur l'aiguille loin du fil espaceur. Le spectre des trois positions autour du fil espaceur est proche, sauf pour les basses fréquences. On n'observe pas d'effet dominant à basse fréquence (0,1 à 10 Hz). Le fil espaceur crée localement une zone de décélération de l'écoulement qui entraîne une augmentation de température d'une amplitude de l'ordre de  $20^{\circ}\text{C}$  mais la diffusivité thermique de sodium est suffisamment grande pour conduire rapidement la chaleur et éviter toute amplitude élevée et limiter les effets à basse fréquence dans cette région.

Le rapport de l'effusivité du sodium et celle de l'acier de la gaine joue un rôle important pour déterminer si ces oscillations se propagent vers les structures. L'effusivité d'un matériau  $E_f$  est définie comme la vitesse du transfert thermique. L'effusivité de l'acier inoxydable (SS316) est égale à  $7526 \text{ J/m}^2\text{Ks}^{0.5}$ . Cette effusivité est du même ordre que celle de sodium ( $8516 \text{ J/m}^2\text{Ks}^{0.5}$ ). Ainsi, les fluctuations du sodium se transmettent immédiatement aux structures qui verront donc les mêmes contraintes thermiques.

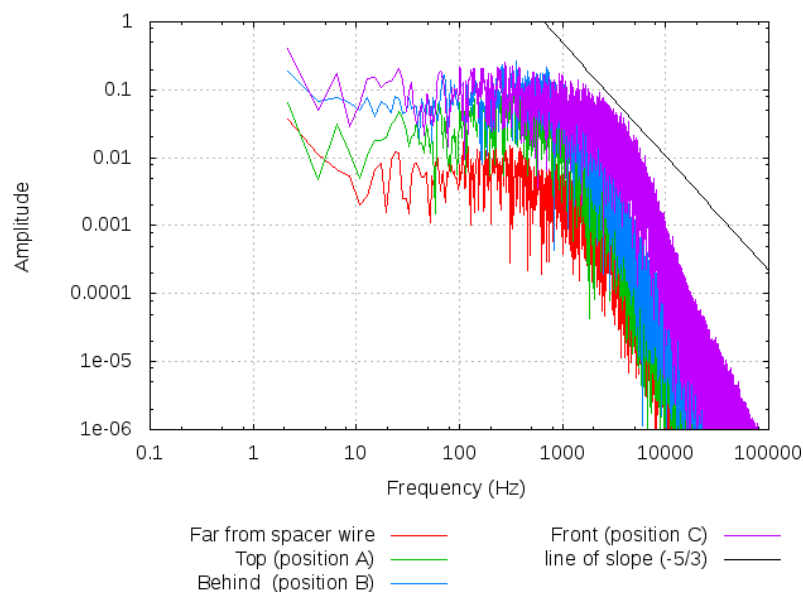


**Figure C.13-Comparaison des spectres des fluctuations de la température (densité de spectre de puissance) à trois positions différentes autour du fil espaceur et loin du fil espaceur**

## C.6. Conclusions

L'objectif principal de la thèse est de faire une étude thermohydraulique de l'écoulement turbulent de sodium à l'intérieur de l'assemblage d'un réacteur à neutrons rapides à caloporteur sodium.

Une évaluation correcte des caractéristiques thermiques et hydrauliques autour du fil espaceur de l'assemblage est importante pour la sûreté du réacteur.

L'étude a été réalisée en utilisant l'approche CFD en condition nominale pour l'écoulement monophasique de sodium.

Le sodium liquide est caractérisé par un très faible nombre de Prandtl ( $Pr \sim 0,001$ ) par rapport à celui de l'eau ( $Pr \sim 1$ ). Les études de DNS pour le faible nombre de Prandtl sont disponibles dans la littérature pour des cas académiques.

L'analogie de Reynolds utilisé dans les approches RANS et LES introduit le concept de nombre de Prandtl turbulent ( $Pr_t$ ). La valeur par défaut égale à 1 ne permet pas déterminer le champ thermique pour un faible nombre de Prandtl.

L'étude DNS porte sur le transfert de chaleur pour un écoulement turbulent pleinement développé de sodium liquide dans l'espace annulaire concentrique avec des parois iso-flux. Il s'agit d'une géométrie simplifiée représentative de l'écoulement de sodium dans l'assemblage.

Les principaux enseignements de cette étude DNS sont rappelés ci-après :

1. **Domaine de calcul** : en sodium, les structures thermiques sont grandes dans les directions axiale et azimutale.
2. **Turbulence thermique** : en sodium, la conduction moléculaire est le mode du transfert de chaleur prépondérant à la paroi contrairement aux fluides comme l'eau ou l'air où les effets turbulents dominent les effets de conduction. En conséquence, une stratification thermique apparaît dans la direction radiale. Cette stratification thermique est bénéfique dans l'assemblage car le sodium peut assurer un refroidissement efficace même à faible vitesse.

3. **Les fluctuations de température** : en sodium, avec un nombre de Reynolds 8900, les variations de température sont inférieures d'un facteur de l'ordre de grandeur de 200 par rapport à celles de l'air et la position des variations de température maximales s'éloigne de la paroi.
4. **Effet du nombre de Reynolds sur le champ thermique** : en sodium, un effet plus marqué du nombre de Reynolds est observé sur le champ thermique.
5. **Nombre de Prandtl turbulent** : en sodium, la valeur du nombre de Prandtl turbulent est supérieure à 1 avec une sensibilité élevée à faible nombre de Reynolds pour un écoulement turbulent. Avec la diminution du nombre de Reynolds (16000 à 8900), le nombre de Prandtl turbulent augmente de 3,5 à 10. Dans la littérature, les corrélations pour le nombre de Prandtl turbulent montrent une grande variation de nombre de Prandtl de 2,5 à 15 pour un nombre de Reynolds de 16000 et 8900. Ces corrélations ont été développées pour les fluides avec un nombre de Prandtl de l'ordre de 0.01. Par conséquent, il est nécessaire d'obtenir des nouvelles corrélations pour déterminer le nombre de Prandtl turbulent.

La comparaison entre les résultats DNS et LES indique que les gradients de vitesse près de la paroi sont sous-estimés par l'approche LES, mais le profil global des fluctuations r.m.s de vitesse et d'énergie cinétique turbulente sont bien prédits. Cependant, les valeurs maximales sont sous-estimées car en LES sont modélisées les petites structures à l'échelle de la grid. Le transfert de chaleur se faisant par conduction moléculaire en sodium liquide, le champ de températures moyennes obtenu en LES est en accord avec celui issu de la DNS.

Cependant, les fluctuations de température sont sous-estimées en LES. La dissipation numérique provenant de l'utilisation du schéma de convection est la principale cause.

L'étude RANS sur l'assemblage donne des informations globales sur l'assemblage. On distingue deux régions de l'assemblage avec des distributions de vitesse et de température différentes ; la région centrale intérieure de l'assemblage a une température relativement élevée par rapport à la région périphérique. La vitesse plus élevée conduit à une température plus faible. L'écoulement autour du fil espaceur crée un mélange local de l'écoulement, mais le brassage entre les deux régions de l'assemblage n'est pas observé. Ce calcul met en

évidence le point chaud (région de température maximale du sodium) présent derrière le fil espaceur avec une augmentation de température d'environ 20°C par rapport à la valeur moyenne.

L'étude LES est réalisée sur un domaine limité de l'assemblage représentant l'écoulement dans l'assemblage avec des conditions périodiques. Cette région contient l'axe central de l'aiguille qui est la région la plus chaude et un tiers de chacune des six aiguilles voisines et un pas d'hélice du fil espaceur. Le calcul LES respecte la géométrie réelle de l'assemblage et les conditions d'écoulement de sodium avec  $Pr = 0,001$  et  $Re = 50000$ . Ce calcul étant proche des conditions réacteur, cela permet de caractériser l'écoulement autour du fil espaceur et de répondre à la problématique du point chaud dans l'assemblage combustible avec fil espaceur refroidi en sodium.

Les domaines hydrauliques et thermiques sont bien représentés par des conditions périodiques. La température maximale du fluide est présente à deux endroits. La première position est en aval du fil espaceur et la seconde se trouve au sommet de fil espaceur quand il se rapproche de l'aiguille de combustible voisine. La différence de température entre le point chaud et la température au niveau du plan est d'environ 18°C. Les calculs statistiques obtenus pour ces points chauds donnent des fluctuations de température de l'ordre de 1°C à 2°C.

La conductivité thermique élevée de sodium transmet ces fluctuations de température rapidement à la paroi solide. L'effusivité de l'acier 316 et du sodium étant comparable, les contraintes thermiques sont du même ordre de grandeur de part et d'autre.

La fréquence des oscillations de température joue un rôle important dans la caractérisation de la résistance mécanique. La densité de puissance spectrale des fluctuations de température a été évaluée et montre l'absence de pic dominant pour une fréquence inférieure à 10Hz. Le risque de fatigue thermique qui affecte la résistance mécanique de la gaine peut être déterminé par l'utilisation de la densité de puissance spectrale avant d'entreprendre une analyse plus détaillée en thermo-mécanique.



## C.7. Perspectives

Il existe de nombreuses perspectives découlant de cette étude.

Une estimation plus précise des variations de la température peut être donnée par l'approche DNS où les petites échelles de l'écoulement et les structures thermiques en longueur et en temps sont complètement résolues avec des schémas numériques d'un ordre supérieur de précision. Cette étude peut montrer l'effet d'un obstacle sur la stratification thermique dans l'écoulement de sodium.

Une autre perspective de ce travail est la représentation de la partie solide de l'aiguille et du fil espaceur dans le domaine de calcul. Dans la présente thèse, nous nous sommes concentrés uniquement au point chaud dans le domaine fluide de l'assemblage et l'effet de l'aiguille a été représenté avec une condition limite en flux de chaleur constant. Cependant, une estimation plus précise du point chaud, ce qui peut probablement affecter l'intégrité mécanique de la gaine, doit englober la partie solide de l'assemblage représentant les pastilles de combustible, le fil espaceur afin de prendre en compte l'anisotropie du flux de chaleur.

Dans l'étude LES de l'assemblage, nous nous sommes concentrés sur l'axe central de l'aiguille combustible pour l'analyse thermohydraulique dans les conditions nominales. A l'échelle locale de l'aiguille centrale, cette étude ne met pas en évidence de conséquences négatives au niveau du point chaud existant. Cependant, il y a d'autres aspects à ce problème :

- Pendant un cycle d'irradiation, l'assemblage subit une déformation avec des phénomènes d'inclinaison et de gonflement du combustible conduisant à une perte de symétrie dans l'assemblage. L'écoulement va être sensiblement modifié, qui pourrait accroître le sous-refroidissement.
- La thermohydraulique de l'assemblage est fortement dépendante des paramètres géométriques comme le rapport entre le diamètre de l'aiguille combustible et le diamètre du fil espaceur ( $D_p/D_w$ ) et le ratio du pas d'hélice ( $H/D_p$ ). Les études de thermohydraulique effectuées dans le passé étaient basées sur des corrélations empiriques et maintenant avec l'avènement des techniques de CFD, l'analyse thermohydraulique est envisageable à l'échelle du l'assemblage.

Les données expérimentales sont limitées sur des design d'assemblage de type CFV (gros diamètre et petit fil espaceur). Un effort de compilation / dépouillement des données existantes est nécessaire.

L'approche numérique nécessite un support expérimental (échelle, géométrie, caloporteur à définir) pour vérifier l'approche numérique, comprendre les phénomènes physiques, et orienter et conforter les choix de design.

# TABLE OF FIGURES

Figure 1- Schema diagram of SFR pool type reactor .....	2
Figure 2-Representation of the CFV core of ASTRID showing radial heterogeneity .....	3
Figure 3- Representation of the CFV core of ASTRID showing axial heterogeneity .....	3
Figure 4-Representation of different parts of 217 fuel-pins sub-assembly on the left (view from above) and fuel pin with helical wrapped spacer wire on the right .....	5
Figure 5-Velocity distribution in the interior sub-channel (Bishop, 1980).....	6
Figure 6-Schematic representation of the CFD methods – DNS, LES and RANS.....	8
Figure 1.1-Examples of turbulence in nature (a) Visualization of wake vortices consecutive passage of a light aircraft through a plume of smoke (Source NASA Langley Research Center - EL 1996 00130) (b) Radiograph of Hurricane Frances approaching the coasts of Florida and taken by the satellite GOES-12. ....	12
Figure 1.2-Energy cascade and spectral energy density of a turbulent flow traced in logarithmic scales.....	15
Figure 1.3-Difference between RANS, LES and DNS method on wave number (K)-energy spectrum (E(K)) .....	17
Figure 1.4-Flame simulated by DNS, LES and RANS (Poitou, 2009).....	17
Figure 1.5-Time evolution of a flow variable $\phi$ obtained by approach DNS, LES and RANS (Dorey, 2012).....	20
Figure 1.6-Scale difference and similarity of the thermal and momentum field in fluids with different molecular Prandtl numbers, Pr (LBE Handbook, 2007) .....	22
Figure 1.7-Sketch of energy spectra $E(K)$ for velocity fluctuations and $E_T(K)$ for temperature fluctuations in forced channel flows at $Pr=1$ and $Pr \ll 1$ (Grötzbach, 2013; Lesieur, 1997) .....	26
Figure 1.8-The different zones of turbulence near wall: hydraulic boundary layer.....	27
Figure 1.9-Non-dimensional velocity profile.....	28
Figure 1.10-The different zones of turbulence near wall: thermal boundary layer.....	30
Figure 1.11-Effect of molecular Prandtl number on the non-dimensional temperature profile at $Re_\tau=1020$ (Abe, 2004). Symbol “O” represents the result of Kader (1981).....	31
Figure 1.12-Influence of Peclet number on the turbulent thermal diffusivity normalized by molecular thermal diffusivity (Grötzbach, 1981) .....	34
Figure 1.13a- Turbulent Prandtl number from various correlations as a function of Prandtl number by keeping Reynolds number constant .....	37
Figure 1.13b- Turbulent Prandtl number from various correlations as a function of Reynolds number by keeping Prandtl number constant.....	37
Figure 1.14-The velocity distribution for 19 pin sub-assembly showing dimensionless streamwise velocity on the left (a) and transverse velocity on the right (b) (Rolfo, 2012) .....	39
Figure 1.15-Photograph of GR19 sub-assembly used for boiling experiments showing the clad melt down locally at the wake of wire .....	41
Figure 1.16-Time averaged velocity field predicted by LES simulation using Nek5000 on the left and steady state velocity field predicted by RANS simulations using Star-CD (Pointer, 2009) .....	43
Figure 1.17-Comparison of LES and RANS simulation predictions of axial distribution of cross-channel flow velocities for four channels (Pointer, 2009) .....	44
Figure 1.18-Computational domain used by fisher (Fischer, 2007) for hydraulic LES study. 45	
Figure 1.19-Schematic geometry studied by Ranjan et al. (Ranjan, 2010).....	46

Figure 1.20-Iso-contours of non-dimensional temperature at (a) $Pr=1$ and (b) $Pr=10^{-2}$ (Ranjan, 2011) .....	47
Figure 1.21-Average temperature distribution at a horizontal cut plane (top) and the three dimensional geometry for the two cases studied by Merzari (Merzari, 2012) a) with contact b) with no contact between the wire and wall .....	49
Figure 2.1- Schematic representation of separation of scales in LES on a calculation grid (Husson, 2007) .....	66
Figure 2.2-Staggered arrangement for interior grid points (left) and at the boundaries of the mesh in $r$ - $z$ plane .....	78
Figure 2.3-Energy balance on a periodic domain ( $z$ ) with a heated wall .....	90
Figure 2.4-Velocity gradient near the wall with and without wall function for a mesh with first mesh cell from wall at a distance, $y +$ of 100 .....	91
Figure 3.1- Schematic representation of the simplified geometry for DNS study- a) Sub-assembly with 217 fuel pins (top view), b) Central region of sub-assembly with 217 fuel pins (top view), c) Simplified representation-concentric annulus (side view), d) top view of the concentric annulus .....	92
Figure 3.2-Mesh of the computational domain with size $\pi/2$ in azimuthal direction and zoom view to show the mesh refinement near the wall in radial direction .....	97
Figure 3.3-Mesh of the computational domain with size $2\pi$ in azimuthal direction and zoom view to show the mesh refinement near the wall in radial direction .....	97
Figure 3.4-Auto-correlation for fluctuations in axial velocity and temperature in a) axial direction b) azimuthal direction .....	102
Figure 3.5-Auto-correlation for fluctuations in axial velocity and temperature in sodium (Na-16K-V1) a) axial direction and b) azimuthal direction .....	103
Figure 3.6-Auto-correlation for fluctuations in temperature in sodium (Na-8.9K-V2) a) axial direction and b) azimuthal direction .....	105
Figure 3.7-Mean velocity profile normalized by the friction velocity at each wall .....	107
Figure 3.8-Root mean square velocity fluctuations (a) Wall- normal (radial) velocity, (b) Azimuthal velocity, (c) Axial velocity .....	110
Figure 3.9-Position of a) maximum velocity and b) zero total shear stress .....	111
Figure 3.10-Mean temperature distributions .....	112
Figure 3.11-Root mean square temperature fluctuations .....	113
Figure 3.12-Turbulent heat flux (a) Axial direction (b) Wall- normal (radial) direction .....	114
Figure 3.13-Distribution of turbulent wall normal heat flux and total heat flux .....	115
Figure 3.14-a) Instantaneous axial velocity and b) Iso surface of $Q$ criteria from DNS calculation for air (AIR-V2) and sodium (Na-8.9K-V2) at Reynolds number 8900 .....	118
Figure 3.15-a) Instantaneous temperature and b) Iso surface of temperature from DNS calculation for air (AIR-V2) and sodium (Na-8.9K-V2) at Reynolds number 8900 .....	119
Figure 3.16-Mean temperature profile for air and sodium at $Re=8900$ and sodium at $Re=16000$ .....	120
Figure 3.17-Mean Temperature profile normalized by friction temperature versus $y +$ .....	121
Figure 3.18- Root mean square temperature fluctuations a) with dimensions for sodium and air and b) non-dimensional normalized by friction temperature versus $y +$ for sodium at different Reynolds number .....	122
Figure 3.19- Wall-normal turbulent heat flux normalized by friction temperature and friction velocity versus $y +$ for sodium at different Reynolds number .....	123
Figure 3.20- Axial turbulent heat flux normalized by friction temperature and friction velocity versus $y +$ for sodium at different Reynolds number .....	124
Figure 3.21-Distribution of turbulent wall normal heat flux and total heat flux (a) with zoom to see the effect of Reynolds number (b) .....	125

Figure 3.22-Energy spectra in axial wave number for air and sodium .....	126
Figure 3.23-Asymptotic behavior of the temperature fluctuations for air and sodium.....	127
Figure 3.24-Asymptotic behavior of the turbulent axial heat flux for sodium and air.....	128
Figure 3.25- Asymptotic behavior of the turbulent wall normal heat flux for sodium and air .....	129
Figure 3.26-Near-wall behavior of turbulent viscosity .....	130
Figure 3.27-Near wall behavior of turbulent thermal diffusivity .....	131
Figure 3.28-Turbulent Prandtl number variation near the wall for sodium at different Reynolds number and compared with air as a function of $y^+$ (a) and log-log scale (b)	132
Figure 3.29-2Dimensional view of the tetrahedral mesh created by ICEM tool .....	136
Figure 3.30-Histogram showing distance of the first cell from wall in wall units.....	136
Figure 3.31-Time variation of axial velocity and temperature at a local point.....	139
Figure 3.32-Fourier transform of velocity and temperature signal showing that the temperature fluctuations follow Kolmogorov law .....	139
Figure 3.33-Comparison of mean axial velocity normalized with bulk velocity between DNS (Na-16K-V1) and LES .....	141
Figure 3.34-Comparison of root mean square velocity fluctuations between DNS (Na-16K-V1) and LES (a) Wall- normal (radial) velocity, (b) Azimuthal velocity, (c) Axial velocity.....	142
Figure 3.35-Turbulent kinetic energy comparison between DNS (Na-16K-V1) and LES ....	143
Figure 3.36-Comparison of mean temperature profile between DNS (Na-16K-V1) and LES .....	144
Figure 3.37-Root-mean-square temperature fluctuations.....	145
Figure 4.1-Schema of 217-fuel pin sub-assembly showing geometry parameters and boundary conditions a) axial view and b) transversal view .....	147
Figure 4.2-Meshing of three different representations of wire-pin contact (Rolfo, 2012).....	150
Figure 4.3-Three dimensional meshing of the computational domain.....	152
Figure 4.4-Heat flux imposed on the fuel pins as a function of axial height .....	153
Figure 4.5-Pressure drop variation with Reynolds number for different correlations and simulation.....	156
Figure 4.6-Streamlines of the flow around the central fuel pin with evolution of temperature .....	157
Figure 4.7-Axial distribution of temperature in 3-D .....	157
Figure 4.8- 1-D profile of temperature variation with respect to axial height .....	158
Figure 4.9-Radial distribution of temperature in 2-D plane near the outlet plane and the curve showing temperature variation with respect to radius .....	159
Figure 4.10-Variation of Nusselt number at the central fuel pin with axial height.....	160
Figure 4.11-Representation of the selected unit cell (red hexagon) inside the complete 217 fuel pin sub-assembly .....	161
Figure 4.12-Schematic representation of the unit cell of sub-assembly. (a) Transverse cut plane showing the solid part (fuel pin +spacer) and the fluid part (in yellow). (b) Axial view of the fluid domain .....	164
Figure 4.13-2-Dimensional view of the tetrahedral mesh created by centaur tool .....	166
Figure 4.14-Representation of periodic boundary conditions in radial direction .....	167
Figure 4.15-Variation of velocity with time showing transition to turbulence at 0.02s at point (0, -0.005,0.09) in the center of sub-channel .....	169
Figure 4.16-Variation of (a) axial velocity and (b) temperature with time at a local point (0, -0.005, 0.09) in the center of sub-channel.....	170
Figure 4.17-Comparison of axial velocity magnitude between RANS and LES.....	171
Figure 4.18-Comparison of transverse velocity magnitude between RANS and LES .....	172

Figure 4.19-Comparison of transverse velocity (vector) between RANS and LES and zoom over the spacer wire .....	173
Figure 4.20-Comparison of temperature drop between RANS and LES .....	174
Figure 4.21-Position and numbering of axial probe in the sub-channel referred as SC .....	175
Figure 4.22-Axial variation of temperature in the sub-channel probes (a) Sub-channel probe 2,4,6 and (b) sub-channel probe 1,3,5 (refer to figure 4.20 for labels SC).....	175
Figure 4.23-Time averaged temperature and root mean square of temperature at different planes .....	177
Figure 4.24-Three positions around the spacer wire to determine the temperature fluctuations .....	178
Figure 4.25-Temperature fluctuations as a function of axial position for three positions around the spacer wire .....	178
Figure 4.26-Power spectral density of a typical thermal stripping (Chellapandi, 2009) .....	180
Figure 4.27-Temperature spectra at different axial position for three positions – (a) Top of the spacer wire (b) Behind the spacer wire and (c) front of the spacer wire .....	181

# LIST OF TABLES

---

Table 1.1-Physical properties of sodium and water (Cebeci, 1984) .....	21
Table 1.2-List of correlations for turbulent Prandtl number .....	35
Table 2.1-Coefficients and terms for the standard k- $\epsilon$ model and Realizable k- $\epsilon$ model .....	64
Table 3.1-Overview of DNS calculations for Pr=0.025 .....	90
Table 3.2-Computational domain and data set for different DNS calculations .....	95
Table 3.3- Data set and grid resolution for the different DNS calculations .....	98
Table 3.4-Mean flow and thermal parameters for the DNS study of sodium at two different Reynolds number .....	116
Table 3.5-Data set for LES calculation compared with the DNS calculation.....	133
Table 3.6-Numerical schemes for LES calculations .....	135
Table 3.7-Grid resolution of tetrahedral mesh for the first three layers around the wall .....	137
Table 3.8-Mean flow parameters for LES and DNS calculation with sodium at Reynolds number 16000 .....	141
Table 4.1-Geometrical parameters of the sub-assembly .....	146
Table 4.2-Flow parameter for different kinds of sub-channels in sub-assembly .....	148
Table 4.3-Summary of different ways to represent the contact point between fuel pin and spacer wire (Bieder, 2010) .....	151
Table 4.4-Thermo-physical properties of sodium at 470 °C .....	154
Table 4.5-Flow conditions for different calculations .....	154
Table 4.6-Numerical schemes for LES calculations .....	162
Table 4.7-Geometrical parameters of the unit cell of sub-assembly for LES calculation.....	164
Table 4.8-Initial conditions for the thermal-hydraulic LES simulation .....	170
Table 4.9-Space and time averaged temperature at different plane to estimate the hot spot temperature .....	176

# ABSTRACT

---

The thesis focuses on the numerical simulation of sodium flow in wire wrapped sub-assembly of Sodium-cooled Fast Reactor (SFR). First calculations were carried out by a time averaging approach called RANS (Reynolds-Averaged Navier-Stokes equations) using industrial code STAR-CCM+. This study gives a clear understanding of heat transfer between the fuel pin and sodium. The main variables of the macroscopic flow are in agreement with correlations used hitherto. However, to obtain a detailed description of temperature fluctuations around the spacer wire, more accurate approaches like LES (Large Eddy Simulation) and DNS (Direct Numerical Simulation) are clearly needed. For LES approach, the code TRIO\_U was used and for the DNS approach, a research code was used. These approaches require a considerable long calculation time which leads to the need of representative but simplified geometry. The DNS approach enables us to study the thermal hydraulics of sodium that has very low Prandtl number inducing a very different behavior of thermal field in comparison to the hydraulic field. The LES approach is used to study the local region of sub-assembly. This study shows that spacer wire generates the local hot spots ( $\sim 20^{\circ}\text{C}$ ) on the wake side of spacer wire with respect to the sodium flow at the region of contact with the fuel pin. Temperature fluctuations around the spacer wire are low ( $\sim 1-2^{\circ}\text{C}$ ). Under nominal operation, the spectral analysis shows the absence of any dominant peak for temperature oscillations at low frequency (0.1-10 Hz). The obtained spectra of temperature oscillations can be used as an input for further mechanical studies to determine its impact on the solid structures.

**Key words :** Turbulent heat transfer, Low Prandtl number, SFR, Sub-assembly with spacer wire, Thermal-hydraulic, ASTRID, DNS, LES

# RÉSUMÉ

---

La thèse porte sur la simulation numérique de l'écoulement du sodium pour les assemblages de réacteurs à neutrons rapides à caloporteur sodium de type aiguille à fil espaceur. Des premiers calculs réalisés par une approche moyennée de type RANS (Reynolds-Averaged Navier-Stokes) à l'aide du code industriel STAR-CCM+. De cette modélisation, il ressort une meilleure compréhension des transferts de chaleur opérés entre les aiguilles et le sodium. Les principales grandeurs macroscopiques de l'écoulement sont en accord avec les corrélations. Cependant, afin d'obtenir une description détaillée des fluctuations de température au niveau des fils espaceur, une approche plus détaillée de type LES (Large Eddy Simulation) et DNS (Direct Numerical Simulation) est apparue indispensable. Pour la partie LES, le code TRIO\_U a été utilisé. Concernant la partie DNS, un code de recherche a été utilisé. Ces approches requièrent des temps de calculs considérables qui ont nécessité des géométries représentatives mais simplifiées. L'approche DNS permet d'étudier l'écoulement à bas nombre de Prandtl, qui induit un comportement très différent du champ thermique relativement au champ hydraulique. Le calcul LES de l'assemblage montre que la présence du fil espaceur génère l'apparition de points chauds locaux ( $\sim 20^{\circ}\text{C}$ ) en aval de celui-ci par rapport à l'écoulement sodium, au niveau de son contact avec l'aiguille. Les fluctuations de température au niveau des fils espaceur sont faibles ( $\sim 1-2^{\circ}\text{C}$ ). En régime nominal, l'analyse spectrale montre l'absence de grande amplitude d'oscillations de température à basse fréquence (0.1-10Hz); les conséquences sur la tenue mécanique des structures devront être analysées.

**Mots clés :** Transfert de chaleur, Bas nombre de Prandtl, Réacteurs à Neutrons Rapides, Assemblage avec fil espaceur, Ecoulement turbulent de Sodium, Thermohydraulique, ASTRID, DNS, LES